



**HAL**  
open science

# Crystal chemistry and thermoelectric properties of bismuth-based ternary and quaternary sulfides

Krishnendu Maji

► **To cite this version:**

Krishnendu Maji. Crystal chemistry and thermoelectric properties of bismuth-based ternary and quaternary sulfides. Cristallographie. Normandie Université, 2023. Français. NNT : 2023NORMC247 . tel-04426611

**HAL Id: tel-04426611**

**<https://theses.hal.science/tel-04426611>**

Submitted on 30 Jan 2024

**HAL** is a multi-disciplinary open access archive for the deposit and dissemination of scientific research documents, whether they are published or not. The documents may come from teaching and research institutions in France or abroad, or from public or private research centers.

L'archive ouverte pluridisciplinaire **HAL**, est destinée au dépôt et à la diffusion de documents scientifiques de niveau recherche, publiés ou non, émanant des établissements d'enseignement et de recherche français ou étrangers, des laboratoires publics ou privés.

# THÈSE

Pour obtenir le diplôme de doctorat

Spécialité **CHIMIE**

Préparée au sein de l'**Université de Caen Normandie**

**Crystal chemistry and thermoelectric properties of bismuth-based ternary and quaternary sulfides**

Présentée et soutenue par  
**KRISHNENDU MAJI**

**Thèse soutenue le 16/11/2023**

devant le jury composé de :

|                       |   |                    |
|-----------------------|---|--------------------|
| M. MICKAËL BEAUDHUIN  | Maître de conférences HDR - Ecole nationale supérieure de chimie de Montpellier | Rapporteur du jury |
| MME MARIA IBANEZ      | Professeur - Institut of Science and Technology Austr                           | Rapporteur du jury |
| M. CARMELO PRESTIPINO | Chargé de recherche au CNRS - UNIVERSITE RENNES 1                               | Membre du jury     |
| MME ADÈLE RENAUD      | Maître de conférences - Université de Rennes (EPE)                              | Membre du jury     |
| M. PHILIPPE BOULLAY   | Directeur de recherche au CNRS - ENSICAEN                                       | Président du jury  |
| M. EMMANUEL GUILMEAU  | Directeur de recherche au CNRS - ENSICAEN                                       | Directeur de thèse |

Thèse dirigée par **EMMANUEL GUILMEAU** (Laboratoire de cristallographie et sciences des matériaux (Caen))



***Dedicated to my parents***



## DECLARATION

I hereby declare that this thesis entitled “**Crystal chemistry and thermoelectric properties of bismuth-based ternary and quaternary sulfides**” is a result of studies carried out by me at the Laboratoire de Cristallographie et Sciences des Matériaux (CRISMAT), Caen, France, under the supervision of **Dr. Emmanuel Guilmeau**. This work has not been submitted elsewhere for the award of any degree or diploma.

In keeping with the general practices of reporting scientific observations, due acknowledgements have been made wherever the work described is based on the findings of other investigators in a collaborative pursuit. Any omission which might have occurred by oversight or error in judgement is regretted.

*Krishnendu Maji*

Caen, France  
22/09/2023

---

Krishnendu Maji



## CERTIFICATE

I hereby certify that the work described in this thesis titled “**Crystal chemistry and thermoelectric properties of bismuth-based ternary and quaternary sulfides**” has been carried out by Mr. Krishnendu Maji at CRISMAT, University of Caen Normandy, France under my supervision and that it has not been submitted elsewhere for the award of any degree or diploma.

Caen, France

08/09/2023

---

Dr. Emmanuel Guilmeau

(Supervisor)

## ACKNOWLEDGEMENTS

Completion of my Ph.D. thesis necessitated a lot of guidance and supports from many people. I take this opportunity to mention a few of them. However, my sincere thanks extend to everyone who has played a role in making this dream a reality.

My research supervisor, Dr. Emmanuel Guilmeau for constant guidance throughout my Ph.D. career and giving me the freedom to carry out and express my scientific thoughts. His inputs in both scientific and non-scientific problems (like how to make better presentations, how to write grant proposals etc.) have led to me become a much well-prepared researcher.

My beloved lab mates: Dr. Paribesh, Dr. Xingchen, Dr. Gabin, Mr. Abdel. Mr. Lucas, Mr. Christophe for their cheerful company and keeping a healthy competitive spirit in the lab.

My sincere thanks go to Dr. Wilfrid Prellier, the director of the CRISMAT laboratory, for not only welcoming to CRISMAT but also for his unwavering support, both personally and professionally.

I would like to thank Prof. Bernard Raveau, Dr. Pierric Lemoine, Dr. Adèle Renaud, Dr. Bin Zhang, Dr. Xiaoyuan Zhou, Dr. Virginia Carnevali, Dr. Christophe Candolfi, Dr. Rabih Al Rahal Al Orabi, Dr. Marco Fornari, Dr. Paz Vaqueiro, Dr. Mathieu Pasturel, Dr. Carmelo Prestipino, Dr. Carmelo Prestipino, Dr. Vincent Pelletier, Dr. Régis Gautier, Dr. Bertrand Lenoir for the fruitful scientific collaborations and all the insightful discussions. I have learnt a lot whenever we had meeting or discussion with them.

Constant assistance and a friendly nature of the technical staff helped me doing my experiments smoothly. Here, I would like to acknowledge Mrs. Chistele, Mr. Jerome, Mrs. Sophie, Msr. Stephanie and others.

I thank all the staff members associated with academic, admin and technician; Marie, Sandrine, Gratien and Eric.

I would like to thank my friends in Caen would never be so meaningful: Anjali, Mufeed, Parameswari, Saumya, Abhishek, Oualyd, Neeraj, Rojeeta, Mudit; Hasanthi, Hari, Pavan, Masmura Jefry, Álvaro, Nishu, Sayan, Indu, Abdel, Moussa, Erica, Sara, Marie, Serge.

I would like to acknowledge my childhood, school, college, and university friends who left an everlasting impression on me.

Lastly, I would like to begin by dedicating this thesis to dearest to my Ma and Baba, whose unwavering love and support have been my strength throughout this journey. To my sisters, Ganga and Namita, your presence in my life has meant the world to me.

---

# TABLE OF CONTENTS

## Chapter 1: Introduction

|         |  |    |
|---------|--|----|
| 1.1     | Environmental crisis-----  | 15 |
| 1.2     | Sustainable energy-----  | 16 |
| 1.3     | Thermoelectricity-----   | 18 |
| 1.3.1   | Thermoelectric devices-----  | 18 |
| 1.3.2   | Performance Assessment of thermoelectric material-----   | 20 |
| 1.3.2.1 | Figure of merit-----   | 20 |
| 1.3.2.2 | Seebeck Coefficient (S)-----   | 21 |
| 1.3.2.3 | Electrical resistivity ( $\rho$ )-----   | 22 |
| 1.3.2.4 | Thermal conductivity ( $\kappa$ )-----   | 22 |
| 1.3.3   | Enhancement of the figure of merit-----  | 23 |
| 1.3.3.1 | Carrier concentration optimization-----  | 23 |
| 1.3.3.2 | Electronic band convergence-----   | 25 |
| 1.3.3.3 | Resonance level-----   | 26 |
| 1.3.3.4 | Reduction of the lattice thermal conductivity-----   | 27 |
| 1.3.4   | State of art thermoelectric materials-----   | 32 |
| 1.3.4.1 | Advantages of sulfides in thermoelectric application----                                       | 32 |
| 1.3.4.2 | State of art thermoelectric sulphides-----   | 33 |
| 1.3.4.3 | Advantages of Bi-based compound in thermoelectric application-----                             | 44 |
| 1.3.4.4 | Conventional Bi-based thermoelectric sulfides and their structure-properties relationship----- | 44 |
| 1.4     | Conclusion-----  | 52 |
| 1.5     | Objectives-----  | 69 |

## Chapter 2: A tunable structural family with ultralow thermal conductivity: copper-deficient $\text{Cu}_{1-x}\text{Pb}_x\text{Bi}_{1+x}\text{S}_3$

|       |  |    |
|-------|--|----|
| 2.1   | Introduction-----  | 77 |
| 2.2   | Methods-----   | 78 |
| 2.2.1 | Reagents-----  | 78 |
| 2.2.2 | Synthesis-----   | 78 |
| 2.3   | Results and discussion-----                                      | 80 |
| 2.3.1 | Crystal structure-----   | 80 |
| 2.3.2 | Scanning Electron Microscopy (SEM) analysis of pristine sample-- |    |

|        |  |     |
|--------|--|-----|
| 2.3.3  | Transmission Electron Microscopy (TEM) analysis of pristine sample |     |
| 2.3.4  | Electrical properties of pristine sample -----                     | 88  |
| 2.3.5  | Electronic Structure -----   | 90  |
| 2.3.6  | Thermal properties of pristine sample -----                        | 93  |
| 2.3.7  | PXRD analysis of doped samples -----                               | 98  |
| 2.3.8  | SEM analysis of doped samples -----                                | 101 |
| 2.3.9  | TEM analysis of doped samples -----                                | 102 |
| 2.3.10 | Band gap experiment -----  | 103 |
| 2.3.11 | Electronic transport properties of doped samples -----             | 104 |
| 2.3.12 | Thermal transport properties and figure of merit of doped samples  |     |
| 2.4    | Conclusion -----   | 110 |
| 2.5    | References -----   | 111 |

### **Chapter 3: Transport properties in the $\text{Cu}_{1-x}\square_x\text{Pb}_{1-x}\text{Bi}_{1+x}\text{S}_3$ series**

|       |   |     |
|-------|---|-----|
| 3.1   | Introduction -----                                    | 123 |
| 3.2   | Methods -----   | 124 |
| 3.2.1 | Reagents -----  | 124 |
| 3.2.2 | Synthesis -----                                       | 124 |
| 3.3   | Results and Discussion -----                          | 125 |
| 3.3.1 | Crystal structure -----                               | 125 |
| 3.3.2 | Scanning Electron Microscopy (SEM) analysis -----     | 131 |
| 3.3.3 | Transmission Electron Microscopy (TEM) analysis ----- | 133 |
| 3.3.4 | Thermal stability study -----                         | 136 |
| 3.3.5 | Band gap study -----                                  | 137 |
| 3.3.6 | Electrical properties -----                           | 138 |
| 3.3.7 | Thermal properties -----                              | 141 |
| 3.4   | Conclusion -----                                      | 143 |
| 3.5   | References -----                                      | 144 |

### **Chapter 4: Rattling of copper in three-fold coordination in $\text{Cu}_3\text{BiS}_3$ : a blockade for hole carrier delocalization but a driving force for ultralow thermal conductivity**

|       |                    |     |
|-------|--------------------|-----|
| 4.1   | Introduction ----- | 149 |
| 4.2   | Methods -----      | 151 |
| 4.2.1 | Reagent -----      | 151 |
| 4.2.2 | Synthesis -----    | 151 |

---

|       |                         |     |
|-------|-------------------------|-----|
| 4.3   | Results and Discussion  | 153 |
| 4.3.1 | Crystal structure study | 153 |
| 4.3.2 | Microstructure study    | 160 |
| 4.3.3 | Thermal stability study | 162 |
| 4.3.4 | Electrical properties   | 164 |
| 4.3.5 | Thermal Properties      | 168 |
| 4.3.6 | Discussion              | 173 |
| 4.4   | Conclusion              | 181 |
| 4.5   | References              | 182 |

### **Chapter 5: Thermoelectric performance enhancement in low thermal conductive *n*-type PbBi<sub>2</sub>S<sub>4</sub> through carrier optimization**

|        |  |     |
|--------|--|-----|
| 5.1    | Introduction   | 195 |
| 5.2    | Methods  | 197 |
| 5.2.1  | Reagent  | 197 |
| 5.2.2  | Synthesis  | 197 |
| 5.3    | Results and Discussion   | 198 |
| 5.3.1  | Crystal structure  | 198 |
| 5.3.2  | Microstructure analysis of pristine PbBi <sub>2</sub> S <sub>4</sub>           | 201 |
| 5.3.3  | Electrical properties of pristine PbBi <sub>2</sub> S <sub>4</sub>             | 202 |
| 5.3.4  | Electronic structure of pristine PbBi <sub>2</sub> S <sub>4</sub>              | 204 |
| 5.3.5  | Thermal properties of pristine PbBi <sub>2</sub> S <sub>4</sub>                | 206 |
| 5.3.6  | XRPD analysis of doped samples   | 212 |
| 5.3.7  | SEM analysis of doped samples  | 213 |
| 5.3.8  | Electrical transport properties of doped samples                               | 214 |
| 5.3.9  | Electronic structure of PbBi <sub>2</sub> S <sub>3.75</sub> Cl <sub>0.25</sub> | 216 |
| 5.3.10 | Thermal transport properties   | 219 |
| 5.4    | Conclusion   | 220 |
| 5.5    | References   | 222 |

### **Chapter 6: General conclusion**

### **Chapter 7: Appendices**

|        |                                  |     |
|--------|----------------------------------|-----|
| 7.1.   | Synthesis                        | 235 |
| 7.1.1. | Mechanical alloying/Ball milling | 235 |

---

|   |            |
|---|------------|
| 7.1.2. High temperature solid state reaction -----                                | 236        |
| 7.1.3. Spark Plasma Sintering (SPS) -----   | 237        |
| 7.2. Structural characterization -----  | 238        |
| Powder X-ray diffraction (PXRD) -----   | 238        |
| 7.3. Electron microscopy -----  | 239        |
| 7.3.1. Scanning electron microscope (SEM) -----                                   | 240        |
| 7.3.2. Energy dispersive X-ray analysis (EDAX) -----                              | 241        |
| 7.3.3. Transmission electron microscope (TEM) -----                               | 242        |
| 7.4. Thermogravimetric analysis (TGA) and differential scanning calorimetry (DSC) |            |
| 7.5. Electronic transport measurement -----                                       | 243        |
| 7.6. Hall effect -----  | 245        |
| 7.7. Thermal conductivity -----   | 245        |
| 7.8. Heat capacity -----  | 247        |
| 7.9. References -----   | 248        |
| <b>List of Publications -----</b>   | <b>249</b> |



# Chapter 1

---

## Introduction

---

---



## 1.1. Environmental crisis

Global warming is mostly attributable to human activity, particularly the use of fossil fuels such as coal, oil, and gas etc. The overwhelming consensus among scientists is that human-caused greenhouse gas emissions, such as carbon dioxide and methane, are the primary drivers of the century-long temperature increase. Global warming has far-reaching consequences, including a variety of environmental and socioeconomic effects. The warming of the seas, which has absorbed nearly 93% of the excess heat generated by greenhouse gas emissions, is a serious effect.<sup>1,2</sup> This increasing heat storage in the oceans has led to the Earth's surface warming. The change in global surface temperature from 1880 to 2020 is shown in **Figure 1.1a**. Rising temperatures have also caused glaciers and ice sheets to melt, causing sea levels to rise. The global average sea level has risen by around 23 cm since 1880, with roughly one-third of the rise occurring in the previous 25 years. The sea level is now rising at a pace of roughly 3.3 mm per year, and this rate is likely to accelerate further as global temperatures rise. The global sea level change since 1993 has been shown in **Figure 1.1b**.

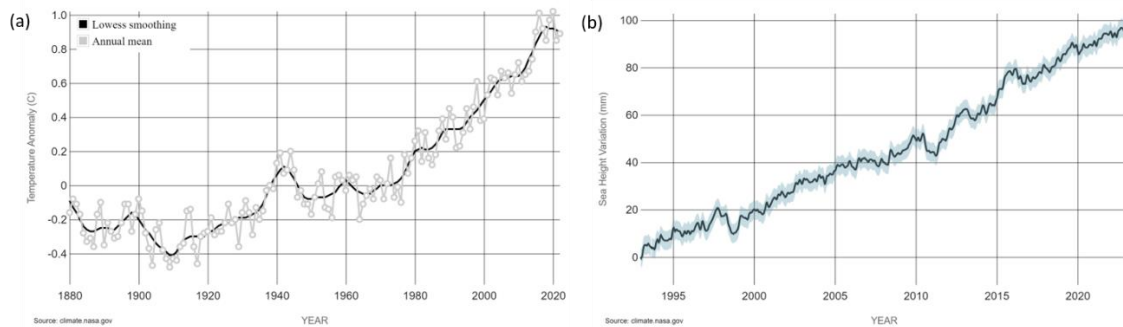


**Figure 1.1.** (a) Change in global surface temperature from 1880 to 2020,<sup>3</sup> (b) the change in global sea level since 1993. These data's are from NASA's Goddard Space Flight Center. (<https://climate.nasa.gov/vital-signs/sea-level/>)

There is an overwhelming consensus among scientists, supported by peer-reviewed scientific studies, that anthropogenic global warming (AGW) is a reality. The AGW theory is supported by approximately 97.1% of articles on global climate change or global warming.<sup>4</sup> This consensus underscores the importance of taking action to slow

down and ultimately reverse the trend of rising global temperatures. The motivations for combating global warming go beyond environmental issues. It is additionally driven by economic considerations since lowering greenhouse gas emissions and shifting to renewable energy sources can result in increased energy efficiency, cost savings, and the establishment of new companies and job opportunities.

## 1.2. Sustainable energy

The growing necessity for sustainable energy sources is a consequence of the escalating emission of greenhouse gases into the atmosphere, which poses a major threat to the ecological balance of the globe. In order to tackle this issue, sustainable energy can be procured through diverse methods such as substituting combustion-based electricity production with sustainable energy sources and promoting energy-harvesting processes in industrial procedures.<sup>5</sup>

Renewable energy sources offer diverse options for sustainable power generation. In 2015, hydroelectric power, which is considered the primary renewable energy source, constituted 16% of the worldwide electricity generation.<sup>6</sup> The product is characterized by its cost-effectiveness, diminished emission of greenhouse gases, and adaptable production process that generates no residual waste. Moreover, the construction of dams for conventional hydroelectricity can have adverse effects on the surrounding ecosystems. Wind power, contributing nearly 5% of global electricity demand, is another significant renewable source.<sup>7</sup> The cost-effectiveness of onshore wind turbines is well-established, whereas offshore installations are known to provide more consistent energy production.<sup>8</sup> Wind power is clean and minimally impacts ecosystems, though it is subject to weather fluctuations. Solar energy, which involves the conversion of light or heat, has a variety of applications including but not limited to water and process heating, artificial photosynthesis, and photovoltaics (PV). Solar photovoltaic (PV) technology enables the direct conversion of solar radiation into electrical energy. As of 2015, solar PV contributed to 1% of the total global electricity generation.<sup>9</sup> Fuel cells exhibit great potential as a technology, as they facilitate the conversion of chemical energy into electrical energy through the utilization of hydrogen ions and an oxidizing agent.<sup>10</sup> These systems offer uninterrupted electricity production while also generating water and heat as secondary productions. Although the current

production costs are elevated, fuel cells exhibit promising prospects, particularly in the context of electric vehicle deployments. Geothermal energy presents a considerable power potential with decreasing generation costs, although its accessibility remains limited.<sup>11</sup> Piezoelectric generators are devices that transform mechanical stress into electrical current.<sup>12</sup> They have the capability to extract energy from both human and industrial vibrations.

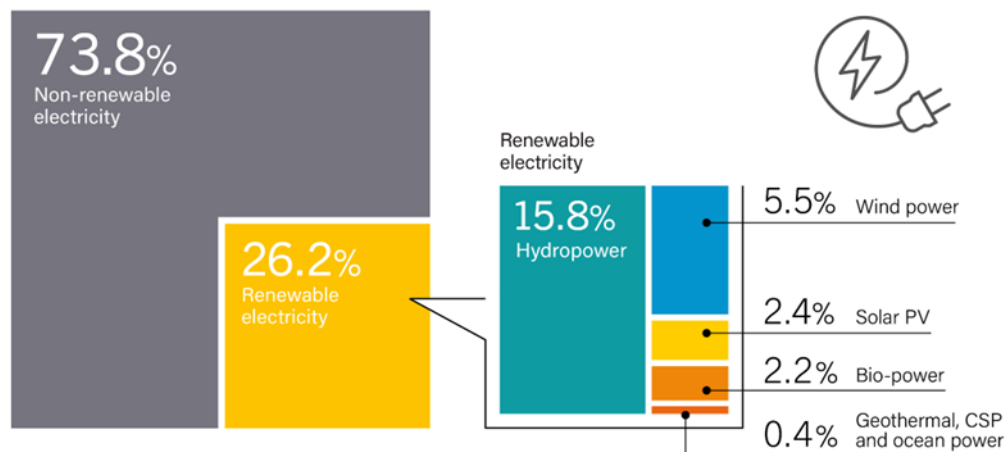


**Figure 1.2.** Estimated renewable energy share of global electricity production. (<https://www.greenoptimistic.com/the-global-transition-to-clean-energy-explained-in-12-charts-20190624/>)

The use of waste heat produced by combustion engines and industrial processes is a prominent area of focus. All the processes mentioned above result in a considerable amount of energy production. However, they also generate residual heat, which is typically released through various methods, including dissipation, cooling water, lubricants, and exhaust gases. Thermoelectric devices offer a feasible solution by converting wasted heat into usable electricity. These devices are capable of functioning within the optimal temperature range to effectively collect residual heat or even renewable heat sources like solar radiation.<sup>13,14</sup>

## 1.3. Thermoelectricity

### 1.3.1. Thermoelectric devices

Thomas Johann Seebeck, an Estonian physicist, made a significant discovery that established the foundations for thermoelectricity in the early 1820s.<sup>15</sup> He

discovered that when a temperature difference was applied to a circuit composed of dissimilar metals, an electrical potential developed between the two extremities. This phenomenon became known as the Seebeck effect and marked the beginning of thermoelectricity, a potential renewable source of electricity as well as a heating and cooling device. Thermoelectric power generation involves converting heat into electricity by utilizing the intrinsic properties of thermoelectric materials. These materials have the extraordinary capacity to transform heat energy directly into electrical energy or vice versa. However, their widespread is constrained by the present thermoelectric materials' low efficiency and relatively high costs of manufacturing.<sup>16</sup> Typically, thermoelectric materials have an energy conversion efficiency below 10%, which restricts their application to specific fields where high reliability outweighs production cost and efficiency considerations. Examples of such uses include gas pipelines, cooling systems for laboratory equipment, and electrical generators on NASA's deep space probes and rovers. Despite existing efficiency constraints, there is optimism about the future of thermoelectric devices as a sustainable energy source.<sup>13,17</sup> Thermoelectric devices are thought to have a future as a sustainable energy source, gathering waste heat from fuel combustion, exothermic reactions, and even directly from sunlight. This can contribute to energy sustainability and reduce environmental impact by turning waste heat into usable electricity.

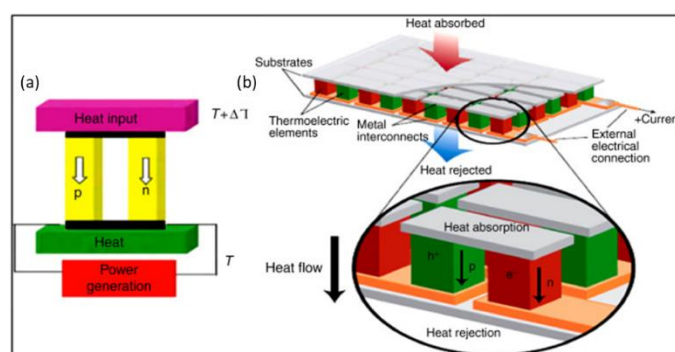


**Figure 1.3.** (a,b) Pictures of thermoelectric module.<sup>18</sup>

The thermocouple, which is made up of two legs made of distinct materials:  $n$ -type and  $p$ -type, is an important component of thermoelectric devices. The electrical flow directions in these materials are opposing. The distinction between  $n$ -type and  $p$ -

type lies in the dominant type of charge carriers present in the material. In  $n$ -type materials, the majority of charge carriers are electrons, whereas, in  $p$ -type materials, the dominating charge carriers are holes. A temperature gradient is established between a heat source at the junction and a heat sink on the other side of the thermocouple device in power-generating mode. The presence of this temperature difference creates a voltage gradient due to the Seebeck effect. Because the thermocouple's  $n$ -type and  $p$ -type legs are connected in series, an electrical current flow across the junction from the  $n$ -type leg to the  $p$ -type leg. This current can be converted into useful electrical power. The process is reversed if a thermocouple is subjected to an electrical current, resulting in a temperature gradient across the device known as Peltier effect. As a result, heat is absorbed from the junction, leading to cooling at that specific location. This cooling effect can be used in a variety of cooling applications.

Overall, the advancement of thermoelectric devices and a better knowledge of thermoelectric principles have increased the possibility of using waste heat as a sustainable energy source. Despite the fact that present thermoelectric materials have low efficiency, continued research and improvements hold promise for enhancing their performance and expanding their practical applications in the future.

## 1.3.2. Performance Assessment of thermoelectric material

### 1.3.2.1. Figure of merit

Thermoelectric materials are able to convert temperature differences into electrical energy and vice versa, making them useful for a variety of applications such as power generation and cooling. To effectively compare and evaluate the thermoelectric performance of different materials, it is important to have a metric that accounts for all relevant properties. In 1959, Abram Fedorovich Ioffe proposed a dimensionless figure of merit to quantify thermoelectric conversion efficiency. This figure of merit is still widely used today and is defined as follows:

$$ZT = \frac{S^2}{\rho\kappa} T = \frac{PF}{\kappa} T$$

where,  $T$  is the absolute temperature (in Kelvin),  $S$  is the Seebeck coefficient (or thermoelectric power) in  $\text{V K}^{-1}$ ,  $\rho$  is the electrical resistivity in  $\Omega \text{ cm}$ ,  $\kappa$  is the total thermal conductivity in  $\text{W m}^{-1} \text{K}^{-1}$ , and  $PF = S^2/\rho$  is the power factor in  $\text{W m}^{-1} \text{K}^{-2}$ .

So, it is obvious to achieve the highest possible thermoelectric efficiency, a material must have certain characteristics. Firstly, a high Seebeck coefficient is necessary, as it indicates the material's ability to generate a large electrical potential (i.e. electrical power) in response to a temperature gradient. Secondly, a low electrical resistivity is desirable, as it allows for better charge carrier transport. Charge carriers are the electrons or holes that carry electrical charge through the material, and low resistivity ensures that these carriers can move easily through the material without losing too much energy as heat due to the Joule effect. Lastly, a low thermal conductivity is important, as it helps to preserve the temperature gradient across the module junctions. If a material has a high thermal conductivity, the heat generated by the temperature gradient will dissipate too quickly and not be effectively converted into electricity. Therefore, a low thermal conductivity ensures that the temperature difference across the module junctions remains significant, leading to higher thermoelectric efficiency.

In order to improve the  $ZT$  value of a material, various strategies have been explored. These include optimizing the carrier concentration and effective mass through doping or alloying, engineering the electronic and phononic band structures, reducing the lattice thermal conductivity through phonon scattering, and introducing nanostructuring or interfaces to enhance the thermoelectric performance. These strategies aim to improve the Seebeck coefficient, electrical resistivity, and/or reduce the thermal conductivity to achieve a high  $ZT$  value for efficient thermoelectric energy conversion.

### 1.3.2.2. Seebeck Coefficient (S)

The Seebeck coefficient (S) measures the voltage generated by a material in response to a temperature gradient, and it is a crucial factor in determining a material's thermoelectric performance. For metals and degenerate semiconductors, the Seebeck coefficient can be expressed using Pisarenko relation:

$$S = \frac{8\pi^2 k_B^2}{3eh^2} m^* T \left(\frac{\pi}{3n}\right)^{2/3}$$

where  $k_B$  is the Boltzmann constant ( $1.381 \times 10^{-23} \text{ kg m}^2 \text{ S}^{-2} \text{ K}^{-1}$ ),  $e$  is the elemental charge ( $1.602 \times 10^{-19} \text{ C}$ ),  $h$  is the Planck constant ( $6.626 \times 10^{-34} \text{ kg m}^2 \text{ s}^{-1}$ ),  $n$  is the charge carrier concentration ( $\text{m}^{-3}$ ),  $m^*$  is the charge carriers' effective mass (kg).

The equation also shows that a low charge carrier concentration ( $n$ ) with a high effective mass ( $m^*$ ) will lead to a high Seebeck coefficient. Therefore, researchers often look for materials that have low carrier concentrations and high effective masses to optimize their thermoelectric performance.

Additionally, the equation highlights the importance of having only one type of charge carrier for optimal thermoelectric performance. When there are both  $n$ -type and  $p$ -type charge carriers, they tend to move towards the colder end of the device, which can cancel out the induced Seebeck voltages and reduce the overall efficiency of the material. Therefore, researchers typically try to develop materials with either  $n$ -type or  $p$ -type conduction for thermoelectric applications.

### 1.3.2.3. Electrical resistivity ( $\rho$ )

As the Seebeck coefficient, the electrical resistivity of a material also depends on the carrier concentration ( $n$ ) and effective mass ( $m^*$ ). However, these two properties have opposite relationships with these constants. The relationship between electrical resistivity and carrier concentration is given below:

$$\rho = \frac{1}{ne\mu}$$

$$\mu \propto \frac{1}{m^*}$$

where  $\mu$  is the charge mobility in  $\text{m}^2 \text{ V}^{-1} \text{ S}^{-1}$ .

Therefore, it is challenging to get desirable electrical resistivity and Seebeck coefficient simultaneously *i.e.* low electrical resistivity and high Seebeck coefficient. Depending on the material, the goal may be to increase the Seebeck coefficient while sacrificing the

electrical resistivity or to achieve a low electrical resistivity while compromising the Seebeck coefficient. To achieve a higher thermoelectric conversion rate, it is more practical to focus on improving the power factor ( $PF$ ). A high power factor enables a strong electrical power output when subjected to a thermal gradient.

#### 1.3.3.4. Thermal conductivity ( $\kappa$ )

To achieve high thermoelectric properties, a material should have a low thermal conductivity. This helps to maintain a maximal temperature gradient between junctions, which generates a strong potential difference through the Seebeck effect ( $S$ ).

The total thermal conductivity ( $\kappa$ ) of a material is the summation of electronic thermal conductivity ( $\kappa_e$ ) and lattice thermal conductivity ( $\kappa_L$ ):

$$\kappa = \kappa_e + \kappa_L$$

The electrical part arises from the heat carried by the charge carrier (both hole and electron). The electrical part of thermal conductivity ( $\kappa_e$ ) is inversely proportional to electrical resistivity ( $\rho$ ) and can be estimated from the Wiedmann – Franz law:

$$\kappa_e = \frac{LT}{\rho}$$

where  $L$  is the Lorenz number in  $W \Omega K^{-2}$ .

In case of a free electron gas, the Lorenz number can be defined as:

$$L = \frac{\pi^2 \kappa_B^2}{3e^2} = 2.45 \times 10^{-8} W \Omega K^{-2}$$

This Lorenz number is commonly used to calculate the electronic thermal conductivity of metals. However, it is not appropriate for semiconductors as the diffusion process of the charge carriers at the Fermi level impacts the Lorenz number. Therefore, thermoelectric compounds tend to have lower Lorenz numbers than for the metal.

For this work, the Lorenz number was calculated from the Seebeck coefficient using the simplified relationship from Kim *et al.*<sup>19</sup>

$$L = 1.5 + \exp\left(\frac{-|S|}{116}\right)$$

On the other hand, the lattice thermal conductivity can be expressed from kinetic theory of gas:

$$\kappa_L = \frac{1}{3}v_S C_p L_{ph}$$

where  $\kappa_L$  is the lattice thermal conductivity,  $v_S$  is the sound velocity in  $\text{m S}^{-1}$ ,  $C_p$  is the lattice specific heat in  $\text{J k}^{-1} \text{m}^{-3}$  and  $L_{ph}$  is the phonon mean free path (m).

### 1.3.3. Enhancement of the figure of merit

It is obvious from the  $ZT$  equation given above that increasing  $ZT$  can also be accomplished by increasing the power factor ( $S^2/\rho$ ). Power factor ( $S^2/\rho$ ) is a purely electronic attribute that is controlled by the electronic makeup and scattering behavior of materials. The following techniques are used to increase power factor: (a) chemical doping to engineer carrier concentration ( $n$ ); (b) convergence of multiple valence/conduction band extrema to increase effective carrier mass ( $m^*$ ) and Seebeck coefficient ( $S$ ); (c) modulation doping to increase carrier mobility, and (d) resonance impurity levels to distort the density of states near Fermi level. On the other hand the  $ZT$  value can also be increased by reducing the total thermal conductivity. The most popular strategies to enhance the TE performance of a material are to lower the thermal conductivity by alloying, grain boundary engineering, mesoscale structuring and nanostructuring, point defects, nano precipitation, different approaches which can effectively scatter phonons. I will describe the most recent approaches for creating high-performance thermoelectric materials here.

#### 1.3.3.1. Carrier concentration optimization

The significant interdependence between the power factor ( $S^2/\rho$ ), thermal conductivity ( $\kappa$ ), and carrier concentration ( $n$ ) poses one of the key design challenges for high  $ZT$  thermoelectric materials. This interdependence can be optimized by controlling the doping level of the material. The optimal carrier concentration for achieving maximum  $ZT$  values is typically found in the range of  $10^{19}$ - $10^{21}$   $\text{cm}^{-3}$ , which falls between the concentrations commonly observed in metals and semiconductors (**Figure 1.4**). Degenerate semiconductors or strongly doped semiconductors, are connected with this spectrum.

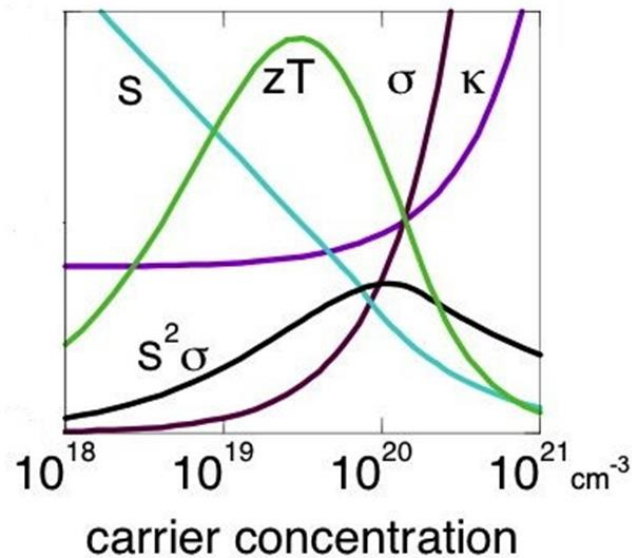


**Figure 1.4.** Graphical representation of Seebeck coefficient ( $S$ ), the power factor, electrical conductivity ( $\sigma$ ), thermal conductivity ( $\kappa$ ), and figure of merit ( $ZT$ ) as a function of carrier concentration ( $n$ ).

However, a problem occurs because the carrier concentration ( $n$ ), which follows a power law relationship of  $T^{3/2}$ , rapidly rises with temperature. While traditional doping techniques can successfully adjust the carrier concentration at room temperature, it becomes difficult to achieve the ideal carrier concentration at high temperatures. As a result, at all operating temperatures, the maximum potential  $ZT$  value cannot be fully achieved. The use of functionally graded doping, which involves integrating two or more segments with different  $n$ , is a successful remedy for this problem. The addition of

temperature-dependent doping behavior to the standard doping approach allows for larger average  $ZT$  values, which are crucial for applications.

### 1.3.3.2. Electronic band convergence

Multiple valleys (different pockets of Fermi surface with the same energy) in valence or conduction band can result in high Seebeck coefficient ( $S$ ) because they have the effect of producing large effective mass ( $m^*$ ) without explicitly lowering mobility ( $\mu$ ), as seen in the following equation:

$$m^* = N_V^{2/3} m_b^*$$

where  $m_b^*$  stands for the single valley density of state effective mass of degenerate valleys and  $N_V$  stands for orbital degeneracy. Therefore, the foundation of the band-convergence technique is effective doping to energetically align the electronic bands for a higher degree of band degeneracy. The objective is to raise the Seebeck coefficient without significantly lowering the electrical conductivity. When the system is extensively doped, carrier redistribution to several valleys can increase total effective mass, which produces a high Seebeck coefficient. Since carrier mobility would not be impacted by this process, valence band convergence results in a carrier optimized system with noticeably high-power factor and  $ZT$  (**Figure 1.5 a**).

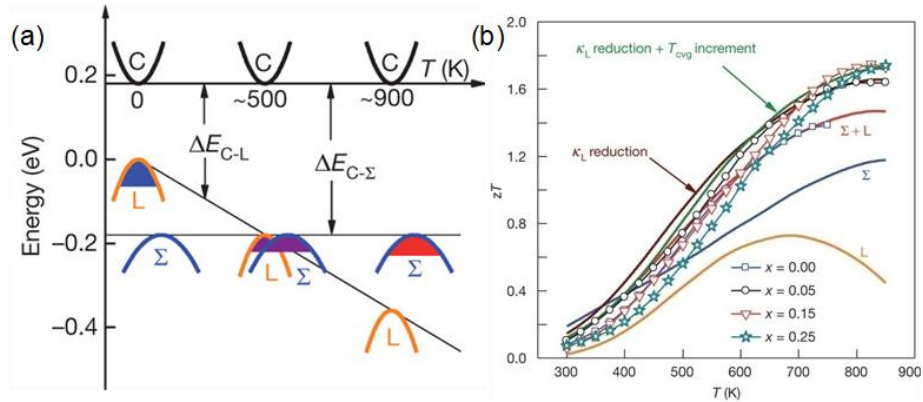


**Figure 1.5.** (a) Relative energy of the valence bands in  $PbTe_{0.85}Se_{0.15}$ . At 500 K the two valence bands converge, resulting in contributions from both the L and  $\Sigma$  bands in the transport properties. (b) Temperature dependent  $ZT$  of  $PbTe_{1-x}Se_x$  materials doped with 2 atom % Na.<sup>20</sup>

Figure 1.5 a,b shows how doped  $\text{PbTe}_{1-x}\text{Se}_x$  alloys exhibit band convergence of at least 12 valleys, which results in an incredibly high  $ZT$  value of 1.8 at roughly 850 K by Pei *et al.*<sup>20</sup> The substitution of Te by Se results in a reduction of the energy difference between the L and  $\Sigma$  bands of PbTe, leading to the effective convergence of the two bands. Therefore, an increase in the  $N_V$  value from 4 (for L band) to 12 (for  $\Sigma$  band) leads to a corresponding increase in both the effective mass ( $m^*$ ) and Seebeck coefficient.

### 1.3.3.3. Resonance level

Resonance level originates from the coupling between electrons of a dilute impurity with those of the valence or conduction band of the host solid near its Fermi level. Thus, resonance dopant creates an excess density of states near the valence or the conduction band edge of the host compound (**Figure 1.6. a**) and results in higher effective mass,  $m^*$  and thereby enhances Seebeck coefficient, according to Mott expression.

$$S = \frac{\pi^2}{3} \frac{k_B}{q} k_B T \left\{ \frac{d[\ln(\sigma(E))]}{dE} \right\}_{E=E_F}$$

$$S = \frac{\pi^2}{3} \frac{k_B}{q} k_B T \left\{ \frac{1}{n} \frac{dn(E)}{dE} + \frac{1}{\mu} \frac{d\mu(E)}{dE} \right\}_{E=E_F}$$

Here,  $\sigma(E)$  is the electrical conductivity determined as a function of the band filling or Fermi energy,  $E_F$  ( $\sigma(e) = n(E)q\mu(E)$ ) and  $n(E)$  ( $n(E) = g(E)f(E)$ ), the carrier density at the energy level,  $E$  (here  $q$  is the carrier charge, and  $\mu(E)$  is the mobility as a function of energy,  $f(E)$  is the Fermi function,  $g(E)$  is density of state).

When electronic scattering is independent of energy,  $\sigma(E)$  is just proportional to the density of states (DOS). The equations presented above indicate that a system exhibiting a rapid change in DOS in nearby of the Fermi level is going to have a substantial Seebeck coefficient. The dependent relationship between Seebeck and carrier concentration is shown by the Pisarenko figure. The observation of resonance

level formation can be inferred from a Pisarenko plot indicating a notably increased  $S$  value, as illustrated in Figure 1.6 (b). The inclusion of dopants from Group III, specifically aluminum, indium, and thallium, results in the formation of a resonance level within the PbTe material. Heremans *et al.* conducted an experimental study which showed that the addition of Tl to PbTe results in an improvement of its Seebeck coefficient through the formation of resonance levels. This led to a doubling of the figure of merit ( $ZT$ ).<sup>21</sup>

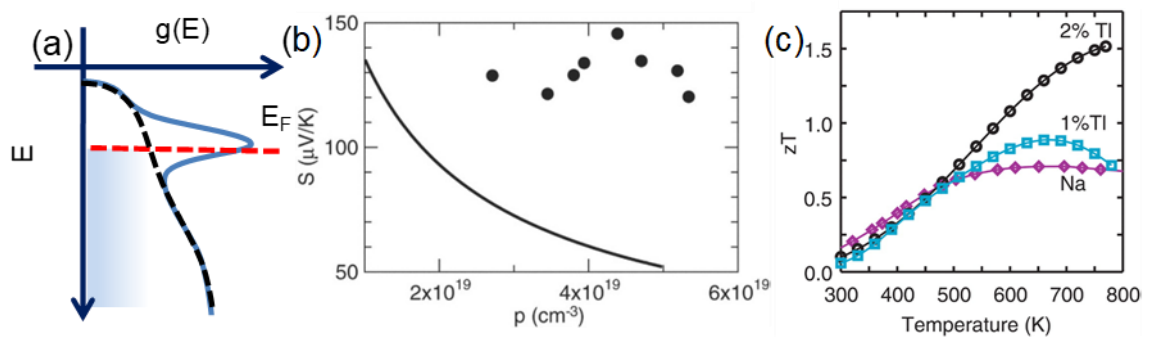


**Figure 1.6.** (a) Schematic diagram of resonance level in the valence band. Tl-doped PbTe shows asymmetric distortion of DOS (blue line) near Fermi level. (b) Pisarenko relation of Seebeck coefficient vs hole concentration,  $p$  for PbTe (solid line) at 300 K compared to the results on Tl-PbTe sample. (c) The temperature dependent  $ZT$  values for  $\text{Tl}_{0.02}\text{Pb}_{0.98}\text{Te}$  (black circles) and  $\text{Tl}_{0.01}\text{Pb}_{0.99}\text{Te}$  (blue squares) compared to that of a reference sample of Na-PbTe (purple diamonds).<sup>21</sup>

#### 1.3.3.4. Reduction of the lattice thermal conductivity

Reducing the thermal conductivity of the materials is one of the conventional methods of developing high-performance thermoelectrics. The electronic thermal conductivity ( $\kappa_e$ ), the lattice thermal conductivity ( $\kappa_L$ ), and the bipolar thermal conductivity ( $\kappa_b$ ) contribute to the total thermal conductivity ( $\kappa$ ) for solids. The thermoelectric figure of merit,  $ZT$  can be written as follows by using the Wiedemann–Franz–Lorenz law for the electronic thermal conductivity,  $\kappa_e = L\sigma T$ ;

$$zT = \frac{S^2}{L} \left[ \frac{1}{1 + \frac{\kappa_L + \kappa_b}{\kappa_e}} \right]$$

Here,  $L$  is the Lorenz number, and the values are typically between  $1.6$  to  $2.5 \times 10^{-8} \text{ V}^2 \text{ K}^{-2}$ . To obtain high TE performance, materials must have minimal lattice mismatch and low  $\kappa_b$ , whereas a high  $\kappa_e$  corresponds to a high-power factor. The contribution of  $\kappa_b$  can be only found at very high temperatures and in semiconductors with very narrow gaps, which is essentially non-existent at ambient temperature. Therefore, developing novel methods to enhance the suppression of  $\kappa_L$  is essential for improved TE performance.

The atomic vibrations in a periodic lattice are known as phonons. Here, we'll focus on crystalline solids that have clearly defined phonon modes and can carry thermal energy. Considering kinetic theory within Boltzmann transport equation,  $\kappa_L$  of a solid can be written as:

$$\kappa_L = \frac{1}{3} \int_0^{\omega_{max}} C(\omega) v(\omega) l_{ph}(\omega) d\omega$$

where  $C(\omega)$  is the spectral volumetric heat capacity,  $v(\omega)$  is the phonon group velocity and  $l_{ph}(\omega)$  is the phonon mean free path. **Figure 1.7. a** depicts a typical temperature-dependent  $\kappa_L$  of a crystalline semiconductor. Since three-phonon scattering or Umklapp scattering strength is weak at low temperatures,  $l_{ph}$  frequently reaches the material's characteristic length scale. Low temperature  $\kappa_L$  grows with temperature as  $\sim T^3$  and follows temperature dependence of  $C_v$ . At high temperature,  $C_v$  becomes constant to the Dulong-Petit value and  $\kappa_L$  decreases with increasing temperature following  $T^{-1}$  temperature dependence due to Umklapp scattering. As a result, a peak in the temperature-dependent  $\kappa_L$  is produced (**Figure 1.7. a**), and this peak is greatly influenced by the degree of disorder and grain boundaries in the materials.

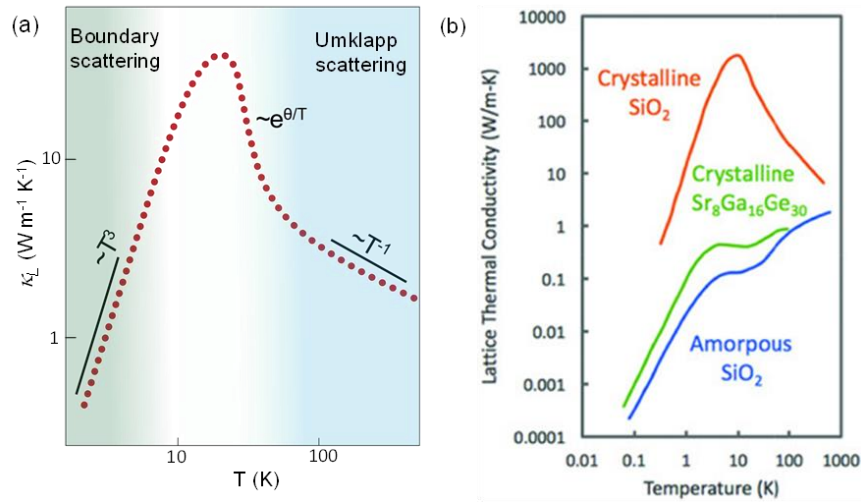


**Figure 1.7.** (a) shows typical temperature dependent  $\kappa_L$  in a crystalline solid and various scattering mechanisms operating in different temperature regimes. (b) Typical temperature dependence of  $\kappa_L$  in a crystalline ( $\alpha$ -quartz) and an amorphous solid (vitreous-silica).<sup>22</sup>

Amorphous materials and glasses conduct thermal transfer very differently from crystalline solids. Compared to crystalline insulators (alpha -quartz) amorphous materials and glasses have substantially lower thermal conductivity and show a distinct temperature dependency (**Figure 1.7b**).<sup>22</sup> Thermal conductivity in amorphous materials rises first with a  $T^2$  temperature dependency at low temperatures, reaches a plateau of nearly constant values, and then increases slowly towards the "glass limit."<sup>23,24</sup> To achieve the "glass limit," it is necessary to further reduce thermal conductivity ( $\kappa_L$ ) in these materials without adversely affecting charge carrier mobility. It is important to note that several crystalline substances, including  $\text{Ba}_8\text{Ga}_{16}\text{Ge}_{30}$ <sup>25</sup> and  $\text{Bi}_4\text{O}_4\text{SeCl}_2$ ,<sup>26</sup> exhibit temperature-dependent behaviors that approach those of glass. However, in crystalline solids,  $\kappa_L$  cannot be arbitrarily low and is typically referred to as the minimum lattice thermal conductivity ( $\kappa_{\min}$ ).  $\kappa_{\min}$  serves as an important parameter guiding the design principles of high-performance thermoelectric materials. The lattice thermal conductivity for bulk materials is properly described by following equation;

$$\kappa_L = \frac{1}{3} C_V v_g^2 \tau,$$

Therefore, to reduce the  $\kappa_L$ , one must design materials that have a lower specific heat ( $C_V$ ), group velocity ( $v_g$ ), or phonon relaxation time ( $\tau$ ). The most targeted parameter in thermoelectrics is often the phonon relaxation time, which can be tuned to a desired value by extrinsically generating 0D point defects, 1D dislocations, 2D grain boundaries, or tiny precipitates (**Figure 1.8**). Each of these flaws improves the phonon-scattering process, reduces the relaxation time ( $\tau$ ), and consequently reduces the  $\kappa_L$ . Each of the aforementioned processes has their own frequency ( $\omega$ ) dependence. For example, the 0D point defects scatters the high frequency phonons ( $\tau_{PD} \sim \omega^{-4}$ ); 1D dislocation scatters the mid frequency phonons ( $\tau_{DC} \sim \omega^{-3}$  for dislocation cores and  $\tau_{DS} \sim \omega^{-1}$  for dislocation strains); 2D interface scattering originating from grain boundaries or precipitates are effective for the low frequency phonons ( $\tau_{inter} \sim \omega^0$ ). The Umklapp process which is universal has a relaxation time,  $\tau_U \sim \omega^{-2}$ , thus being effective in scattering the phonons of all frequencies. Callaway developed a phenomenological model that takes into account the contributions arising from microstructural effects on phonon scattering at different length scales. The model is expressed as follows:

$$\kappa_{lat} = \frac{k_B}{2\pi^2 v_g} \left( \frac{k_B T}{\hbar} \right)^3 \int_0^{\theta_{D/T}} \tau_C(x) \frac{x^4 e^x}{(e^x - 1)^2} dx$$

Where,  $k_B$  in equation corresponds to Boltzmann's constant;  $\hbar$ ,  $T$  and  $\tau_C$  denotes Plank's constant, absolute temperature and total relaxation time respectively.  $\tau_C$  corresponds to the individual relaxation time via the relation  $\tau_C^{-1} = \tau_U^{-1} + \tau_{PD}^{-1} + \tau_{DS}^{-1} + \tau_{DC}^{-1} + \tau_{inter}^{-1} + \dots$ , where  $\tau_U$ ,  $\tau_{PD}$ ,  $\tau_{DS}$ ,  $\tau_{DC}$  and  $\tau_{inter}$  corresponds to relaxation times arising from the contributions of Umklapp scattering, point defects, dislocation strain, dislocation cores and interface scattering respectively. This equation offers a guide for accessing each microstructural effect's contributions quantitatively.

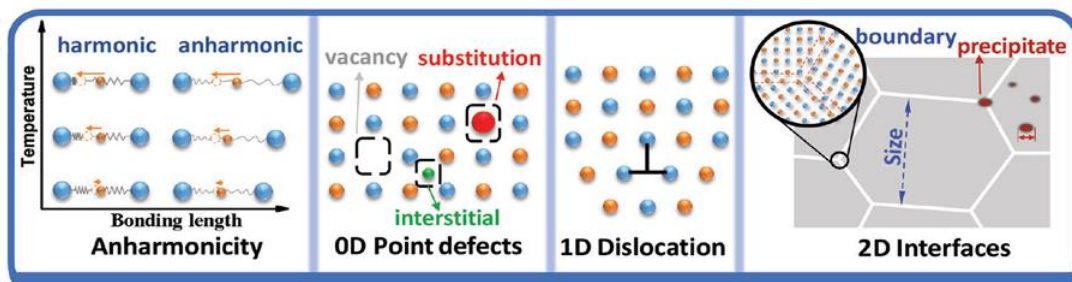


**Figure 1.8.** A simple schematic to explain the various routes to suppress  $\kappa_L$  in the crystal system.<sup>27</sup>

An effective method to boost thermoelectric performance without reducing electrical mobility is to look for materials having innately low lattice thermal conductivity ( $\kappa_L$ ). Finding materials with naturally low  $\kappa_L$  makes it possible to independently adjust their thermoelectric characteristics, improving power factor and total thermoelectric efficiency. This approach offers a promising avenue for the rational design of high-performance thermoelectric materials.

### 1.3.4. State of art thermoelectric materials

There are many commercially viable options and more potential materials in the area of thermoelectric materials. The material selection is influenced by the intended operating temperature for a given application. At the moment, derivatives of bismuth and antimony tellurides are widely used for temperatures below 200 °C.<sup>28–30</sup> Lead tellurides and silicon germanium alloys are the most popular options at intermediate and high temperatures, above 700 °C.<sup>21,31–35</sup>

A new generation of thermoelectric materials with a high thermoelectric figure of merit ( $ZT$ ) has been developed as a result of extensive study on bismuth and lead tellurides and the use of nanostructuring approaches in the wake of Hicks and Dresselhaus' work.<sup>36</sup> Notably,  $ZT$  values above 2 have been attained by hierarchical lead telluride (PbTe) structures.<sup>37</sup> At about 300 K, thin-film superlattice thermoelectrics, such as Bi<sub>2</sub>Te<sub>3</sub>/Sb<sub>2</sub>Te<sub>3</sub> superlattices, have shown a  $ZT$  above 2.5.<sup>38</sup> Though their usage of heavy and poisonous metals like tellurium or lead makes them unsuitable for large-scale manufacture, nanostructured or thin-film materials are only suitable for limited applications.

In addition to the tellurides and selenides of bismuth and lead, a number of additional material families have demonstrated promising performance with  $ZT$  values of more than one. These include half-Heusler alloys,<sup>39–42</sup> skutterudites,<sup>43–45</sup> clathrates,<sup>46,47</sup> silicides,<sup>48,49</sup> and Zintl phases<sup>50,51,52</sup>. Thermoelectric materials for large-scale power generation should ideally be simple to produce and rely on naturally occurring, environmentally safe ingredients. Unfortunately, they are still less effective than selenides or tellurides now in use.

Oxides have been actively investigated as prospective thermoelectric materials over the past 20 years, including doped zinc oxides (ZnO), layered cobalt oxides, and oxides of the perovskite variety (such as SrTiO<sub>3</sub>).<sup>53,54</sup> However, the best  $ZT$  values are found at high temperatures and remain below unity because of the ionic nature of oxide atomic bonding and their high electrical resistivity along with high thermal conductivity due to ionic nature of the compounds.<sup>54</sup>

While the toxicity of some elements (such as lead and tellurium), the scarcity of tellurium, and the high price of germanium and tellurium limit the applications for these materials, a number of potential substitute materials have been investigated during the 1990s. These materials, which are currently in development, may outperform their indications. As a result, thermoelectric sulfides have become a viable substitute for toxic selenides and tellurides as well as oxides.

#### **1.3.4.1. Advantages of sulfides in thermoelectric application**

Sulfide materials have shown promise as thermoelectric technology alternatives, providing a number of benefits over other materials. They are a desirable option for effective energy conversion due to their special characteristics and quantity of constituent materials. The following are the benefits of investigating sulfides over other thermoelectric materials.

- **Environmental friendliness:** Sulfide materials are regarded as being environmentally benign due to their non-toxicity and reliance on plentiful components. Their use in thermoelectric applications lessens reliance on toxic materials like tellurides and selenides, advancing environmentally friendly energy options.
- **Abundance and Cost-effectiveness:** Sulfide materials typically consist of components like sulfur, copper, zinc, and iron, which are both plentiful and economical. Sulfides provide an affordable alternative for thermoelectric devices, making them more commercially viable than other rare or expensive

elements. Figure 1.6. shown the earth abundance and relative cost of chalcogenides.<sup>55</sup>

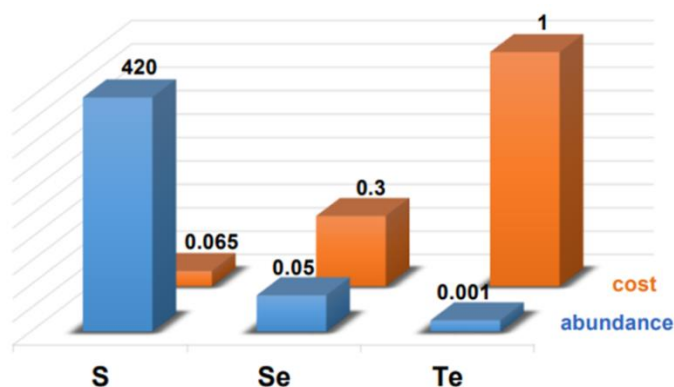


**Figure 1.9.** Earth abundance (ppm) and relative cost of chalcogenides.

#### 1.3.4.2. State of art thermoelectric sulfides

In recent times, there has been a notable focus on metal sulfides as prospective thermoelectric materials. Due to their affordability, non-toxic nature, and abundance, these materials are considered highly favourable for potential utilization in future commercial thermoelectric applications, as previously mentioned. Depending on the complexity in the crystal structure we can categorize TE sulfides based compounds in two categories, (a) binary sulfides which includes  $\text{TiS}_2$ ,  $\text{SnS}$ ,  $\text{PbS}$ ,  $\text{Cu}_2\text{S}$  etc. and (b) copper based ternary and quaternary sulfides. In the following paragraphs, I will provide a comprehensive description of various states of art thermoelectric sulfides.

##### **Binary sulfides.**

Imai *et al.* reported the thermoelectric properties of the single crystals of *n*-type  $\text{TiS}_2$  which demonstrate a thermoelectric power factor of  $3.71 \text{ mW cm}^{-1} \text{ K}^{-2}$  at 300 K, a value that is comparable to that of commercial  $\text{Bi}_2\text{Te}_3$ .  $\text{TiS}_2$  has gained attention as a promising thermoelectric material due to its layered structure and capacity for modifying transport properties through intercalation or substitution, despite its higher thermal conductivity. The crystal structure is shown in **Figure 1.10 a**. Optimization of the charge carrier concentration was achieved through the self-intercalation of titanium,

which was accompanied by transfer of charge carriers to the Ti 3d band.  $\text{Ti}_{1.025}\text{S}_2$  exhibited a  $ZT$  value of 0.48 at 700 K, while  $\text{Ti}_{1.008}\text{S}_2$ , prepared through the sulfurization of  $\text{TiO}_2$  and consolidated by SPS, achieved  $ZT = 0.34$  at 663 K. The incorporation of copper and silver through intercalation has also demonstrated efficacy in enhancing the thermoelectric figure of merit by concomitantly mitigating thermal conductivity and electrical resistivity. The compounds  $\text{Cu}_{0.1}\text{TiS}_2$  and  $\text{Ag}_{0.1}\text{TiS}_2$  show thermoelectric figure of merit ( $ZT$ ) values of 0.45 at temperatures of 800 K and 700 K, respectively. Furthermore, it is possible to generate superlattices through the process of intercalation, wherein complete block layers are inserted between successive  $\text{TiS}_2$  layers. The resulting superlattice can be represented by the formula  $(\text{MX})_{1+x}(\text{TiS}_2)_n$ , where M denotes Pb, Bi, Sn, Sb, rare-earth elements, and n can assume values of 1, 2, or 3. The presence of stacking faults within the superlattices results in a significant reduction of the lattice's contribution to thermal conductivity.

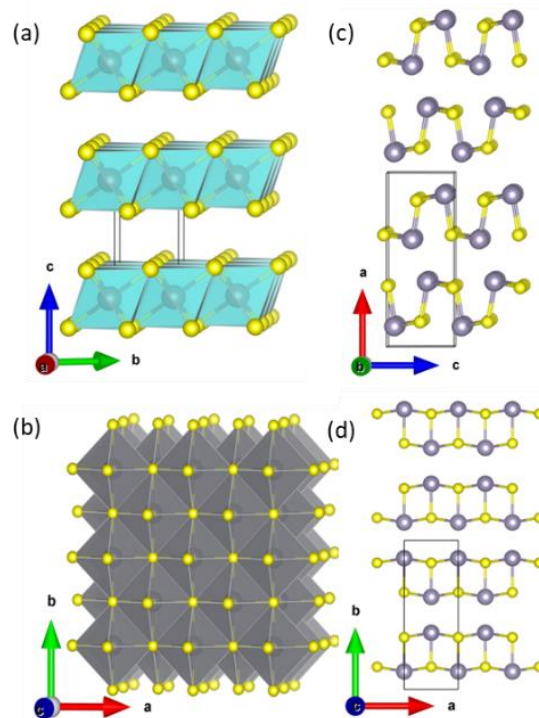


**Figure 1.10.** The crystal structure of (a)  $\text{TiS}_2$ , (b)  $\text{PbS}$ , (c)  $\text{SnS}$  ( $Pnma$ ), (d)  $\text{SnS}$  ( $Cmcm$ ).

On the other hand, tin (II) sulphide (SnS), has attracted considerable interest thanks to its distinct characteristics and its possible application in thermoelectric devices. One of the key reasons of considering semiconducting SnS for thermoelectric applications is its intrinsically low thermal conductivity and high Seebeck coefficient. SnS exhibits a direct band gap, making it a viable candidate for effective energy conversion. Moreover, SnS exhibits a number of favourable properties including cost-effectiveness, non-toxicity, and abundance in the natural environment, rendering it a compelling contender for prospective thermoelectric implementations. At high temperatures, around 875 K, SnS, which have an orthorhombic crystal structure, change from the *Pnma* phase to the *Cmcm* phase shown in **Figure 1.10 c, d**. Tan *et al.* reported a maximum dimensionless figure of merit (*ZT*) value for undoped SnS at 873 K of 0.16 in their study. Nonetheless, it is noteworthy that the thermal conductivity was comparatively high, i.e.  $\sim 1.25 \text{ W m}^{-1} \text{ K}^{-1}$  at a temperature of 300 K. In order to enhance the thermoelectric efficiency, the carrier concentration of SnS was optimized through Ag for Sn substitution. Due to the considerable decrease in thermal conductivity, down to  $0.5 \text{ W m}^{-1} \text{ K}^{-1}$  at 873 K, the *ZT* value increased to 0.6. Subsequently, Han *et al.* improved the thermoelectric figure of merit (*ZT*) by incorporating a SnS solid solution with tin selenide (SnSe). A *ZT* value of 0.82 was attained at a temperature of 823 K for the  $\text{SnS}_{0.2}\text{Se}_{0.8}$  composition. In a recent study, He *et al.* improved the efficiency of carrier mobility and effective mass ( $m^*$ ) by incorporating selenium (Se) into SnS. A maximum figure of merit *ZT* of 1.6 at 873 K was obtained for  $\text{SnS Se}_{0.09}$ . Furthermore, an average *ZT* value ( $ZT_{\text{ave}}$ ) of approximately 1.25 was acquired for the  $\text{SnS}_{0.91}\text{Se}_{0.09}$  over the temperature range of 300 to 873 K. Lately, Zhan *et al.* reported *n*-type sulfide  $\text{PbSnS}_2$  with isostructural to SnS is obtained through Pb alloying and achieves a maximum *ZT* of about 1.2 at 773 K and an average *ZT* of 0.75 within 300-773 K, which results from enhanced power factor and intrinsically ultralow thermal conductivity.<sup>56</sup>

Additionally, PbS (lead sulfide) has been studied as an alternative to its telluride and selenide analogues.<sup>57,58</sup> Both of these compounds have a structure that is similar to that of NaCl and Pb and S/Se/Te are present in the cation and anion sites, respectively (**Figure 1.10. b**). In bulk *n*-type PbS samples that were synthesised by mechanically

milled followed by spark plasma sintering (SPS), a  $ZT$  value of 0.31 was achieved at 723 K.<sup>59</sup> When sodium-doped PbS samples were prepared under the same conditions, they exhibited  $p$ -type conductivity. Among them,  $\text{Pb}_{0.975}\text{Na}_{0.025}\text{S}$  showed a maximum  $ZT$  value of 0.54 at 723 K.<sup>59</sup> Incorporating a second phase of SrS or CaS into sodium-doped PbS led to additional improvements in the material's performance.<sup>59</sup> At 723 K, the  $ZT$  values reached 0.73 and 0.72, respectively, when 3.0% SrS or CaS was added, and a maximum  $ZT$  values reached 1.22 and 1.12, respectively at 923 K. This enhancement in performance can be attributed to phonon scattering caused by point defects in the solid solution and the nanostructuring that was accomplished by the presence of a secondary phase. Both of these factors contributed to the increase the  $ZT$  value. In a study that was quite comparable to this one, the presence of ZnS and CdS nanophase precipitates produced results that were slightly more favorable.<sup>60</sup> At a temperature of 923 K, the  $ZT$  value of  $\text{Pb}_{0.975}\text{Na}_{0.025}\text{S}$  containing 3.0 % CdS reached 1.3.

Recently, Cu-sulfides attracted attention in thermoelectric community.  $\text{Cu}_{2-x}\text{S}$  has a complex crystal structure and the nomenclature can be confusing due to the different forms and phases it can possess.<sup>61-66</sup>  $\text{Cu}_{2-x}\text{S}$  compounds are made up of a lattice of sulfur (S) atoms with copper (Cu) atoms occupying interstitial positions. Chalcocite is a stoichiometric form of  $\text{Cu}_2\text{S}$  with a copper to sulfur ratio of 2:1. Depending on the temperature range and the copper amount, Potter *et al.* claims that  $\text{Cu}_2\text{S}$  can exist in three different modifications or phases.<sup>67</sup> Low chalcocite is a monoclinic phase that exists below a temperature of roughly 103 °C. A hexagonal phase known as high chalcocite is seen between this temperature and roughly 436 °C. The cubic phase of  $\text{Cu}_2\text{S}$  is adopted above this temperature.<sup>67</sup> The migration of copper ions in the high-temperature cubic phase is intricately linked to the phonon-liquid electron-crystal (PLEC) concept. The thermoelectric properties of the  $\text{Cu}_2\text{S}$  crystal structure are influenced by the migration of ions, which can have benefits as well as drawbacks. On the one hand, the material exhibits a favourable impact as it reduces thermal conductivity while simultaneously enhancing electrical conductivity. The previous observation implies that the thermoelectric efficiency of  $\text{Cu}_2\text{S}$  can be improved through ionic migration. However, on the other hand, the migration of ions can cause a lack of stability in the  $\text{Cu}_2\text{S}$  structure under electric current. A lack of copper atoms in the

crystal structure could arise from this, which could impact the material's transport properties and lead to decomposition. Evans *et al.* identified the crystal structure of the monoclinic phase (low chalcocite), which is closely similar to that of the high chalcocite phase.<sup>62</sup> It is important to note that  $\text{Cu}_{1.8}\text{S}$ , also known as digenite, is regarded as a distinct phase. The thermoelectric (TE) properties of *p*-type  $\text{Cu}_{1.8}\text{S}$  were investigated and reported by Ge *et al.*<sup>68</sup> The high-temperature (HT) form of  $\text{Cu}_{1.8}\text{S}$  was synthesized by optimizing the mechanical alloying (MA) step of the synthesis process, and then the material was densified by spark plasma sintering (SPS). The material displayed a combination of a metallic electrical resistivity ( $\rho$ ) which leads to a high-power factor (*PF*) of  $1 \text{ mW m}^{-1} \text{ K}^{-2}$  at 673 K. However, due to high total thermal conductivity, the *ZT* value is constrained.

### **Complex copper-based ternary and quaternary sulfides.**

Thermoelectric materials with high performance, typically exhibiting transport properties resembling those of heavily doped semiconductors or semi-metals, often possess a carrier concentration ranging from  $10^{19}$  to  $10^{21} \text{ cm}^{-3}$ . Interestingly, several naturally occurring minerals give rise to ternary and quaternary copper sulfides that demonstrate these desirable characteristics. These materials often have complex structures that inherently lead to reduced intrinsic thermal conductivities. These semiconductors have the capability to be doped in order to enhance the carrier concentration, or they possess an inherent characteristic of being "intrinsic" degenerate semiconductors. According to the recent classification, the copper sulfide phases (both ternary and quaternary) can be classified into five groups (group A to E) (Figure 1.11) depending on the nature and coordination of the metal sulfide polyhedral and the complexity of their 3D ordering.

Group A consists of sphalerite-type structures characterized by corner-sharing  $MS_4$  tetrahedral networks. These compounds exhibit a three-dimensional network where a central metal atom is surrounded by four sulfur atoms arranged in a tetrahedral fashion like chalcopyrite ( $\text{CuFeS}_2$ ), Stannite ( $\text{Cu}_2\text{FeSnS}_4$ ), briartite ( $\text{Cu}_2\text{FeGeS}_4$ ) and kesterite ( $\text{Cu}_2\text{ZnSnS}_4$ ). Group B, also sphalerite-type structures, contains isolated  $[TS_4]M_6$

complexes. These complexes consist of an interstitial atom ( $T$ ) forming tetrahedra ( $TS_4$ ) connected to octahedra ( $TM_6$ ) like colusite and germanite. However, unlike Group A, these complexes are not part of a continuous network. Group C comprises sylvanite-type structures and metal-poor sylvanite-type derivatives. These structures contain  $[TS_4]M_6$  complexes that are connected either in a three-dimensional (3D) or two-dimensional (2D) manner like sylvanite and mooihoekite. The arrangement of these complexes defines the sylvanite-type structure. Group D is characterized by anti-fluorite-type structures, which exhibit two interpenetrating networks of corner-sharing  $MS_4$  and  $TS_4$  tetrahedra. This arrangement leads to a global network of corner and edge sharing between  $(M, T)S_4$  tetrahedra. Bornite ( $Cu_5FeS_4$ ) belongs to this group. Lastly, Group E includes compounds that possess at least one polyhedron with a metal coordination other than tetrahedral. This difference in chemical surrounding arises due to factors such as the presence of elements incompatible with tetrahedral coordination, high local disorder, or a smaller proportion of  $Cu^+$  ions compared to previous groups. The degenerate semiconductor tetrahedrite ( $Cu_{12}Sb_4S_{13}$ ) belongs to this group.

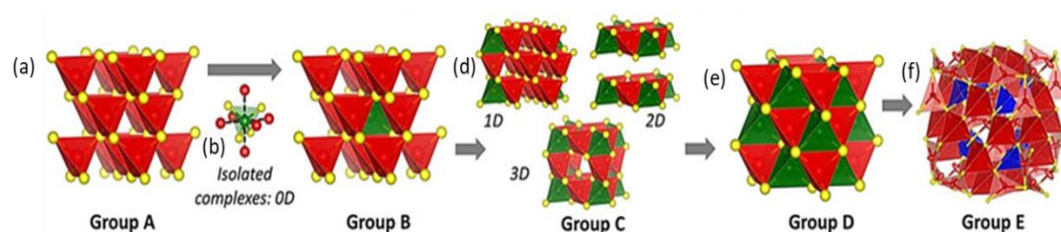


**Figure 1.11.** (a) the group A sphalerite-type structures, (b) the tetrahedral–octahedral  $[TS_4]M_6$  complex, (c) the group B sphalerite-type structures containing isolated  $[TS_4]M_6$  complexes, (d) the group C sylvanite-type structures and metal-poor sylvanite-type derivatives containing  $[TS_4]M_6$  complexes connected in a 3D and 2D manner, (e) the group D anti-fluorite-type structures.

A semiconducting Cu-Fe-S ternary phase from group A,  $CuFeS_2$ , also known as chalcopyrite, is a naturally occurring mineral that crystallizes into a tetragonal structure (**Figure 1.1238a**), where  $CuS_4$  and  $FeS_4$  tetrahedra combine to produce a double-sphalerite structure with ordered cationic sub-lattices.<sup>69,70</sup> A gradual increase in efficiency can be seen in this system by improving electrical properties and

decreasing thermal conductivity with the help of chemical doping. Other example of group A compounds that also attracted attention to the scientific community are stannite ( $\text{Cu}_2\text{FeSnS}_4$ ), briartite ( $\text{Cu}_2\text{FeGeS}_4$ ) and kesterite ( $\text{Cu}_2\text{ZnSnS}_4$ ). stannite ( $\text{Cu}_2\text{FeSnS}_4$ ), a semiconductor, crystallizes in a tetragonal structure (space group  $I-42m$ ) derived from sphalerite. It consists of corner-sharing tetrahedra composed of  $[\text{CuS}_4]$ ,  $[\text{FeS}_4]$ , and  $[\text{SnS}_4]$  units. Other minerals with a similar crystal structure, such as briartite ( $\text{Cu}_2\text{FeGeS}_4$ ) and kesterite ( $\text{Cu}_2\text{ZnSnS}_4$ ), are  $p$ -type semiconductors. All compounds in group A are consider to be semiconductor and can be easily doped. The doping in these compounds improves the charge delocalization and improves the efficiency.

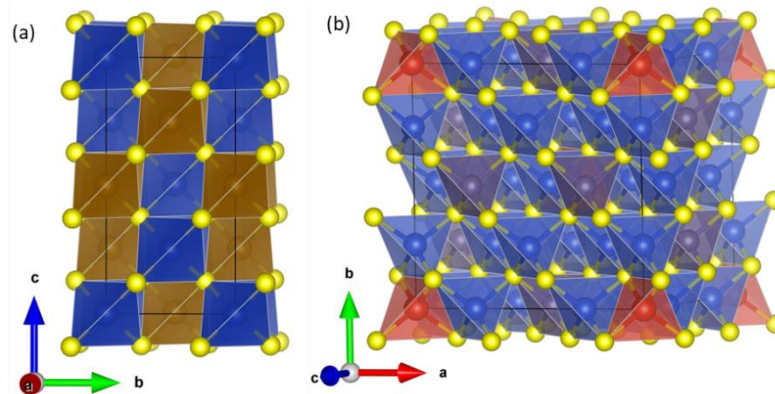


**Figure 1.12.** (a) The group A compound  $\text{CuFeS}_2$ , (b) the group B compound  $\text{Cu}_{26}\text{V}_2\text{M}_6\text{S}_{32}$

Moving into Group B materials, which have a structural similarity and similar electronic structure to group A compounds, exhibit many shared characteristics. One important aspect is the multi-band nature of the top of the valence band, primarily composed of Cu 3d and S 3p orbitals, creating a conductive network known as "Cu-S". This makes group B materials degenerate semiconductors which show compelling electrical transport properties. Nevertheless, the introduction of an "interstitial" atom and the resulting alterations in the crystal structure significantly impact their performance. Notably, the unit cell can expand considerably to

accommodate the new elements at specific crystallographic sites. Consequently, the combination of large unit cells and the presence of at least two different cations at similar crystal sites generally lead to lower thermal conductivities compared to group A sulfides.

Group B compounds, colusite and germenite are widely explored compounds which are degenerate semiconductors in nature. Colusite, with the general chemical formula  $\text{Cu}_{24+x}\text{V}_2(\text{As,Sb})_{6-x}(\text{Ge,Sn})_x\text{S}_{32}$  ( $x \leq 2$ ), demonstrates a superstructure derived from sphalerite. Colusite's crystal structure is defined by a simple cubic unit cell (with  $a \sim 10.5 \text{ \AA}$  and belonging to the  $P-43n$  space group) with 66 atoms scattered among seven crystallographic sites (**Figure 1.12. b**). There are three sites for Cu (6d, 8e, 2f), one for V (2a), one for  $M$  (As, Sb, Sn, Ge) (6c), and two sites for S (8e, 24i). The  $[\text{VS}_4]$  and  $[\text{CuS}_4]$  tetrahedra in the structure share edges, whereas the  $[\text{MS}_4]$  and  $[\text{CuS}_4]$  tetrahedra share corners, resulting in a three-dimensional network. Whereas, the mineral germenite has a cubic structure like colusite derived from ZnS, sphalerite and is characterized by the formula " $\text{Cu}_{26}\text{Fe}_4\text{Ge}_4\text{S}_{32}$ ". It has a cationic distribution distinct from colusite. The initial formula proposed by De Jong was  $\text{Cu}_3(\text{Fe,Ge})\text{S}_4$ ,<sup>71</sup> while a revised formula by Sclar et al. included a wider variety of elements and the possibility of sulfur substitution with arsenic,  $\text{Cu}_3(\text{Fe, Ge, Zn, Ga})(\text{S, As})_4$ .<sup>72</sup>

Consequently, group C materials characterized by a connectivity of a tetrahedral-octahedral  $[\text{TS}_4]\text{M}_6$  complex, such as the mooihoekite and sylvanite-type compounds and , have been moderately investigated for their poor transport properties. One example is the semi-conducting sylvanite ( $\text{Cu}_3\text{VS}_4$ ) (**Figure 1.13**), which has a suitable band gap for photovoltaic applications but a heavier hole effective mass compared to its selenium (Se) and tellurium (Te) counterparts. Similarly, little research has been done on optimizing the thermoelectric properties of the parent sylvanite and its Group 5 counterparts  $\text{Cu}_3\text{TS}_4$  ( $T = \text{Nb, Ta}$ ). One notable feature of sylvanite-type compounds is their ability to accommodate d-block elements with various oxidation states (+IV, +V, and +VI) by modifying the "Cu-S" network to balance the charge. The materials in this group are not suitable for

thermoelectric applications due to their high electrical resistivity resulting from large band gap.

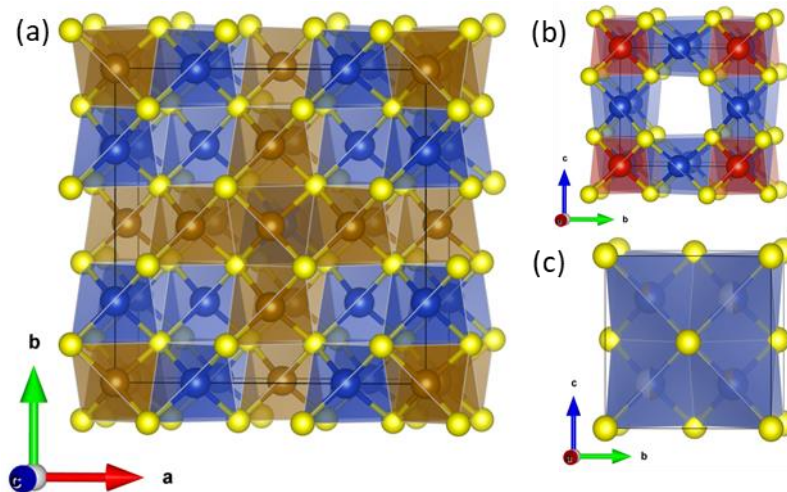


**Figure 1.13.** The crystal structure of (a)  $\text{Cu}_9\text{Fe}_9\text{S}_{16}$ , (b)  $\text{Cu}_3\text{VS}_4$ , (c)  $\text{Cu}_5\text{FeS}_4$

Subsequently, Bornite from Group D possesses anti-fluorite-type structures, which exhibit two interpenetrating networks of corner-sharing  $MS_4$  and  $TS_4$  tetrahedra. This arrangement leads to a global network of corner and edge sharing between  $(M, T)S_4$  tetrahedra. The liquid-like nature of the cation sub-lattice in  $\text{Cu}_{1.8}\text{S}$  makes it unsuitable for thermoelectric (TE) applications due to high ionic mobility. However, solving the stability issue would result in a loss of performance from its unique "liquid-like" character. On the other hand, bornite ( $\text{Cu}_5\text{FeS}_4$ ) provides a solution to suppress ionic conductivity by utilizing the pinning effect of iron (Fe) in specific "interstitial" positions. This allows bornite-based materials to address the stability issue while still offering potential for thermoelectric applications.

At last tetrahedrite belongs to group E, a naturally-occurring minerals with the chemical composition  $A_{10}B_2C_4Q_{13}$ , where  $A$  can be Cu or Ag,  $B$  includes elements such as Mn, Fe, Co, Ni, Zn, Cu, Hg, and Cd,  $C$  comprises As, Sb, or Bi, and  $Q$  represents S or Se.<sup>73–75</sup> These minerals have a complex crystal structure with the space group  $I-43m$ .<sup>65</sup> The structure is derived from sphalerite, with six transition

metals occupying tetrahedral sites and the other six occupying trigonal planar sites, while the pnictogen atoms occupy trigonal pyramidal sites.<sup>76</sup> Among the twelve transition metals, two are divalent (*A*), and the rest are monovalent cations (*B*). Previous studies have established that only monovalent cations occupy the trigonal planar sites, while the tetrahedral sites are shared between four monovalent and two divalent cations (**Figure 1.14**). Tetrahedrite has gained attention for its thermoelectric properties after the report by Suekuni *et al.* and Lu *et al.*<sup>71,72</sup> The degenerate semiconductor tetrahedrite ( $\text{Cu}_{12}\text{Sb}_4\text{S}_{13}$ ) has three structural components that interact to produce distinct performance characteristics. The above-mentioned blocks comprise a sub-lattice of sphalerite type, which is composed of tetrahedral  $\text{CuS}_4$  units and forms a conductive network known as "Cu-S" making it degenerate semiconductor. Additionally, there are  $\text{CuS}_3$  trigonal planar units and  $\text{SbS}_3$  trigonal pyramids, both contributing to reducing the material's thermal conductivity. There has been debate about whether Sb interacts with a Cu ion in a trigonal planar site via weak bonding to increase out-of-plane vibration or whether Sb essentially forms a lone pair of electrons that only affects the rattling of the copper atoms.

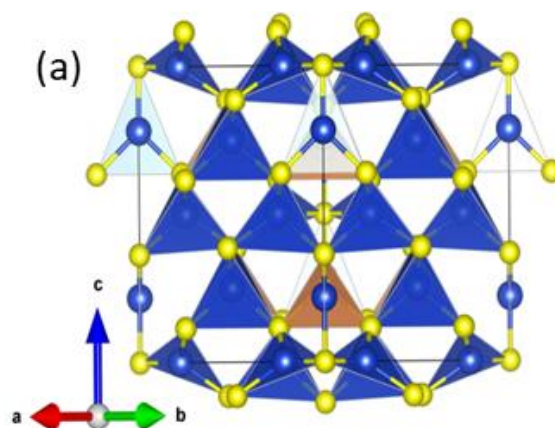


**Figure 1.14.** The crystal structure of tetrahedrite ( $\text{Cu}_{12}\text{Sb}_4\text{S}_{13}$ )

**Table 1.1.** Characteristics of some of complex copper-based ternary and quaternary sulfides .

| Groups  | Compounds   | Composition  | Temp. range (K) | Type     | ZT         | $T_{ZTmax}$ (K)                  | Advantages   | Disadvantage           | References |
|---|---|--|-----------------|----------|------------|----------------------------------|--|------------------------|------------|
| Group A   | Chalcopyrite (CuFeS <sub>2</sub> )  | Cu <sub>0.96</sub> Co <sub>0.04</sub> FeS <sub>2</sub>                                 | 300 – 650       | <i>n</i> | 0.22       | 675                              | S high, ρ moderate   | κ very high            | 70,77–80   |
|   |   | CuFeS <sub>1.9</sub> Se <sub>0.1</sub>   | 80 - 670        |          | 0.16       | 670                              |  |                        |            |
|   |   | Cu <sub>0.95</sub> Fe <sub>1.05</sub> S <sub>2</sub>                                   | 300-700         |          | 0.3        | 700                              |  |                        |            |
|   | Stannite (Cu <sub>2</sub> FeSnS <sub>4</sub> )                                | Cu <sub>2.08</sub> Fe <sub>0.92</sub> SnS <sub>4</sub>                                 | 80-300          | <i>p</i> | 0.04       | 300                              | S high, ρ moderate   | κ high                 | 81         |
| Kesterite (Cu <sub>2</sub> ZnSnS <sub>4</sub> ) | Cu <sub>2.125</sub> Zn <sub>0.875</sub> SnS <sub>4</sub>                      | 300-700  | <i>p</i>        | 1        | 700        | S high, stable in air upto 830 K | κ moderate, ρ high   | 82                     |            |
| Group B   | Colusite (Cu <sub>26</sub> V <sub>2</sub> Sn <sub>6</sub> S <sub>32</sub> )   | Cu <sub>26</sub> V <sub>2</sub> Sn <sub>6</sub> S <sub>32</sub>                        | 300-700         | <i>p</i> | 1          | 700                              | S high, ρ low, κ very low (disordered)   | -                      | 83–86      |
|   |   | Cu <sub>26</sub> Nb <sub>2</sub> Ge <sub>6</sub> Co <sub>0.5</sub> S <sub>32</sub>     | 300-665         |          | 0.7        | 665                              |  |                        |            |
|   |   | Cu <sub>26</sub> V <sub>2</sub> M <sub>6</sub> S <sub>32</sub><br>M = (Ge, Sn)         | 350-650         |          | 0.8<br>0.6 | 650                              |  |                        |            |
|   | Germanite (Cu <sub>22</sub> Fe <sub>8</sub> Ge <sub>4</sub> S <sub>32</sub> ) | Cu <sub>22</sub> Fe <sub>8</sub> Ge <sub>4</sub> S <sub>32</sub>                       | 300-575         | <i>p</i> | 0.17       | 575                              | ρ low (Cu <sup>+</sup> /Cu <sup>2+</sup> )   | κ moderate             | 87         |
| Group C   | Sulvanite (Cu <sub>3</sub> VS <sub>4</sub> )                                  | -  | -               | <i>p</i> | -          | -                                | κ low (high band gap)  | ρ high (high band gap) | -          |
|   | Mooihoekite (Cu <sub>9</sub> Fe <sub>9</sub> S <sub>16</sub> )                | -  | -               | <i>n</i> | -          | -                                |  |                        | -          |
| Group D   | Bornite (Cu <sub>5</sub> FeS <sub>4</sub> )                                   | Cu <sub>5.02</sub> Fe <sub>0.98</sub> S <sub>4</sub>                                   | 2-700           | <i>p</i> | 0.4        | 700                              | S high, κ very low   | ρ very high            | 88,89      |
|   |   | Cu <sub>5</sub> FeS <sub>3.6</sub> Se <sub>0.4</sub>                                   | 350-673         |          | 0.65       | 673                              |  |                        |            |
| Group E   | Tetrahedrite (Cu <sub>12</sub> Sb <sub>4</sub> S <sub>13</sub> )              | Cu <sub>10.5</sub> Ni <sub>1.5</sub> Zn <sub>0.5</sub> Sb <sub>4</sub> S <sub>13</sub> | 300-700         | <i>p</i> | 1          | 723                              | ρ very low (Cu <sup>+</sup> /Cu <sup>2+</sup> ), S moderate, low κ (Cu atom vibration) | Presence of Sb         | 90–96      |
|   |   | Cu <sub>10.4</sub> Ni <sub>1.6</sub> Sb <sub>4</sub> S <sub>13</sub>                   | 300-700         |          | 0.75       | 700                              |  |                        |            |
|   |   | Cu <sub>10.4</sub> Ni <sub>1.6</sub> Sb <sub>4</sub> S <sub>13</sub>                   | 300-700         |          | 0.8        | 700                              |  |                        |            |

The previous paragraph discusses the thermoelectric properties of different types of sulfides, including binary, ternary, and quaternary compounds. It points out that many of the advanced materials in this field are either transition metal-based or antimony-based. The paragraph also suggests that bismuth-based sulfides have not been extensively studied in the context of thermoelectric applications and could offer interesting possibilities.

### **1.3.4.3. Advantages of Bi-based compound in thermoelectric application**

There are various benefits to using Bi-based compounds in addition to their lower toxicity as compared to other heavy element-based compounds like Pb and Te. At first, it is noteworthy that bismuth possesses active lone pairs due to the inert pair effect, which is not covalently bonded to the counter anion. The presence of lone pair electrons in bismuth is likely to result in an increased degree of asymmetry in electron density, thereby leading to more pronounced lattice anharmonic vibration. The existence of pairs of electrons that are not shared typically results in heightened nonlinearity in the arrangement of atoms in the crystal lattice, impeding the propagation of vibrational waves and diminishing the thermal conductance. Additionally, it should be noted that the mass of its constituent atoms influences the thermal conductivity of a lattice. Typically, a heavy atomic mass results in a decrease in acoustic phonon frequency, group velocity, and lattice thermal conductivity.

### **1.3.4.4. Conventional Bi-based thermoelectric sulfides and their structure-properties relationship**

The simplest bismuth-based sulfide, bismuthinite ( $\text{Bi}_2\text{S}_3$ ), has caught the interest of the thermometric community due to its efficiency as well as the fact that sulfur is non-toxic and earth-abundant.  $\text{Bi}_2\text{S}_3$  exhibits a highly anisotropic one-dimensional orthorhombic structure with a space group of  $Pbnm$ , characterized by infinite  $\text{Bi}_2\text{S}_3$  chains aligned along the crystallographic  $c$ -axis. The lattice parameters are  $a = 11.170 \text{ \AA}$ ,  $b = 11.319 \text{ \AA}$ ,  $c = 3.992 \text{ \AA}$ ,  $\alpha = \beta = \gamma = 90^\circ$ ,  $\text{Bi}_2\text{S}_3$  is primarily held together by weak van der Waals forces, forming what is known as a quasio-one-dimensional structure with properties resembling those of low-dimensional materials. Similar to  $\text{Sb}_2\text{S}_3$ ,  $\text{Bi}_2\text{S}_3$  is a common chain-like structure in which two  $[\text{BiS}_3]$  trigonal cone units are linked together in serrated chains that expand in the  $[001]$  direction to create  $[\text{Bi}_4\text{S}_6]$ .<sup>97</sup> The presence of both 6 and 5 coordination in  $\text{Bi}_2\text{S}_3$  shows that the bismuth atoms have a lone pair of electrons. This lone pair has been observed to enhance the scattering probability of phonons in the direction perpendicular to the Bi-S covalent chain, resulting in a reduction of the material's thermal conductivity.

Biswas *et al.* reported high-temperature solid-state synthesis of needle-like morphology in  $\text{Bi}_2\text{S}_3$  and found out the anisotropy in thermoelectric properties.<sup>97</sup> The optimization of carrier concentration was achieved through the introduction of Cl doping, resulting in a measured  $ZT$  value of 0.6 at 760 K for  $\text{Bi}_2\text{S}_3$ -0.5 mol%  $\text{BiCl}_3$  sample perpendicular to the growth direction of the ingot. Guo *et al.* utilized a hydrothermal method to introduce halogen elements, resulting in a significant enhancement of the carrier concentration of  $\text{Bi}_2\text{S}_3$  by two orders of magnitude.<sup>98</sup> This approach ultimately led to the attainment of an exceptional  $ZT$  value of 0.8 at 673 K for the  $\text{Bi}_2\text{S}_{2.96}\text{Cl}_{0.04}$  sample, which is among the highest reported values for  $\text{Bi}_2\text{S}_3$ . In over a decade, multiple efforts have been done to enhance carrier concentration through diverse methods such as chemical doping with elements like Co, I, Br, Ag, and Cr, as well as hierarchical structure manipulation, and nanocomposite formation.<sup>99–102</sup>

Ternary silver bismuth sulfide,  $\text{AgBiS}_2$ , is a representative example of the I-V-VI<sub>2</sub> family.  $\text{AgBiS}_2$  crystallizes in the hexagonal phase with the space group  $P-3m1$  when it is at room temperature.<sup>103</sup> However, it goes through a phase change at a

temperature of about 473 K and takes on a cubic rocksalt structure with the space group  $Fm-3m$ .<sup>103</sup>  $\text{AgBiS}_2$  displays a disorderly arrangement of silver (Ag) and bismuth (Bi) atoms in its high-temperature cubic form. In the compound  $\text{AgBiX}_2$  (where X is S, Se, and Te), bismuth (Bi) has the electronic configuration  $6s^2 6p^3$ . Only the  $6p^3$  electrons of Bi participate in the bonding process with the chalcogen (X) valence electrons, whereas the interesting  $6s^2$  electrons of Bi form a lone pair. The electrostatic attraction between the stereochemically active lone pair of Bi and the valence bonding charge of the chalcogen is the cause of the anharmonicity in the Bi-X (X = S/Se/Te) bond.<sup>104</sup>

The thermoelectric properties of solution based synthesised cubic  $\text{AgBiS}_2$  were reported by Guin et. al. In this study, *n*-type  $\text{AgBiS}_2$  and  $\text{AgBiS}_{2-x}\text{Se}_x$  nanocrystals were synthesized utilizing a bottom-up solution-based method to produce rocksalt structures that are stable at room temperature. The nanocrystals exhibited thermoelectrically important cubic phases.<sup>103</sup> The disordered cation sublattice, bond anharmonicity, and nanoscale grain boundaries in the nanocrystals caused significant phonon scattering, which led to a low lattice thermal conductivity of  $0.4\text{--}0.5 \text{ W m}^{-1} \text{ K}^{-1}$  in the 290–830 K temperature range. An extremely low lattice thermal conductivity of  $0.68\text{--}0.48 \text{ W m}^{-1} \text{ K}^{-1}$  was attained in bulk cubic  $\text{AgBiS}_2$ , showing a strong suppression of phonon propagation in the 298–820 K range.

First-principal phonon dispersion calculations using density functional theory supported the existence of low-energy Einstein modes that were suggested by low-temperature heat capacity measurements resulting from the gentle vibration of Ag and Bi. The local structure of  $\text{AgBiS}_2$ , analyzed using PDF of synchrotron X-ray scattering data, exhibited distortions caused by the stereochemical activity of the  $6s^2$  lone pair on Bi, resulting in lattice anharmonicity and substantial suppression of the lattice thermal conductivity. Finally, at 823 K, *n*-type bulk  $\text{AgBiS}_2$  showed a maximum thermoelectric figure of merit (*ZT*) of about 0.7.<sup>105</sup>

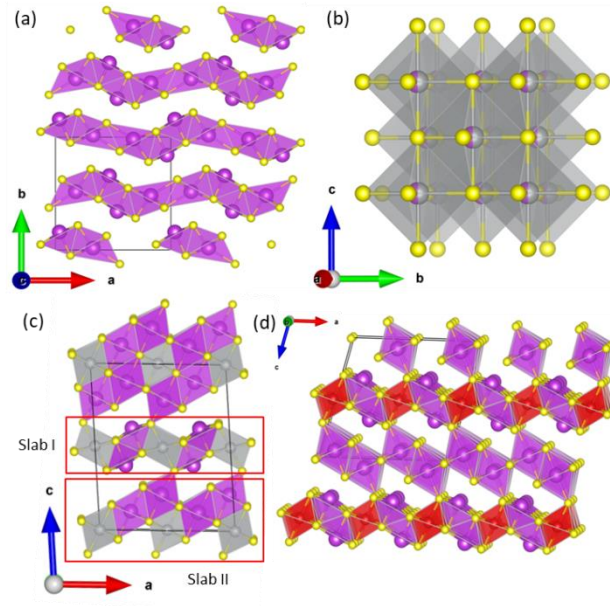


**Figure 1.16.** The crystal structure of (a)  $\text{Bi}_2\text{S}_3$ , (b)  $\text{AgBiS}_2$ , (c)  $\text{AgBi}_3\text{S}_5$ , (d)  $\text{MBi}_4\text{S}_7$  ( $M = \text{Mn}, \text{Fe}$ )

$\text{AgBi}_3\text{S}_5$ 's crystal structure exhibits a monoclinic system with a  $C2/m$  space group. The lattice parameters are as follows:  $a = 13.345(3) \text{ \AA}$ ,  $b = 4.0416(8) \text{ \AA}$ ,  $c = 16.439(3) \text{ \AA}$ , and  $\beta = 94.158(3) \text{ \AA}$ .<sup>106</sup> Two different sorts of alternating slabs compose the structure, which comes together to create a three-dimensional design. The slabs in  $\text{AgBi}_3\text{S}_5$  can be described as blocks extracted from a cubic NaCl lattice along the  $[311]$  direction, can be named as Slab I and Slab II. Slab I is thinner and made out of one  $\text{Ag}_2\text{S}_6$  octahedron that is joined to two square pyramids that together make up a  $[\text{Bi}_3\text{S}_5]$  unit. Slab II, in contrast, has a thicker and deformed NaCl-type lattice structure. It has three octahedra: one  $[\text{Ag}_1\text{S}_6]$ , two  $[\text{Bi}_1\text{S}_6]$ , and two  $[\text{Bi}_2\text{S}_6]$ . To denote different members of the pavonite homologous series, the number ( $N$ ) of octahedra per one diagonal octahedral chain of the thicker slabs is used. In the thicker slabs of  $\text{AgBi}_3\text{S}_5$ ,  $N = 5$  denotes the arrangement of five octahedra side by side. These five-octahedral pieces are joined to one another to produce layers that traverse the  $ab$ -plane in the step-like configuration.

For the first time Kim *et. al.* synthesised  $\text{AgBi}_3\text{S}_5$  and its solid solution  $\text{AgSb}_x\text{Bi}_{3-x}\text{S}_5$  ( $x = 0.3$ ) by using the bridgeman technique. At room temperature, both compounds show very low thermal conductivities ( $\sim 1 \text{ W m}^{-1} \text{ K}^{-1}$ ).<sup>107</sup> Later,

this phase was synthesised by Zhang *et al.* using the ball milling and spark plasma sintering (SPS) techniques, where the thermal conductivity of the bulk phase decreased from 0.70 to 0.64 W m<sup>-1</sup> K<sup>-1</sup> from 300 K to 573 K and a peak  $ZT$  value of 0.20 was reached at 573 K.<sup>108</sup> Recently, Tan *et al.* rediscover this phase and explain the origin of low thermal conductivity. Phase pure AgBi<sub>3</sub>S<sub>5</sub> and Cl-doped AgBi<sub>3</sub>S<sub>5</sub> were synthesised by high-temperature melting and an exceptionally low thermal conductivity of 0.5–0.3 W m<sup>-1</sup> K<sup>-1</sup> in the temperature range of 300–800 K, which is ascribed to its unusual vibrational properties, “double rattling” phonon modes associated with Ag and Bi atoms. For 0.33% Cl-doped AgBi<sub>3</sub>S<sub>5</sub> a maximum  $ZT$  value of 1 was obtained which is one of the most effective  $n$ -type sulfides to date.<sup>106</sup> Later several attempts to increase the efficiency of AgBi<sub>3</sub>S<sub>5</sub> were carried out, but never successful in achieving the highest  $ZT$  value of 1.<sup>109</sup> For instance, effective mass and carrier mobility optimization by doping Nb on the Ag site results in a maximum  $ZT$  value of 0.5 at 773 K for Ag<sub>0.97</sub>Nb<sub>0.03</sub>Bi<sub>3</sub>S<sub>5</sub>,<sup>110</sup> whereas both entropy engineering and carrier optimization are done by Se-doping, which not only reduces thermal conductivity but also improves power factor, and the highest  $ZT$  of 0.42 at 723 K was found for AgBi<sub>3</sub>(Se<sub>0.9</sub>S<sub>0.1</sub>)<sub>5</sub>.<sup>108</sup>

Cu<sub>1.6</sub>Bi<sub>4.8</sub>S<sub>8</sub>, a non-stoichiometric degenerate semiconductor, crystallizes in a monoclinic system with a  $C2/m$  space group and has a complex crystal structure with lattice parameters  $a = 13.2188$  (1) Å,  $b = 4.0299$  (1) Å,  $c = 14.0912$  (2) Å,  $\alpha = \gamma = 90^\circ$ , and  $\beta = 115.5238(8)^\circ$ .<sup>55</sup> Cu<sub>1.6</sub>Bi<sub>4.8</sub>S<sub>8</sub> consists of seemingly two distinct alternating slabs, referred to as slab I and slab II, which are interconnected to each other. Different numerical values are given to each element occupying a separate lattice in order to simplify the explanation. For instance, the three places of bismuth are designated as Bi1, Bi2, and Bi3, the five positions of copper (Cu) atoms are designated as Cu1 to Cu5, and the four positions of sulfur are designated as S1 to S4. Bi1, S3, and S4 atoms are arranged in face-shared square pyramids called Bi<sub>3</sub>S<sub>5</sub> substructures that make up Slab I. Each S atom is shared by three Bi atoms in these square pyramidal Bi<sub>3</sub>S<sub>5</sub> substructures, which are oriented along the crystallographic  $b$  direction. These square pyramidal substructures are separated from one another along  $a$  direction by interstitial Cu atoms (Cu1, Cu2, and Cu3) with fractional

occupancies. These interstitial Cu atoms form weak bonds and are distributed along the  $b$  axis. In slab II, positional disorder between the atoms of Bi and Cu may increase phonon-phonon scattering, while contrasted substructures in slab I with disordered Cu atoms in the interstices may do the same in slab I. Due to this structural complexity,  $\text{Cu}_{1.6}\text{Bi}_{4.8}\text{S}_8$  may have a low thermal conductivity ( $\kappa_L$ ). A recent study conducted by Bhui *et al.* involved the synthesis of a pure phase of  $\text{Cu}_{1.6}\text{Bi}_{4.8}\text{S}_8$  using high-temperature melting. The pristine sample of  $\text{Cu}_{1.6}\text{Bi}_{4.8}\text{S}_8$  exhibited an exceptionally low thermal conductivity of approximately  $0.71\text{--}0.44\text{ W m}^{-1}\text{K}^{-1}$  within the temperature range of  $296\text{--}736\text{ K}$ . This low thermal conductivity was attributed to the synchronized constructive influence of several factors including the complex crystal structure, bonding heterogeneity, and intrinsic rattling atoms present in the material. As a result, a maximum  $ZT$  value of 0.25 was achieved.<sup>55</sup>

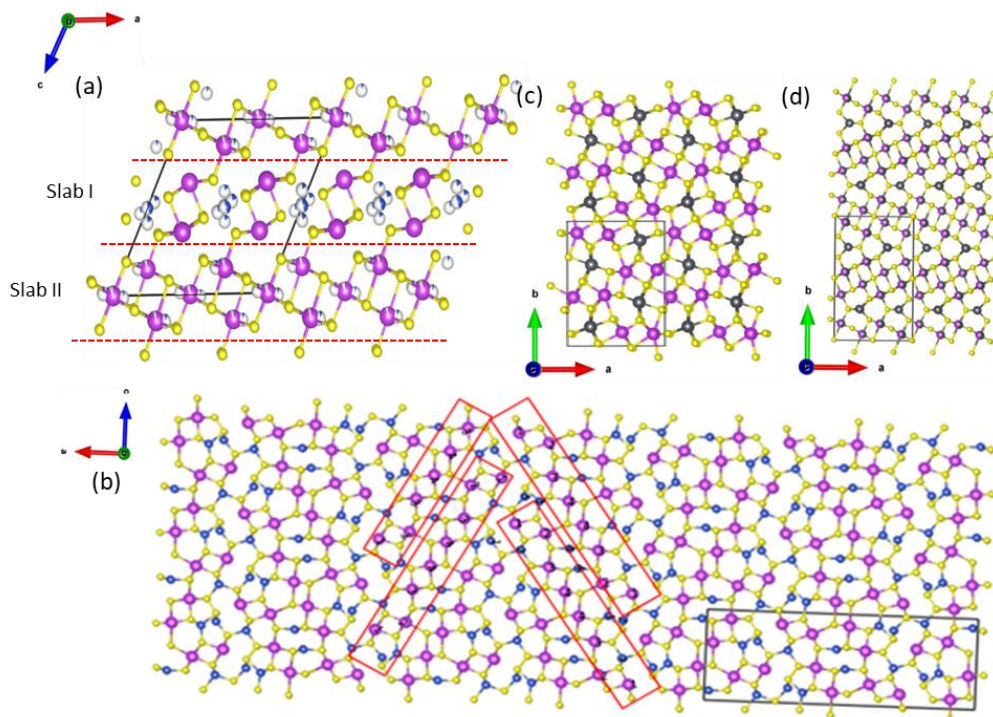


**Figure 1.17.** The crystal structure of (a)  $\text{Cu}_{1.6}\text{Bi}_{4.8}\text{S}_8$ , (b)  $\text{Cu}_4\text{Bi}_4\text{S}_9$ , (c)  $\text{PbBi}_2\text{S}_4$  and (d)  $\text{Pb}_3\text{Bi}_2\text{S}_6$ .

The crystal structure of  $\text{Cu}_4\text{Bi}_4\text{S}_9$ , which crystallizes in the orthorhombic space group  $Pnma$ .<sup>111,112</sup> The crystal structure of  $\text{Cu}_4\text{Bi}_4\text{S}_9$  is well explained by Jiang *et al.*<sup>113</sup> It is composed of layers of Bi/S that are connected by Cu counter cations, as seen by the (010) direction. Each Bi/S layer is eight Bi atoms broad and is made up of a Bi3–Bi4–Bi4–Bi3 fragment that is capped by a Bi1–Bi2 column on both ends. The Bi4 adopts 6-folded octahedral coordination, sharing an edge with a  $\text{Bi}_3\text{S}_5$  square pyramid and another edge with a nearby  $\text{Bi}_4\text{S}_6$  octahedron to create a motif with a connection pattern resembling that of PbS. The Bi1 and Bi2 are 5-fold coordinated and form a column along the  $b$ -axis. These Bi/S layers are stacked along the  $c$ -direction with the connection of Cu1 atoms (at Bi1 and Bi2 via S1 atoms and at Bi3 and Bi4 via S5 atoms), Cu3 atoms (at Bi1 via S9 atoms and through a S8–S4 bond at Bi3 via S4 atoms), and Cu4–Cu4 dimeric species (at Bi4 and Bi3 via S3 atoms), whereas two neighboring Bi/S layers are connected along the  $a$ -direction by Cu2 atoms at Bi1 and Bi2 via S2 atoms, at Bi3 via S4, and at Bi1 via S9. Here Cu3 is only thrice coordinated in  $\text{Cu}_4\text{Bi}_4\text{S}_9$ . Additionally, Cu4 is completely occupied. The complex crystal structure and rattling of Cu atoms and diverse bonding environments may contribute to the low thermal conductivity. For the first time, Jian *et al.* reported a complex phase of  $\text{Cu}_4\text{Bi}_4\text{S}_9$  that demonstrates an extraordinarily low intrinsic lattice thermal conductivity, with values ranging from 0.49 to 0.44  $\text{W m}^{-1} \text{K}^{-1}$  between 300 and 550 K. The presence of rattling Cu and a lone pair of Bi at the same time gives rise to a high degree of lattice anharmonicity and considerably amplifies the phonon scattering, which ultimately results in an extraordinarily low intrinsic lattice thermal conductivity.<sup>113</sup>

$\text{MnBi}_4\text{S}_7$  and  $\text{FeBi}_4\text{S}_7$  are complex, layered crystal structures with monoclinic structural systems that have low symmetry. The crystals of  $\text{MnBi}_4\text{S}_7$  and  $\text{FeBi}_4\text{S}_7$  exhibit monoclinic symmetry in the  $C2/m$  space group, with lattice parameters of  $a = 12.927(6) / 12.762(2) \text{ \AA}$ ,  $b = 3.973(6) / 3.964(1) \text{ \AA}$ ,  $c = 11.823(6)/11.804(5) \text{ \AA}$ , and  $\beta = 104.666(4)/104.422(2) \text{ \AA}$ , respectively.<sup>114</sup> The 2P structure of the pavonite homologous series is adopted by both compounds, as initially reported by Luo *et al.*, in their respective crystal structures.<sup>115</sup> The low thermal conductivity exhibited by

both samples can be attributed to their intricate layered structure and the presence of active lone pairs of bismuth. The  $\text{MnBi}_4\text{S}_7$  and  $\text{FeBi}_4\text{S}_7$  materials yielded a  $ZT$  of 0.21 at 700 K and 0.19 at 600 K, respectively, indicating moderate thermoelectric performance.<sup>114</sup> A peak  $ZT$  value of 0.31 for  $\text{MnBi}_4\text{S}_{5.46}\text{Se}_{1.4}$  at 770 K was obtained by Xi *et al.* as a result of their endeavour to optimize the carrier concentration with the aid of Se alloying.<sup>116</sup>

$\text{Pb}_m\text{Bi}_2\text{S}_{3+m}$  ( $m = 0, 1, 3$ ) is a promising homologous series in new ternary system that has shown promising efficiency.  $\text{Pb}_3\text{Bi}_2\text{S}_6$  is a member of the lillianite homologous series,  $\text{PbBi}_2\text{S}_4$  is a member of the galenobismuthite homologous series.<sup>117,118</sup> Both compounds are formed by connecting diverse cationic coordination geometries to each other by point- or edge-sharing sulfur atoms.  $\text{Pb}_2\text{Bi}_2\text{S}_5$  ( $m = 2$ ) could not be prepared may be because this phase is not a real phase or there are kinetic difficulties in the Pb–Bi–S system.  $\text{Pb}_m\text{Bi}_2\text{S}_{3+m}$  ( $m = 0, 1$ , and 3) crystal structures are composed of slabs of the PbS and  $\text{Bi}_2\text{S}_3$  types alternately. The crystal structure of  $\text{PbBi}_2\text{S}_4$  is made up of NaCl-type and  $\text{Bi}_2\text{S}_3$ -type strips, whereas that of  $\text{Pb}_3\text{Bi}_2\text{S}_6$  is made up of stacking NaCl-type (Pb/Bi)S layers.<sup>117,118</sup> Ohta *et al.* first synthesised  $\text{PbBi}_2\text{S}_4$  and  $\text{Pb}_3\text{Bi}_2\text{S}_6$  by a solid solution reaction of the binary precursors PbS and  $\text{Bi}_2\text{S}_3$ . These materials exhibited effective phonon scattering, leading to extremely low lattice thermal conductivity 0.6 to 0.58  $\text{W m}^{-1} \text{K}^{-1}$  for  $\text{PbBi}_2\text{S}_4$  and 0.8 to 0.6  $\text{W m}^{-1} \text{K}^{-1}$  in the temperature range of 300 K to 723 K.<sup>119</sup>

The pristine samples of  $\text{Pb}_3\text{Bi}_2\text{S}_6$  achieved a maximum  $ZT$  value of 0.26 at 715 K, while  $\text{PbBi}_2\text{S}_4$  reached a maximum  $ZT$  of 0.33 at 710 K.<sup>119</sup> Subsequently, Cai *et al.* developed a solution-based synthesis method for this homologous series. The resulting materials exhibited low lattice thermal conductivity and relatively high electrical conductivity, leading to improved  $ZT$  values. Specifically,  $\text{PbBi}_2\text{S}_4$  obtained a  $ZT$  of 0.46 at 800 K, while  $\text{Pb}_3\text{Bi}_2\text{S}_6$  achieved a  $ZT$  of 0.2 at the same temperature.<sup>120</sup> These findings demonstrate the potential of the solution-based synthesis approach in enhancing the thermoelectric properties of the materials.<sup>120</sup>

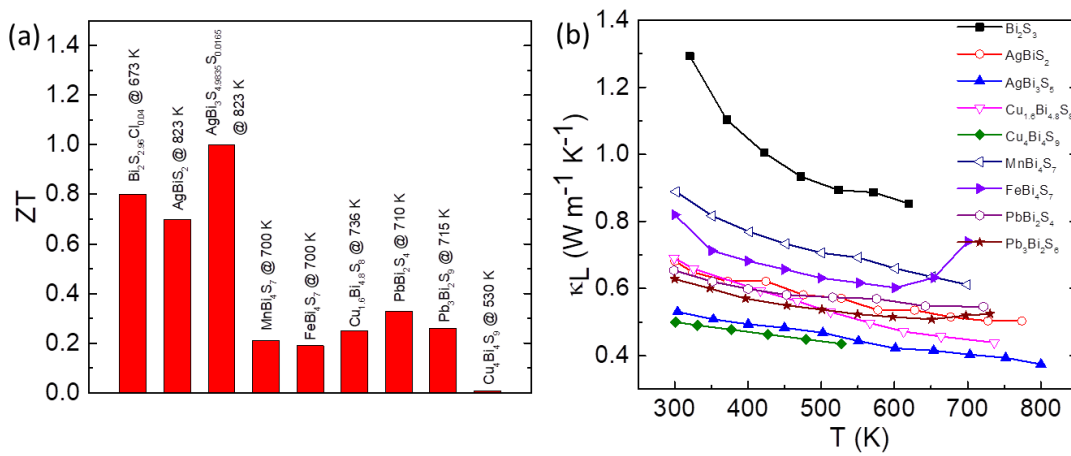


**Figure 1.18.** (a) Maximum  $ZT$  values of state of art Bi-based thermoelectric sulphides, (b) lattice thermal conductivity of those states of art Bi-based thermoelectric sulphides.<sup>91,97,121–123</sup>

**Figure 1.18** presents a graphical representation of the thermoelectric figure of merit ( $ZT$ ) and lattice thermal conductivity ( $\kappa_L$ ) values for various Bi-based ternary sulfides, including the binary compound  $\text{Bi}_2\text{S}_3$ . The observed temperature-dependent lattice thermal conductivity clearly demonstrates the significant impact of complex structural characteristics in reducing thermal conductivity. In addition, it is interesting that the  $n$ -type sulfide-based compounds exhibit remarkably high  $ZT$  values compared to other state-of-the-art materials.

## 1.4. Conclusion

My thesis highlights the significance of devising sustainable and environmentally friendly approaches for energy management, specifically regarding reducing dependence on non-renewable energy sources. The utilization of thermoelectricity presents a viable prospect for the conversion of waste heat into electrical energy. However, conventional thermoelectric compounds encounter obstacles stemming from their inadequate performance-to-price ratio and restricted material accessibility. According to contemporary research, sulfur-based compounds have been recognized as a potentially effective category of materials for tackling these issues. However, their limited efficiency hampers their extensive acceptance. The

---

present thesis focuses on the investigation of Bi-based sulfides as alternatives for thermoelectric purposes.

This study aims to enhance the thermoelectric characteristics of readily accessible and cost-effective transition metal sulfides and optimize scalability. By investigating the effects of chemical substitution on the structural and physical properties, the goal is to optimize the thermoelectric response by carefully tuning the electrical and thermal properties of the materials. In general, this thesis makes a valuable contribution to the progress of thermoelectric materials and their feasibility as a sustainable energy generation option. The results of this research can open the door for the wider use of thermoelectricity in the shift to a more sustainable energy future by resolving the drawbacks of traditional compounds and investigating new materials.

## 1.5. References

- (1) Kosaka, Y.; Xie, S. P. Recent Global-Warming Hiatus Tied to Equatorial Pacific Surface Cooling. *Nature* **2013**, *501* (7467), 403–407. <https://doi.org/10.1038/nature12534>.
- (2) England, M. H.; McGregor, S.; Spence, P.; Meehl, G. A.; Timmermann, A.; Cai, W.; Gupta, A. Sen; Mcphaden, M. J.; Purich, A.; Santoso, A. Recent Intensification of Wind-Driven Circulation in the Pacific and the Ongoing Warming Hiatus. *Nat. Clim. Chang.* **2014**, *4* (3), 222–227. <https://doi.org/10.1038/nclimate2106>.
- (3) Hansen, J.; Ruedy, R.; Sato, M.; Lo, K. Global Surface Temperature Change. *Rev. Geophys.* **2010**, *48* (4), 1–29. <https://doi.org/10.1029/2010RG000345>.
- (4) Cook, J.; Nuccitelli, D.; Green, S. A.; Richardson, M.; Winkler, B.; Painting, R.; Way, R.; Jacobs, P.; Skuce, A. Quantifying the Consensus on Anthropogenic Global Warming in the Scientific Literature. *Environ. Res. Lett.* **2013**, *8* (2). <https://doi.org/10.1088/1748-9326/8/2/024024>.
- (5) Abbasi, T.; Premalatha, M.; Abbasi, S. A. The Return to Renewables: Will It Help in Global Warming Control? *Renew. Sustain. Energy Rev.* **2011**, *15* (1), 891–894. <https://doi.org/10.1016/j.rser.2010.09.048>.
- (6) International Hydropower association. *Hydropower Status Report*; 2015.
- (7) C.W.E. association. *World Wind Energy Association Bulletin*; 2016.
- (8) Walwyn, D. R.; Brent, A. C. Renewable Energy Gathers Steam in South Africa. *Renew. Sustain. Energy Rev.* **2015**, *41*, 390–401. <https://doi.org/10.1016/j.rser.2014.08.049>.
- (9) I. E. energy. *World Energy Outlook, Global Energy Trend, Online*; 2015.
- (10) Steele, B. C. H.; Heinzl, A. Materials for Fuel-Cell Technologies. **2001**, *414* (November), 345–352.
- (11) Jacobson, M. Z. Review of Solutions to Global Warming, Air Pollution, and Energy Security. *Energy Environ. Sci.* **2009**, *2* (2), 148–173. <https://doi.org/10.1039/b809990c>.
- (12) Curie, J.; Curie, P. Phénomènes Électriques Des Cristaux Hémihédres à Faces Inclinaées Jacques Curie , Pierre Curie To Cite This Version : HAL Id : Jpa-

00237932. *J. Phys. Theor. Appl.* **1882**, *1*, 245–251.
- (13) Bell, L. E. Cooling, Heating, Generating Power, and Recovering Waste Heat with Thermoelectric Systems. *Science (80-. )*. **2008**, *321* (5895), 1457–1461. <https://doi.org/10.1126/science.1158899>.
- (14) Rowe, D. M. Thermoelectrics, an Environmentally-Friendly Source of Electrical Power. *Renew. Energy* **1999**, *16* (1–4), 1251–1256. [https://doi.org/10.1016/s0960-1481\(98\)00512-6](https://doi.org/10.1016/s0960-1481(98)00512-6).
- (15) Velmre, E. Thomas Johann Seebeck (1770-1831). *Proc. Est. Acad. Sci. Eng.* **2007**, *13* (4), 276–282.
- (16) D.M. Rowe. *CRD Handbook of Thermoelectrics*; D. M. Rowe, Ed.; CRD Press, 1995.
- (17) Yang, J.; Caillat, T. Thermoelectric Materials for Space and Automotive Power Generation. *MRS Bull.* **2006**, *31* (3), 224–229. <https://doi.org/10.1557/mrs2006.49>.
- (18) Zoui, M. A.; Bentouba, S.; Stocholm, J. G.; Bourouis, M. A Review on Thermoelectric Generators: Progress and Applications. *Thermoelectr. Des. Mater.* **2020**, *13* (14), 3606. <https://doi.org/10.1002/9781118848944>.
- (19) Kim, H. S.; Gibbs, Z. M.; Tang, Y.; Wang, H.; Snyder, G. J. Characterization of Lorenz Number with Seebeck Coefficient Measurement. *APL Mater.* **2015**, *3* (4). <https://doi.org/10.1063/1.4908244>.
- (20) Pei, Y.; Shi, X.; Lalonde, A.; Wang, H.; Chen, L.; Snyder, G. J. Convergence of Electronic Bands for High Performance Bulk Thermoelectrics. *Nature* **2011**, *473* (7345), 66–69. <https://doi.org/10.1038/nature09996>.
- (21) Heremans, J. P.; Jovovic, V.; Toberer, E. S.; Saramat, A.; Kurosaki, K.; Charoenphakdee, A.; Yamanaka, S.; Snyder, G. J. Enhancement of Thermoelectric of the Electronic Density of States. *Science (80-. )*. **2008**, *321* (July), 1457–1461.
- (22) Cahill, D. G.; Pohl, R. O. Heat Flow and Lattice Vibrations in Glasses. *Solid State Commun.* **1989**, *70* (10), 927–930. [https://doi.org/10.1016/0038-1098\(89\)90630-3](https://doi.org/10.1016/0038-1098(89)90630-3).
- (23) Zhou, W. X.; Cheng, Y.; Chen, K. Q.; Xie, G.; Wang, T.; Zhang, G. Thermal

- Conductivity of Amorphous Materials. *Adv. Funct. Mater.* **2020**, *30* (8), 1–17. <https://doi.org/10.1002/adfm.201903829>.
- (24) Beekman, M.; Cahill, D. G. Inorganic Crystals with Glass-Like and Ultralow Thermal Conductivities. *Cryst. Res. Technol.* **2017**, *52* (10), 1–13. <https://doi.org/10.1002/crat.201700114>.
- (25) Avila, M. A.; Suekuni, K.; Umeo, K.; Fukuoka, H.; Yamanaka, S.; Takabatake, T. Glasslike versus Crystalline Thermal Conductivity in Carrier-Tuned  $\text{Ba}_8\text{Ga}_{16}\text{X}_{30}$  Clathrates (X=Ge,Sn). *Phys. Rev. B - Condens. Matter Mater. Phys.* **2006**, *74* (12), 125109–125116. <https://doi.org/10.1103/PhysRevB.74.125109>.
- (26) Gibson, Q. D.; Zhao, T.; Daniels, L. M.; Walker, H. C.; Daou, R.; Hébert, S.; Zanella, M.; Dyer, M. S.; Claridge, J. B.; Slater, B.; Gaultois, M. W.; Corà, F.; Alaria, J.; Rosseinsky, M. J. Low Thermal Conductivity in a Modular Inorganic Material with Bonding Anisotropy and Mismatch. *Science (80-. )*. **2021**, *373* (6558), 1017–1022. <https://doi.org/10.1126/science.abh1619>.
- (27) Chen, Z.; Zhang, X.; Pei, Y. Manipulation of Phonon Transport in Thermoelectrics. *Adv. Mater.* **2018**, *30* (17), 1–12. <https://doi.org/10.1002/adma.201705617>.
- (28) Poudel, B.; Hao, Q.; Ma, Y.; Lan, Y.; Minnich, A.; Yu, B.; Yan, X.; Wang, D.; Muto, A.; Vashaee, D.; Chen, X.; Liu, J.; Dresselhaus, M. S.; Chen, G.; Ren, Z. High-Thermoelectric Performance of Nanostructured Bismuth Antimony Telluride Bulk Alloys. *Science (80-. )*. **2008**, *320* (5876), 634–638. <https://doi.org/10.1126/science.1156446>.
- (29) Witting, I. T.; Ricci, F.; Chasapis, T. C.; Hautier, G.; Snyder, G. J. The Thermoelectric Properties of N-Type Bismuth Telluride: Bismuth Selenide Alloys  $\text{Bi}_2\text{Te}_{3-x}\text{Se}_x$ . *Research* **2020**, *2020*. <https://doi.org/10.34133/2020/4361703>.
- (30) Goldsmid, H. J. Bismuth Telluride and Its Alloys as Materials for Thermoelectric Generation. *Materials (Basel)*. **2014**, *7* (4), 2577–2592. <https://doi.org/10.3390/ma7042577>.
- (31) Pei, Y.; Heinz, N. A.; Lalonde, A.; Snyder, G. J. Combination of Large Nanostructures and Complex Band Structure for High Performance

- Thermoelectric Lead Telluride. *Energy Environ. Sci.* **2011**, *4* (9), 3640–3645. <https://doi.org/10.1039/c1ee01928g>.
- (32) Singh, M. P.; Bhandari, C. M. High-Temperature Thermoelectric Behavior of Lead Telluride. *J. Phys.* **2004**, *62* (6), 1309–1317. <https://doi.org/10.1007/BF02704444>.
- (33) Lalonde, A. D.; Pei, Y.; Wang, H.; Jeffrey Snyder, G. Lead Telluride Alloy Thermoelectrics. *Mater. Today* **2011**, *14* (11), 526–532. [https://doi.org/10.1016/S1369-7021\(11\)70278-4](https://doi.org/10.1016/S1369-7021(11)70278-4).
- (34) Steele, M. C.; Rosi, F. D. Thermal Conductivity and Thermoelectric Power of Germanium-Silicon Alloys. *J. Appl. Phys.* **1958**, *29* (11), 1517–1520. <https://doi.org/10.1063/1.1722984>.
- (35) Basu, R.; Singh, A. High Temperature Si–Ge Alloy towards Thermoelectric Applications: A Comprehensive Review. *Mater. Today Phys.* **2021**, *21*, 100468. <https://doi.org/10.1016/j.mtphys.2021.100468>.
- (36) Hicks, L. D.; Dresselhaus, M. S. Effect of Quantum-Well Structures on the Thermoelectric Figure of Merit. *Phys. Rev. B* **1989**, *47* (19), 12727. <https://doi.org/10.1177/000306518903700411>.
- (37) Biswas, K.; He, J.; Blum, I. D.; Wu, C. I.; Hogan, T. P.; Seidman, D. N.; Drazdov, V. P.; Kanatzidis, M. G. High-Performance Bulk Thermoelectrics with All-Scale Hierarchical Architectures. *Nature* **2012**, *489* (7416), 414–418. <https://doi.org/10.1038/nature11439>.
- (38) Venkatasubramanian, R.; Siivola, E.; Colpitts, T.; O’Quinn, B. Thin-Film Thermoelectric Devices with High Room-Temperature Figures of Merit. *Nature* **2001**, *413* (6856), 597–602. <https://doi.org/10.1038/35098012>.
- (39) Mitra, M.; Benton, A.; Akhanda, M. S.; Qi, J.; Zebarjadi, M.; Singh, D. J.; Poon, S. J. Conventional Half-Heusler Alloys Advance State-of-the-Art Thermoelectric Properties. *Mater. Today Phys.* **2022**, *28* (October), 100900. <https://doi.org/10.1016/j.mtphys.2022.100900>.
- (40) Qiu, P.; Yang, J.; Huang, X.; Chen, X.; Chen, L. Effect of Antisite Defects on Band Structure and Thermoelectric Performance of ZrNiSn Half-Heusler Alloys. *Appl. Phys. Lett.* **2010**, *96* (15), 1–4. <https://doi.org/10.1063/1.3396981>.

- (41) Qiu, P.; Huang, X.; Chen, X.; Chen, L. Enhanced Thermoelectric Performance by the Combination of Alloying and Doping in TiCoSb-Based Half-Heusler Compounds Enhanced Thermoelectric Performance by the Combination of Alloying and Doping in TiCoSb-Based Half-Heusler Compounds. **2009**, No. December. <https://doi.org/10.1063/1.3238363>.
- (42) Dong, Z.; Luo, J.; Wang, C.; Jiang, Y.; Tan, S.; Yu, Z.; Guo, K.; Zhang, J.; Zhang, W.; Zhang, Y.; Grin, Y. Half-Heusler-like Compounds with Wide Continuous Compositions and Tunable *p*- to *n*-Type Semiconducting Thermoelectrics. *Nat. Commun.* **2022**, *13* (1). <https://doi.org/10.1038/s41467-021-27795-3>.
- (43) Tang, Y.; M. G., Z.; A. A., L.; L., G.; K., H.-S.; B. N., M.; C., S.; Snyder, J. G. Convergence of Multi-Valley Bands as the Electronic Origin of High Thermoelectric Performance in CoSb<sub>3</sub> Skutterudites. *Nat. Mater.* **2015**, *14* (12), 1223–1228. <https://doi.org/10.1038/NMAT4430>.
- (44) Shi, X.; Bai, S.; Xi, L.; Yang, J.; Zhang, W.; Chen, L. Realization of High Thermoelectric Performance in *n*-Type Partially Filled Skutterudites Realization of High Thermoelectric Performance in *n*-Type Partially Filled Skutterudites. **2011**, No. September 2015. <https://doi.org/10.1557/jmr.2011.84>.
- (45) Li, W.; Wang, J.; Xie, Y.; Gray, J. L.; Heremans, J. J.; Kang, H. B.; Poudel, B.; Huxtable, S. T.; Priya, S. Enhanced Thermoelectric Performance of Yb-Single-Filled Skutterudite by Ultralow Thermal Conductivity. **2019**. <https://doi.org/10.1021/acs.chemmater.8b03994>.
- (46) Kim, J.; Okamoto, N. L.; Kishida, K.; Tanaka, K.; Inui, H. High Thermoelectric Performance of Type-III Clathrate Compounds of the Ba-Ge-Ga System. **2006**, *54*, 2057–2062. <https://doi.org/10.1016/j.actamat.2005.12.032>.
- (47) Zhang, Y.; Brorsson, J.; Qiu, R.; Palmqvist, A. E. C. Enhanced Thermoelectric Performance of Ba<sub>8</sub>Ga<sub>16</sub>Ge<sub>30</sub> Clathrate by Modulation Doping and Improved Carrier Mobility. **2021**. <https://doi.org/10.1002/aelm.202000782>.
- (48) Liu, W.; Yin, K.; Zhang, Q.; Uher, C.; Tang, X. *Materials*. **2017**, 611–626. <https://doi.org/10.1093/nsr/nwx011>.
- (49) Luo, W.; Li, H.; Yan, Y.; Lin, Z.; Tang, X.; Zhang, Q.; Uher, C. *Intermetallics*

- Rapid Synthesis of High Thermoelectric Performance Higher Manganese Silicide with In-Situ Formed Nano-Phase of MnSi. *Intermetallics* **2011**, *19* (3), 404–408. <https://doi.org/10.1016/j.intermet.2010.11.008>.
- (50) Shuai, J.; Geng, H.; Lan, Y.; Zhu, Z.; Wang, C.; Liu, Z.; Bao, J.; Chu, C. Higher Thermoelectric Performance of Zintl Phases Strain Fluctuation. **2016**, 4125–4132. <https://doi.org/10.1073/pnas.1608794113>.
- (51) He, A.; Bux, S. K.; Hu, Y.; Uhl, D.; Li, L.; Donadio, D.; Kauzlarich, S. M. Structural Complexity and High Thermoelectric Performance of the Zintl Phase:  $\text{Yb}_{21}\text{Mn}_4\text{Sb}_{18}$ . **2019**. <https://doi.org/10.1021/acs.chemmater.9b02671>.
- (52) Liu, W.; Jie, Q.; Kim, H. S.; Ren, Z. Current Progress and Future Challenges in Thermoelectric Power Generation: From Materials to Devices. *Acta Mater.* **2015**, *87* (155), 357–376. <https://doi.org/10.1016/j.actamat.2014.12.042>.
- (53) He, J.; Liu, Y.; Funahashi, R. Oxide Thermoelectrics: The Challenges, Progress, and Outlook. *J. Mater. Res.* **2011**, *26* (15), 1762–1772. <https://doi.org/10.1557/jmr.2011.108>.
- (54) Hébert, S.; Berthebaud, D.; Daou, R.; Bréard, Y.; Pelloquin, D.; Guilmeau, E.; Gascoin, F.; Lebedev, O.; Maignan, A. Searching for New Thermoelectric Materials: Some Examples among Oxides, Sulfides and Selenides. *J. Phys. Condens. Matter* **2016**, *28* (1). <https://doi.org/10.1088/0953-8984/28/1/013001>.
- (55) Bhui, A.; Dutta, M.; Mukherjee, M.; Rana, K. S.; Singh, A. K.; Soni, A.; Biswas, K. Ultralow Thermal Conductivity in Earth-Abundant  $\text{Cu}_{1.6}\text{Bi}_{4.8}\text{S}_8$ : Anharmonic Rattling of Interstitial Cu. *Chem. Mater.* **2021**, *33* (8), 2993–3001. <https://doi.org/10.1021/acs.chemmater.1c00659>.
- (56) Zhan, S.; Hong, T.; Qin, B.; Zhu, Y.; Feng, X.; Su, L.; Shi, H.; Liang, H.; Zhang, Q.; Gao, X.; Ge, Z. H.; Zheng, L.; Wang, D.; Zhao, L. D. Realizing High-Ranged Thermoelectric Performance in  $\text{PbSnS}_2$  Crystals. *Nat. Commun.* **2022**, *13* (1), 1–9. <https://doi.org/10.1038/s41467-022-33684-0>.
- (57) Luo, Z.; Hao, S.; Cai, S.; Bailey, T. P.; Tan, G.; Luo, Y.; Spanopoulos, I.; Uher, C.; Wolverton, C.; Dravid, V. P.; Yan, Q.; Kanatzidis, M. G. Enhancement of Thermoelectric Performance for  $n$  - Type PbS through Synergy of Gap State and Fermi Level Pinning. *J. Am. Chem. Soc.* **2019**, *141* (6403–6412).

- <https://doi.org/10.1021/jacs.9b01889>.
- (58) Zhao, L.; Lo, S.; He, J.; Li, H.; Biswas, K.; Androulakis, J.; Wu, C.; Hogan, T. P.; Chung, D.; Dravid, V. P.; Kanatzidis, M. G. High Performance Thermoelectrics from Earth-Abundant Materials: Enhanced Figure of Merit in PbS by Second Phase Nanostructures. *J. Am. Chem. Soc.* **2011**, *133*, 20476–20487.
- (59) Dravid, V. P.; Kanatzidis, M. G. Thermoelectrics with Earth Abundant Elements: High Performance p- Type PbS Nanostructured with SrS and CaS. *J. Am. Chem. Soc.* **2012**, *134*, 7902–7912.
- (60) Zhao, L.; He, J.; Hao, S.; Wu, C.; Hogan, T. P.; Wolverton, C.; Dravid, V. P.; Kanatzidis, M. G. Raising the Thermoelectric Performance of p - Type PbS with Endotaxial Nanostructuring and Valence-Band Offset Engineering Using CdS and ZnS. *J. Am. Chem. Soc.* **2012**, *134*, 16327–16336.
- (61) Howard T. Evans, J. Djurleite ( $\text{Cu}_{1.94}\text{S}$ ) and Low Chalcocite ( $\text{Cu}_2\text{S}$ ): New Crystal Structure Studies. *Science* (80-. ). **1979**, *203*, 356.
- (62) Evans, H. T. The Crystal Structures of Low Chalcocite and Djurleite. *Zeitschrift fur Krist. - New Cryst. Struct.* **1979**, *150* (1–4), 299–320. <https://doi.org/10.1524/zkri.1979.150.1-4.299>.
- (63) Will, G.; Hinze, E.; Abdelrahman, A. R. M. Crystal Structure Analysis and Refinement of Digenite,  $\text{Cu}_{1.8}\text{S}$ , in the Temperature Range 20 to 500 ° C under Controlled Sulfur Partial Pressure. *Eur. J. Miner.* **2002**, *14*, 591–598. <https://doi.org/10.1127/0935-1221/2002/0014-0591>.
- (64) Lukashev, P.; Lambrecht, W. R. L.; Kotani, T.; Schilfgaarde, M. Van. Electronic and Crystal Structure of  $\text{Cu}_{2-x}\text{S}$ : Full-Potential Electronic Structure Calculations. *Phys. Rev. B* **2007**, *76*, 195202. <https://doi.org/10.1103/PhysRevB.76.195202>.
- (65) J. W., B.; Buerger, M. J. The Crystal Structure of Chalcocite,  $\text{Cu}_2\text{S}$ . *Mineral. Soc. Am.* **1963**, 164–170.
- (66) Hirahara, E. The Physical Properties of Cuprous Sulfides-Semiconductors. 1950, p 422.
- (67) Potter, R. W. An Electrochemical Investigation of the System Copper-Sulfur. *Econ. Geol.* **1977**, *72* (8), 1524–1542.

- <https://doi.org/10.2113/gsecongeo.72.8.1524>.
- (68) Ge, Z. H.; Zhang, B. P.; Chen, Y. X.; Yu, Z. X.; Liu, Y.; Li, J. F. Synthesis and Transport Property of  $\text{Cu}_{1.8}\text{S}$  as a Promising Thermoelectric Compound. *Chem. Commun.* **2011**, 47 (47), 12697–12699. <https://doi.org/10.1039/c1cc16368j>.
- (69) Hall, B. Y. S. R.; Stewart, J. M.; Hall, C.; Mines, S. W.; Island, V.; Ui, I. The Crystal Structure Refinement of Chalcopyrite,  $\text{CuFeS}_2$ . *Acta Crystallogr. Sect. B* **1973**, 289 (50), 579. <https://doi.org/10.1107/S0567740873002943>.
- (70) Tsujii, N.; Mori, T.; Isoda, Y. Phase Stability and Thermoelectric Properties of  $\text{CuFeS}_2$ -Based Magnetic Phase Stability and Thermoelectric Properties of  $\text{CuFeS}_2$  -Based Magnetic Semiconductor. *J. Electron. Mater.* **2014**, 43 (6). <https://doi.org/10.1007/s11664-014-3072-y>.
- (71) Suekuni, K.; Tsuruta, K.; Kunii, M.; Nishiate, H.; Nishibori, E.; Maki, S.; Ohta, M.; Yamamoto, A.; Koyano, M. High-Performance Thermoelectric Mineral  $\text{Cu}_{12-x}\text{Ni}_x\text{Sb}_4\text{S}_{13}$  Tetrahedrite. *J. Appl. Phys.* **2013**, 113 (4), 043712. <https://doi.org/10.1063/1.4789389>.
- (72) Lu, X.; Morelli, D. T.; Xia, Y.; Zhou, F.; Ozolins, V.; Chi, H.; Zhou, X.; Uher, C. High Performance Thermoelectricity in Earth-Abundant Compounds Based on Natural Mineral Tetrahedrites. *Adv. Energy Mater.* **2013**, 3 (3), 342–348. <https://doi.org/10.1002/aenm.201200650>.
- (73) Charlat, M.; Lévy, C. Influence Des Principales Substitutions Sur Le Paramètre Cristallin Dans La Série Tennantite - Tétraédrite. *Bull. la Société française Minéralogie Cristallogr.* **1975**, 98, 152–158.
- (74) Charlat, M.; Lévy, C.; Levy, C.; Minéralogie-cristallographie, L. De; Vi, U. P.; S, C. R. N. Substitutions Multiples Dans La Série Tennantite - Tétraédrite. *Bull. la Société française Minéralogie Cristallogr.* **1974**, 97, 241–250.
- (75) Johnson, N. E.; Craig, J. R.; Rimstidt, J. D. Compositional Trends in Tetrahedrite. *Can. Mineral.* **1986**, 24, 385–397.
- (76) Charnock, J. M.; Garner, C. D.; Patrick, R. A. D.; Vaughan, D. J. Coordination Sites of Metals in Tetrahedrite Minerals Determined by EXAFS. *J. Solid State Chem.* **1989**, 82, 279–289.
- (77) Tsujii, N.; Mori, T. High Thermoelectric Power Factor in a Carrier-Doped

- Magnetic Semiconductor CuFeS<sub>2</sub>. *Appl. Phys. Express* **2013**, *6*, 043001. <https://doi.org/10.7567/APEX.6.043001>.
- (78) Berthebaud, D.; Lebedev, O. I.; Maignan, A. Thermoelectric Properties of N-Type Cobalt Doped Chalcopyrite Cu<sub>1-x</sub>Co<sub>x</sub>FeS<sub>2</sub> and *p*-Type Eskebornite CuFeSe<sub>2</sub>. *J. Mater.* **2015**, *1*, 68–74. <https://doi.org/10.1016/j.jmat.2015.03.007>.
- (79) Carr, W. D.; Morelli, D. T. The Thermoelectric Properties and Solubility Limit of CuFeS<sub>2(1-x)</sub>Se<sub>2x</sub>. *J. Electron. Mater.* **2015**, *2*. <https://doi.org/10.1007/s11664-015-4029-5>.
- (80) Li, Y.; Zhang, T.; Qin, Y.; Day, T.; Snyder, G. J.; Shi, X.; Chen, L. Thermoelectric Transport Properties of Diamond-like Cu<sub>1-x</sub>Fe<sub>1+x</sub>S<sub>2</sub> Tetrahedral Compounds. *J. Appl. Phys.* **2014**, *116*, 203705. <https://doi.org/10.1063/1.4902849>.
- (81) Goto, Y.; Naito, F.; Sato, R.; Yoshiyasu, K.; Itoh, T.; Kamihara, Y.; Matoba, M. Enhanced Thermoelectric Figure of Merit in Stannite–Kuramite Solid Solutions Cu<sub>2+x</sub>Fe<sub>1-x</sub>SnS<sub>4-y</sub> (*x* = 0–1) with Anisotropy Lowering. *Inorg. Chem.* **2013**, *52*, 9861–9866.
- (82) Jiang, Q.; Yan, H.; Reece, M. J. Colossal Thermoelectric Enhancement in Cu<sub>2+x</sub>Zn<sub>1-x</sub>SnS<sub>4</sub> Solid Solution by Local Disordering of Crystal Lattice and Multi-Scale Defect Engineering. *J. Mater. Chem. A* **2020**, *8*, 10909–10916. <https://doi.org/10.1039/d0ta01595d>.
- (83) Bourgès Yohan; Supka, Andrew; Orabi, Rabih Al Rahal Al; Lemoine, Pierrick; Lebedev, Oleg I.; Ohta, Michihiro; Suekuni, Koichiro; Nassif, Vivian; Hardy, Vincent; Daou, Ramzy; Miyazaki, Yuzuru; Fornari, Marco; Guilmeau, Emmanuel, C. B. High-Performance Thermoelectric Bulk Colusite by Process Controlled Structural Disordering. *J. Am. Chem. Soc.* **2018**, *140* (6), 2186–2195. <https://doi.org/10.1021/jacs.7b11224>.
- (84) Suekuni, K.; Kim, F. S.; Nishiata, H.; Ohta, M.; Tanaka, H. I.; Takabatake, T. High-Performance Thermoelectric Minerals: Colusites Cu<sub>26</sub>V<sub>2</sub>M<sub>6</sub>S<sub>32</sub> (*M* = Ge, Sn). *Appl. Phys. Lett.* **2014**, *105* (13), 132107. <https://doi.org/10.1063/1.4896998>.
- (85) Bouyrie, Y.; Ohta, M.; Suekuni, K.; Jood, P.; Takabatake, T. Addition of Co, Ni, Fe and Their Role in the Thermoelectric Properties of Colusite Cu<sub>26</sub>Nb<sub>2</sub>Ge<sub>6</sub>S<sub>32</sub>. *J.*

- Alloys Compd.* **2018**, *735*, 1838–1845.  
<https://doi.org/10.1016/j.jallcom.2017.11.199>.
- (86) Kikuchi, Y.; Bouyrie, Y.; Ohta, M.; Suekuni, K.; Aihara, M.; Takabatake, T. Vanadium-Free Colusites  $\text{Cu}_{26}\text{A}_2\text{Sn}_6\text{S}_{32}$  ( $\text{A} = \text{Nb}, \text{Ta}$ ) for Environmentally Friendly Thermoelectrics. *J. Mater. Chem. A* **2016**, *4* (39), 15207–15214.  
<https://doi.org/10.1039/c6ta05945g>.
- (87) Kumar, V. P.; Paradis-fortin, L.; Lemoine, P.; Caignaert, V.; Raveau, B.; Malaman, B. Designing a Thermoelectric Copper-Rich Sul Fi de from a Natural Mineral : Synthetic Germanite  $\text{Cu}_{22}\text{Fe}_8\text{Ge}_4\text{S}_{32}$ . *Inorg. Chem.* **2017**, *56*, 13376–13381. <https://doi.org/10.1021/acs.inorgchem.7b02128>.
- (88) Kumar, V. P.; Barbier, T.; Lemoine, P.; Raveau, B.; Nassif, V.; Guilmeau, E. The Crucial Role of Selenium for Sulphur Substitution in the Structural Transitions and Thermoelectric Properties of  $\text{Cu}_5\text{FeS}_4$  Bornite. *Dalt. Trans.* **2017**, *46*, 2174–2183. <https://doi.org/10.1039/c6dt04204j>.
- (89) Qiu, P.; Zhang, T.; Qiu, Y.; Chen, L. Sulfide Bornite Thermoelectric Material: A Natural Mineral with Ultralow Thermal Conductivity. *Energy Environ. Sci.* **2014**, *7*, 4000–4006. <https://doi.org/10.1039/c4ee02428a>.
- (90) Barbier, T.; Rollin-martinet, S.; Lemoine, P.; Gascoin, F.; Kaltzoglou, A.; Vaqueiro, P.; Powell, A. V.; Guilmeau, E. Thermoelectric Materials: A New Rapid Synthesis Process for Nontoxic and High-Performance Tetrahedrite Compounds. *J. Am. Ceram. Soc.* **2016**, *99* (1), 51–56.  
<https://doi.org/10.1111/jace.13838>.
- (91) Barbier, T.; Lemoine, P.; Gascoin, S.; Lebedev, O. I.; Kaltzoglou, A.; Vaqueiro, P.; Powell, A. V.; Smith, R. I.; Guilmeau, E. Structural Stability of the Synthetic Thermoelectric Ternary and Nickel-Substituted Tetrahedrite Phases. *J. Alloys Compd.* **2015**, *634*, 253–262. <https://doi.org/10.1016/j.jallcom.2015.02.045>.
- (92) Chetty, R.; Bali, A.; Naik, M. H.; Rogl, G.; Rogl, P.; Jain, M.; Suwas, S.; Mallik, R. C. Acta Materialia Thermoelectric Properties of Co Substituted Synthetic Tetrahedrite. *Acta Mater.* **2015**, *100*, 266–274.  
<https://doi.org/10.1016/j.actamat.2015.08.040>.
- (93) Weller, D. P.; Morelli, D. T. Rapid Synthesis of Zinc and Nickel Co-Doped

- Tetrahedrite Thermoelectrics by Reactive Spark Plasma Sintering and Mechanical Alloying. *J. Alloys Compd.* **2017**, *710*, 794–799. <https://doi.org/10.1016/j.jallcom.2017.03.272>.
- (94) Harish, S.; Sivaprahasam, D.; Battabyal, M. Phase Stability and Thermoelectric Properties of  $\text{Cu}_{10.5}\text{Zn}_{1.5}\text{Sb}_4\text{S}_{13}$  Tetrahedrite. *J. Alloys Compd.* **2016**, *667*, 323–328. <https://doi.org/10.1016/j.jallcom.2016.01.094>.
- (95) Bouyrie, Y.; Candolfi, C.; Ohorodniichuk, V.; Malaman, B.; Dauscher, A.; Tobola, J.; Lenoir, B. Crystal Structure, Electronic Band Structure and High-Temperature Thermoelectric Properties of Te-Substituted Tetrahedrites  $\text{Cu}_{12}\text{Sb}_{4-x}\text{Te}_x\text{S}_{13}$  ( $0.5 \leq x \leq 2.0$ ). *J. Mater. Chem. C* **2015**, *3*, 10476–10487. <https://doi.org/10.1039/c5tc01636c>.
- (96) Lu, X.; Morelli, D. T.; Xia, Y.; Ozolins, V. Increasing the Thermoelectric Figure of Merit of Tetrahedrites by Co-Doping with Nickel and Zinc. *Chem. Mater.* **2015**, *27*, 408–413. <https://doi.org/10.1021/cm502570b>.
- (97) Biswas, K.; Zhao, L. D.; Kanatzidis, M. G. Tellurium-Free Thermoelectric: The Anisotropic *n*-Type Semiconductor  $\text{Bi}_2\text{S}_3$ . *Adv. Energy Mater.* **2012**, *2* (6), 634–638. <https://doi.org/10.1002/aenm.201100775>.
- (98) Guo, J.; Zhang, Y. X.; Wang, Z. Y.; Zheng, F.; Ge, Z. H.; Fu, J.; Feng, J. High Thermoelectric Properties Realized in Earth-Abundant  $\text{Bi}_2\text{S}_3$  Bulk via Carrier Modulation and Multi-Nano-Precipitates Synergy. *Nano Energy* **2020**, *78* (July), 105227. <https://doi.org/10.1016/j.nanoen.2020.105227>.
- (99) Yang, J.; Liu, G.; Yan, J.; Zhang, X.; Shi, Z.; Qiao, G. Enhanced the Thermoelectric Properties of *n*-Type  $\text{Bi}_2\text{S}_3$  Polycrystalline by Iodine Doping. *J. Alloys Compd.* **2017**, *728*, 351–356. <https://doi.org/10.1016/j.jallcom.2017.08.148>.
- (100) Yan, J.; Yang, J.; Ge, B.; Liu, G.; Shi, Z.; Duan, Z.; Qiao, G. Effect of Silver and Iodine Co-Doping on the Thermoelectric Properties of *n*-Type  $\text{Bi}_2\text{S}_3$ . *J. Electron. Mater.* **2019**, *48* (1), 503–508. <https://doi.org/10.1007/s11664-018-6741-4>.
- (101) Fortulan, R.; Aminorroaya Yamini, S.; Nwanebu, C.; Li, S.; Baba, T.; Reece, M. J.; Mori, T. Thermoelectric Performance of *n*-Type Magnetic Element Doped  $\text{Bi}_2\text{S}_3$ . *ACS Appl. Energy Mater.* **2022**, *5* (3), 3845–3853.

- <https://doi.org/10.1021/acsaem.2c00295>.
- (102) Guo, J.; Yang, J.; Ge, Z. H.; Jiang, B.; Qiu, Y.; Zhu, Y. K.; Wang, X.; Rong, J.; Yu, X.; Feng, J.; He, J. Realizing High Thermoelectric Performance in Earth-Abundant Bi<sub>2</sub>S<sub>3</sub> Bulk Materials via Halogen Acid Modulation. *Adv. Funct. Mater.* **2021**, *31* (37). <https://doi.org/10.1002/adfm.202102838>.
- (103) Guin, S. N.; Biswas, K. Cation Disorder and Bond Anharmonicity Optimize the Thermoelectric Properties in Kinetically Stabilized Rocksalt AgBiS<sub>2</sub> Nanocrystals. *Chem. Mater.* **2013**, *25* (15), 3225–3231. <https://doi.org/10.1021/cm401630d>.
- (104) Manimozhi, T.; Kavirajan, S.; Kamala Bharathi, K.; Senthil Kumar, E.; Navaneethan, M. Ultra-Low Thermal Conductivity of AgBiS<sub>2</sub> via Sb Substitution as a Scattering Center for Thermoelectric Applications. *J. Mater. Sci. Mater. Electron.* **2022**, *33* (16), 12615–12628. <https://doi.org/10.1007/s10854-022-08211-y>.
- (105) Rathore, E.; Juneja, R.; Culver, S. P.; Minafra, N.; Singh, A. K.; Zeier, W. G.; Biswas, K. Origin of Ultralow Thermal Conductivity in *n*-Type Cubic Bulk AgBiS<sub>2</sub>: Soft Ag Vibrations and Local Structural Distortion Induced by the Bi 6s<sup>2</sup> Lone Pair. *Chem. Mater.* **2019**, *31* (6), 2106–2113. <https://doi.org/10.1021/acs.chemmater.9b00001>.
- (106) Tan, G.; Hao, S.; Zhao, J.; Wolverton, C.; Kanatzidis, M. G. High Thermoelectric Performance in Electron-Doped AgBi<sub>3</sub>S<sub>5</sub> with Ultralow Thermal Conductivity. *J. Am. Chem. Soc.* **2017**, *139* (18), 6467–6473. <https://doi.org/10.1021/jacs.7b02399>.
- (107) Kim, J. H.; Chung, D. Y.; Bilc, D.; Loo, S.; Short, J.; Mahanti, S. D.; Hogan, T.; Kanatzidis, M. G. Crystal Growth, Thermoelectric Properties, and Electronic Structure of AgBi<sub>3</sub>S<sub>5</sub> and AgSb<sub>x</sub>Bi<sub>3-x</sub>S<sub>5</sub> (*x* = 0.3). *Chem. Mater.* **2005**, *17* (14), 3606–3614. <https://doi.org/10.1021/cm0502931>.
- (108) Wu, Y.; Su, X.; Yang, D.; Zhang, Q.; Tang, X. Boosting Thermoelectric Properties of AgBi<sub>3</sub>(Se<sub>y</sub>S<sub>1-y</sub>)<sub>5</sub> solid Solution via Entropy Engineering. *ACS Appl. Mater. Interfaces* **2021**, *13* (3), 4185–4191. <https://doi.org/10.1021/acsaami.0c19387>.

- (109) Liu, X. C.; Yang, M. Enhanced Thermoelectric Performance of  $\text{AgBi}_3\text{S}_5$  by Antimony Doping. *Rare Met.* **2020**, *39* (3), 289–295. <https://doi.org/10.1007/s12598-020-01373-w>.
- (110) Qian, X.; Zhang, X.; Guo, H.; Ding, B.; Chen, M.; Wang, J. L.; Zhao, L. D.; Wang, S. F. Enhancing Thermoelectric Performance of  $n$ -Type  $\text{AgBi}_3\text{S}_5$  through Synergistically Optimizing the Effective Mass and Carrier Mobility. *J. Mater.* **2023**. <https://doi.org/10.1016/j.jmat.2023.02.010>.
- (111) Takéuchi, Y.; Ozawa, T. The Structure of  $\text{Cu}_4\text{Bi}_4\text{S}_9$  and Its Relation to the Structures of Covellite,  $\text{CuS}$  and Bismuthinite,  $\text{Bi}_2\text{S}_3$ . *Zeitschrift für Krist. - New Cryst. Struct.* **1975**, *141*, 217–232. <https://doi.org/10.1524/zkri.1975.141.3-4.217>.
- (112) Hobbis, D.; Wang, H.; Martin, J.; Nolas, G. S. Thermal Properties of the Very Low Thermal Conductivity Ternary Chalcogenide  $\text{Cu}_4\text{Bi}_4\text{M}_9$  ( $M = \text{S}, \text{Se}$ ). *Phys. Status Solidi - Rapid Res. Lett.* **2020**, *14* (8), 10–13. <https://doi.org/10.1002/pssr.202000166>.
- (113) Jiang, Y.; Jia, F.; Chen, L.; Wu, L. M.  $\text{Cu}_4\text{Bi}_4\text{Se}_9$ : A Thermoelectric Symphony of Rattling, Anharmonic Lone-Pair, and Structural Complexity. *ACS Appl. Mater. Interfaces.* **2019**, *11* (40), 36616–36625. <https://doi.org/10.1021/acsami.9b11115>.
- (114) Labégorre, J. B.; Virfeu, A.; Bourhim, A.; Willeman, H.; Barbier, T.; Appert, F.; Juraszek, J.; Malaman, B.; Huguenot, A.; Gautier, R.; Nassif, V.; Lemoine, P.; Prestipino, C.; Elkaim, E.; Pautrot-d’Alençon, L.; Le Mercier, T.; Maignan, A.; Al Rahal Al Orabi, R.; Guilmeau, E.  $\text{XBi}_4\text{S}_7$  ( $X = \text{Mn}, \text{Fe}$ ): New Cost-Efficient Layered  $n$ -Type Thermoelectric Sulfides with Ultralow Thermal Conductivity. *Adv. Funct. Mater.* **2019**, *29* (48), 1904112–1904124. <https://doi.org/10.1002/adfm.201904112>.
- (115) Luo, Z. Z.; Lin, C. S.; Cheng, W. D.; Zhang, W. L.; Li, Y. B.; Yang, Y.; Zhang, H.; He, Z. Z. From One-Dimensional Linear Chain to Two-Dimensional Layered Chalcogenides  $\text{XBi}_4\text{S}_7$  ( $X = \text{Mn}, \text{Fe}$ ): Syntheses, Crystal and Electronic Structures, and Physical Properties. *Cryst. Growth Des.* **2013**, *13* (9), 4118–4124. <https://doi.org/10.1021/cg4009398>.
- (116) Xi, M.; Zhu, H.; Wu, H.; Yang, Y.; Yan, Y.; Wang, G.; Wang, G.; Li, J. Y.; Lu,

- X.; Zhou, X. Thermoelectricity of *n*-Type  $\text{MnBi}_4\text{S}_{7-7x}\text{Se}_{7x}$  Solid Solution. *Chem. Eng. J.* **2020**, *396*, 125219. <https://doi.org/10.1016/j.cej.2020.125219>.
- (117) Zhao, J.; Hao, S.; Islam, S. M.; Chen, H.; Tan, G.; Ma, S.; Wolverton, C.; Kanatzidis, M. G. Six Quaternary Chalcogenides of the Pavonite Homologous Series with Ultralow Lattice Thermal Conductivity. *Chem. Mater.* **2019**, *31* (9), 3430–3439. <https://doi.org/10.1021/acs.chemmater.9b00585>.
- (118) Savory, C. N.; Ganose, A. M.; Scanlon, D. O. Exploring the  $\text{PbS-Bi}_2\text{S}_3$  Series for Next Generation Energy Conversion Materials. *Chem. Mater.* **2017**, *29* (12), 5156–5167. <https://doi.org/10.1021/acs.chemmater.7b00628>.
- (119) Ohta, M.; Chung, D. Y.; Kunii, M.; Kanatzidis, M. G. Low Lattice Thermal Conductivity in  $\text{Pb}_5\text{Bi}_6\text{Se}_{14}$ ,  $\text{Pb}_3\text{Bi}_2\text{S}_6$ , and  $\text{PbBi}_2\text{S}_4$ : Promising Thermoelectric Materials in the Cannizzarite, Lillianite, and Galenobismuthite Homologous Series. *J. Mater. Chem. A* **2014**, *2* (47), 20048–20058. <https://doi.org/10.1039/c4ta05135a>.
- (120) Cai, F.; Dong, R.; Sun, W.; Lei, X.; Yu, B.; Chen, J.; Yuan, L.; Wang, C.; Zhang, Q.  $\text{Pb}_m\text{Bi}_2\text{S}_{3+m}$  MHomologous Series with Low Thermal Conductivity Prepared by the Solution-Based Method as Promising Thermoelectric Materials. *Chem. Mater.* **2021**, *33* (15), 6003–6011. <https://doi.org/10.1021/acs.chemmater.1c01387>.
- (121) Bhui Moinak; Mukherjee, Madhubanti; Rana, Kewal Singh; Singh, Abhishek K.; Soni, Ajay; Biswas, Kanishka, A. D. Ultralow Thermal Conductivity in Earth-Abundant  $\text{Cu}_{1.6}\text{Bi}_{4.8}\text{S}_8$ : Anharmonic Rattling of Interstitial Cu. *Chem. Mater.* **2021**, *33* (8), 2993–3001. <https://doi.org/10.1021/acs.chemmater.1c00659>.
- (122) Labégorre, J. B.; Virfeu, A.; Bourhim, A.; Willeman, H.; Barbier, T.; Appert, F.; Juraszek, J.; Malaman, B.; Huguenot, A.; Gautier, R.; Nassif, V.; Lemoine, P.; Prestipino, C.; Elkaim, E.; Pautrot-d’Alençon, L.; Le Mercier, T.; Maignan, A.; Al Rahal Al Orabi, R.; Guilmeau, E.  $\text{XBi}_4\text{S}_7$  ( $X = \text{Mn, Fe}$ ): New Cost-Efficient Layered *n*-Type Thermoelectric Sulfides with Ultralow Thermal Conductivity. *Adv. Funct. Mater.* **2019**, *29* (48). <https://doi.org/10.1002/adfm.201904112>.



---

## Objective

---



The increasing demand for sustainable energy sources derives from the increasing release of greenhouse gases into the atmosphere, which poses a significant threat to the global ecological equilibrium. To address this issue, the implementation of sustainable energy can be achieved through several approaches, including the replacement of combustion-based power generation with sustainable energy alternatives and the promotion of energy harvesting in industrial processes. At present, the contribution of renewable energy sources, namely solar, hydro, wind, and geothermal, to the overall electricity consumption remains low. This concerns all the residual heat produced by numerous and diverse sources (industrial activities, car exhausts, incinerators, etc.) up to the very generous solar radiation. This energy can be recovered and transformed into electricity, in particular using thermoelectric devices.

The foundations of thermoelectric technology have traditionally been the conventional thermoelectric materials, such as bismuth telluride ( $\text{Bi}_2\text{Te}_3$ ) for room temperature, lead-telluride (Pb-Te) system for intermediate temperatures, and silicon-germanium (Si-Ge) for high temperatures. However, they possess several disadvantages. To begin with, compounds containing lead and tellurium present significant environmental and toxicity issue. Additionally, the limited availability and high cost of tellurium and germanium hinder their widespread application. Finally, these materials exhibit relatively low thermoelectric efficiency (below 10%).

In the 1990s, a wave of innovation and exploration led to the discovery of new thermoelectric materials, breaking away from the limitations of conventional choices. For example, oxides possess certain benefits due to their high thermal stability and low toxicity. Nevertheless, the thermoelectric performance of these materials still failed to meet the desired levels of ideal efficiency. Intermetallic and selenium and tellurium-based compounds exhibit high efficiency at moderate temperature. However, the cost and toxicity of certain elements used in these compounds remain obstacles to widespread industrial applications. Within this landscape of thermoelectric exploration, Bi-based sulphides have gained attention. These materials, composed of relatively abundant and inexpensive elements, offer a compelling avenue for research and development.

## Objective

The focus of my thesis research is on the synthesis, structural analysis, and characterization of Bi-based sulphides possessing thermoelectric properties. This study was centred on various families of compounds.

To create materials with ultralow thermal conductivity ( $\kappa$ ), it is essential to comprehend the connection between heat transfer and crystal structures. My thesis work began with exploring the complexities of the gladite phase ( $\text{CuPbBi}_5\text{S}_9$ ) (chapter 2) which has demonstrated a remarkably low  $\kappa$  value  $0.6\text{-}0.4 \text{ W m}^{-1} \text{ K}^{-1}$  in the temperature range of 300-700 K. Surprisingly, the synthetic sulfide did not exhibit the ordered gladite structure, contrary to the previous report. Instead, it adopts a disordered copper deficient aikinite structure, with random distribution of copper, vacancy, Pb and Bi. Through the integration of experimental data and lattice dynamics computations we conclude that the remarkably low  $\kappa$  value is due to low energy optical modes linked to Pb, Bi, and Cu ions. Although the pristine compound exhibits poor thermoelectric properties, Cl and Bi doping to S and Pb sites show a remarkable enhancement of figure of merit.

Subsequently, in chapter 3, we have modified the crystal structure to optimize the thermoelectric properties. The goal was to modify the crystal structure of aikinite-series by introducing more Bi in  $\text{Cu}_{1-x}\text{Pb}_{1-x}\text{Bi}_{1+x}\text{S}_3$ . By introducing more Bi and forming  $\text{Bi}_2\text{S}_3$  chains, the aim was to increase the electrical conductivity and enhance mobility within the system.

In chapter 4, our attention shifted to copper-rich sulfides, particularly wittichenite ( $\text{Cu}_3\text{BiS}_3$ ), which contains lone pairs in Bi and a developed Cu-S network ( $\text{Cu/Bi} = 3$ ), supports *p*-type conduction channel and exhibits extremely low thermal conductivity. Here, we demonstrate the impact of cationic coordination on electrical and thermal properties by comparing the structural and transport properties of  $\text{Cu}_3\text{BiS}_3$  to tetrahedrite ( $\text{Cu}_{12}\text{Sb}_4\text{S}_{13}$ ) and other Cu-rich sulfides. By combining experiment and theory, we have shown that the low thermal conductivity of  $\text{Cu}_3\text{BiS}_3$  is mostly attributable to high anisotropic thermal vibration of triangular coordinated Cu. DFT

simulations show that these Cu atoms are poorly linked, resulting low-energy Einstein-like vibrational modes that strongly scatter heat-carrying acoustic phonons. Importantly, we have shown that the three-fold coordination of copper in  $\text{Cu}_3\text{BiS}_3$  and other copper-rich sulfides with interconnected  $\text{CuS}_3$  networks blocks holes. This prevents mixed valency of  $\text{Cu}^+/\text{Cu}^{2+}$  which does not allow the optimisation of the carrier concentration unlike tetrahedrite and most other copper-rich chalcogenides, where the main interconnected Cu-S network is built of  $\text{CuS}_4$  tetrahedra. Comparing other copper-rich sulphides, we have shown that frameworks with tetrahedral and threefold coordinated copper are interesting for discovering effective thermoelectric copper sulphides.

Finally in chapter 5, our motivation is to control the synthesis of galenobismuthite ( $\text{PbBi}_2\text{S}_4$ ), a mineral sulfide to obtain high purity and crystalline compound. We have synthesized highly pure  $\text{PbBi}_2\text{S}_4$  phase using mechanical alloying and spark plasma sintering that allowed us to control the stoichiometry and show semiconducting behaviour in electrical properties. Further, in order to understand the origin of low thermal conductivity, we have performed DFT calculations and low temperature heat capacity study. Both the experimental evidence and theoretical calculation suggest that the effective scattering of acoustic phonons result in very low thermal conductivity of  $\text{PbBi}_2\text{S}_4$ . Furthermore, to improve the thermoelectric performance, carrier concentration optimization has been carried out by introducing Cl on S site.



---

### A tunable structural family with ultralow thermal conductivity: copper-deficient $\text{Cu}_{1-x}\square_x\text{Pb}_{1-x}\text{Bi}_{1+x}\text{S}_3$

---

---

†**K. Maji**, P. Lemoine, A. Renaud, B. Zhang, X. Zhou, V. Carnevali, C. Candolfi, B. Raveau, R. Al Rahal Al Orabi, M. Fornari, P. Vaqueiro, M. Pasturel, C. Prestipino, E. Guilmeau. *J. Am. Chem. Soc.* 2022, **144**, 1846-1860.



## 2.1. Introduction

Based on the discussion presented in the introductory section, it is evident that sulfide-based materials hold significant promise as a prospective path for advancing thermoelectric technology. The main objective of this chapter is to explore and investigate new complex sulfides based on bismuth (Bi) for potential applications in thermoelectrics. The use of heavy element sulfides like Bi sulfides offer the advantage of low thermal conductivity, not only because of the presence of active lone pairs but also due to the formation of complex structures that introduce anharmonicity into the system. This anharmonicity leads to reduce thermal conductivity, which is a crucial characteristic for high-performance thermoelectric materials.

Inspired by previous studies that have demonstrated the structural diversity and promising efficiency of various natural minerals, my research is driven by the desire to explore new mineral sulfides and their thermoelectric properties. Mineralogy books have cataloged thousands of complex minerals, many of which have not been extensively studied in the context of thermoelectric applications. One such compound is gladite, which has a chemical formula of  $\text{CuPbBi}_5\text{S}_9$  and is derived from the parent compound  $\text{Bi}_2\text{S}_3$ .

However, after six months of work on this phase, a report was published on this particular phase by Liang *et al.*,<sup>1</sup> covering similar aspects of our research. They reported a promising figure of merit,  $ZT \approx 0.42$  at 723 K, for the sulfide compound  $\text{CuPbBi}_5\text{S}_9$ , which possesses a gladite-type structure. Their findings indicated that this material has potential as an *n*-type thermoelectric candidate, as it exhibited low thermal conductivity and a moderate power factor. However, the synthesis process resulted in impure samples, with the presence of  $\text{BiS}_2$  and metallic Bi secondary phases, making it challenging to interpret the intrinsic transport properties of the material. The authors proposed that the electron transport properties were improved by the inclusion of Bi nanoparticles, while the existence of pores and interfaces between the matrix and Bi particles contributed to reducing the lattice thermal conductivity. Unfortunately, this explanation, which considers multiple effects, does not provide a clear understanding of the relationship between the gladite structure and the thermoelectric properties of the material, nor offer strategies for enhancing its energy conversion performance. To

address these issues, it is crucial to investigate a highly pure gladite phase. Since  $\text{CuPbBi}_5\text{S}_9$  corresponds to a member ( $x = 2/3$ ) of a series of copper-deficient  $\text{Cu}_{1-x}\text{Pb}_x\text{Bi}_{1+x}\text{S}_3$  minerals,<sup>2-8</sup> we conducted a new study on the crystal chemistry of this composition using mechanical alloying and spark plasma sintering (SPS). Our synthetic pathway allows to obtain highly pure sample and the structure does not exhibit ordered gladite mineral structure as reported by Liang *et al.*<sup>1</sup> Instead, it displays a copper-deficient, partially disordered aikinite structure where Bi replaces Pb, as described by the chemical formula  $\text{Cu}_{1/3}\text{Pb}_{2/3}\text{Bi}_{5/3}\text{S}_3$ . While the charge-balanced  $\text{Cu}^+\text{Pb}^{2+}\text{Bi}^{3+}_5\text{S}_9$  results in electronic properties typical of intrinsic semiconductors, we further demonstrate that this series provides an intriguing platform for designing novel *n*-type sulfides with extremely low thermal conductivity. In fact, through doping this sulfide with excess bismuth or by introducing chlorine on the Pb or S sites respectively, we were able to significantly enhance the *ZT* values, achieving a value of 0.43 at 700 K. This study opens up avenues for systematically exploring a wide range of dopable *n*-type thermoelectric sulfides.

## 2.2. Methods

### 2.2.1. Reagents

High-purity copper powder (Cu, Alfa Aesar, >99.99%), lead needles (Pb, Alfa Aesar, 99.99%), bismuth powder (Bi, Alfa Aesar, >99.5%), sulfur powder (S, Alfa Aesar, >99.99%), and bismuth (III) chloride ( $\text{BiCl}_3$ , Alfa Aesar, >99.99%) were used as precursors without further purification.

### 2.2.2. Synthesis

All samples were synthesized by mechanical alloying followed by spark plasma sintering. The high-energy ball milling was executed in a Fritsch Pulverisette 7 Premium line planetary ball mill operating at room temperature (RT) at a rotation speed of 600 rpm and a powder to ball ratio of around 1:18. Typically, pristine  $\text{CuPbBi}_5\text{S}_9$  was synthesized by milling stoichiometric amounts of Cu, Pb, Bi, and S powders (total amount of 6 g) for 6 h (12 cycles of 30 min with 1 min pause) under an argon atmosphere. X-ray diffraction patterns of mechanically alloyed powders after 30 min, 1 h, 3 h, and 6 h of milling are displayed in **Figure 2.1**. It can be observed that the

formation of the phase is fast, as the main broad diffraction peaks corresponding to the  $\text{CuPbBi}_5\text{S}_9$  phase appear after only 30 min.

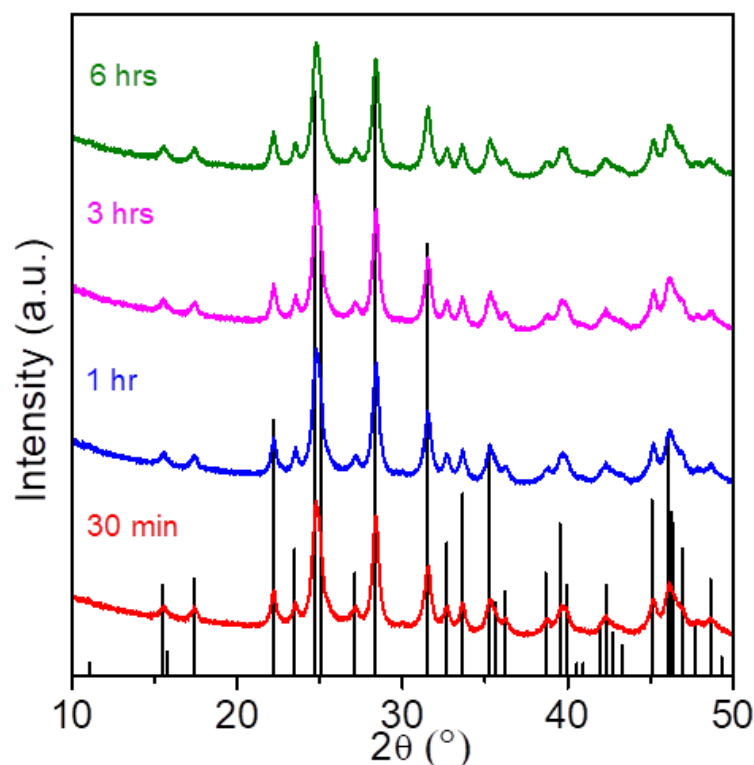


**Figure 2.1.** XRPD patterns of ball-milled powders for different ball-milling times.

*The theoretical pattern for gladiate,  $\text{CuPbBi}_5\text{S}_9$  is shown as black vertical lines.*

The presence of a broad diffraction peak suggests that the sample may not possess a high degree of crystallinity, even after undergoing mechanical alloying for duration of 6 hours. Alternatively, this broad peak could be attributed to the small crystallite size of the materials used. However, following the spark plasma sintering process of the sample, it was observed that all the peaks in the powder X-ray diffraction (PXRD) became significantly sharper, as shown in **Figure 2.2**. This observation suggests that the sample underwent a fast crystallization process during spark plasma sintering (SPS). However, the width of the diffraction peak's remain broaden which indicates small crystallite grain site in the samples.

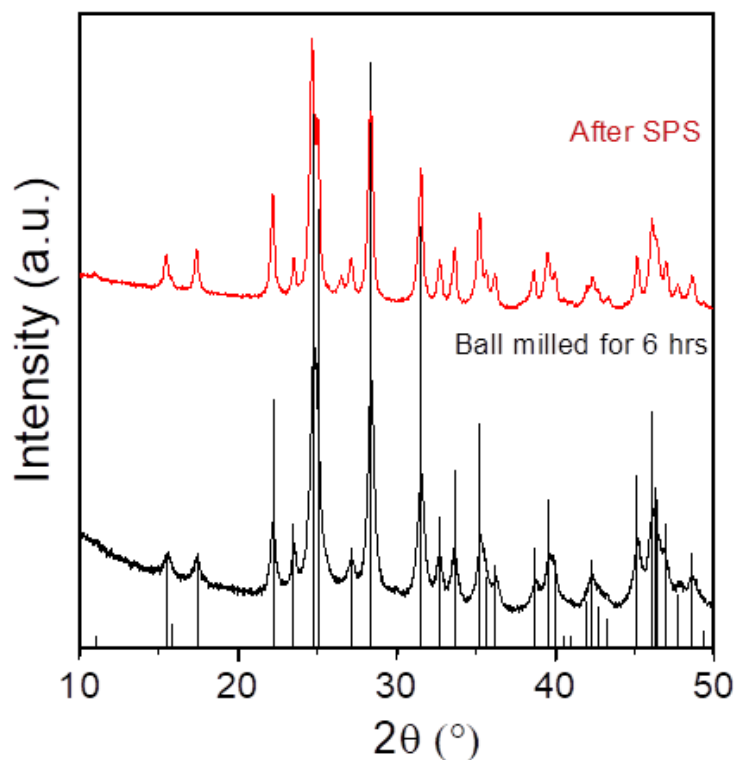


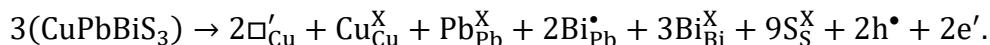
**Figure 2.2.** The XRPD pattern of ball-milled powder after 6 hrs and after SPS along with theoretical pattern for gladite,  $\text{CuPbBi}_5\text{S}_9$  is shown as black vertical lines.

## 2.3. Results and discussion

### 2.3.1. Crystal structure

The quaternary Cu-Pb-Bi-S system contains a large number of minerals that are structurally related to aikinite  $\text{CuPbBiS}_3$ <sup>4,9</sup> and bismuthinite  $\text{Bi}_2\text{S}_3$ <sup>10,11</sup> (space group  $Pnma$  with  $a \approx a_a \approx 11.5 \text{ \AA}$ ,  $b \approx b_a \approx 4 \text{ \AA}$  and  $c \approx c_a \approx 11.3 \text{ \AA}$ ). These phases can be formulated as  $(\text{Cu}_{1-x}\square_x)\text{Pb}_{1-x}\text{Bi}_{1+x}\text{S}_3$ , where  $\square$  refers to vacancies on the cationic sublattice of aikinite  $\text{CuPbBiS}_3$ . They crystallize either in the (normalized) space group  $Pnma$  with  $a \approx a_a$ ,  $b \approx b_a$  and  $c \approx n \times c_a$ , or in the space group  $Pmc2_1$  with  $a \approx b_a$ ,  $b \approx n \times c_a$  and  $c \approx a_a$ ,  $n$  being a positive integer number. The ordered phases arising from the

aikinite series can be constructed by substituting one  $\text{Pb}^{2+}$  plus one  $\text{Cu}^+$  by one  $\text{Bi}^{3+}$  plus one vacancy; using two vacancies on three Cu sites as in gladite, we obtain:



The descriptions of these structures are based on three types of ribbons, which are arranged in a herringbone pattern.<sup>7,12</sup> A summary of the structural information of the ordered Cu-Pb-Bi-S phases arising from the aikinite – bismuthinite  $(\text{Cu}_{1-x}\Box_x)\text{Pb}_{1-x}\text{Bi}_{1+x}\text{S}_3$  series is presented in **Table 2.1**. In addition to these fully ordered  $(\text{Cu}_{1-x}\Box_x)\text{Pb}_{1-x}\text{Bi}_{1+x}\text{S}_3$  phases, some others were reported with mixed occupancy of some crystallographic sites and/or partial site occupancy, such as emilite  $\text{Cu}_{10.7}\text{Pb}_{10.7}\text{Bi}_{21.3}\text{S}_{48}$  ( $x = 0.33$ ,  $Pmc2_1$ ,  $n = 4$ ),<sup>13</sup>  $\text{Cu}_{1.63}\text{Pb}_{1.63}\text{Bi}_{6.37}\text{S}_{12}$  ( $x = 0.60$ ,  $Pnma$ ,  $n = 3$ ),<sup>14</sup> or  $\text{Cu}_{1.435}\text{Pb}_{1.5}\text{Bi}_{6.5}\text{S}_{12}$  ( $x = 0.60$ ,  $Pmc2_1$ ,  $n = 4$ ).<sup>15</sup> From a diffraction point of view, the long-range ordering of cations and vacancies leads to the presence of superstructure diffraction peaks on powder diffraction patterns and superstructure spots in the selected area electron diffraction (SAED) patterns.

**Table 2.1.** Main structural information about ordered Cu-Pb-Bi-S phases arising from the aikinite – bismuthinite  $(\text{Cu}_{1-x}\Box_x)\text{Pb}_{1-x}\text{Bi}_{1+x}\text{S}_3$  series.

| $x$  | Chemical composition   | Mineral name | Space group | $n$ | Structure | Ref.    |
|------|--|--------------|-------------|-----|-----------|---------|
| 0.00 | $\text{CuPbBiS}_3$   | Aikinite     | $Pnma$      | 1   | 2A        | 4,9,16  |
| 0.17 | $\text{Cu}_5\text{Pb}_5\text{Bi}_7\text{S}_{18}$             | Friedrichite | $Pmc2_1$    | 3   | 4A + 2K   | 17      |
| 0.33 | $\text{Cu}_2\text{Pb}_2\text{Bi}_4\text{S}_9$                | Hammarite    | $Pnma$      | 3   | 2A + 4K   | 18      |
| 0.40 | $\text{Cu}_3\text{Pb}_3\text{Bi}_7\text{S}_{15}$             | Lindströmite | $Pnma$      | 5   | 2A + 8K   | 19,20   |
| 0.50 | $\text{CuPbBi}_3\text{S}_6$                                  | Krupkaite    | $Pmc2_1$    | 1   | 2K        | 21      |
| 0.60 | $\text{Cu}_{1.6}\text{Pb}_{1.6}\text{Bi}_{6.4}\text{S}_{12}$ | Paarite      | $Pnma$      | 5   | 8K + 2B   | 22      |
| 0.67 | $\text{CuPbBi}_5\text{S}_9$                                  | Gladite      | $Pnma$      | 3   | 4K + 2B   | 21,23   |
| 0.83 | $\text{CuPbBi}_{11}\text{S}_{18}$                            | Pekoite      | $Pmc2_1$    | 3   | 2K + 4B   | 4       |
| 1.00 | $\text{Bi}_2\text{S}_3$                                      | Bismuthinite | $Pnma$      | 1   | 2B        | 5,11,13 |

When Pb and Bi, on the one hand, and Cu and vacancies, on the other hand, are disordered, the crystal structure can be described in the space group  $Pnma$  with  $a \approx a_a$ ,

$b \approx b_a$  and  $c \approx c_a$  as for aikinite. In that case, only minor changes in the intensity of the peaks associated with the aikinite structure are observed in non-resonant X-ray diffraction patterns. Indeed, from an X-ray diffraction point of view, these phases differ only by the Cu/vacancies content since  $\text{Pb}^{2+}$  and  $\text{Bi}^{3+}$  cations are isoelectronic. Consequently, their accurate identification remains difficult even with high-quality powder diffraction patterns. Note that an alternative to the above-mentioned individual superstructures (**Table 2.1**) was proposed by Petricek and Makovicky with the refinement of krupkaite  $\text{Cu}_2\text{Pb}_2\text{Bi}_6\text{S}_{12}$ , paarite  $\text{Cu}_{1.7}\text{Pb}_{1.7}\text{Bi}_{6.3}\text{S}_{12}$ , salzburgite  $\text{Cu}_{1.6}\text{Pb}_{1.6}\text{Bi}_{6.4}\text{S}_{12}$  and gladite  $\text{Cu}_{1.33}\text{Pb}_{1.33}\text{Bi}_{6.67}\text{S}_{12}$  phases as commensurately modulated structures by using the superspace group  $Pm\bar{c}n(0\beta 0)00s$ , where  $\beta$  was assumed to be 2, 1/5, 1/4 and 1/3, respectively.<sup>12</sup>

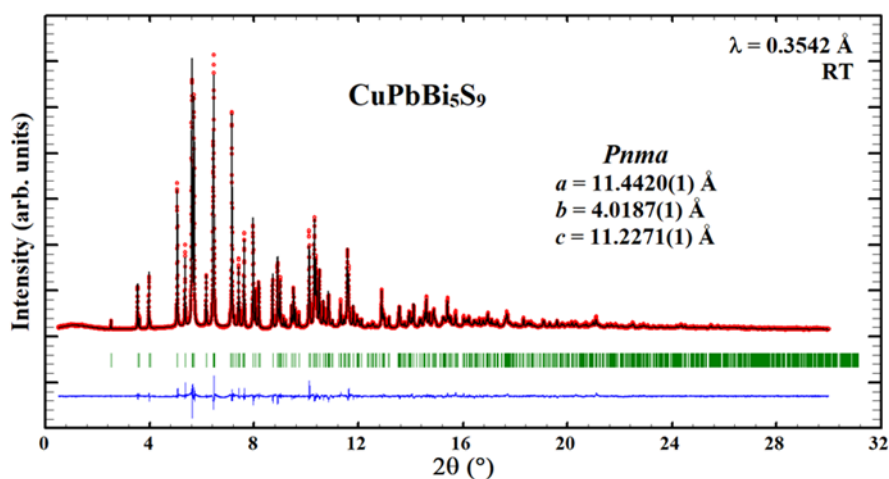


**Figure 2.3.** Rietveld refinement of the synchrotron XRPD data recorded at RT for pristine  $\text{CuPbBi}_5\text{S}_9$  sample ( $\lambda = 0.3542 \text{ \AA}$ ).

To determine the crystal structure, synchrotron X-ray powder diffraction (XRPD) patterns were recorded at room temperature (RT) on the pristine  $\text{CuPbBi}_5\text{S}_9$  sample (after SPS). The XRD patterns were successfully indexed with an orthorhombic unit cell of the  $Pnma$  space group and parameters  $a = 11.4420(1) \text{ \AA}$ ,  $b = 4.0187(1) \text{ \AA}$  and  $c = 11.2271(1) \text{ \AA}$  (**Figure 2.3**). The high purity of the sample is confirmed by the absence of extra diffraction peaks as well as the good quality of the Rietveld refinement. Despite its chemical composition, which corresponds to gladite (**Table 2.1**), the absence of

superstructure diffraction peaks (i.e.,  $c$  parameter equal to  $\approx 11.2$  Å instead of  $\sim 33.5$  Å) suggests that the crystal structure of this  $\text{CuPbBi}_5\text{S}_9$  sample can be described by considering disorder between Cu atoms and vacancies.

A Rietveld refinement of synchrotron XRPD data was performed by considering an aikinite structural model (**Table 2.2**) with, according to the nominal composition, a  $1/3$  occupation of the Cu site. The differences between the two structural models are shown in **Figure 2.4**. Finally, as previously mentioned,  $\text{Pb}^{2+}$  and  $\text{Bi}^{3+}$  cannot be distinguished from non-resonant X-ray diffraction only. Consequently, the final Rietveld refinement was performed by considering the structural model reported by Mumme and Watts (**Figure 2.3 and Table 2.2**). Our synthetic  $\text{CuPbBi}_5\text{S}_9$  can be described as a copper deficient aikinite  $(\text{Cu}_{1/3}\square_{2/3})\text{Pb}_{1/3}\text{Bi}_{5/3}\text{S}_3$ , with complete disorder between  $\text{Cu}^+$  and vacancies on the copper site on the one hand and between  $\text{Pb}^{2+}$  and  $\text{Bi}^{3+}$  on the Pb site on the other hand. Note that an exchange of the cations between the initial Pb and Bi aikinite sites cannot be ruled out.

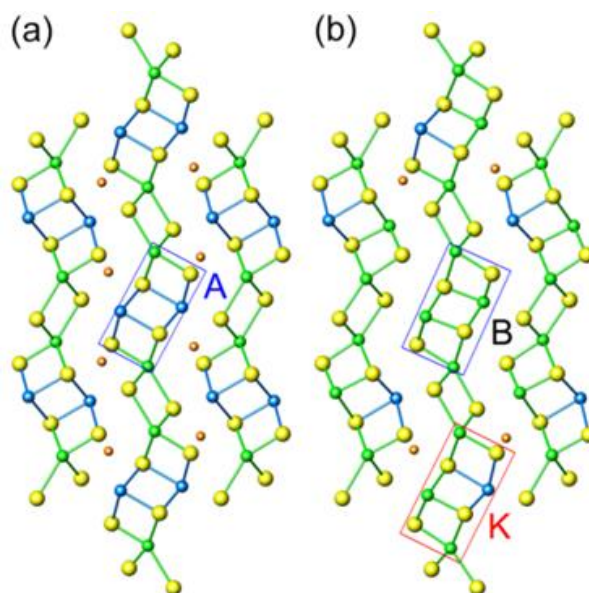


**Figure 2.4.** Comparison between the crystal structure of (a) aikinite and (b) gladite, with the aikinite-like (A), bismuthinite-like (B) and krupkaite-like (K) ribbons highlighted. Key: copper, orange spheres; bismuth, green spheres; lead, blue spheres; sulphur, yellow spheres.

**Table 2.2.** Refined cell parameters and atomic coordinates of  $\text{CuPbBi}_5\text{S}_9$  ( $Pnma$ ) from RT synchrotron XRPD data.

| Atom | Site | x         | y   | z         | $B_{\text{iso}}$ | SOF  |
|------|------|-----------|-----|-----------|------------------|------|
| Cu1  | 4c   | 0.2315(5) | 1/4 | 0.2106(6) | 4.23(20)         | 0.33 |
| Pb2  | 4c   | 0.3377(1) | 1/4 | 0.4739(1) | 3.15(3)          | 0.33 |
| Bi2  | 4c   | 0.3377(1) | 1/4 | 0.4739(1) | 3.15(3)          | 0.67 |
| Bi3  | 4c   | 0.0167(1) | 1/4 | 0.6772(1) | 1.84(2)          | 1.00 |
| S1   | 4c   | 0.0471(4) | 1/4 | 0.1309(4) | 3.14(13)         | 1.00 |
| S2   | 4c   | 0.3784(4) | 1/4 | 0.0571(4) | 2.62(12)         | 1.00 |
| S3   | 4c   | 0.2151(3) | 1/4 | 0.8037(4) | 1.52(10)         | 1.00 |

$a = 11.4420(1) \text{ \AA}$ ,  $b = 4.0187(1) \text{ \AA}$ ,  $c = 11.2271(1) \text{ \AA}$

$R_{\text{Bragg}} = 4.01$ ,  $R_{\text{F}} = 3.92$ ,  $R_{\text{wp}} = 4.57$ ,  $R_{\text{exp}} = 2.22$ ,  $\chi^2 = 4.24$

### 2.3.2. Scanning Electron Microscopy (SEM) analysis of pristine sample

The pristine  $\text{CuPbBi}_5\text{S}_9$  was further characterized by scanning electron microscopy (SEM). Micrographs, taken by scanning electron microscopy (SEM) on the fractured (**Figure 2.5**) and polished (**Figure 2.19 a**) surfaces, confirm the high purity of the pristine sample and the fine microstructure. The very small grain size around 200-300 nm, is induced by the combined mechanical-alloying and SPS processes. Backscattered electron imaging (BSE) combined with EDX analysis (**Figure 2.5b and c**) confirms the homogeneous distribution of all elements for the pristine sample and highlights the presence of bubble-like cavities, probably occurring from sulfur volatilization during the SPS process.

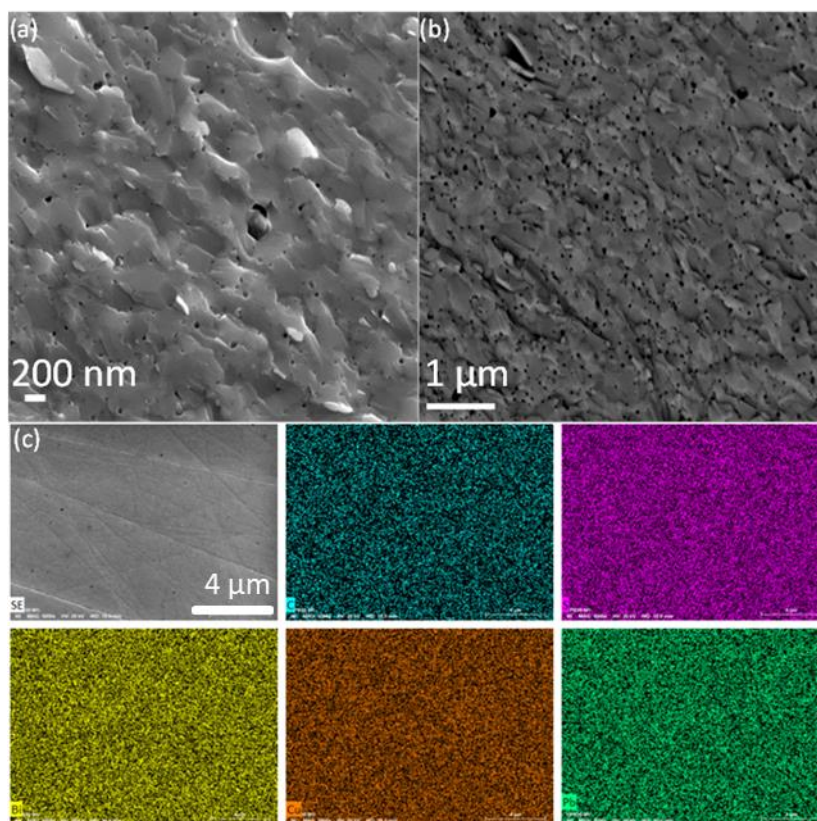


**Figure 2.5.** (a,b) SEM images of pristine  $\text{CuPbBi}_5\text{S}_9$ , (c) the EDS mappings demonstrate the generally uniform elemental distribution.

### 2.3.3. Transmission Electron Microscopy (TEM) analysis of pristine sample.

To investigate the crystal structure and the microstructure of  $\text{CuBiPb}_5\text{S}_9$  sample, systematic transmission electron microscopy (TEM) studies were conducted. As shown in **Figures 2.6a and b**, the sample exhibits nano-grains with size of  $\sim 200$  nm and irregular shapes which was previously confirmed by SEM analysis. Numerous bubble-like cavities shown as bright contrast in TEM (**Figure 2.6a**) and dark contrast in high-angle annular dark-field (HAADF, **Figure 2.6b**) can be observed near the grain boundaries, especially at the trigeminal ones. Those cavities may be due to element diffusion or volatilization at high temperature during sintering. The electron dispersion spectroscopy (EDS) mapping images (**Figure 2.6c**) demonstrate a uniform chemical distribution with the exception of minor Cu/Pb-rich precipitations.

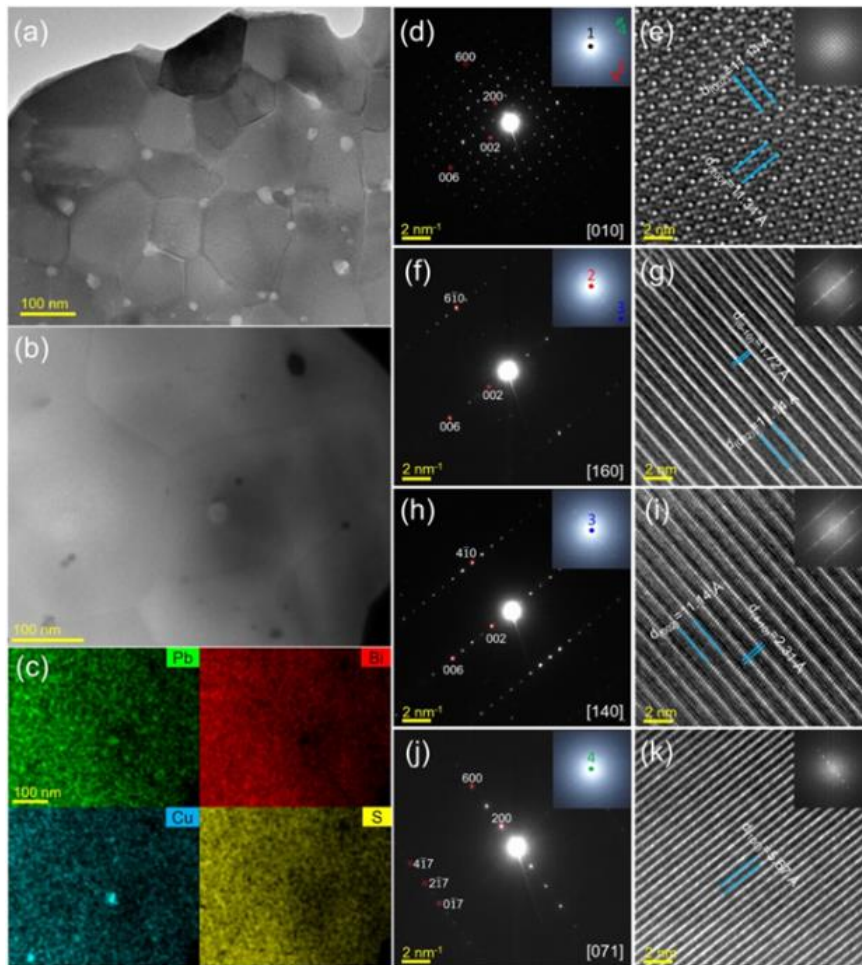


**Figure 2.6.** Structure analysis of  $\text{CuBiPb}_5\text{S}_9$  sample by TEM. (a) low-mag TEM image, (b) HAADF image and (c) the corresponding EDS mappings of Pb, Bi, Cu, S, respectively, (d-k) SAED patterns (Kikuchi patterns as inset) and the related HRTEM images (inset: FFT patterns). Bubble-like cavities appear as opposite contrast with white and dark in (a) TEM and (b) STEM-HAADF images, respectively, due to different imaging modes.

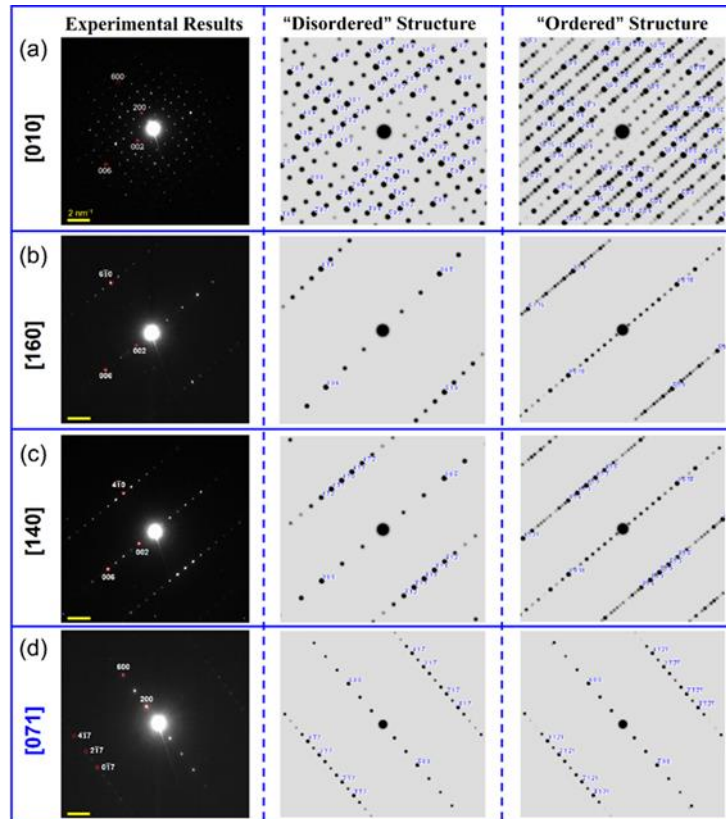


**Figure 2.7.** Comparison of experimental SAED patterns with the simulated patterns of “disordered” and “ordered” structures. Generally, the sample we obtained are similar to the “disordered” structure, but significantly distinct from the “ordered” structure. Therefore, the vacancies are randomly distributed in our sample. It is worth noting that these two phases can be well distinguished by the SAED patterns along the right zones (e.g., (a-c)). However, the “missing” zones (e.g., [071] d) will give out the undistinguished SAED patterns.

To prove the cationic disorder of these samples we took the help of local TEM analysis. A detailed comparison of SAED patterns between ordered gladite and disordered phases are presented in **Figure 2.7**. Tilting series were carried out for structure identification, during which SAED patterns and corresponding high-resolution TEM images were recorded (**Figure 2.6d and k**). The inserted Kikuchi patterns in **Figure 2.6 d, f and h** support the orientation relationships between different SAED patterns. The fast Fourier transform patterns are also shown in the TEM images. A grain was continuously tilted to the [010] (**Figure 2.6d and e**), the [160] (**Figure 2.6f and g**)

and the [140] (**Figure 2.6 h and i**) directions, respectively. As expected, these SAED patterns do not have the super structure spot and are consistent with those of the disordered simulated patterns which were proved by synchrotron PXRD analysis. Further tilting of the thin slice to the [071] zone (**Figure 2.7j and k**), made the ordered and disordered configurations almost indistinguishable (**Figure 2.7d**).

### 2.3.4. Electrical properties of pristine sample

The electrical properties of pristine  $\text{CuPbBi}_5\text{S}_9$  over the temperature range 300 - 700 K, are displayed in **Figure 2.8**. The undoped pristine  $\text{CuPbBi}_5\text{S}_9$  is highly resistive (electrical resistivity  $\rho = 3.5 \times 10^5 \text{ } \Omega \text{ cm}$  and  $S = -1370 \text{ } \mu\text{V K}^{-1}$  at 375 K. Both the electrical resistivity and absolute value of the Seebeck coefficient  $|S|$  decrease with increasing temperature to  $1.25 \text{ } \Omega \text{ cm}$  and  $560 \text{ } \mu\text{V K}^{-1}$  at 700 K, respectively, indicative of a nondegenerate semiconducting behavior. Negative values of the Seebeck coefficient are measured for all compositions over the entire temperature range, indicating, that electrons are the dominant charge carriers. The *n*-type conduction is mainly due to sulfur vacancies, similar to the case in other systems such as  $\text{Bi}_2\text{S}_3$ ,  $\text{MnBi}_4\text{S}_7$ ,  $\text{FeBi}_4\text{S}_7$ , and  $\text{AgBi}_3\text{S}_5$ ,<sup>24-26</sup> or may originate from a possible mixed valence  $\text{Bi}^{3+}/\text{Bi}^{2+}$  as discussed further. In comparison to other Bi-S-based compounds, the pristine phase  $\text{CuPbBi}_5\text{S}_9$  is quite resistive at RT. For example, pristine  $\text{Bi}_2\text{S}_3$  has an electrical resistivity of  $0.25 \text{ } \Omega \text{ cm}$  at RT, whereas other well-known ternary compounds, such as  $\text{AgBi}_3\text{S}_5$ ,  $\text{MnBi}_4\text{S}_7$ , and  $\text{FeBi}_4\text{S}_7$  have a RT electrical resistivity values of 0.024,  $5.3 \times 10^{-3}$ , and  $7.1 \times 10^{-3} \text{ } \Omega \text{ cm}$ , respectively. The thermopower is also quite large in our compound and significantly higher than those in other Bi-based sulfides. For instance,  $\text{Bi}_2\text{S}_3$  and  $\text{AgBi}_3\text{S}_5$  have  $|S|$  values of 350 and  $155 \text{ } \mu\text{V K}^{-1}$  at RT, respectively. Those lower values are mainly explained by the larger carrier concentrations (respectively  $3.7 \times 10^{16} \text{ cm}^{-3}$  and  $4.1 \times 10^{18} \text{ cm}^{-3}$  for  $\text{Bi}_2\text{S}_3$  and  $\text{AgBi}_3\text{S}_5$ ) due to non-stoichiometric effects. Pristine  $\text{CuPbBi}_5\text{S}_9$  sample exhibits a carrier concentration at RT around  $4.5 \times 10^{12} \text{ cm}^{-3}$  which is exceptionally low and rare in polycrystalline chalcogenides. Such low carrier concentration, in agreement with the large Seebeck coefficient, suggests that our material is highly stoichiometric thanks to the synthesis

process combining mechanical-alloying and SPS. As seen in other sulfides, the optimized mechanical-alloying process combined with SPS densification favors the crystallization of stoichiometric compounds, by preventing loss in quartz tubes exposed to high temperature and small temperature gradients inside a furnace.<sup>27,28</sup> Note that  $|S|$  and  $\rho$  values of, respectively,  $950 \mu\text{V K}^{-1}$  and  $7.1 \times 10^3 \Omega \text{ cm}$  at RT were measured by Liang *et al.* on a  $\text{CuPbBi}_5\text{S}_9$  sample prepared by mechanical alloying flowed by SPS,<sup>29</sup> suggesting a significant stoichiometry deviation in their sample.

The power factor ( $PF$ ) as a function of temperature for pristine  $\text{CuPbBi}_5\text{S}_9$  is shown in **Figure 2.8c**. The pristine sample exhibits a very low power factor of  $0.22 \mu\text{W cm}^{-1} \text{ K}^{-2}$  at 700 K. This value is lower than the value of  $2.9 \mu\text{W cm}^{-1} \text{ K}^{-2}$  reported by Liang *et al.* which can be the effect from the impurity in the system.<sup>1</sup> In comparison to other systems, the  $PF$  values in this system are comparable with those of  $\text{MnBi}_4\text{S}_7$  and  $\text{FeBi}_4\text{S}_7$  ( $\sim 2.1 \mu\text{W cm}^{-1} \text{ K}^{-2}$  at 550 K),<sup>30</sup> but remain lower than the best performing compounds, in particular, 0.5 mol%  $\text{BiCl}_3$  doped  $\text{Bi}_2\text{S}_3$  sample and 0.33% Cl doped  $\text{AgBi}_3\text{S}_5$  samples, which exhibit very high  $PF$  values of 6.7 and  $7.0 \mu\text{W cm}^{-1} \text{ K}^{-2}$ ,<sup>31,32</sup> respectively. The difference is mainly explained by intrinsic effects (crystal structure, electronic structure, defects) and extrinsic effects (grain size).

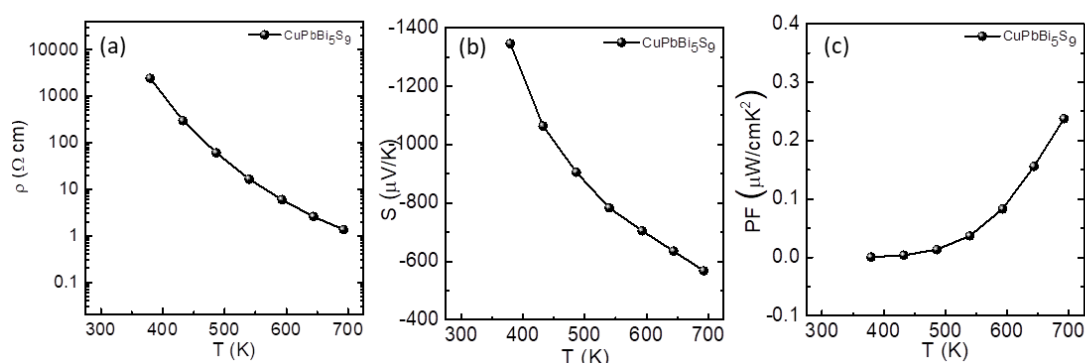


**Figure 2.8.** The temperature dependent (a) electrical resistivity ( $\rho$ ), (b) seebeck coefficient, ( $S$ ) (c) power factor ( $PF$ ), (d) total thermal conductivity ( $\kappa$ ) and (e) thermoelectric figure of merit ( $ZT$ ) of pristine  $\text{CuPbBi}_5\text{S}_9$ .

### 2.3.5. Electronic Structure

First-principles density functional theory (DFT) calculations were used to complement the experimental data. We studied the fully ordered gladite and several disordered models which have different level of disorder: a combination of vacancies on the Cu site, Bi on the Pb site, and Cl-S substitutions. As mentioned earlier, the formation energy surface is reasonably flat ( $\Delta E \leq 13$  meV/atom). From the electronic structure perspective, pristine gladite is an intrinsic semiconductor/insulator with a forbidden energy gap of 0.92 eV (**Figure 2.9**).

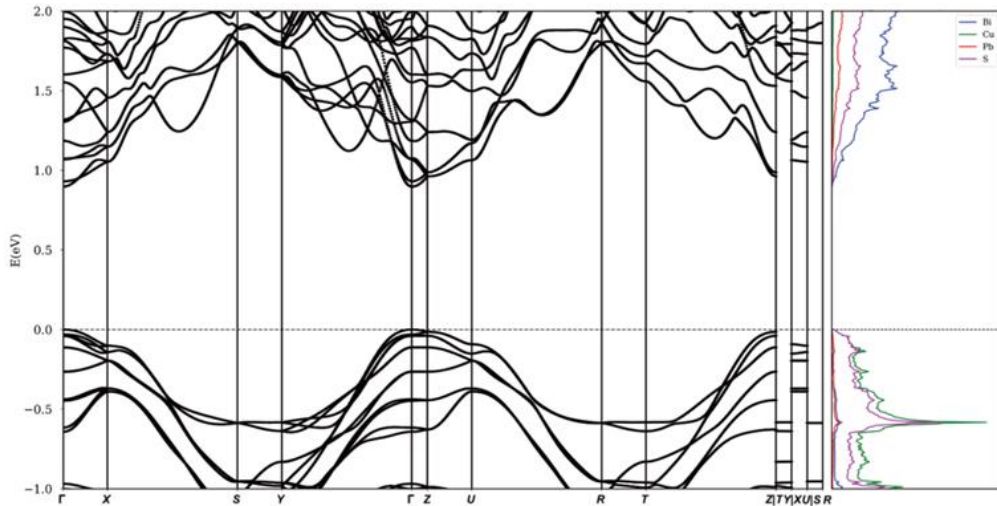


**Figure 2.9.** *Electronic band structure (left) and electronic projected density of states (right) of ordered  $\text{CuPbBi}_5\text{S}_9$  computed within the ACBN0 approach with  $U(\text{Pb}) = 0.005$ ,  $U(\text{Cu}) = 1.269$ ,  $U(\text{Bi}) = 0.043$ , and  $U(\text{S}) = 2.774$ . The horizontal line indicates the zero-energy reference that we arbitrarily set to the top of the valence band. The Fermi level is not drawn and always sits near the middle of the band gap for an intrinsic semiconductor.*

Note that the band-structure is meaningful only for ordered gladite. The computed value is in agreement with the band gap determined from Kubelka-Munk transform which provides values ranging from 0.89 to 0.95 eV, assuming direct transitions. As expected, the valence manifold is mainly formed by Cu and S states while the conduction band has a larger Bi and Pb contribution. From a purely theoretical point of

view, the top of the valence band could provide holes with large effective masses (**Figure 2.10**). However the large amount of Bi compared to Cu forms the Bi-S network, which leads to electrons are the main carriers, resulting to  $n$ -type behavior. It is important to point out that the theoretical calculations are conducted on the ordered gladite system. However, the synthetic samples exhibit two distinct forms of disorder, including vacancies on the Cu site and Pb on the Bi site. This disorder state may have an impact on the system's main carrier. Worth to note that a recent report from Carnevali *et al.* shows that the synthetic aikinite system, the Cu forms conductive network is more extended compared to  $\text{CuPbBi}_5\text{S}_9$  allowing  $p$ -type behavior.<sup>33</sup>

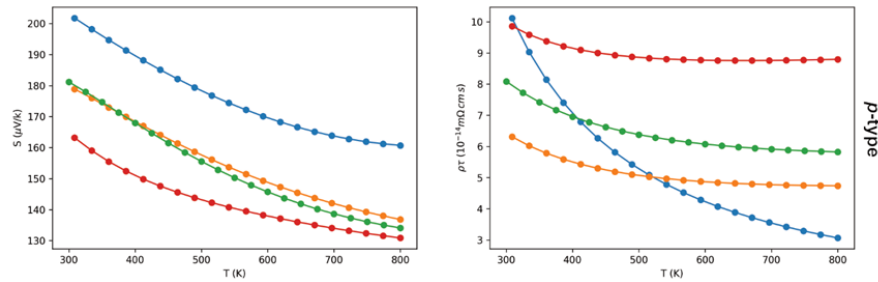


**Figure 2.10.** Temperature dependence of Seebeck coefficient,  $S$ , and electrical resistivity,  $\rho$ , for ordered gladite and different disordered models for  $p$ -type doping. First-principles calculations performed in the constant scattering time approximation shows that this material might have promising thermoelectric performances also as  $p$ -type semiconductor. Notice the sensitivity of the theoretical transport coefficients to disorder.

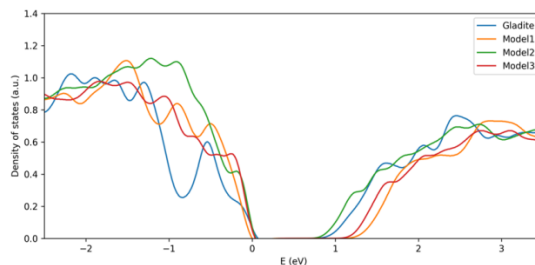


**Figure 2.11.** Electronic density of states ( $e\text{DoS}$ ) for pristine gladite (blue) and three different supercells used to model Cu-vacancies and Bi-Pb disorder. The bottom of the conduction manifold is quite sensitive to the disordering.

In proximity of the forbidden energy gap, the electronic properties are, of course, sensitive to the effect of disorder as well as chemical replacements. **Figure 2.12** shows the electronic density of states (eDoS) for gladite and several models of Cu-deficient disordered aikinite. We have averaged the different contributions to reasonably represent the eDoS of the macroscopic sample. eDoS, Seebeck coefficient, and electrical resistivity are also greatly affected by the specific supercell used to model the disordered configurations (**Figure 2.11**) making it difficult to reconcile a microscopic theoretical perspective with experiments. Transport calculations within the constant scattering time approximation are limited in the presence of substantial disorder.

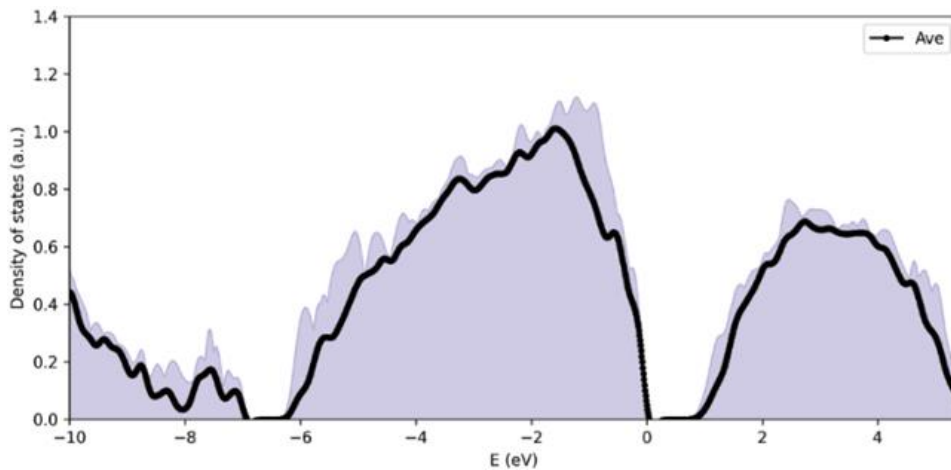


**Figure 2.12.** Average eDoS on the several computational cells used to model the ordered gladite as well as vacancies and Pb-Bi disordered system. The average gap between valence and conduction bands is of the order of 0.9 eV.

The gladite structure includes a chain of Bi atoms in the proximity of Cu vacancies. The electron localization function (ELF) and the charge density isosurfaces (**Figure 2.13**) clearly points to the presence of lone-pair near Bi and to charge rearrangements near S atoms surrounding the vacancies.

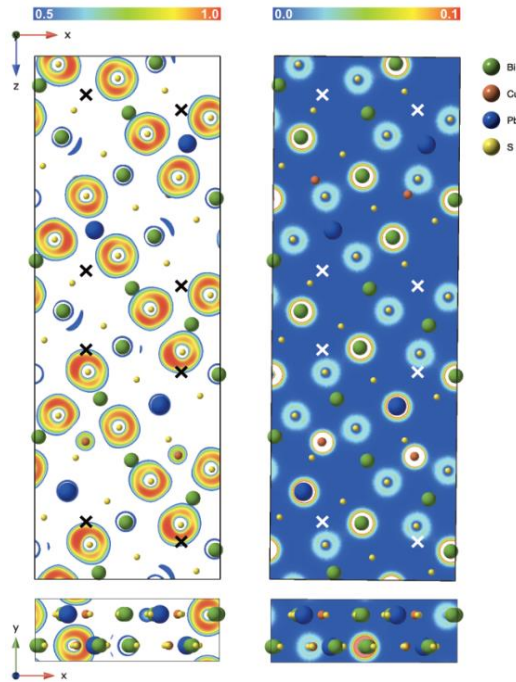


**Figure 2.13.** Side (top panel) and top (bottom panel) view of the contour of the electron localization function (left) and charge density (right) of ordered  $\text{CuPbBi}_5\text{S}_9$ . Values for the ELF range between 0 and 1: ELF = 0.5 (blue contours) indicates free-electron behavior and ELF = 1.0 (red contour) indicates strong localization. Values smaller than 0.5 are not easily interpretable. Values for the charge density range between 0.0 (blue) and 0.1 (red). Black and white crosses indicate the positions for the Cu vacancies in the ELF and charge density plots respectively.

### 2.3.6. Thermal properties of pristine sample

The temperature dependence of thermal conductivity of the pristine sample is shown in **Figure 2.14**. The pristine phase exhibits a very low total thermal conductivity  $\kappa$  of  $0.59 \text{ W m}^{-1} \text{ K}^{-1}$  at 300 K, which decreases upon warming to  $0.47 \text{ W m}^{-1} \text{ K}^{-1}$  at 700 K. Both the magnitude and temperature dependence of  $\kappa$  are in agreement with the data reported by Liang *et al.* on pristine  $\text{CuPbBi}_5\text{S}_9$ .<sup>29</sup> Due to the relatively high electrical resistivity of the samples, the electronic contribution  $\kappa_e$  to  $\kappa$  is negligible making the lattice component  $\kappa_L$  the primary contribution. Interestingly,  $\kappa_L$  exhibits a weaker temperature dependence than the  $T^{-1}$  law expected for Umklapp scattering, with a

decrease following  $T^{0.35}$  and  $T^{0.5}$  dependences for the Cl and Pb/Bi series, respectively. This deviation from the conventional law has been observed in several chain-like compounds TlSe, InTe, TlInTe<sub>2</sub>, TlCuSe or Tl<sub>3</sub>MX<sub>4</sub> ( $M = V, Nb$  and  $Ta$ ;  $X = S$  and  $Se$ ) and in tetrahedrites, all of them showing ultralow  $\kappa_L$  at high temperatures.<sup>34–45</sup> Theoretically, these deviations have been shown to be a signature of strong intrinsic anharmonicity resulting in pronounced renormalization effects on the phonon frequencies of optical modes that shape the low-energy part of the phonon spectrum of these materials. These similarities suggest that CuPbBi<sub>5</sub>S<sub>9</sub> may also show an anharmonic behavior. At high temperatures,  $\kappa_L$  approaches the minimum lattice thermal conductivity  $\kappa_{\min}$  of  $0.26 \text{ W m}^{-1} \text{ K}^{-1}$ , calculated from the measured room-temperature longitudinal ( $v_l = 3074 \text{ m s}^{-1}$ ) and transverse ( $v_t = 1565 \text{ m s}^{-1}$ ) sound velocities according to the model of Cahill and Pohl,<sup>46</sup> indicating a near-minimum phonon mean free path. The lack of significant decrease upon varying the Cl and Bi contents indicates that the crystal structure is the dominant factor that limits the propagation of heat carriers. Of note,  $\kappa_L$  is significantly lower than those measured in binary and ternary sulfides such as Bi<sub>2</sub>S<sub>3</sub>, PbS, TiS<sub>2</sub>, MnBi<sub>4</sub>S<sub>7</sub>,<sup>25,26,47,48</sup> and is comparable with those measured in several Bi-based sulfides such as AgBiS<sub>2</sub> and AgBi<sub>3</sub>S<sub>5</sub>.<sup>24,49</sup>

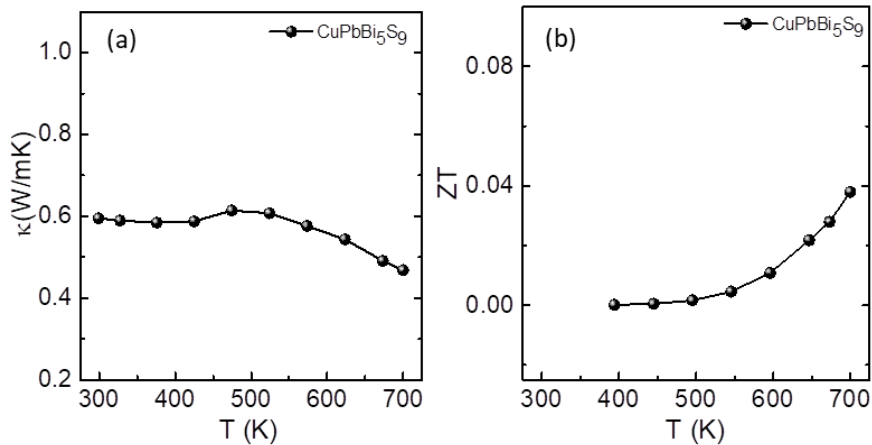


**Figure 2.14.** Temperature dependence of (a) total thermal conductivity and (b) figure of merit  $ZT$  of pristine CuPbBi<sub>5</sub>S<sub>9</sub>.

To further understand the origin of the very low  $\kappa_L$  values, insights into the lattice dynamics of in  $\text{CuPbBi}_5\text{S}_9$  have been obtained by low-temperature specific heat  $C_p$  measurements. The low-temperature data follow the conventional relation  $C_p = \gamma T + \beta T^3$  where  $\gamma T$  and  $\beta T^3$  are the electronic and lattice contributions, respectively. The zero value of  $\gamma$  confirms the semiconducting ground state of  $\text{CuPbBi}_5\text{S}_9$ . The Debye temperature  $\theta_D$ , inferred from the relation  $\theta_D = (12\pi^4 nR/5\beta)^{1/3}$  where  $n$  is the number of atoms per formula unit and  $R$  is the ideal gas constant, is equal to 156.5 K. As observed in several families of sulfides such as tetrahedrites and colusites, and in cage-like materials,<sup>43,44,50–56</sup> the  $C_p(T)$  data show a pronounced peak centered near 10 K upon plotting the  $C_p(T)/T^3$  versus  $T$ . This plot shows that low-energy optical modes exist in the phonon spectrum. To model this peak, we used a combination of a Debye term with two additional Einstein-like terms to account for the low-lying optical modes. In this model, the Debye temperature, the number of Debye and Einstein oscillators, and the characteristic Einstein temperatures are considered as free parameters. The best fits to the data, shown in **Figure 2.15**, yield Einstein temperatures  $\theta_{E1}$  and  $\theta_{E2}$  of 32 and 48.4 K with spectral weights of 0.40 and 0.33, respectively.

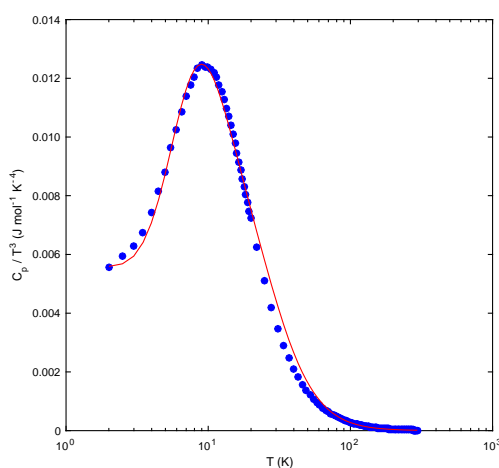


**Figure 2.15.**  $C_p(T)/T^3$  versus  $T$  for  $\text{CuPbBi}_5\text{S}_9$ . The red solid curve stands for the best fit to the data according to the above-mentioned equation with  $\theta_{E1} = 32$  K,  $\theta_{E2} = 48.4$

$$\text{K, } p_1 N_{E1} = 0.33, p_2 N_{E2} = 0.4 \text{ and } \theta_D = 156.5 \text{ K.}$$

According to atomic mass considerations, this excess contribution to  $C_p$  is mainly associated with low-energy optical modes from the Bi and Pb atoms. First-principles lattice dynamics calculations on aikinite confirm such a conjecture (**Figure 2.16**).

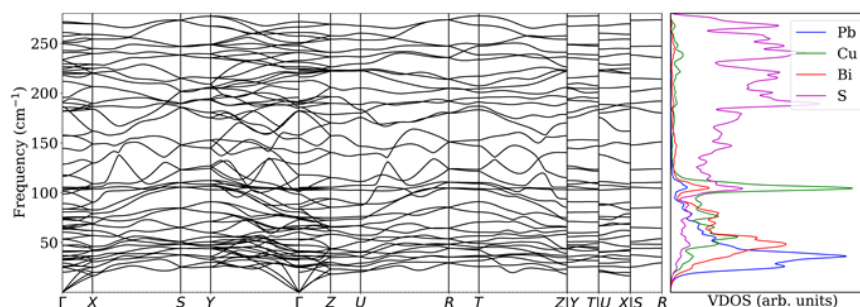


**Figure 2.16.** Phonon dispersions (left) and projected phonon density of states (PDOS) (right) of aikinite  $\text{CuPbBiS}_3$ , which we used as a proxy for the Cu-deficient disordered aikinite. The low-frequency optical vibrations are mainly associated with the heavier cations. The contribution of Cu in the low-frequency region of the spectrum is not negligible, as was recognized in other sulfides.

Indeed, using aikinite as a proxy for the Cu-deficient disordered aikinite, the phonon dispersions indicate the presence of very low energy optical modes associated with Pb and Bi ions and, to a smaller extent, Cu. The Einstein temperatures inferred from the specific heat data, that correspond to wavenumbers of  $22.2$  and  $33.6 \text{ cm}^{-1}$ , respectively, are in good agreement with the two lowest peaks ( $25.0$  and  $35.2 \text{ cm}^{-1}$ , respectively) observed in the PDOS mainly associated with Pb-weighted thermal motions. This vibrational complexity at low energy hints to possible substantial anharmonic effects that contribute to lower  $\kappa_L$ . This is in agreement with the high value of the Grüneisen parameter  $\gamma$  of  $1.93$ , obtained from the sound velocity measurement at  $300 \text{ K}$ . Such a large value, close to those reported for other ultralow- $\kappa_L$  materials (**Table 2.4**), is consistent with strong phonon-phonon scattering in  $\text{CuPbBi}_5\text{S}_9$ . Similar characteristics have been observed in the phonon spectra of the above-mentioned chain-like and sulfide compounds, all of them exhibiting ultralow  $\kappa_L$ . The presence of soft bonding interaction in  $\text{CuPbBi}_5\text{S}_9$  is further supported by the low average sound velocity  $v_s$  of  $1758 \text{ m s}^{-1}$ , which is comparable with published data on  $\text{CuPbBi}_5\text{S}_9$  and with other

low-thermal-conductivity chalcogenides (**Table 2.4**). The average sound velocity ( $v_s$ ), grüneisen parameter ( $\gamma$ ), and debye temperature ( $\theta_D$ ) are calculated from measured transverse and longitudinal sound velocity by using following equations:

$$v_s^3 = \frac{3}{v_l^{-3} + v_t^{-3}} \quad (\text{Eq. 2})$$

$$v_p = \frac{1 - 2\left(\frac{v_t}{v_l}\right)^2}{2 - 2\left(\frac{v_t}{v_l}\right)^2} \quad (\text{Eq. 3})$$

$$\gamma = \frac{3(1+v_p)}{2(2-3v_p)} \quad (\text{Eq. 4})$$

$$\theta_D = \frac{h}{k_B} \left[ \frac{3N}{4\pi V} \right]^{1/3} v_a \quad (\text{Eq. 5})$$

Where,  $N$ ,  $V$ ,  $h$ , and  $k_B$  are the number of atoms in unit cell, the volume of the unit cell, the Planck constant and the Boltzmann constant respectively.

**Table 2.4.** Grüneisen parameter and Debye temperature from sound velocity measurements: comparison including Cu-deficient aikinite and several other sulfides.

| Compound                           | Average sound velocity (m/sec) | Grüneisen parameter | Debye T (K) | Ref.      |
|------------------------------------|--------------------------------|---------------------|-------------|-----------|
| CuPbBi <sub>5</sub> S <sub>9</sub> | 1758                           | 1.93                | 178.5       | This work |
| MnBi <sub>4</sub> S <sub>7</sub>   | 1767                           | 1.16                | 179.4       | 25        |
| FeBi <sub>4</sub> S <sub>7</sub>   | 1967                           | 1.28                | 200.8       | 25        |
| AgSbTe <sub>2</sub>                | 1727                           | 2.05                | 125         | 57        |
| BiSbSe <sub>3</sub>                | 1629                           | 1.89                | 165         | 58        |
| SnSe                               | 1420                           | 3.13                | 142         | 59        |
| Bi <sub>2</sub> Se <sub>3</sub>    | 2083                           | 1.65                | 205         | 60        |
| Sb <sub>2</sub> Se <sub>3</sub>    | 1882                           | 1.58                | 180         | 58        |

### 2.3.7. PXRD analysis of doped samples

The electrical resistivity of pristine gladite is high due to its very low carrier concentration, leading to a low power factor and consequently a low  $ZT$  value, despite its low thermal conductivity. To overcome this limitation and achieve higher performance, we employed chemical doping techniques. In our study, we substituted chlorine (Cl) for sulfur (S) and bismuth (Bi) for lead (Pb) in gladite. By synthesizing a series of doped compounds with varying concentrations, we aimed to optimize the carrier concentration and improve performance. Through the doping process, we successfully increased the carrier concentration in the gladite compound. This led to a significant improvement in the power factor, which is a crucial factor in thermoelectric performance.

Typically, all the doped samples,  $\text{CuPbBi}_5\text{S}_{9-z}\text{Cl}_z$  (where  $z = 0.03, 0.09, 0.18$ ) and  $\text{CuPb}_{1-y}\text{Bi}_{5+y}\text{S}_9$  (where  $y = 0.05, 0.1, 0.25, 0.5$ ) were synthesized by milling stoichiometric amounts of Cu, Pb, Bi,  $\text{BiCl}_3$  and S powders (total amount of 6 g) for 6 h (12 cycles of 30 min with 1 min pause) under an argon atmosphere, as presented earlier (same as for pristine  $\text{CuPbBi}_5\text{S}_9$ ).

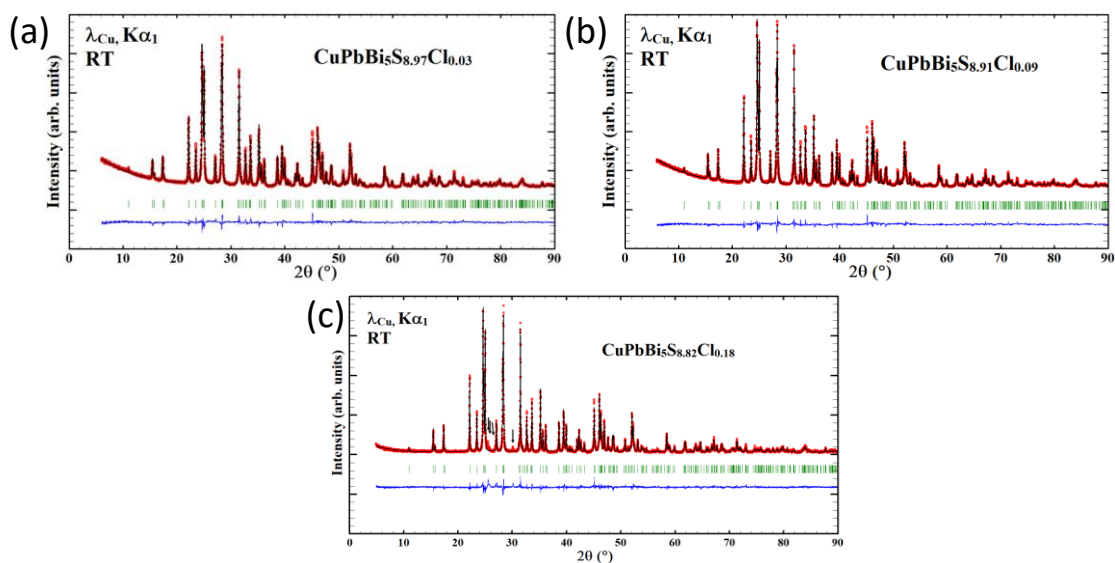


**Figure 2.17.** Rietveld refinement of the XRPD data recorded at room temperature (RT) for (a)  $\text{CuPbBi}_5\text{S}_{8.97}\text{Cl}_{0.03}$ , (b)  $\text{CuPbBi}_5\text{S}_{8.91}\text{Cl}_{0.09}$ , (c)  $\text{CuPbBi}_5\text{S}_{8.82}\text{Cl}_{0.18}$  sample ( $\lambda = 1.5406 \text{ \AA}$ ). The experimental data are plotted as red symbols, the calculated pattern as black line and the difference between them as lower blue line. The Bragg positions for aikinite are plotted as vertical green ticks.

Rietveld refinement of the XRPD data confirms the Cu/vacancies disordered crystal structure and the high purity of the  $\text{CuPbBi}_5\text{S}_{9-z}\text{Cl}_z$  samples with  $z = 0.03$  and  $z = 0.09$  (**Figures 2.17a and b**) and  $\text{CuPb}_{1-y}\text{Bi}_{5+y}\text{S}_9$  sample with  $y = 0.05$  (**Figure 2.18a**). For the same reasons that  $\text{Pb}^{2+}$  and  $\text{Bi}^{3+}$  are undistinguishable by non-resonant XRPD,  $\text{S}^{2-}$  and  $\text{Cl}^-$  cannot be as well distinguished. The Rietveld refinements of the Cl-doped samples were then conducted by considering the same structural model as the one used for pristine sample, i.e. only S atoms are considered in the structural model. These refinements show that Cl for S substitution does not modify significantly the crystal structure of the Cu-deficient aikinite  $\text{CuPbBi}_5\text{S}_9$  (**Table 2.17**). The presence of extra diffraction peaks in the  $\text{CuPbBi}_5\text{S}_{9-z}\text{Cl}_z$  sample with  $z = 0.18$  (**Figure 2.17c**) and  $\text{CuPb}_{1-y}\text{Bi}_{5+y}\text{S}_9$  samples with  $y = 0.10, 0.25$  and  $0.50$  (**Figure 2.18b, c and d**) is related to the presence of a secondary phase in the Cu-(Bi,Pb)-S system. However, due to the almost identical atomic number of Bi and Pb, the exact nature and composition of this phase

have not been identified. This indicates that Cl for S and Bi for Pb substitutions may be limited due to the key role of the (Cu+Pb)/Bi ratio to stabilize the structure.

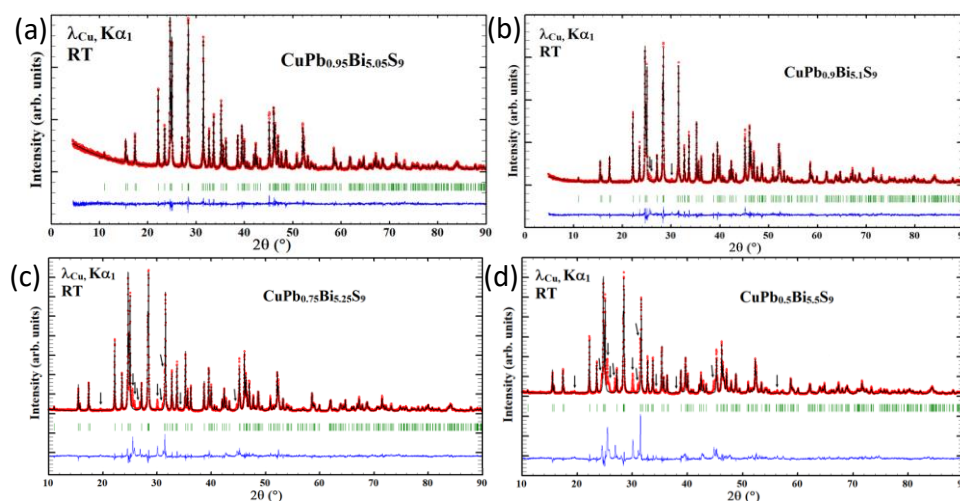


**Figure 2.18.** Rietveld refinement of the XRPD data recorded at room temperature (RT) for (a)  $\text{CuPb}_{0.95}\text{Bi}_{5.05}\text{S}_9$ , (b)  $\text{CuPb}_{0.90}\text{Bi}_{5.10}\text{S}_9$ , (c)  $\text{CuPb}_{0.75}\text{Bi}_{5.25}\text{S}_9$  (d)  $\text{CuPb}_{0.5}\text{Bi}_{5.5}\text{S}_9$  sample ( $\lambda = 1.5406 \text{ \AA}$ ). The experimental data are plotted as red symbols, the calculated pattern as black line and the difference between them as lower blue line. The Bragg positions for aikinite are plotted as vertical green ticks.

**Table 2.5.** Refined unit cell parameters and reliability factors of the pristine and  $\text{CuPb}_{1-y}\text{Bi}_{5+y}\text{S}_{9-z}\text{Cl}_z$  samples from the Rietveld analysis of the room temperature XRPD data.

| Compound                            | $\text{CuPbBi}_5\text{S}_9$ | $\text{CuPbBi}_5\text{S}_{8.97}\text{Cl}_{0.03}$ | $\text{CuPbBi}_5\text{S}_{8.91}\text{Cl}_{0.09}$ | $\text{CuPb}_{0.95}\text{Bi}_{5.05}\text{S}_9$ |
|-------------------------------------|-----------------------------|--|--|--|
| Space group                         | <i>Pnma</i>                 | <i>Pnma</i>                                      | <i>Pnma</i>                                      | <i>Pnma</i>                                    |
| a (Å)                               | 11.4342(2)                  | 11.4301(3)                                       | 11.4345(2)                                       | 11.4301(3)                                     |
| b (Å)                               | 4.0152(1)                   | 4.0138(1)  | 4.0131(1)  | 4.0111(1)                                      |
| c (Å)                               | 11.2191(2)                  | 11.2108(3)                                       | 11.2067(2)                                       | 11.2079(3)                                     |
| V (Å <sup>3</sup> )                 | 515.08(2)                   | 514.33(3)  | 514.26(2)  | 513.85(2)                                      |
| R <sub>Bragg</sub> , R <sub>F</sub> | 4.73, 3.30                  | 4.44, 2.96                                       | 5.41, 3.70                                       | 4.79, 3.50                                     |
| R <sub>wp</sub> , R <sub>exp</sub>  | 7.25, 4.85                  | 5.70, 4.10                                       | 6.26, 4.20                                       | 8.73, 7.47                                     |
| $\chi^2$                            | 2.24                        | 1.94   | 2.22   | 1.37   |

### 2.3.8. Scanning Electron Microscopy (SEM) analysis of doped samples

The samples of the  $\text{CuPbBi}_5\text{S}_9$ ,  $\text{CuPbBi}_5\text{S}_{9-z}\text{Cl}_z$  series (with  $z$  values of 0.09 and 0.18, respectively) and the  $\text{CuPb}_{1-y}\text{Bi}_{5+y}\text{S}_9$  series (with  $y$  values of 0.05, 0.25, and 0.5) were subjected to additional characterization using scanning electron microscopy (SEM). The high purity of the pristine samples for  $\text{CuPbBi}_5\text{S}_9$ ,  $\text{CuPbBi}_5\text{S}_{9-z}\text{Cl}_z$  (where  $z = 0.09$ ), and  $\text{CuPb}_{1-y}\text{Bi}_{5+y}\text{S}_9$  (where  $y = 0.05$ ) is confirmed by analyzing backscattered electron images obtained through SEM on the polished surfaces. The presence of bubble-like cavities, as observed through TEM, is evident in all of the samples. These cavities are likely a result of sulfur volatilization that occurred during the spark plasma sintering (SPS) process. The Cu-Bi-S phase impurity phases (dark contrast) could be seen in the Cl-doped ( $z = 0.18$ ) and Bi-doped ( $y = 0.25$  and 0.50) samples (**Figure 2.19**).

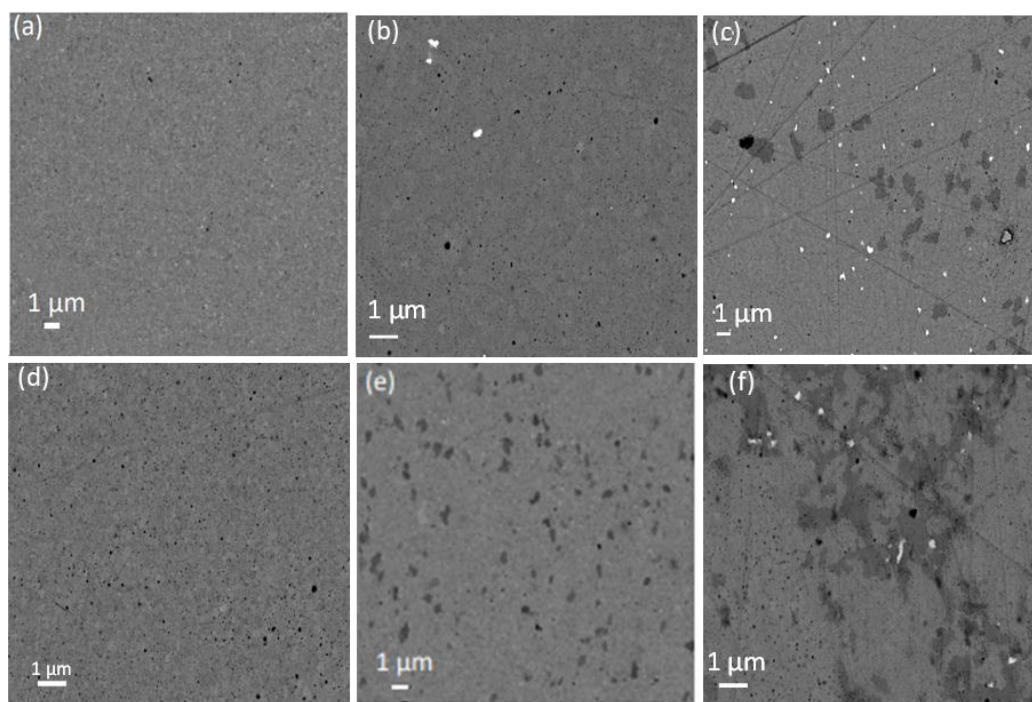


**Figure 2.19.** (a) Backscattered electron images of pristine  $\text{CuPbBi}_5\text{S}_9$ , (b, c)  $\text{CuPbBi}_5\text{S}_{9-z}\text{Cl}_z$  series ( $z = 0.09$  and  $z = 0.18$ , respectively) and (d, e, f)  $\text{CuPb}_{1-y}\text{Bi}_{5+y}\text{S}_9$  series ( $y = 0.05$ , 0.25 and 0.5) samples.

### 2.3.9. Transmission electron microscopy (TEM) analysis of doped samples.

Transmission electron microscopy (TEM) analysis was utilized to conduct a more in-depth examination of the microstructure of the doped samples. Distinctive grains with a few hundred nanometers were observed in the samples  $\text{CuPb}_{0.95}\text{Bi}_{5.05}\text{S}_9$  (**Figure 2.20a**) and  $\text{CuPbBi}_5\text{S}_{8.91}\text{Cl}_{0.09}$  (**Figure 2.21a**), which are comparable to the grains observed in the original  $\text{CuPbBi}_5\text{S}_9$  sample.

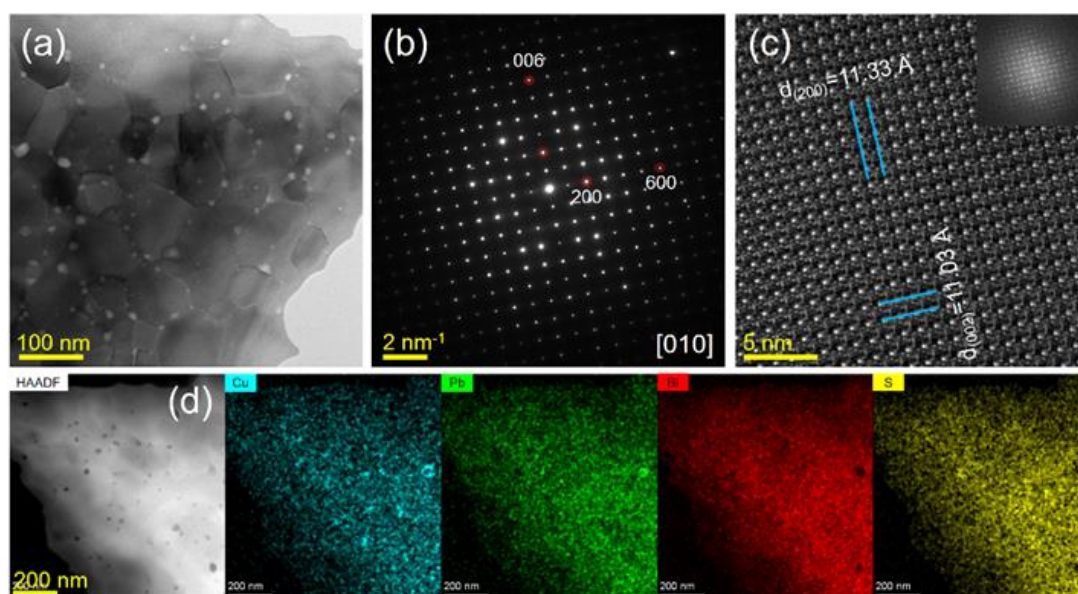


**Figure 2.20.** TEM characterization of Bi-doped sample ( $y = 0.05$ ). (a) shows the grain and bubble-like cavities, (b, c) the [010] SAED pattern and HRTEM image confirm “disordered” structure, (d) the EDS mappings demonstrate the generally uniform elemental distribution. Bubble-like cavities appear as dark contrast in Figure S8d due to different detector.

Additionally, the Spark Plasma Sintering (SPS) process yielded the formation of bubble-like cavities as a consequence of sulfur evaporation. The color mapping analysis revealed a uniform dispersion of all elements in the samples, without any noticeable presence of additional phases. (**Figure 2.20d and Figure 2.21d**) Furthermore, the

disordered state of copper (Cu) and the existence of vacancies were verified through the analysis of selected area electron diffraction (SAED) patterns for both samples.

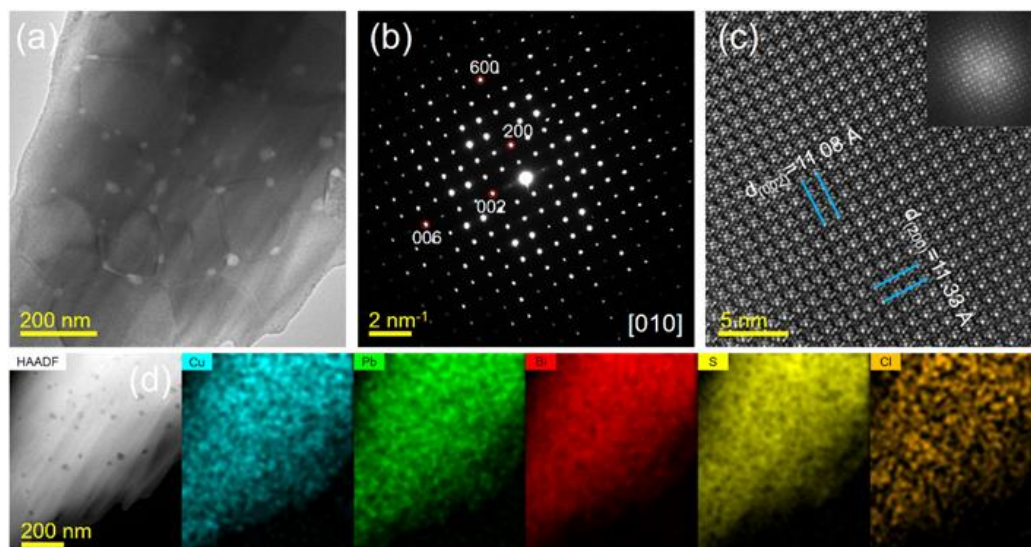


**Figure 2.21.** TEM characterization of Cl-doped sample ( $z = 0.09$ ). (a) shows the grain and bubble-like cavities, (b, c) the [010] SAED pattern and HRTEM image confirm “disordered” structure, (d) the EDS mappings demonstrate the homogenous elemental distribution. Bubble-like cavities appear as dark contrast in Figure S9d due to different detector.

### 2.3.10. Band gap.

Band gaps, determined from Kubelka-Munk transforms (**Figure 2.22 a**), indicate that the substitution of chlorine for sulfur tends to slightly open the band gap from 0.89 eV for  $\text{CuPbBi}_5\text{S}_9$  to 0.95 eV for  $\text{CuPbBi}_5\text{S}_{8.82}\text{Cl}_{0.18}$ , assuming direct transitions. Cl-doping affects the localization of the Fermi level, as the flat band potential values, extrapolated at  $C^{-2} = 0$  from the Mott-Schottky plots, (**Figure 2.22b**) exhibit a slight shift towards lower energy of the Fermi level, suggesting a complex interplay between Cl-doping, S-vacancies, and possibly other defects.

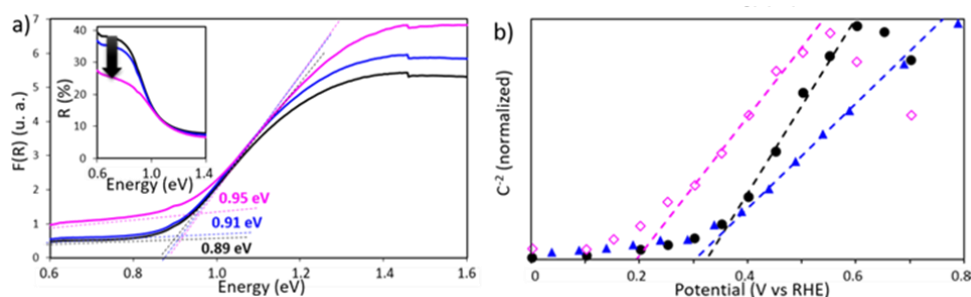


**Figure 2.22.** a) Kubelka-Munk transforms, and b) Mott-Schottky plots for  $\text{CuPbBi}_5\text{S}_9$  (black, ●),  $\text{CuPbBi}_5\text{S}_{8.91}\text{Cl}_{0.09}$  (blue, ▲) and  $\text{CuPbBi}_5\text{S}_{8.82}\text{Cl}_{0.18}$  (purple, ◇) samples.

### 2.3.11. Electronic transport properties of doped samples

The electrical properties in the series  $\text{CuPbBi}_5\text{S}_{9-z}\text{Cl}_z$  ( $z = 0.00, 0.03, 0.09, 0.18$ ) over the temperature range 300 - 700 K, are displayed in **Figure 2.23**. Both  $|S|$  and  $\rho$  values decrease gradually with the increase of Cl content, down to 350  $\mu\text{V/K}$  and 0.41  $\Omega\text{ cm}$  for  $z = 0.09$  at 300 K.  $|S|$  and  $\rho$  decrease monotonically with increasing temperature for all the compositions, which indicates that the materials behave as non-degenerate semiconductor upon Cl-doping, although additional electrons are injected. The decrease of  $|S|$  and  $\rho$  with increasing Cl content, however, is consistent with the role of Cl as an electron donor as it replaces sulfur. With increasing Cl content, the carrier concentrations at room temperature increases up to  $5.5 \times 10^{16}$  for  $z = 0.03$ ,  $1.5 \times 10^{18}$  for  $z = 0.09$  and  $1.9 \times 10^{18} \text{ cm}^{-3}$  for  $z = 0.18$ . The RT mobility ( $\mu$ ) values are equal to 3.7, 4.15, 7.0 and 2.5  $\text{cm}^2 \text{ V}^{-1} \text{ s}^{-1}$  for  $z = 0, 0.03, 0.09, 0.18$ , respectively. Those values are significantly smaller than those measured in the other Bi-based compounds mentioned before, which is mainly explained by the very small grain size and/or the disordered structure in our samples. Further investigations are ongoing to determine the impact of the crystal structure and microstructure on the electron mobility.

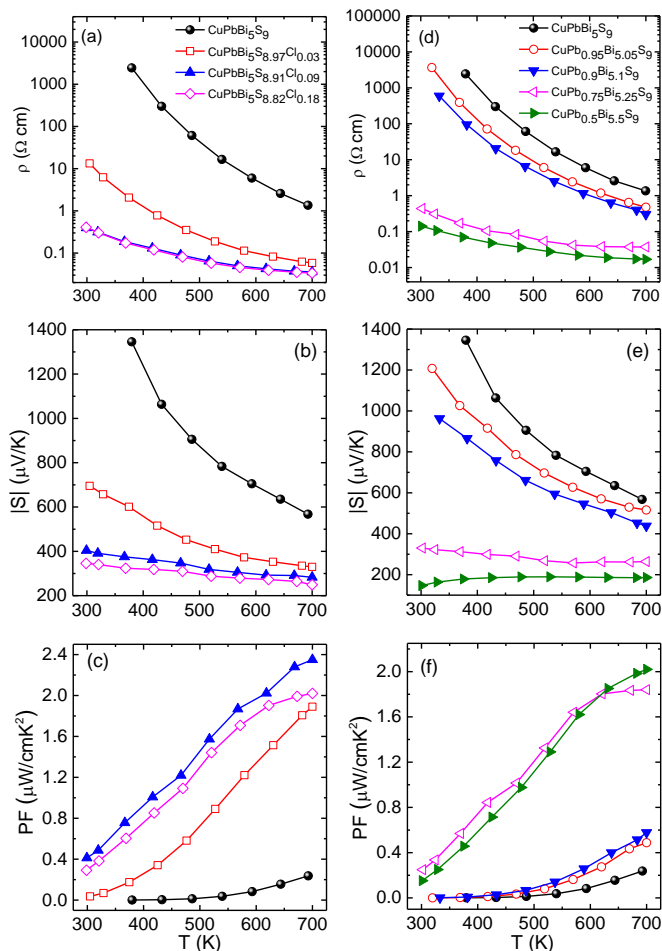


**Figure 2.23.** Temperature dependence of (a,d) electrical resistivity, (b,e) Seebeck coefficient and (c,f) power factor in the  $\text{CuPbBi}_5\text{S}_{9-z}\text{Cl}_z$  and  $\text{CuPb}_{1-y}\text{Bi}_{5+y}\text{S}_9$  series, respectively.

Finally, it must be noted that the measurements are well reversible up to 680 K (3 cycles from 350 K to 630 K + 3 cycles from 350 K to 680 K) which attests the stability of our material in this working temperature range (**Figure 2.24**). A slight drift is observed with the addition of 3 more cycles up to 700 K. This phenomenon can be related to surface oxidation of the sample in the ZEM3 chamber and/or  $n$ -type doping or phase decomposition. Interestingly, a hysteresis loop can be observed at around 370-520 K, which is most probably related to order/disorder phenomena. Different studies on related natural minerals, such as pekoite  $\text{CuPbBi}_{11}\text{S}_{18}$ , hammarite  $\text{CuPb}_2\text{Bi}_4\text{S}_9$  and krupkaite  $\text{CuPbBi}_3\text{S}_6$ , have shown that the temperature limit to order vacancies is below

473-573 K.<sup>4,7,61</sup> When heating up our sample up to 448 K, the vacancies on the Cu site probably start to order, and then disorder above 473 K. This point is under investigation.

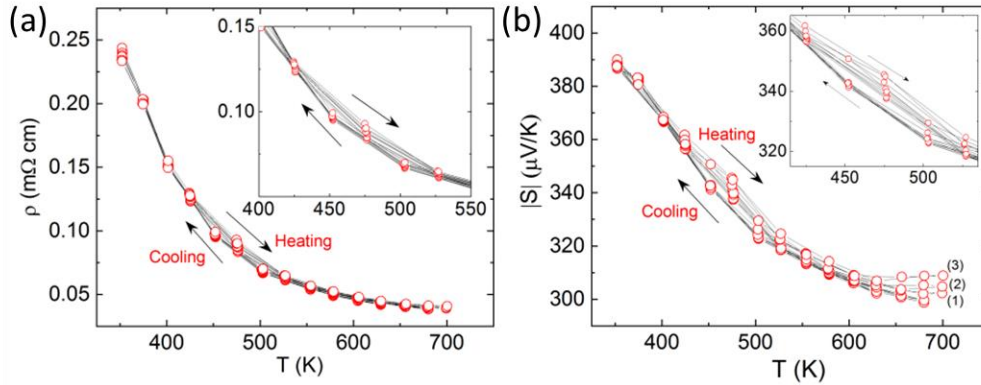


**Figure 2.24.** Cycling measurements of the electrical resistivity,  $\rho$ , and Seebeck coefficient,  $S$ , of  $\text{CuPbBi}_5\text{S}_{8.91}\text{Cl}_{0.09}$  sample. 3 cycles from 350 K to 630 K + 3 cycles from 350 K to 680 K + 3 cycles from 350 K to 700 K.

The power factor ( $PF$ ) as a function of temperature in the series  $\text{CuPbBi}_5\text{S}_{9-z}\text{Cl}_z$  is shown in Figure 2.19.c. The undoped sample exhibits a very low power factor of  $0.22 \mu\text{W cm}^{-1} \text{K}^{-2}$  at 700 K. The power factor increases significantly with Cl content to a maximum value of  $2.2 \mu\text{W cm}^{-1} \text{K}^{-2}$  at 700 K for  $z = 0.09$ .

The electrical transport properties in the second series  $\text{CuPb}_{1-y}\text{Bi}_{5+y}\text{S}_9$  are displayed in **Figure 2.23d-f**. The electrical resistivity and absolute value of the Seebeck coefficient decrease as the Bi content increases. The lowest value of  $\rho$  of  $0.14 \Omega \text{ cm}$  and  $|S|$  of  $144 \mu\text{V K}^{-1}$  at 300 K are obtained for  $\text{CuPb}_{0.5}\text{Bi}_{5.5}\text{S}_9$ . For this sample, the electrical resistivity slightly decreases with increasing temperature while  $|S|$  increases. The carrier concentration in this series increases with Bi doping to  $7.7 \times 10^{13} \text{ cm}^{-3}$  for  $y = 0.05$ ,  $4.6 \times 10^{18} \text{ cm}^{-3}$  for  $y = 0.25$ , and reaches a maximum of  $1.86 \times 10^{19} \text{ cm}^{-3}$  for  $y = 0.5$ . Those values and trends must be, however, taken with caution as the material is composed of different phases for  $y = 0.25$  and  $y = 0.5$ . The highest  $PF$  value of  $0.24 \mu\text{W cm}^{-1} \text{K}^{-2}$  at RT is obtained for  $\text{CuPb}_{0.75}\text{Bi}_{5.25}\text{S}_9$  ( $PF = 1.83 \mu\text{W cm}^{-1} \text{K}^{-2}$  at 700 K). As expected,  $|S|$  decreases with increasing the electron concentration  $n_{\text{H}}$  for both series. This general trend, illustrated by the Ioffe-Pisarenko plot shown in **Figure 2.25**, is well

captured by a single-parabolic band (SPB) model with acoustic phonon scattering and a conduction density-of-states effective mass  $m_{\text{DOS}}^*$  of  $0.88 m_e$ . This good agreement suggests that Cl or Bi doping weakly influences  $m_{\text{DOS}}^*$ , with no evident sign of multiband behavior at these doping levels.

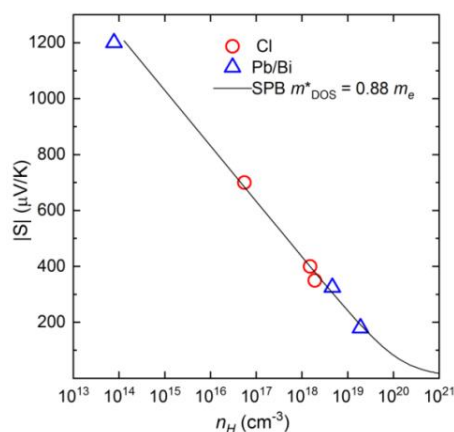


**Figure 2.25.** Ioffe-Pisarenko representation of the Seebeck coefficients  $|S|$  as a function of the electron concentration  $n_H$  at 300 K. The solid black curve was calculated using a single-parabolic band approximation.

### 2.3.12. Thermal transport properties and figure of merit of doped samples

The temperature dependent total thermal conductivity of  $\text{CuPbBi}_5\text{S}_{9-z}\text{Cl}_z$  and  $\text{CuPb}_{1-y}\text{Bi}_{5+y}\text{S}_9$  samples are shown in Figure 2.26. The pristine phase shows a significantly low total thermal conductivity ( $\kappa$ ) of  $0.59 \text{ W m}^{-1} \text{ K}^{-1}$  at 300 K. This value decreases to  $0.47 \text{ W m}^{-1} \text{ K}^{-1}$  at 700 K, which matches the results reported by Liang *et al.* The thermal conductivity exhibits a slight variation with the increasing concentrations of Cl and Bi, with values ranging from  $0.50$  to  $0.65 \text{ W m}^{-1} \text{ K}^{-1}$  at 300 K. Due to the relatively high electrical resistivity of the samples, the electronic contribution  $\kappa_e$  to  $\kappa$  is negligible, making the lattice component  $\kappa_L$  the primary contribution as already discussed earlier. The electrical contribution in total thermal conductivity exhibits an increasing relationship with the doping content, while simultaneously leading to an increase in point defects within the system. These two factors counterbalance each other, resulting in keeping of the overall low thermal conductivity.

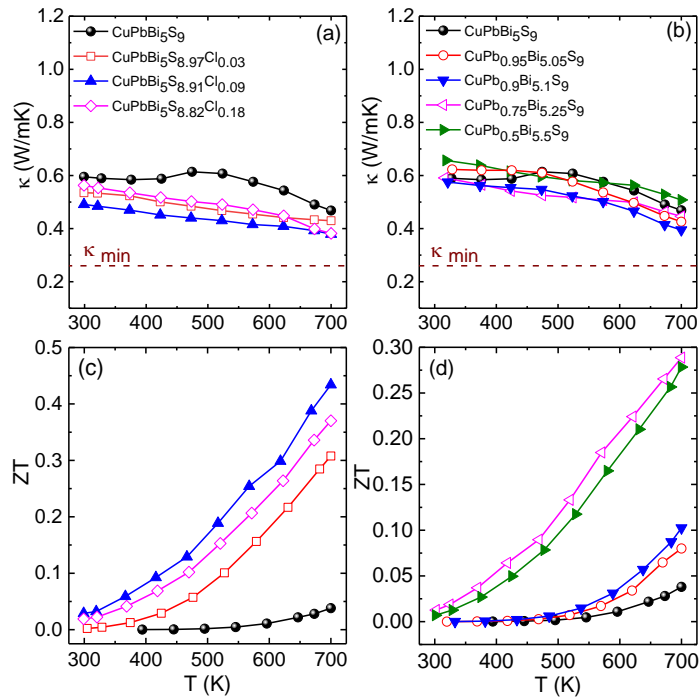


**Figure 2.26.** Temperature dependence of (a,b) thermal conductivity and (c,d) figure of merit  $ZT$  in the  $\text{CuPbBi}_5\text{S}_{9-z}\text{Cl}_z$  and  $\text{CuPb}_{1-y}\text{Bi}_{5+y}\text{S}_9$  series, respectively.

The temperature dependence of  $ZT$  in the  $\text{CuPbBi}_5\text{S}_{9-z}\text{Cl}_z$  and  $\text{CuPb}_{1-y}\text{Bi}_{5+y}\text{S}_9$  series (**Figure 2.26c and d**, respectively) points to limited thermoelectric efficiency for pristine  $\text{CuPbBi}_5\text{S}_9$  ( $ZT = 0.04$  at 700 K), however, the figure of merit increases remarkably with Cl-doping reaching 0.43 for  $z = 0.09$ . A similar increase in  $ZT$  is also observed with increasing Bi content, reaching 0.29 for  $y = 0.25$  sample (**Figure 2.26d**). Comparing the performance at 700 K with other Bi-based  $n$ -type thermoelectric sulfides (**Figure 2.27**), it is possible to qualitatively estimate the interplay between lattice thermal conductivity and power factors on  $ZT$ . Cl-doped  $\text{CuPbBi}_5\text{S}_9$  exhibits similar  $ZT$  compared to Cl-doped  $\text{Bi}_2\text{S}_3$  compound, one of best  $n$ -type state-of-the-art thermoelectric sulfides.  $\text{CuPbBi}_5\text{S}_9$  presents a significantly lower lattice thermal conductivity compared to this material thanks to its structural complexity and enhanced structural disorder. However, this is counterbalanced by a lower power factor ( $2.2 \mu\text{W cm}^{-1} \text{K}^{-2}$  compared to  $6.0 \mu\text{W cm}^{-1} \text{K}^{-2}$ ) due to a carrier concentration one order of magnitude larger in Cl-doped  $\text{Bi}_2\text{S}_3$ . The absence of cationic disorder in the latter compound also favors a higher electron mobility. The very large  $ZT$  in  $\text{AgBi}_3\text{S}_5$  mainly

originates from a larger carrier concentration, at least 15 times higher than in our compounds, due to a higher concentration of defects, while presenting similar lattice thermal conductivity. This suggests that a drastic improvement of  $ZT$  can be achieved in  $\text{CuPbBi}_5\text{S}_9$  and in the large family of  $\text{Cu}_{1-x}\square_x\text{Pb}_{1-x}\text{Bi}_{1+x}\text{S}_3$  compounds, provided that a higher carrier concentration can be reached. To estimate the maximum  $ZT$  value achievable upon doping in  $\text{CuPbBi}_5\text{S}_9$ , the dimensionless quality factor  $B$  has been calculated for the  $z = 0.09$  sample. This parameter, which encompasses all the inherent material properties that determines the  $ZT$  values,<sup>62–64</sup> enables to calculate the dependence of the  $ZT$  values on the reduced chemical potential  $\eta$ , that is, on the doping level. Using the  $S$  and  $\kappa_L$  values of the  $z = 0.09$  sample measured at 700 K yield a  $B$  value of  $\sim 0.3$  that corresponds to a maximum  $ZT$  of 0.8 reached at an optimum  $S$  value of  $\sim 200 \mu\text{V K}^{-1}$ . This last value, which fits well with the range of optimum  $S$  values predicted in several studies<sup>63,65,66</sup> shows that the carrier concentration should be further increased using other aliovalent substitutions.

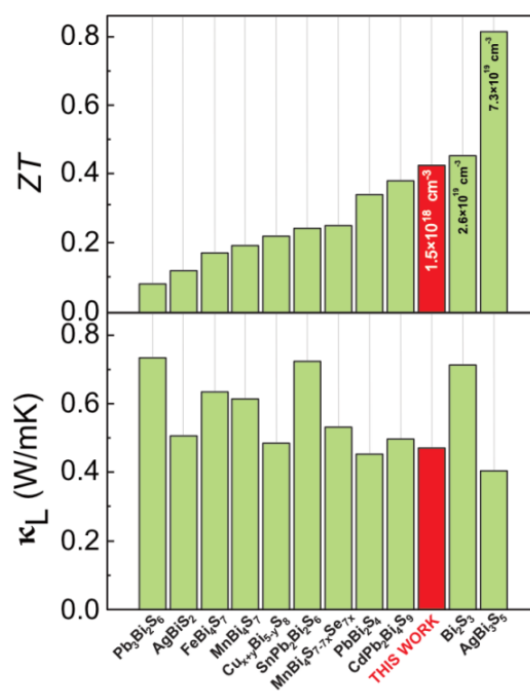


**Figure 2.27.** (Top panel)  $ZT$  and (bottom panel) lattice thermal conductivity in state-of-the-art thermoelectric  $n$ -type Bi-based sulphides.<sup>25,26,32,49,67–71</sup> The values inside the histogram bars are the carrier concentration.

## 2.4. Conclusion

In conclusion, in this chapter, a new Cu-deficient aikinite-type sulfide has been synthesized with the composition  $\text{CuPbBi}_5\text{S}_9$  by combining mechanical alloying and SPS techniques. The structure of this sulfide, though closely related to gladite with the same composition reported by Liang *et al.*, differs from the latter by the disordered distribution of copper and vacancies on the cationic sites. In contrast to their  $\text{CuPbBi}_5\text{S}_9$  compound, which could only be obtained with the presence of secondary phases, this Cu-deficient aikinite is highly pure allowing for a detailed investigation of its transport properties. In particular, we have demonstrated that the ultralow lattice thermal conductivity observed for this structural type is intrinsic and does not originate from secondary phases. Despite being a nearly intrinsic semiconductor ( $\rho \sim 5.10^3 \Omega \text{ cm}$  and  $S \sim -1300 \mu\text{V K}^{-1}$  at 400 K) with extremely low carrier concentration ( $4.5 \times 10^{12} \text{ cm}^{-3}$ ), this synthetic sulfide is an exceptional prototype for generating high thermoelectric performance by doping with Cl or Bi, leading to thermoelectric figures of merit varying between 0.30 and 0.43 at 700 K. The good thermoelectric performance stems from the exceptionally low lattice thermal conductivity due to the presence of very low energy vibrations involving Bi, Pb, and Cu. The dramatic improvement of the thermoelectric figure of merit upon Cl- or Bi-doping may be related to the ability of the Bi-S framework to generate *n*-type conductivity due to the so induced mixed valence  $\text{Bi}^{3+}/\text{Bi}^{2+}$ . This statement is supported by the existence of the sub-valent bismuth compound  $\text{Bi}_{13}\text{S}_{18}\text{I}_2$  which exhibits  $[\text{Bi}_2]^{4+}$  dimers. It is worth pointing out that the present compound, which represents the member  $x = 2/3$  of a large series of closely related sulfides  $(\text{Cu}_{1-x}\square_x)\text{Pb}_{1-x}\text{Bi}_{1+x}\text{S}_3$  with  $0 \leq x \leq 1$ , is paradigmatic for a broad family of *n*-type thermoelectric materials that are susceptible to optimization by varying the chemical composition, by controlling the order-disorder phenomena, and by tuning the carrier concentration through doping.

### 3.5. References

- (1) Liang, H.; Guo, J.; Zhou, Y. X.; Wang, Z. Y.; Feng, J.; Ge, Z. H. CuPbBi<sub>5</sub>S<sub>9</sub> Thermoelectric Material with an Intrinsic Low Thermal Conductivity: Synthesis and Properties. *J. Mater.* **2021**, *13*. <https://doi.org/10.1016/j.jmat.2021.03.016>.
- (2) Ohmasa, M.; Nowacki, W. A Redetermination of the Crystal Structure of Aikinite [BiS<sub>2</sub>]S[Cu<sup>IV</sup>Pb<sup>VII</sup>]. *Z. Krist.* **1970**, *132*, 71–86. <https://doi.org/10.1021/ic50036a025>.
- (3) Kohatsu, I.; Wuensch, B. J. The Crystal Structure of Aikinite, PbCuBiS<sub>3</sub>. *Acta Crystallogr. Sect. B Struct. Crystallogr. Cryst. Chem.* **1971**, *27* (6), 1245–1252. <https://doi.org/10.1107/s0567740871003819>.
- (4) Mumme, W. G.; Watts, J. A. Pekoite, CuPbBi<sub>11</sub>S<sub>18</sub>, A New Member of the Bismuthinite-Aikinite Mineral Series: Its Crstal Struture and Relationship with Naturally- and Synhthetically-Formed Members. *Can. Mineral.* **1976**, *14*, 322–333.
- (5) Kupčičk, V.; Veselá-Nováková, L. Zur Kristallstruktur Des Bismuthinits, Bi<sub>2</sub>S<sub>3</sub>. *Tschermaks Mineral. und Petrogr. Mitteilungen* **1970**, *14* (1), 55–59. <https://doi.org/10.1007/BF01081780>.
- (6) Lundegaard, L. F.; Makovicky, E.; Boffa-Ballaran, T.; Balic-Zunic, T. Crystal Structure and Cation Lone Electron Pair Activity of Bi<sub>2</sub>S<sub>3</sub> between 0 and 10 GPa. *Phys. Chem. Miner.* **2005**, *32*, 578–584. <https://doi.org/10.1007/s00269-005-0033-2>.
- (7) Pring, A. Annealing of Synthetic Hammarite, Cu<sub>2</sub>Pb<sub>2</sub>Bi<sub>4</sub>S<sub>9</sub>, and the Nature of Cation-Ordering Processes in the Bismuthinite-Aikinite Series. *Am. Mineral.* **1995**, *80* (11), 1166–1173. <https://doi.org/10.2138/am-1995-11-1207>.
- (8) Petříček, V.; Makovicky, E. Interpretation of Selected Structures of the Bismuthinite - Aikinite Series as Commensurately Modulated Structures. *Can. Mineral.* **2006**, *44* (1), 189–206. <https://doi.org/10.2113/gscanmin.44.1.189>.
- (9) Kohatsu B. J., I. . W. The Crystal Structure of Aikinite, PbCuBiS<sub>3</sub>. *Acta Crystallogr. Sect. B Struct. Crystallogr. Cryst. Chem.* **1971**, *27* (6), 1245–1252. <https://doi.org/10.1107/s0567740871003819>.
- (10) Kupčičk Ludmila, V. . V.-N. Zur Kristallstruktur Des Bismuthinits, Bi<sub>2</sub>S<sub>3</sub>.

- Tschermaks Mineral. und Petrogr. Mitteilungen* **1970**, *14* (1), 55–59.  
<https://doi.org/10.1007/bf01081780>.
- (11) Lundegaard Emil; Boffa-Ballaran, Tiziana; Balic-Zunic, Tonci, L. F. . M. Crystal Structure and Cation Lone Electron Pair Activity of  $\text{Bi}_2\text{S}_3$  between 0 and 10 GPa. *Phys. Chem. Miner.* **2005**, *32* (8), 578–584.  
<https://doi.org/10.1007/s00269-005-0033-2>.
- (12) Petricek Emil, V. M. Interpretation of selected structures of the Bismuthanite - Aikinite series as commensurately modulated structures. *Can. Mineral.* **2006**, *44* (1), 189–206. <https://doi.org/10.2113/gscanmin.44.1.189>.
- (13) Kanishcheva, A. S.; Mikhailov, Y. N.; Trippel, A. F. Refinement of the Crystal Structure of Synthetic Bismuthinite. *Inorg. Mater.* **1981**, No. 17, 1466–1468.
- (14) Burstein, E. Anomalous Optical Absorption Limit in InSb. *Phys. Rev.* **1954**, *93* (3), 632–633. <https://doi.org/10.1103/PhysRev.93.632>.
- (15) Moss, T. S. The Interpretation of the Properties of Indium Antimonide. *Proc. Phys. Soc. Sect. B* **1954**, *67* (10), 775–782. <https://doi.org/10.1088/0370-1301/67/10/306>.
- (16) Ohmasa Werner, M. N. A Redetermination of the Crystal Structure of Aikinite [ $\text{BiS}_2/\text{S}/\text{Cu}^{\text{IV}}\text{Pb}^{\text{VII}}$ ]. *Zeitschrift für Krist.* **1970**, *132* (1–6), 71–86.  
<https://doi.org/10.1524/zkri.1970.132.1-6.71>.
- (17) Chen, T. T.; Kirchner, E.; Paar, W. Friedrichite,  $\text{Cu}_5\text{Pb}_5\text{Bi}_7\text{S}_{18}$ , A New Member of the Aikinite-Bismuthinite Series. *Can. Mineral.* **2015**, *16*, 127–130.
- (18) Horiuchi, H.; Wuensch, B. J. The Ordering Scheme for Metal Atoms in the Crystal Structure of Hammarite,  $\text{Cu}_2\text{Pb}_2\text{Bi}_4\text{S}_9$ . *Can. Mineral.* **1976**, *14*, 536–539.
- (19) Horiuchi, H.; Wuensch, B. J. Lindstromite,  $\text{Cu}_3\text{Pb}_3\text{Bi}_7\text{S}_{15}$ : Its Space Group and Ordering Scheme for Metal Atoms in the Crystal Structure. *Can. Mineral.* **1977**, *15*, 527–535.
- (20) Topa Vaclav; Dušek, Michal; Makovicky, Emil; Balic-Zunic, Tonci, D. P. Simultaneous refinement of two components of an exsolution intergrowth: Crystal structures of the lindströmite - Krupkaite pair. *Can. Mineral.* **2008**, *46* (2), 525–539. <https://doi.org/10.3749/canmin.46.2.525>.
- (21) Syneček, V.; Hybler, J. The Crystal Structure of Krupkaite,  $\text{CuPbBi}_3\text{S}_6$ , and of

- Gladite,  $\text{CuPbBi}_5\text{S}_9$ , and the Classification of Superstructures in the Bismuthinite–Aikinite Group. *Neues Jahrb. Miner. Monatsh.* **1974**, 541–560.
- (22) Makovicky Dan; Balić-Žunić, Tonči, E. T. The crystal structure of Paarite, the newly discovered 56 Å derivative of the bismuthinite-aikinite solid-solution series *Can. Mineral.* **2001**, 39 (5), 1377–1382. <https://doi.org/10.2113/gscanmin.39.5.1377>.
- (23) Kohatsu B. J., I. W. The Crystal Structure of Gladite,  $\text{PbCuBi}_5\text{S}_9$ , a Superstructure Intermediate in the Series  $\text{Bi}_2\text{S}_3$ – $\text{PbCuBi}_3$  (Bismuthinite–Aikinite). *Acta Crystallogr. Sect. B Struct. Crystallogr. Cryst. Chem.* **1976**, 32 (8), 2401–2409. <https://doi.org/10.1107/s0567740876007851>.
- (24) Tan Shiqiang; Zhao, Jing; Wolverton, Chris; Kanatzidis, Mercouri G., G. H. High Thermoelectric Performance in Electron-Doped  $\text{AgBi}_3\text{S}_5$  with Ultralow Thermal Conductivity. *J. Am. Chem. Soc.* **2017**, 139 (18), 6467–6473. <https://doi.org/10.1021/jacs.7b02399>.
- (25) Labégorre Agathe; Bourhim, Abdelhamid; Willeman, Héloïse; Barbier, Tristan; Appert, Florian; Juraszek, Jean; Malaman, Bernard; Huguenot, Arthur; Gautier, Régis; Nassif, Vivian; Lemoine, Pierrick; Prestipino, Carmelo; Elkaim, Erik; Pautrot-d’Alençon, Lauri, J.-B. V.  $\text{XBi}_4\text{S}_7$  ( $X = \text{Mn}, \text{Fe}$ ): New Cost-Efficient Layered N-Type Thermoelectric Sulfides with Ultralow Thermal Conductivity. *Adv. Funct. Mater.* **2019**, 29 (48), 1904112-NA. <https://doi.org/10.1002/adfm.201904112>.
- (26) Biswas, K.; Zhao, L. D.; Kanatzidis, M. G. Tellurium-Free Thermoelectric: The Anisotropic  $n$ -Type Semiconductor  $\text{Bi}_2\text{S}_3$ . *Adv. Energy Mater.* **2012**, 2 (6), 634–638. <https://doi.org/10.1002/aenm.201100775>.
- (27) Bourgès Yohan; Supka, Andrew; Orabi, Rabih Al Rahal Al; Lemoine, Pierrick; Lebedev, Oleg I.; Ohta, Michihiro; Suekuni, Koichiro; Nassif, Vivian; Hardy, Vincent; Daou, Ramzy; Miyazaki, Yuzuru; Fornari, Marco; Guilmeau, Emmanuel, C. B. High-Performance Thermoelectric Bulk Colusite by Process Controlled Structural Disordering. *J. Am. Chem. Soc.* **2018**, 140 (6), 2186–2195. <https://doi.org/10.1021/jacs.7b11224>.
- (28) Bourgès Pierrick; Lebedev, Oleg I.; Daou, Ramzy; Hardy, Vincent; Malaman,

- Bernard; Guilmeau, Emmanuel, C. L. Low Thermal Conductivity in Ternary  $\text{Cu}_4\text{Sn}_7\text{S}_{16}$  Compound. *Acta Mater.* **2015**, *97*, 180–190. <https://doi.org/10.1016/j.actamat.2015.06.046>.
- (29) Liang Jun; Zhou, Yunxuan; Wang, Zi-Yuan; Feng, Jing; Ge, Zhen-Hua, H. G.  $\text{CuPbBi}_5\text{S}_9$  Thermoelectric Material with an Intrinsic Low Thermal Conductivity: Synthesis and Properties. *J. Mater.* **2022**, *8* (1), 174–183. <https://doi.org/10.1016/j.jmat.2021.03.016>.
- (30) Labégorre, J. B.; Virfeu, A.; Bourhim, A.; Willeman, H.; Barbier, T.; Appert, F.; Juraszek, J.; Malaman, B.; Huguenot, A.; Gautier, R.; Nassif, V.; Lemoine, P.; Prestipino, C.; Elkaim, E.; Pautrot-d'Alençon, L.; Le Mercier, T.; Maignan, A.; Al Rahal Al Orabi, R.; Guilmeau, E.  $\text{XBi}_4\text{S}_7$  (X = Mn, Fe): New Cost-Efficient Layered *n*-Type Thermoelectric Sulfides with Ultralow Thermal Conductivity. *Adv. Funct. Mater.* **2019**, *29* (48). <https://doi.org/10.1002/adfm.201904112>.
- (31) Biswas, K.; Zhao, L. D.; Kanatzidis, M. G. Tellurium-Free Thermoelectric: The Anisotropic *n*-Type Semiconductor  $\text{Bi}_2\text{S}_3$ . *Adv. Energy Mater.* **2012**, *2* (6), 634–638. <https://doi.org/10.1002/aenm.201100775>.
- (32) Tan, G.; Hao, S.; Zhao, J.; Wolverton, C.; Kanatzidis, M. G. High Thermoelectric Performance in Electron-Doped  $\text{AgBi}_3\text{S}_5$  with Ultralow Thermal Conductivity. *J. Am. Chem. Soc.* **2017**, *139* (18), 6467–6473. <https://doi.org/10.1021/jacs.7b02399>.
- (33) Carnevali, V.; Mukherjee, S.; Voneshen, D. J.; Maji, K.; Guilmeau, E.; Powell, A. V.; Vaqueiro, P.; Fornari, M. Lone Pair Rotation and Bond Heterogeneity Leading to Ultralow Thermal Conductivity in Aikinite. *J. Am. Chem. Soc.* **2023**, *145* (16), 9313–9325. <https://doi.org/10.1021/jacs.3c02536>.
- (34) Dutta Shidaling; Prasad, Matukumilli V. D.; Pandey, Juhi; Warankar, Avinash; Mandal, Pankaj; Soni, Ajay; Waghmare, Umesh V.; Biswas, Kanishka, M. M. Ultralow Thermal Conductivity in Chain Like  $\text{TlSe}$  Due to Inherent  $\text{Tl}^+$  Rattling. *J. Am. Chem. Soc.* **2019**, *141* (51), 20293–20299. <https://doi.org/10.1021/jacs.9b10551>.
- (35) Misra Céline; Crivello, Jean-Claude; Giordano, Valentina M.; Castellan, John-Paul; Sidis, Yvan; Levinský, Petr; Hejtmánek, Jiří; Malaman, Bernard; Dauscher,

- Anne; Lenoir, Bertrand; Candolfi, Christophe; Pailhès, Stéphane, S. B. Reduced Phase Space of Heat-Carrying Acoustic Phonons in Single-Crystalline InTe. *Phys. Rev. Res.* **2020**, *2* (4), 043371-NA. <https://doi.org/10.1103/physrevresearch.2.043371>.
- (36) Zhang Nikolaj; Tolborg, Kasper; Takahashi, Seiya; Song, Lirong; Bondesgaard, Martin; Nishibori, Eiji; Iversen, Bo B., J. R. Direct Observation of One-Dimensional Disordered Diffusion Channel in a Chain-like Thermoelectric with Ultralow Thermal Conductivity. *Nat. Commun.* **2021**, *12* (1), 6709. <https://doi.org/10.1038/s41467-021-27007-y>.
- (37) Pal Yi; Wolverton, Chris, K. X. Microscopic Mechanism of Unusual Lattice Thermal Transport in TlInTe<sub>2</sub>. *npj Comput. Mater.* **2021**, *7* (1), 1–8. <https://doi.org/10.1038/s41524-020-00474-5>.
- (38) Jana Koushik; Warankar, Avinash; Mandal, Pankaj; Waghmare, Umesh V.; Biswas, Kanishka, M. K. . P. Intrinsic Rattler-Induced Low Thermal Conductivity in Zintl Type TlInTe<sub>2</sub>. *J. Am. Chem. Soc.* **2017**, *139* (12), 4350–4353. <https://doi.org/10.1021/jacs.7b01434>.
- (39) Lin Jiangang; Su, Xianli; Zhang, Xiaomi; Xia, Yi; Bailey, Trevor P.; Stoumpos, Constantinos C.; Tan, Ganjian; Rettie, Alexander J. E.; Chung, Duck Young; Dravid, Vinayak P.; Uher, Ctirad; Wolverton, Chris; Kanatzidis, Mercouri G., W. H. Ultralow Thermal Conductivity, Multiband Electronic Structure and High Thermoelectric Figure of Merit in TlCuSe. *Adv. Mater.* **2021**, *33* (44), 2104908-NA. <https://doi.org/10.1002/adma.202104908>.
- (40) Mukhopadhyay David S.; Sales, Brian C.; Puzos, Alexander A.; McGuire, Michael A.; Lindsay, Lucas, S. P. Two-Channel Model for Ultralow Thermal Conductivity of Crystalline Tl<sub>3</sub>VSe<sub>4</sub>. *Science* **2018**, *360* (6396), 1455–1458. <https://doi.org/10.1126/science.aar8072>.
- (41) Suekuni Hiromi I.; Kim, Fiseong S.; Umeo, Kazunori; Takabatake, Toshiro, K. T. Glasslike versus Crystalline Thermophysical Properties of the Cu-S Based Minerals: Tetrahedrite and Colusite. *J. Phys. Soc. Japan* **2015**, *84* (10), 103601-NA. <https://doi.org/10.7566/jpsj.84.103601>.
- (42) Lara-Curzio Andrew F.; Delaire, Olivier; McGuire, Michael A.; Lu, Xu; Liu,

- Cheng Yun; Case, Eldon D.; Morelli, Donald T., E. M. Low-Temperature Heat Capacity and Localized Vibrational Modes in Natural and Synthetic Tetrahedrites. *J. Appl. Phys.* **2014**, *115* (19), 193515. <https://doi.org/10.1063/1.4878676>.
- (43) Candolfi, C.; Guélou, G.; Bourgès, C.; Supka, A. R.; Al Rahal Al Orabi, R.; Fornari, M.; Malaman, B.; Le Caër, G.; Lemoine, P.; Hardy, V.; Zanotti, J. M.; Chetty, R.; Ohta, M.; Suekuni, K.; Guilmeau, E. Disorder-Driven Glasslike Thermal Conductivity in Colusite  $\text{Cu}_{26}\text{V}_2\text{Sn}_6\text{S}_{32}$  Investigated by Mössbauer Spectroscopy and Inelastic Neutron Scattering Christophe. *Phys. Rev. Mater.* **2020**, *4* (2), 25404–25413. <https://doi.org/10.1103/PhysRevMaterials.4.025404>.
- (44) Mutka Michael Marek; Johnson, Mark R.; Hiroi, Zenji; Yamaura, Jun-ichi; Nagao, Yohei, H. K. Generalized Density-of-States and Anharmonicity of the Low-Energy Phonon Bands from Coherent Inelastic Neutron Scattering Response in the Pyrochlore Osmates  $\text{AOs}_2\text{O}_6$  ( $A = \text{K}, \text{Rb}, \text{Cs}$ ). *Phys. Rev. B* **2008**, *78* (10), 104307. <https://doi.org/10.1103/physrevb.78.104307>.
- (45) Koza Hannu; Okamoto, Yoshihiko; Yamaura, Jun-ichi; Hiroi, Zenji, M. M. M. On the Microscopic Dynamics of the ‘Einstein Solids’  $\text{AlV}_2\text{Al}_{20}$  and  $\text{GaV}_2\text{Al}_{20}$ , and of  $\text{YV}_2\text{Al}_{20}$ : A Benchmark System for ‘Rattling’ Excitations. *Phys. Chem. Chem. Phys.* **2015**, *17* (38), 24837–24850. <https://doi.org/10.1039/c5cp04005a>.
- (46) Cahill, D. G.; Watson, S. K.; Pohl, R. O. Lower Limit to the Thermal Conductivity of Disordered Crystals. *Phys. Rev.* **1992**, *46* (10), 6131–6140.
- (47) Guilmeau Yohann; Maignan, A., E. B. Transport and Thermoelectric Properties in Copper Intercalated  $\text{TiS}_2$  Chalcogenide. *Appl. Phys. Lett.* **2011**, *99* (5), 052107-NA. <https://doi.org/10.1063/1.3621834>.
- (48) Zhao Jiaqing; Wu, Chun I.; Hogan, Timothy P.; Zhou, Xiaoyuan; Uher, Ctirad; Dravid, Vinayak P.; Kanatzidis, Mercouri G., L.-D. H. Thermoelectrics with Earth Abundant Elements: High Performance  $p$ -Type PbS Nanostructured with SrS and CaS. *J. Am. Chem. Soc.* **2012**, *134* (18), 7902–7912. <https://doi.org/10.1021/ja301772w>.
- (49) Guin, S. N.; Biswas, K. Cation Disorder and Bond Anharmonicity Optimize the Thermoelectric Properties in Kinetically Stabilized Rocksalt  $\text{AgBiS}_2$

- Nanocrystals. *Chem. Mater.* **2013**, *25* (15), 3225–3231. <https://doi.org/10.1021/cm401630d>.
- (50) Bhui, A.; Dutta, M.; Mukherjee, M.; Rana, K. S.; Singh, A. K.; Soni, A.; Biswas, K. Ultralow Thermal Conductivity in Earth-Abundant  $\text{Cu}_{1.6}\text{Bi}_{4.8}\text{S}_8$ : Anharmonic Rattling of Interstitial Cu. *Chem. Mater.* **2021**, *33* (8), 2993–3001. <https://doi.org/10.1021/acs.chemmater.1c00659>.
- (51) Suekuni, K.; Tanaka, H. I.; Kim, F. S.; Umeo, K.; Takabatake, T. Glasslike versus Crystalline Thermophysical Properties of the Cu-S Based Minerals: Tetrahedrite and Colusite. *J. Phys. Soc. Japan* **2015**, *84* (10), 103601–103604. <https://doi.org/10.7566/JPSJ.84.103601>.
- (52) Lara-Curzio, E.; May, A. F.; Delaire, O.; McGuire, M. A.; Lu, X.; Liu, C. Y.; Case, E. D.; Morelli, D. T. Low-Temperature Heat Capacity and Localized Vibrational Modes in Natural and Synthetic Tetrahedrites. *J. Appl. Phys.* **2014**, *115* (19), 193515–193521. <https://doi.org/10.1063/1.4878676>.
- (53) Koza, M. M.; Mutka, H.; Okamoto, Y.; Yamaura, J. I.; Hiroi, Z. On the Microscopic Dynamics of the “Einstein Solids”  $\text{AlV}_2\text{Al}_{20}$  and  $\text{GaV}_2\text{Al}_{20}$ , and of  $\text{YV}_2\text{Al}_{20}$ : A Benchmark System for “Rattling” Excitations. *Phys. Chem. Chem. Phys.* **2015**, *17* (38), 24837–24850. <https://doi.org/10.1039/c5cp04005a>.
- (54) Avila Koichiro; Umeo, Kazunori; Fukuoka, Hiroshi; Yamanaka, Shoji; Takabatake, Toshiro, M. A. . S. Glasslike versus Crystalline Thermal Conductivity in Carrier-Tuned  $\text{Ba}_8\text{Ga}_{16}\text{X}_{30}$  Clathrates ( $X=\text{Ge},\text{Sn}$ ). *Phys. Rev. B* **2006**, *74* (12), 125109-NA. <https://doi.org/10.1103/physrevb.74.125109>.
- (55) Koza Andreas; Rosner, Helge; Schnelle, Walter; Mutka, Hannu; Johnson, Mark R.; Krisch, Michael; Capogna, Lucia; Grin, Yuri, M. M. . L.-J. Vibrational Dynamics of the Filled Skutterudites  $M_{1-x}\text{Fe}_4\text{Sb}_{12}$  ( $M=\text{Ca}, \text{Sr}, \text{Ba}, \text{and Yb}$ ): Temperature Response, Dispersion Relation, and Material Properties. *Phys. Rev. B* **2011**, *84* (1), 14306–14312. <https://doi.org/10.1103/physrevb.84.014306>.
- (56) Troć, R.; Wawryk, R.; Gajek, Z.; Pasturel, M.; Samsel-Czekała, M. Comparative Studies of the Cage Systems  $\text{ThFe}_2\text{Al}_{10}$  and  $\text{UFe}_2\text{Al}_{10}$ . *J. Alloys Compd.* **2017**, *727*, 1302–1313. <https://doi.org/10.1016/j.jallcom.2017.08.225>.
- (57) Morelli Vladimir; Heremans, Joseph P., D. T. . J. Intrinsically Minimal Thermal

- Conductivity in Cubic I-V-VI<sub>2</sub> Semiconductors. *Phys. Rev. Lett.* **2008**, *101* (3), 35901. <https://doi.org/10.1103/physrevlett.101.035901>.
- (58) Liu Dongyang; Wu, Haijun; Wang, Jinfeng; Zhang, Yang; Wang, Guangtao; Pennycook, Stephen J.; Zhao, Li-Dong, X. W. Intrinsically Low Thermal Conductivity in BiSbSe<sub>3</sub>: A Promising Thermoelectric Material with Multiple Conduction Bands. *Adv. Funct. Mater.* **2018**, *29* (3), 1806558. <https://doi.org/10.1002/adfm.201806558>.
- (59) Xiao, Y.; Chang, C.; Pei, Y.; Wu, D.; Peng, K.; Zhou, X.; Gong, S.; He, J.; Zhang, Y.; Zeng, Z.; Zhao, L. D. Origin of Low Thermal Conductivity in SnSe. *Phys. Rev. B* **2016**, *94* (12), 125203. <https://doi.org/10.1103/PhysRevB.94.125203>.
- (60) Gao Meng; Cheng, Yan; Ji, Guang-Fu, X. Z. First-Principles Study of Structural, Elastic, Electronic and Thermodynamic Properties of Topological Insulator Bi<sub>2</sub>Se<sub>3</sub> under Pressure. *Philos. Mag.* **2016**, *96* (2), 208–222. <https://doi.org/10.1080/14786435.2015.1128126>.
- (61) Mumme, W. G. The Crystal Structure of Krupkaite, CuPbBi<sub>3</sub>S<sub>6</sub>, from the Juno Mine at - Tennant Creek, Northern Territory, Australia. *Am. Mineral.* **1975**, *60* (3–4), 300–308.
- (62) Chasmar R., R. P. . S. The Thermoelectric Figure of Merit and Its Relation to Thermoelectric Generators. *J. Electron. Control* **1959**, *7* (1), 52–72. <https://doi.org/10.1080/00207215908937186>.
- (63) Mahan, G. D.; Sofot, J. The Best Thermoelectric. *Proc. Natl. Acad. Sci. United States Am.* **1996**, *93*, 7436–7439.
- (64) Wang Yanzhong; LaLonde, Aaron D.; Snyder, G. Jeffery, H. P. Material Design Considerations Based on Thermoelectric Quality Factor. In *Thermoelectric Nanomaterials*; 2013, 3–32. [https://doi.org/10.1007/978-3-642-37537-8\\_1](https://doi.org/10.1007/978-3-642-37537-8_1).
- (65) Zhang, X.; Bu, Z.; Shi, X.; Chen, Z.; Lin, S.; Shan, B.; Wood, M.; Snyder, A. H.; Chen, L.; Snyder, G. J.; Pei, Y. Electronic Quality Factor for Thermoelectrics. *Sci. Adv.* **2020**, *6*, 6–11.
- (66) Hong Wangyu; Wang, Yuan; Zou, Jin; Chen, Zhigang, M. L. Establishing the Golden Range of Seebeck Coefficient for Maximizing Thermoelectric

- Performance. *J. Am. Chem. Soc.* **2020**, *142* (5), 2672–2681. <https://doi.org/10.1021/jacs.9b13272>.
- (67) Xi, M.; Zhu, H.; Wu, H.; Yang, Y.; Yan, Y.; Wang, G.; Wang, G.; Li, J. Y.; Lu, X.; Zhou, X. Thermoelectricity of *n*-Type  $\text{MnBi}_4\text{S}_{7-7x}\text{Se}_{7x}$  Solid Solution. *Chem. Eng. J.* **2020**, *396*, 125219. <https://doi.org/10.1016/j.cej.2020.125219>.
- (68) Cai, F.; Dong, R.; Sun, W.; Lei, X.; Yu, B.; Chen, J.; Yuan, L.; Wang, C.; Zhang, Q.  $\text{Pb}_m\text{Bi}_2\text{S}_{3+m}$  Homologous Series with Low Thermal Conductivity Prepared by the Solution-Based Method as Promising Thermoelectric Materials. *Chem. Mater.* **2021**, *33* (15), 6003–6011. <https://doi.org/10.1021/acs.chemmater.1c01387>.
- (69) Ahn, J. Y.; Hwang, J. Y.; Ryu, B. K.; Oh, M. W.; Lee, K. H.; Kim, S. W. Importance of Crystal Chemistry with Interstitial Site Determining Thermoelectric Transport Properties in Pavonite Homologue Cu-Bi-S Compounds. *CrystEngComm* **2016**, *18* (8), 1453–1461. <https://doi.org/10.1039/c5ce02143j>.
- (70) Li Yiming; Hao, Shiqiang; Zhang, Tianyan; Wolverton, Chris; Zhao, Jing; Zhao, Li-Dong, J. Z. Thermoelectric Material  $\text{SnPb}_2\text{Bi}_2\text{S}_6$ : The 4,4L Member of Lillianite Homologous Series with Low Lattice Thermal Conductivity. *Inorg. Chem.* **2018**, *58* (2), 1339–1348. <https://doi.org/10.1021/acs.inorgchem.8b02899>.
- (71) Zhao, J.; Hao, S.; Islam, S. M.; Chen, H.; Tan, G.; Ma, S.; Wolverton, C.; Kanatzidis, M. G. Six Quaternary Chalcogenides of the Pavonite Homologous Series with Ultralow Lattice Thermal Conductivity. *Chem. Mater.* **2019**, *31* (9), 3430–3439. <https://doi.org/10.1021/acs.chemmater.9b00585>.



## Chapter 3

---

# Transport properties in the $\text{Cu}_{1-x}\square_x\text{Pb}_{1-x}\text{Bi}_{1+x}\text{S}_3$ series

---



### 3.1. Introduction

In the previous chapter, a Cu-deficient aikinite-type sulfide has been synthesized with the composition  $\text{CuPbBi}_5\text{S}_9$  by combining mechanical alloying and SPS techniques. The crystal structure is closely related to that of gladite, reported by Liang *et al.*<sup>1</sup>, but differs by the random distribution of copper and vacancies on the copper site. In contrast to previous reports, our sample is highly pure, allowing for a detailed investigation of its transport properties. This disordered  $\text{CuPbBi}_5\text{S}_9$  phase shows exceptionally low thermal conductivity ( $0.6 \text{ W m}^{-1} \text{ K}^{-1}$  at 300 K) approaching to intrinsic semiconducting behavior with a very low carrier concentration ( $4.5 \times 10^{12} \text{ cm}^{-3}$  at 300 K) and high Seebeck coefficient ( $1370 \mu\text{V K}^{-1}$  at 400 K). The interstitial Cu ions and stereochemically active lone pairs on Pb play a crucial role in lowering the lattice thermal conductivity in this series of compounds, reported by Balijapelly *et al.*<sup>2</sup> In addition to bond heterogeneity, a temperature-dependent interaction between  $\text{Cu}^+$  and the rotating  $\text{Pb}^{2+}$  lone pair is a key contributor to the scattering effects that lower the thermal conductivity in aikinite  $\text{CuPbBiS}_3$  reported by Carnevali *et al.*<sup>3</sup> To increase the carrier concentration, multiple attempts were investigated through chemical doping, such as introducing chlorine (Cl) and bismuth (Bi) in the sulfur (S) and lead (Pb) sites, respectively. Another interesting approach to lower the electrical resistivity and achieve a high  $ZT$  value would be to change the composition of  $\text{Cu}_{1-x}\square_x\text{Pb}_{1-x}\text{Bi}_{1+x}\text{S}_3$  by increasing the number of vacancies ( $x$ ), and by compensation to reduce the content of Pb in Bi sites.

In this chapter, we report the efficient and viable synthesis of Cu-deficient aikinite-type compounds with the chemical formula  $\text{Cu}_{1-x}\square_x\text{Pb}_{1-x}\text{Bi}_{1+x}\text{S}_3$  (where  $x = 0, 0.17, 0.33, 0.4, 0.5, 0.6, 0.83, \text{ and } 1$ ) using mechanical alloying followed by spark plasma sintering. Except for the sample with  $x = 0$ , all the other compounds were highly pure, as confirmed by powder X-ray diffraction, scanning electron microscopy, and transmission electron microscopy analyses. Rietveld refinement revealed that the samples with  $x = 0.17, 0.33, 0.4, 0.5, 0.6, \text{ and } 0.83$  did not exhibit the ordered gladite mineral structure, but instead formed a copper-deficient disordered aikinite structure,

with random distribution of Pb and Bi similar to  $x = 0.67$  presented in the previous chapter. We investigate the influence of the structures on the electrical and thermal properties in this series of compounds.

## 3.2. Methods

### 3.2.1. Reagents.

High-purity copper powder (Cu, Alfa Aesar, >99.99%), lead needles (Pb, Alfa Aesar, 99.99%), bismuth powder (Bi, Alfa Aesar, >99.5%), sulfur powder (S, Alfa Aesar, >99.99%), were used as precursors without further purification.

### 3.2.2. Synthesis.

The samples were synthesized using a two-step process - mechanical alloying and spark plasma sintering (SPS). Mechanical alloying involved high-energy ball milling of stoichiometric amounts of Cu, Pb, Bi, and S powders (total 6 g) for 6 hrs under an argon atmosphere. This was done using a fritsch pulverisette seven premium line planetary ball mill operating at room temperature (600 rpm, powder to ball ratio of around 1:18). The resulting material showed broad diffraction peaks corresponding to the main phase of disordered aikinite along with minor PbS phase, indicating low crystallinity or the presence of small particle sizes (**Figure 3.1a**). This could be due to the synthesis process which was previously explained in chapter 2. After subjecting the material to spark plasma sintering (SPS), the samples become pure as the peaks correspond to PbS are not observed. Addition to that the X-ray powder diffraction (XRPD) peaks become indicating the crystallization process during the SPS process (**Figure 3.1b**).

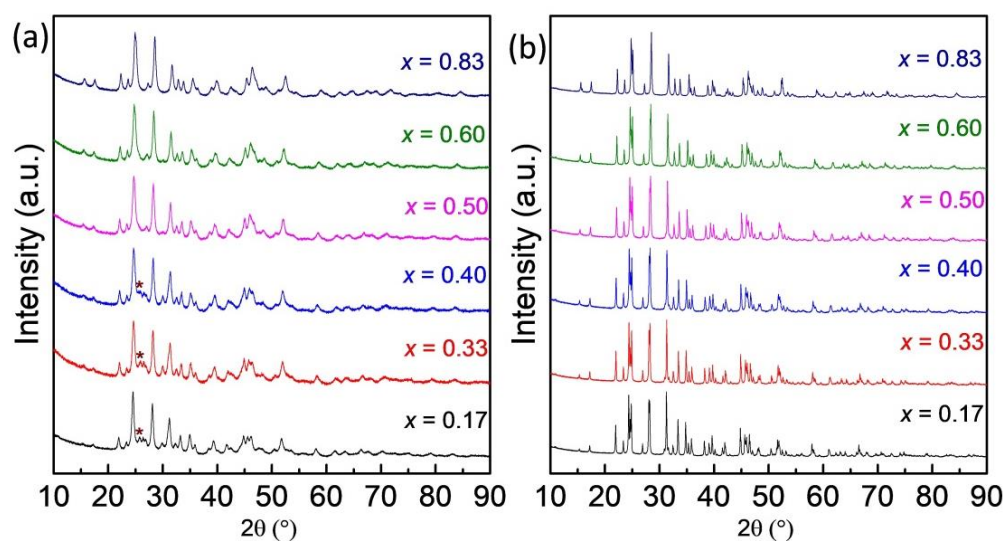


**Figure 3.1.** XRPD patterns of (a) 6 hrs ball milled samples and (b) SPS samples.

### 3.3. Results and discussion

#### 3.3.1. Crystal structure

A large number of structurally related minerals have been discussed in the previous chapter, *i.e.* from aikinite ( $\text{CuPbBiS}_3$ ) to bismuthinite ( $\text{Bi}_2\text{S}_3$ ) with space group  $Pnma$ . These phases can be expressed as  $\text{Cu}_{1-x}\square_x\text{Pb}_{1-x}\text{Bi}_{1+x}\text{S}_3$ , where  $\square$  represents vacancies on the cationic sublattice of aikinite  $\text{CuPbBiS}_3$ . They crystallize either in the space group  $Pnma$  with approximate lattice parameters of  $a \approx a_a$ ,  $b \approx b_a$ , and  $c \approx n \times c_a$  or in the space group  $Pmc21$  with approximate lattice parameters of  $a \approx b_a$ ,  $b \approx n \times c_a$ , and  $c \approx a_a$ , where  $n$  is a positive integer. **Table 3.1** in chapter 2 summarizes the structural information of the ordered Cu–Pb–Bi–S phases derived from the aikinite–bismuthinite series,  $(\text{Cu}_{1-x}\square_x)\text{Pb}_{1-x}\text{Bi}_{1+x}\text{S}_3$  series. Besides the fully ordered  $(\text{Cu}_{1-x}\square_x)\text{Pb}_{1-x}\text{Bi}_{1+x}\text{S}_3$  phases, there have been reports of other phases with mixed occupancy of crystallographic sites and/or partial site occupancy. Examples include emilite  $\text{Cu}_{10.7}\text{Pb}_{10.7}\text{Bi}_{21.3}\text{S}_{48}$  ( $x = 0.33$ ,  $Pmc21$ ,  $n = 4$ ),<sup>4</sup>  $\text{Cu}_{1.63}\text{Pb}_{1.63}\text{Bi}_{6.37}\text{S}_{12}$  ( $x = 0.60$ ,  $Pnma$ ,  $n = 3$ ),<sup>5</sup> and  $\text{Cu}_{1.435}\text{Pb}_{1.5}\text{Bi}_{6.5}\text{S}_{12}$  ( $x = 0.60$ ,  $Pmc21$ ,  $n = 4$ ).<sup>6</sup> These phases exhibit superstructure diffraction peaks on the powder diffraction patterns and superstructure spots in selected area electron diffraction

(SAED) patterns due to the long-range ordering of cations and vacancies. When there is a random distribution between Pb and Bi, as well as Cu and vacancies, the crystal structure can be described as disordered. In such cases, XRPD show only minor changes in peak intensities associated with the aikinite structure. Since  $\text{Pb}^{2+}$  and  $\text{Bi}^{3+}$  cations are isoelectronic, distinguishing between these phases becomes difficult based solely on X-ray diffraction analysis. Accurate identification of these phases remains challenging, even with high-quality powder diffraction patterns.

The crystal structure evolution within the aikinite series,  $\text{Cu}_{1-x}\square_x\text{Pb}_{1-x}\text{Bi}_{1+x}\text{S}_3$ , from aikinite ( $\text{CuPbBiS}_3$ ) to bismuthanite ( $\text{Bi}_2\text{S}_3$ ), was described intricately in our previous chapter taking into account the disorder caused by the random presence of Cu and vacancies in the crystal lattice. Aikinite ( $\text{CuPbBiS}_3$ ,  $x = 0$ ), which serves as the starting point of the series, is represented by the crystal structure shown in **Figure 3.2**. In this structure, the Cu position is fully occupied by Cu atom. The coordination of Cu is tetrahedral which further connects to the  $\text{Bi}_2\text{S}_3$  chain, forming a complex 3D crystal structure. As we move along the aikinite series by increasing the value of  $x$  in  $\text{Cu}_{1-x}\square_x\text{Pb}_{1-x}\text{Bi}_{1+x}\text{S}_3$ , the proportion of vacant Cu positions gradually increases. This progression can be observed in **Figure 3.2**, which represents different compositions within the series. When  $x = 0.5$ , corresponding to  $\text{CuPbBi}_2\text{S}_6$ , 50% of the Cu positions are vacant. In addition to this, the amount of Pb in the materials decrease as the value of  $x$  rises, this leads to a reduction in the point defects that are caused by the presence of Pb atoms on the Bi site.

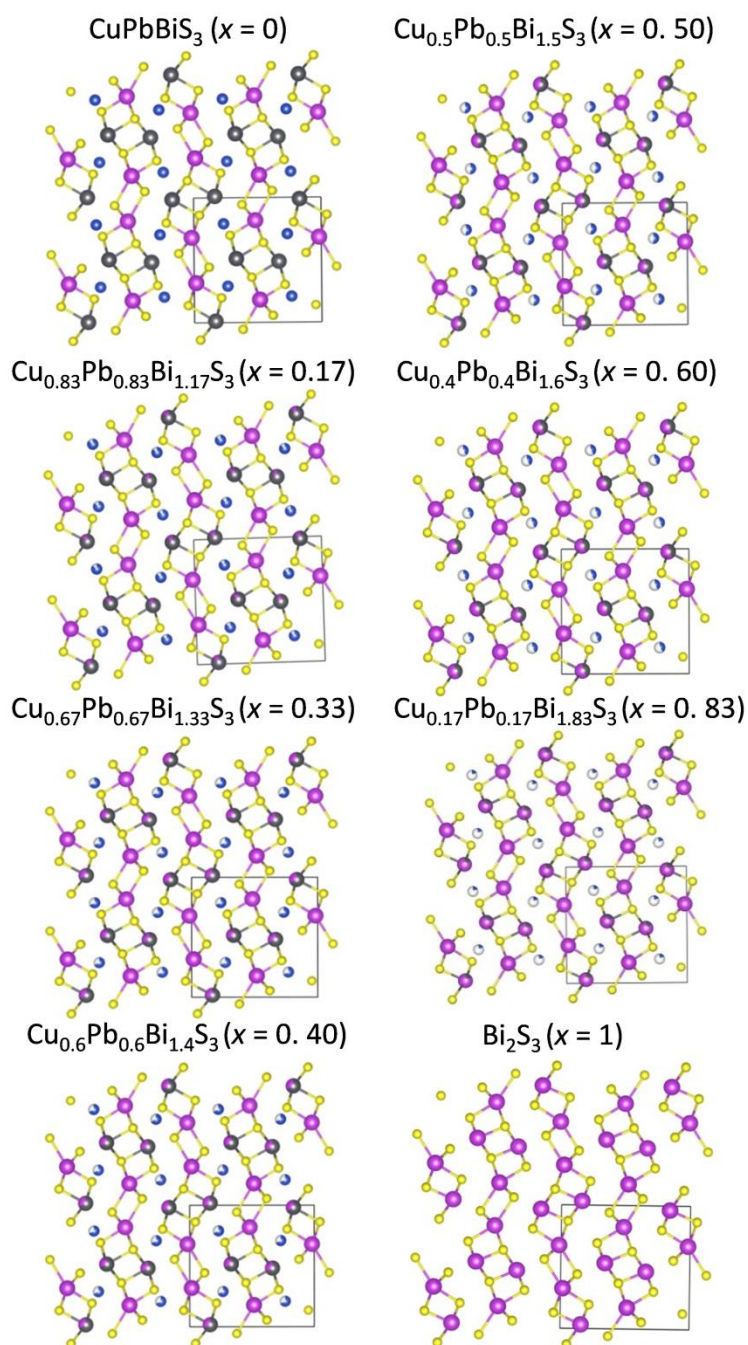


**Figure 3.2.** Crystal structure of  $\text{CuPbBiS}_3 (x = 0)$ ,  $\text{Cu}_{0.83}\text{Pb}_{0.83}\text{Bi}_{1.17}\text{S}_3 (x = 0.17)$ ,  $\text{Cu}_{0.67}\text{Pb}_{0.67}\text{Bi}_{1.33}\text{S}_3 (x = 0.33)$ ,  $\text{Cu}_{0.6}\text{Pb}_{0.6}\text{Bi}_{1.4}\text{S}_3 (x = 0.40)$ ,  $\text{Cu}_{0.5}\text{Pb}_{0.5}\text{Bi}_{1.5}\text{S}_3 (x = 0.50)$ ,  $\text{Cu}_{0.4}\text{Pb}_{0.4}\text{Bi}_{1.6}\text{S}_3 (x = 0.60)$ ,  $\text{Cu}_{0.17}\text{Pb}_{0.17}\text{Bi}_{1.83}\text{S}_3 (x = 0.83)$  and  $\text{Bi}_2\text{S}_3 (x = 1)$  after Rietveld refinement. Cu, Pb, Bi and S atom presented in blue, black, pink and yellow color respectively.

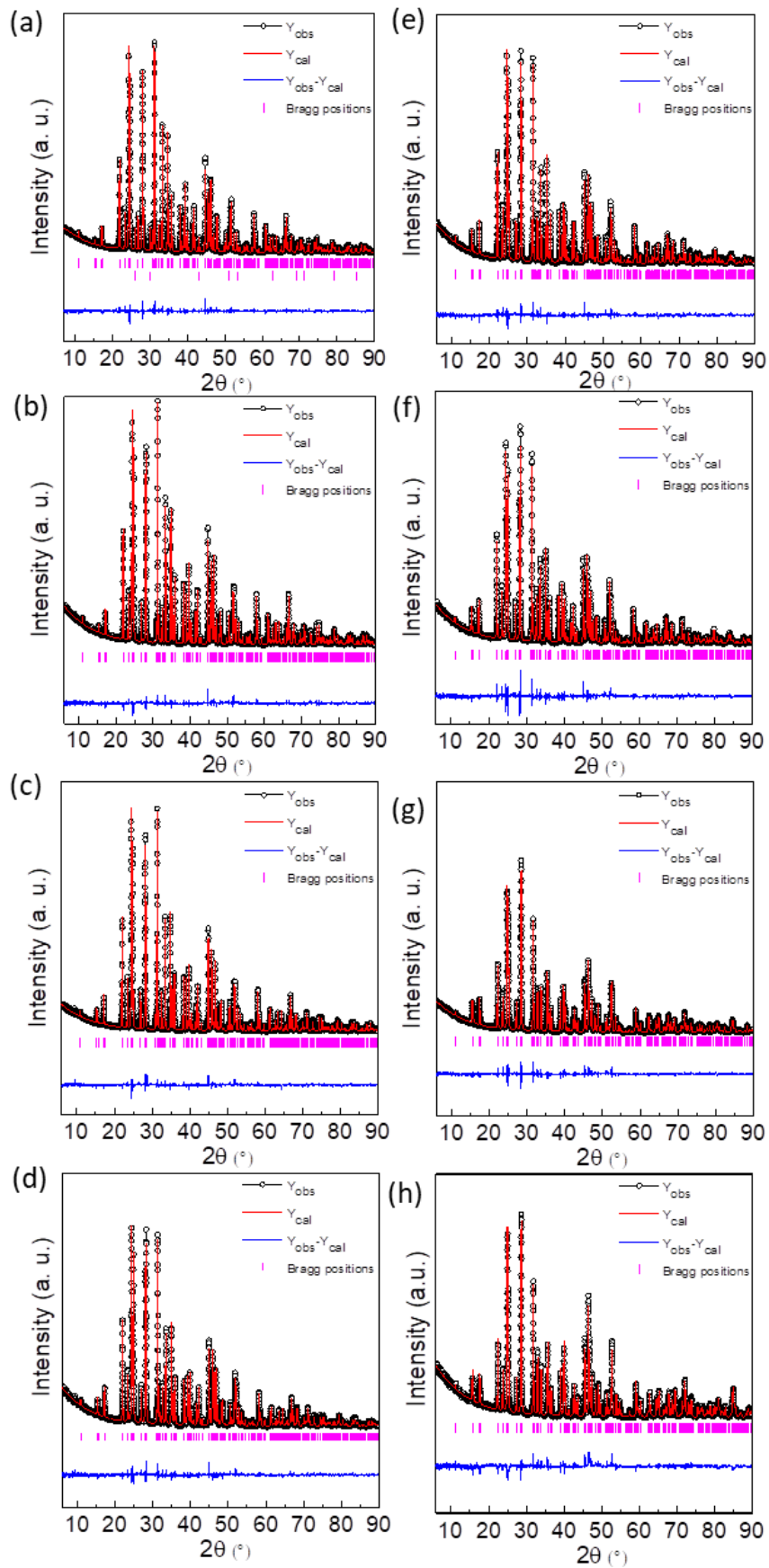


**Figure 3.3.** -Rietveld refinement of the XRPD data recorded at room temperature (RT) for (a)  $\text{CuPbBiS}_3$  ( $x = 0$ ), (b)  $\text{Cu}_{0.83}\text{Pb}_{0.83}\text{Bi}_{1.17}\text{S}_3$  ( $x = 0.17$ ), (c)  $\text{Cu}_{0.67}\text{Pb}_{0.67}\text{Bi}_{1.33}\text{S}_3$  ( $x = 0.33$ ), (d)  $\text{Cu}_{0.6}\text{Pb}_{0.6}\text{Bi}_{1.4}\text{S}_3$  ( $x = 0.40$ ), (e)  $\text{Cu}_{0.5}\text{Pb}_{0.5}\text{Bi}_{1.5}\text{S}_3$  ( $x = 0.50$ ), (f)  $\text{Cu}_{0.4}\text{Pb}_{0.4}\text{Bi}_{1.6}\text{S}_3$  ( $x = 0.60$ ), (g)  $\text{Cu}_{0.17}\text{Pb}_{0.17}\text{Bi}_{1.83}\text{S}_3$  ( $x = 0.83$ ) and (h)  $\text{Bi}_2\text{S}_3$  ( $x = 1$ ) ( $\lambda = 1.5406 \text{ \AA}$ ). The experimental data are plotted as black line and symbols, the calculated pattern as red line and the difference between them as lower blue line. The Bragg positions are plotted as vertical purple ticks.

**Table 3.1.** Refined unit cell parameters and reliability factors of  $\text{Cu}_{1-x}\square_x\text{Pb}_{1-x}\text{Bi}_{1+x}\text{S}_3$  ( $x = 0$  to 1) samples from the Rietveld analysis of the room temperature XRPD data.

| $x$<br>value           | $x = 0$     | $x = 0.17$  | $x = 0.33$  | $x = 0.40$  | $x = 0.5$   | $x = 0.6$   | $x = 0.83$  | $x = 1$     |
|------------------------|-------------|-------------|-------------|-------------|-------------|-------------|-------------|-------------|
| Space group            | <i>Pnma</i> |
| $a$ ( $\text{\AA}$ )   | 11.6018(1)  | 11.5851(1)  | 11.5500(2)  | 11.5251(2)  | 11.4926(3)  | 11.4575(2)  | 11.3614(3)  | 11.2897(1)  |
| $b$ ( $\text{\AA}$ )   | 4.0448(1)   | 4.0426(1)   | 4.0347(1)   | 4.0311(1)   | 4.0233(1)   | 4.0168(1)   | 3.9977(1)   | 3.9825 (1)  |
| $c$ ( $\text{\AA}$ )   | 11.3710(1)  | 11.3182(1)  | 11.2693(2)  | 11.2565(3)  | 11.2339(2)  | 11.2190(2)  | 11.1853(3)  | 11.1447(1)  |
| $V$ ( $\text{\AA}^3$ ) | 533.61(1)   | 530.08(1)   | 525.17(2)   | 522.97(2)   | 519.44(2)   | 516.34(2)   | 508.04(2)   | 501.08(1)   |
| $R_{\text{Bragg}}$     | 2.78        | 4.65        | 5.25        | 4.89        | 4.98        | 7.68        | 4.31        | 6.58        |
| $R_F$                  | 2.21        | 3.17        | 3.73        | 3.53        | 3.63        | 9.62        | 2.61        | 3.52        |
| $R_{\text{wp}}$        | 6.22        | 6.53        | 7.18        | 6.76        | 6.65        | 5.70        | 6.91        | 8.30        |
| $R_{\text{exp}}$       | 5.78        | 10.12       | 9.92        | 9.73        | 9.23        | 4.10        | 9.45        | 6.20        |
| $\chi^2$               | 1.24        | 0.44        | 0.57        | 0.50        | 0.56        | 0.65        | 0.55        | 1.88        |

Finally, when  $x$  reaches 1, representing  $\text{Bi}_2\text{S}_3$ , all the Cu positions are vacant and Pb is not present in Bi sites. This implies that no Cu atoms occupy the crystal lattice, resulting in a completely free  $\text{Bi}_2\text{S}_3$  one dimensional chain structure. This vacancy-induced change in the crystal structure can significantly impact the properties of the materials. The disorder nature within the crystal structure, arising from the random presence of Cu and vacancies, can be further confirmed through transmission electron microscopy. This technique allows for the direct observation and analysis of the crystal structure at the atomic scale, revealing disorder nature within the lattice. Generally, the aikinite series demonstrates a transition from a fully occupied Cu position in aikinite ( $\text{CuPbBiS}_3$ ) to increasingly vacant Cu positions as  $x$  increases. Furthermore, it can be

observed that the Pb content decreases as the  $x$  value increases, indicating a corresponding decrease in the point defects resulting from the presence of Pb atoms on Bi site. This vacancy-induced disorder and the changing Bi to Pb ratio with  $x$  values influence the structural characteristics and can have implications for the electrical conductivity of the material. **Figure 3.4c** clearly demonstrated the decrease of Bi to Pb ratio with increasing  $x$  values that generates point defects in the system.

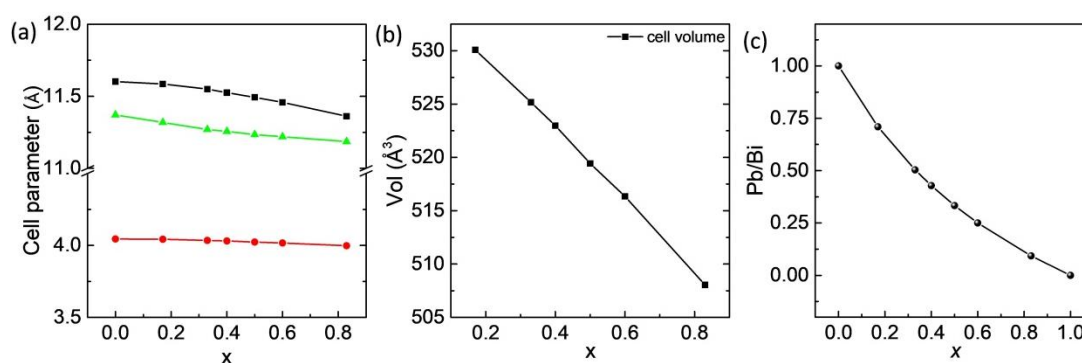


**Figure 3.4.** The plot of variation of (a) cell parameters (a, b and c are in black, red and green respectively), (b) unit cell volume and (c) theoretical Pb to Bi ratio of  $\text{CuPbBiS}_3$  ( $x = 0$ ),  $\text{Cu}_{0.83}\text{Pb}_{0.83}\text{Bi}_{1.17}\text{S}_3$  ( $x = 0.17$ ),  $\text{Cu}_{0.67}\text{Pb}_{0.67}\text{Bi}_{1.33}\text{S}_3$  ( $x = 0.33$ ),  $\text{Cu}_{0.6}\text{Pb}_{0.6}\text{Bi}_{1.4}\text{S}_3$  ( $x = 0.40$ ),  $\text{Cu}_{0.5}\text{Pb}_{0.5}\text{Bi}_{1.5}\text{S}_3$  ( $x = 0.50$ ),  $\text{Cu}_{0.4}\text{Pb}_{0.4}\text{Bi}_{1.6}\text{S}_3$  ( $x = 0.60$ ),  $\text{Cu}_{0.17}\text{Pb}_{0.17}\text{Bi}_{1.83}\text{S}_3$  ( $x = 0.83$ ) and  $\text{Bi}_2\text{S}_3$  ( $x = 1$ ) after Rietveld refinement.

The X-ray diffraction data obtained at RT can be indexed on an orthorhombic unit cell with the  $Pnma$  space group. The obtained lattice parameters from Rietveld refinement analysis are shown in **Table 3.1**. The lattice parameters for aikinite ( $\text{CuPbBiS}_3$ ) closely resemble to previously reported values. Moreover, the XRPD refinement has demonstrated that the sample contains 99% of the aikinite phase and only a trace amount of PbS (approximately 1%). Notably, the previous report by Carnevali *et al.* also indicated the presence of PbS as an impurity. The XRPD pattern after Rietveld refinement of  $\text{Cu}_{1-x}\text{Pb}_x\text{Bi}_{1+x}\text{S}_3$  series, where  $x = 0, 0.17, 0.33, 0.4, 0.5, 0.6, 0.83$ , and 1 are shown in **Figure 3.3**. **Figure 3.4** shows the evolution of cell parameters and unit cell volume with respect to the  $x$  value. As expected, the unit cell

parameters and cell volume gradually decrease with increasing vacancy content indicating the contraction of the unit cell.

### 3.3.2. Scanning Electron Microscopy (SEM) analysis

**Figure 3.5a and b** display the scanning electron microscopy (SEM) and backscattered electron imaging (BSE) of  $\text{CuPbBiS}_3$  and  $\text{Bi}_2\text{S}_3$ , respectively. For the sample  $\text{CuPbBiS}_3$  ( $x = 0$ ), the backscattered micrograph obtained by SEM on the fractured sample reveal the presence of a small content of  $\text{PbS}$  (**Figure 3.5a**). This finding aligns with the previous report by Carnevali *et al.*,<sup>3</sup> and also observed in our XRD pattern. In the case of  $\text{Bi}_2\text{S}_3$ , the backscattered SEM micrographs (**Figure 3.5b**) demonstrate that the sample is highly pure, as confirmed by XRPD analysis. **Figure 3.6** displays the secondary electron micrographs of all the samples starting from  $\text{CuPbBiS}_3$  to  $\text{Bi}_2\text{S}_3$ . The grain size observed in these samples, except  $\text{Bi}_2\text{S}_3$ , is similar, ranging from 200 to 300 nm. This small grain size can be attributed to the combined mechanochemical alloying and SPS techniques employed for the sample preparation. In contrast, the grain size of  $\text{Bi}_2\text{S}_3$  is observed to be smaller, around 100 nm (**Figure 3.6h**).

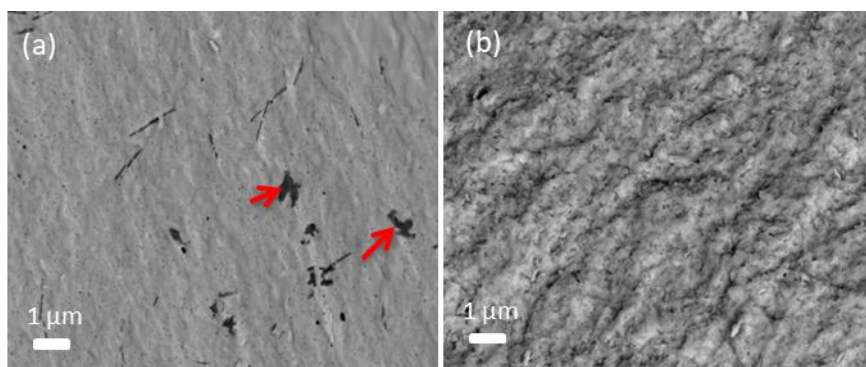


**Figure 3.5.** Back scattered electron SEM images of fractured (a)  $\text{CuPbBiS}_3$  ( $x = 0$ ) and (b)  $\text{Bi}_2\text{S}_3$  ( $x = 1$ )

**Figure 3.7** displays the backscattered SEM image of fractured and polished samples of  $\text{Cu}_{1-x}\square_x\text{Pb}_{1-x}\text{Bi}_{1+x}\text{S}_3$  ( $x = 0.17, 0.33, 0.4, 0.5, 0.6,$  and  $0.83$ ). The samples from  $x = 0.33$  to  $x = 0.89$ , do not contain impurities, supporting the results obtained from the XRPD analysis. However, for the  $x = 0.17$  sample, the BSE image reveals the presence

of PbS precipitates, similar to what is observed in the  $\text{CuPbBiS}_3$  sample ( $x = 0$ ) shown in **Figure 3.7b**.

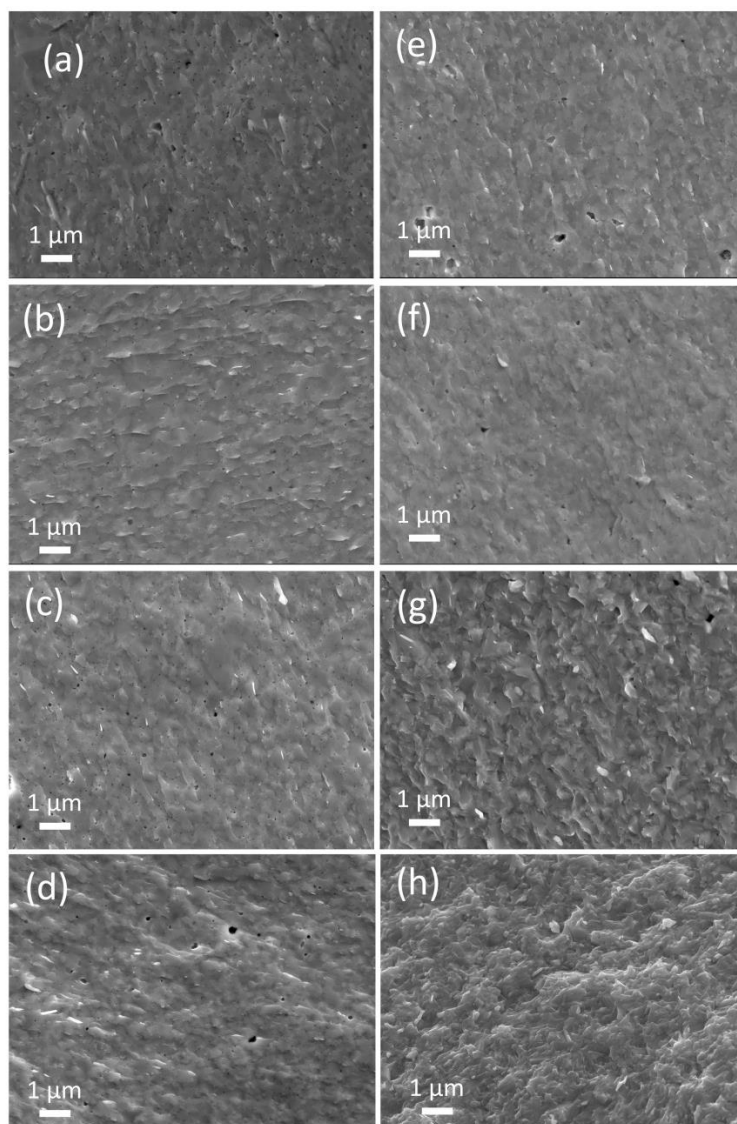


**Figure 3.6.** Secondary electron SEM images on fractured surface of (a)  $\text{CuPbBiS}_3$  ( $x = 0$ ), (b)  $\text{Cu}_{0.83}\text{Pb}_{0.83}\text{Bi}_{1.17}\text{S}_3$  ( $x = 0.17$ ), (c)  $\text{Cu}_{0.67}\text{Pb}_{0.67}\text{Bi}_{1.33}\text{S}_3$  ( $x = 0.33$ ), (d)  $\text{Cu}_{0.6}\text{Pb}_{0.6}\text{Bi}_{1.4}\text{S}_3$  ( $x = 0.40$ ), (e)  $\text{Cu}_{0.5}\text{Pb}_{0.5}\text{Bi}_{1.5}\text{S}_3$  ( $x = 0.50$ ), (f)  $\text{Cu}_{0.4}\text{Pb}_{0.4}\text{Bi}_{1.6}\text{S}_3$  ( $x = 0.60$ ), (g)  $\text{Cu}_{0.17}\text{Pb}_{0.17}\text{Bi}_{1.83}\text{S}_3$  ( $x = 0.83$ ) and (h)  $\text{Bi}_2\text{S}_3$  ( $x = 1$ ).

The presence of impurity phases in both samples with  $x = 0$  and  $x = 0.17$  could be attributed to close similarities in their crystal structure (in terms of Cu vacancy).

Furthermore, the BSE images show the presence of bubble-like cavities in all the samples, regardless of their composition ( $x = 0.17, 0.33, 0.04, 0.5, 0.6, 0.83$ ). These cavities are likely formed due to sulfur vaporization during the SPS process at high temperature. The sulfur vaporizes at high temperature and creates voids or cavities within the samples, as discussed in chapter 2. This observation is further supported by TEM analysis conducted on a few samples, which provides more details about the structure and microstructure.

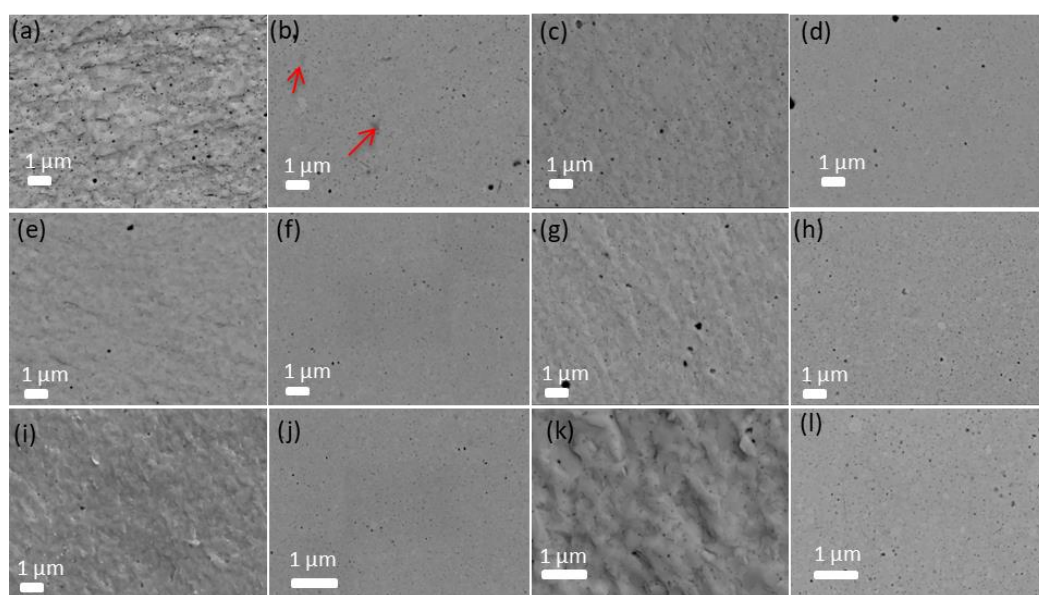


**Figure 3.7.** Back scattered electron SEM images of fractured and polished samples of (a,b)  $\text{Cu}_{0.83}\text{Pb}_{0.83}\text{Bi}_{1.17}\text{S}_3$  ( $x = 0.17$ ), (c,d)  $\text{Cu}_{0.67}\text{Pb}_{0.67}\text{Bi}_{1.33}\text{S}_3$  ( $x = 0.33$ ), (e,f)  $\text{Cu}_{0.6}\text{Pb}_{0.6}\text{Bi}_{1.4}\text{S}_3$  ( $x = 0.40$ ), (g,h)  $\text{Cu}_{0.5}\text{Pb}_{0.5}\text{Bi}_{1.5}\text{S}_3$  ( $x = 0.50$ ), (i,j)  $\text{Cu}_{0.4}\text{Pb}_{0.4}\text{Bi}_{1.6}\text{S}_3$  ( $x = 0.60$ ) and (k,l)  $\text{Cu}_{0.17}\text{Pb}_{0.17}\text{Bi}_{1.83}\text{S}_3$  ( $x = 0.83$ ), respectively.

### 3.3.3. Transmission Electron Microscopy (TEM) analysis

The microstructure and the crystal structure of samples with  $x = 0.17$  and  $0.83$  are further analyzed by TEM. **Figure 3.8a** illustrates the microstructure of the sample with the composition  $x = 0.17$  where it is clear that the sample has a small grain size ranging from 200 to 300 nm. Additionally, bubble-like cavities are observed, appearing as bright contrast in TEM images as shown in **Figure 3.8a**. The color mapping also reveals that

the sample is highly homogeneous, except for the presence of very small amounts of Pb-oxide, shown in **Figure 3.8b**. This Pb-oxide is likely due to surface oxidation of the sample. The high resolution TEM images and the corresponding fast Fourier transform patterns are also displayed in **Figure 3.8c**. The simulate SAED pattern is consistent with those of the disordered simulated patterns (**Figure 3.8d**) along [001] zone.

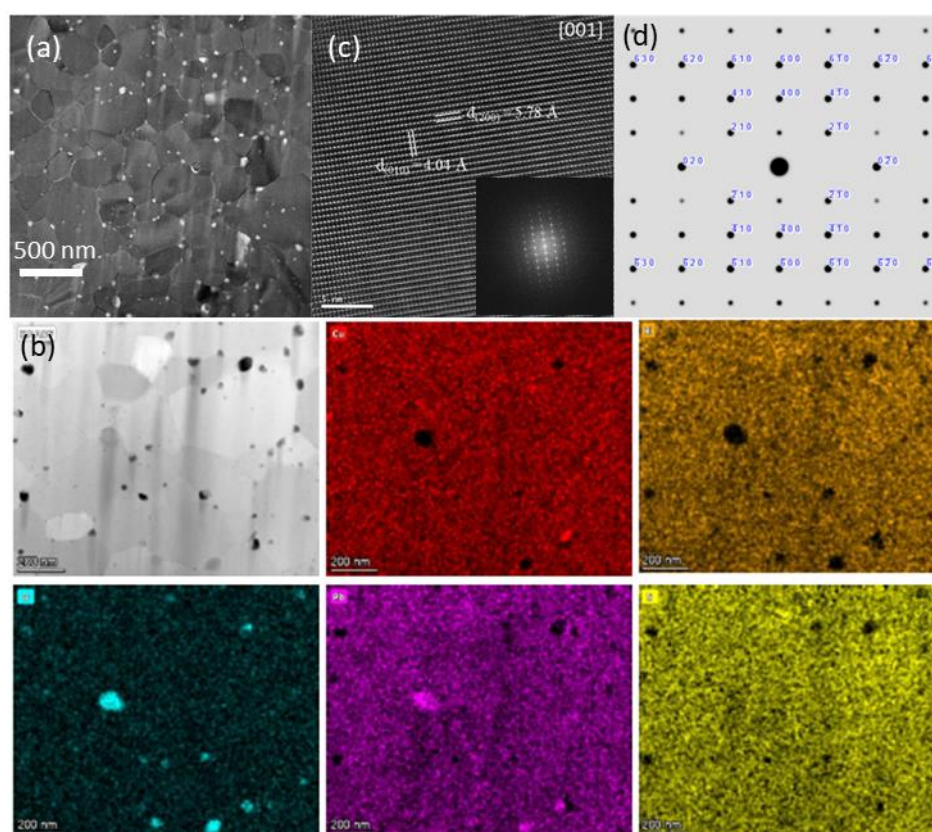


**Figure 3.8.** TEM characterization of  $\text{Cu}_{0.83}\text{Pb}_{0.83}\text{Bi}_{1.17}\text{S}_3$  ( $x = 0.17$ ). (a) grain and bubble-like cavities, (b) EDS mappings demonstrate the generally uniform elemental distribution (impurity of Pb-oxide), (c) HRTEM images (insets FFT patterns), (d) simulated SAED pattern along [001] corresponding to the disordered phase.

Furthermore, a similar grain size along with bubble like cavities is found for the sample with  $x = 0.83$ , shown in **Figure 3.9**. Additionally, the color mapping suggests highly homogeneous sample, as displayed in **Figure 3.9b**. A detailed structural characterization is carried out for the sample  $x = 0.83$  with the help of SAED analysis. The SAED pattern and corresponding high resolution TEM are recorded along different

directions, as shown in **Figure 3.10**. The fast Fourier transform patterns are also shown in inset of **Figure 3.10a,d**. The SAED patterns along both  $[10\text{-}2]$  and  $[010]$  direction are consistent with those of disordered simulated patterns (**Figure 3.10b, c, e and f**), demonstrating the disordered nature of our sample.

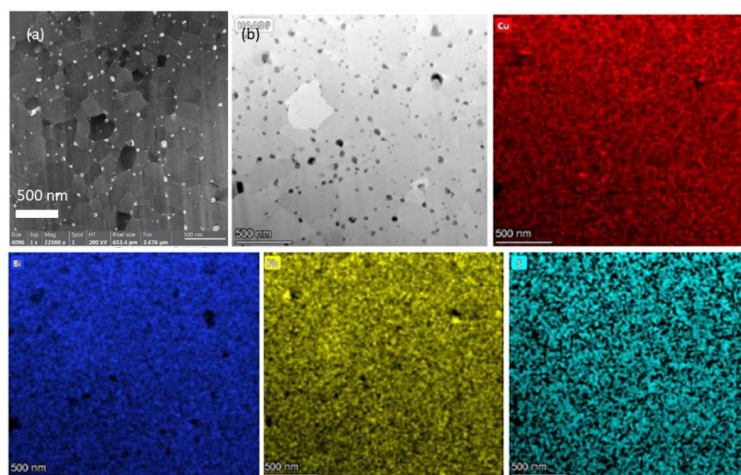


**Figure 3.9.** TEM characterization of  $\text{Cu}_{0.17}\text{Pb}_{0.17}\text{Bi}_{1.83}\text{S}_3$  ( $x = 0.83$ ). (a) Grain and bubble-like cavities, (b) EDS mappings demonstrate the generally uniform elemental distribution

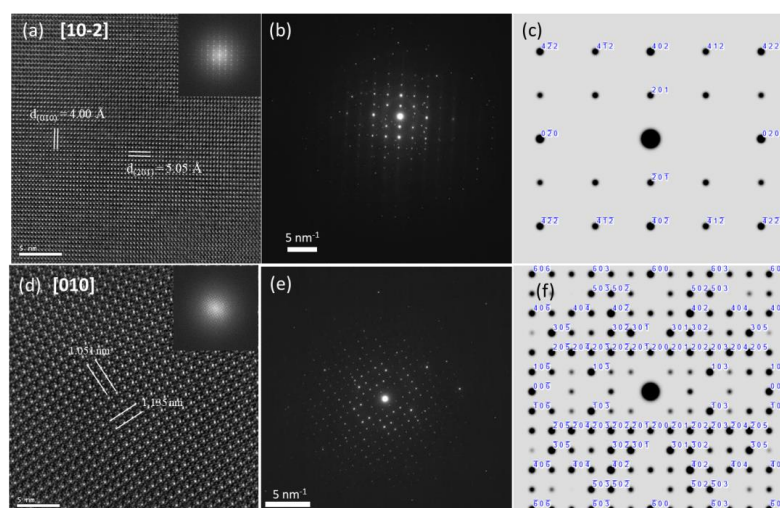


**Figure 3.10.** (a) HRTEM images (insets FFT patterns), (b) experimental SAED pattern and (c) simulated SAED pattern along  $[10\text{-}2]$  and  $[010]$  of  $\text{Cu}_{0.17}\text{Pb}_{0.17}\text{Bi}_{1.83}\text{S}_3$  ( $x = 0.83$ ) confirming the “disordered” structure.

### 3.3.4. Thermal stability study

The thermal stability of all samples from  $CuPbBiS_3$  ( $x = 0$ ) to  $Bi_2S_3$  ( $x = 1$ ) in the temperature range of 300 - 723 K is investigated using the thermal gravimetric analysis (TGA) experiment. **Figure 3.11** demonstrates a continuous decrease in the mass of samples with  $x$  values of 0, 0.17, 0.33 and 0.4 as temperature increases, indicating partial crystallization throughout the SPS process. In contrast, samples with  $x$  values of 0.5, 0.6, 0.83 and 1 exhibit a consistent mass throughout the temperature range. The enhanced thermal stability seen in samples with larger vacancy can be attributed to the increased Bi content, which leads to a closer to the thermal stability of  $Bi_2S_3$  (773 K). Due to the thermal stability issue, the electrical and thermal properties are carried out up to 673 K.

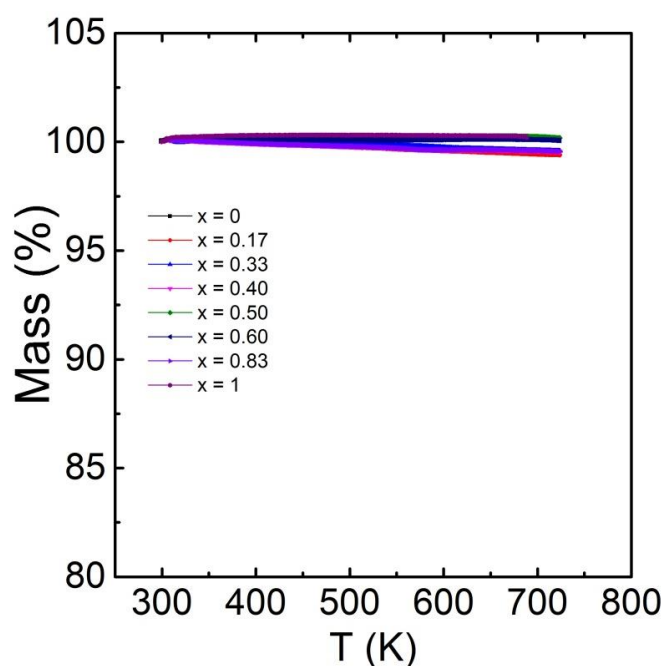


**Figure 3.11.** Thermal gravimetric analysis (TGA) of  $CuPbBiS_3$  ( $x = 0$ )

$Cu_{0.83}Pb_{0.83}Bi_{1.17}S_3$  ( $x = 0.17$ ),  $Cu_{0.67}Pb_{0.67}Bi_{1.33}S_3$  ( $x = 0.33$ ),  $Cu_{0.6}Pb_{0.6}Bi_{1.4}S_3$  ( $x = 0.40$ ),  $Cu_{0.5}Pb_{0.5}Bi_{1.5}S_3$  ( $x = 0.50$ ),  $Cu_{0.4}Pb_{0.4}Bi_{1.6}S_3$  ( $x = 0.60$ ),  $Cu_{0.17}Pb_{0.17}Bi_{1.83}S_3$  ( $x = 0.83$ ) and  $Bi_2S_3$  ( $x = 1$ ) show the stability of samples in the temperature range of 330 K to 725 K.

### 3.3.4. Band gap study

The plots shown in **Figure 3.12** illustrate the Kubelka–Munk plot of  $\text{Cu}_{1-x}\square_x\text{Pb}_{1-x}\text{Bi}_{1+x}\text{S}_3$  for the  $x$  value of 0 to 1. A small decrease and then increase in band gap can be seen with increase of  $x$  from  $\text{CuPbBiS}_3$  to  $\text{Bi}_2\text{S}_3$ , which denote to the effect of Cu vacancy in the electronic band structure as the valence band of the aikinite series is mainly contributed by Cu and Bi, described in our previous chapter. Notably, the disordered  $\text{CuPbBi}_5\text{S}_9$  ( $x = 0.67$ ) shows experimental band gap 0.89 eV.

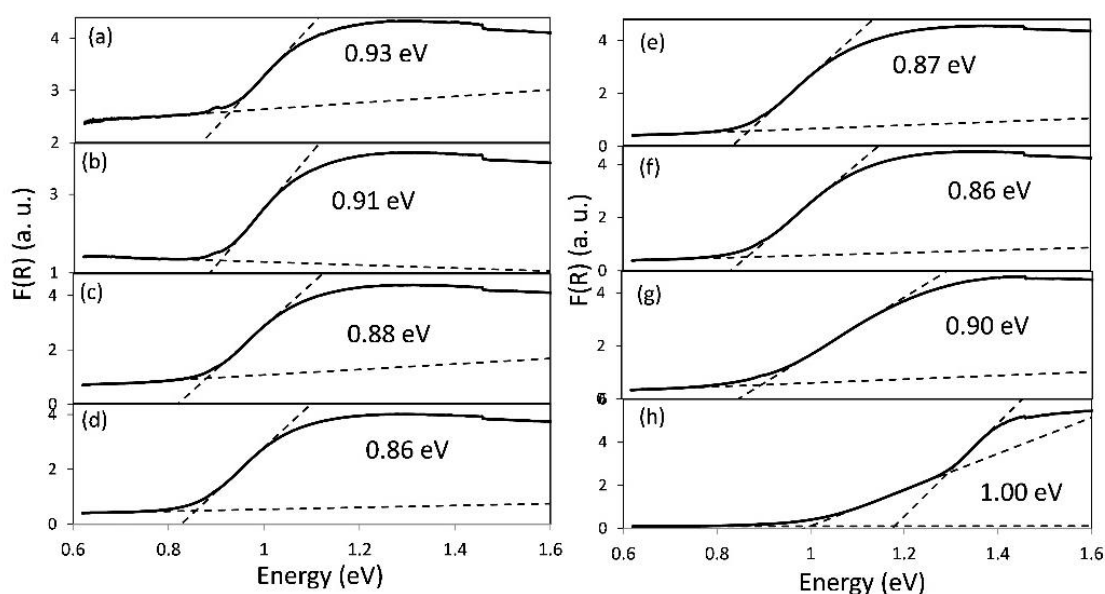


**Figure 3.12.** The Kubelka–Munk plot (a)  $\text{CuPbBiS}_3$  ( $x = 0$ ), (b)  $\text{Cu}_{0.83}\text{Pb}_{0.83}\text{Bi}_{1.17}\text{S}_3$  ( $x = 0.17$ ), (c)  $\text{Cu}_{0.67}\text{Pb}_{0.67}\text{Bi}_{1.33}\text{S}_3$  ( $x = 0.33$ ), (d)  $\text{Cu}_{0.6}\text{Pb}_{0.6}\text{Bi}_{1.4}\text{S}_3$  ( $x = 0.40$ ), (e)  $\text{Cu}_{0.5}\text{Pb}_{0.5}\text{Bi}_{1.5}\text{S}_3$  ( $x = 0.50$ ), (f)  $\text{Cu}_{0.4}\text{Pb}_{0.4}\text{Bi}_{1.6}\text{S}_3$  ( $x = 0.60$ ), (g)  $\text{Cu}_{0.17}\text{Pb}_{0.17}\text{Bi}_{1.83}\text{S}_3$  ( $x = 0.83$ ) and (h)  $\text{Bi}_2\text{S}_3$  ( $x = 1$ ) indicating the band gap.

The dependence of Cu vacancy on band gap exhibits non-linearity (**Figure 3.13**) which can be attributed to various factors. Firstly, the compositional changes from aikinite to bismuthanite along with random occupation of cations have a significant effect in the crystal structure which can have an effect on band gap. Furthermore, the non-linearity of the band gap phenomena can be influenced by the energy mismatch

between the orbitals that constitute the band edges of the alloy.<sup>7</sup> To further understand these changes in the band gap values, theoretical calculations are ongoing.

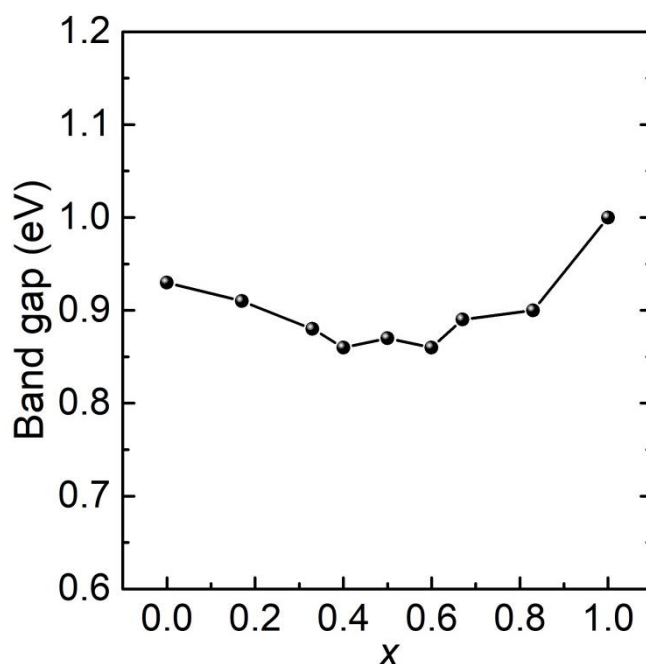


*Figure 3.13. Bandgap of all samples in aikinite series plotted against x value.*

### 3.3.5. Electrical properties

The temperature dependence of the electrical resistivity of samples in the  $\text{Cu}_{1-x}\text{Pb}_x\text{Bi}_{1+x}\text{S}_3$  series is presented in **Figure 3.14a**. All samples in the series, except  $\text{Bi}_2\text{S}_3$ , are highly resistive. For example,  $x = 0.17$  shows electrical resistivity and Seebeck coefficient values are  $8.3 \times 10^3 \Omega \text{ cm}$  and  $-1057 \mu\text{V K}^{-1}$  at 346 K, respectively, whereas  $x = 0.83$  sample shows values of  $3.7 \times 10^3 \Omega \text{ cm}$  and  $-1204 \mu\text{V K}^{-1}$  at 345 K. It is important to note that the electric resistivity of these samples could not be measured at RT using the ZEM 3 instrument due to their very high resistivity. Consequently, our measurements are conducted by raising the temperature and subsequently measuring the electrical transport properties during the cooling. Such a high resistivity of our samples is due to low carrier concentration (around  $10^{12}$  to  $10^{13}$ ) (**Table 3.2**). On the hand,  $\text{Bi}_2\text{S}_3$  shows relatively low electrical resistivity  $200 \Omega \text{ cm}$  due to high carrier concentration ( $1.1 \times 10^{16} \text{ cm}^{-3}$ ). The overall decrease in electrical resistivity with increasing  $x$  is

explained by the steady increase of electrical mobility of the samples with vacancy. The carrier concentration value decrease from  $1.9 \times 10^{14} \text{ cm}^{-3}$  for  $\text{CuPbBiS}_3$  to  $2.9 \times 10^{12} \text{ cm}^{-3}$  for  $x = 0.5$  and followed by increase to  $1.11 \times 10^{16} \text{ cm}^{-3}$  for  $\text{Bi}_2\text{S}_3$ . The comparable high carrier concentration for  $x$  values 0, 0.17 may be due to the presence of impure phase,  $\text{PbS}$ , hence stoichiometric deviation observed for  $x = 0$  and  $x = 0.17$ .  $\text{CuPbBiS}_3$  shows hall mobility value of  $2.2 \text{ cm}^2 \text{ V}^{-1} \text{ s}^{-1}$ , similar to disordered gladite phase ( $3.2 \text{ cm}^2 \text{ V}^{-1} \text{ s}^{-1}$ ). The overall mobility value increases with increasing  $x$  value in the system (**Table 3.2**). This phenomenon can be explained by the fact that an increase in the  $x$  value leads to a decrease in the Pb content in the system, as well as an increase in the ratio of Bi to Pb, which results in a reduction of the point defect. The decrease in point defect causes an increase in electrical mobility. A reduction of mobility can be seen for  $\text{Bi}_2\text{S}_3$  ( $3.2 \text{ cm}^2 \text{ V}^{-1} \text{ s}^{-1}$ ) due to the combining effect of lower grain size and relatively high carrier concentration. Moreover, all compositions exhibit negative values of the Seebeck coefficient (except aikinite) which suggests that electrons are the major charge carriers. This  $n$ -type conduction is may be due to the presence of sulfur vacancies, similar to other systems such as  $\text{Bi}_2\text{S}_3$ ,  $\text{MnBi}_4\text{S}_7$ ,  $\text{FeBi}_4\text{S}_7$ , and  $\text{AgBi}_3\text{S}_5$ .<sup>8-11</sup> The bismuthinite-aikinite series contain two type of conduction network, corner shared one dimensional network of  $[\text{CuS}_4]^{7-}$  tetrahedral and Bi-S network. All the members of the bismuthinite-aikinite series,  $\text{Cu}_{1-x}\text{Pb}_x\text{Bi}_{1+x}\text{S}_3$  except aikinite ( $x = 0$ ) contain vacant sites in the one-dimensional  $[\text{Cu}_{1-x}\text{S}_3]^{(5+x)-}$  chain that leads Bi-S network as main conduction network making them  $n$ -type conduction, as discussed in previous chapter. On the other hand, for aikinite, the one-dimensional network of corner-sharing  $[\text{CuS}_4]^{7-}$  tetrahedra implicates the electrical conduction making it  $p$ -type semiconductor. Aikinite shows high electrical resistivity and relatively low Seebeck coefficient value of  $3.3 \times 10^3 \text{ } \Omega \text{ cm}$  and  $407 \text{ } \mu\text{V K}^{-1}$  at 363 K, respectively. The increasing trend of Seebeck coefficient value from 563 K is due to thermal degradation. Such behavior was not seen in previous report by Carnevali *et al.*<sup>3</sup> as the addition step of annealing for 48 hours make their sample more thermally stable. As the temperature increases, both the electrical resistivity and the absolute value of the Seebeck coefficient ( $|S|$ ) decrease, indicating a nondegenerate semiconducting behavior. The temperature dependent Seebeck coefficient is shown in **Figure 3.14b**. The Seebeck coefficient values are also very large

in our compounds and significantly higher than those in other Bi-based sulfides. Such a large Seebeck coefficient indicates low carrier concentration which is in agreement with highly stoichiometry compound, thanks to the synthesis process combining mechanical alloying and SPS.

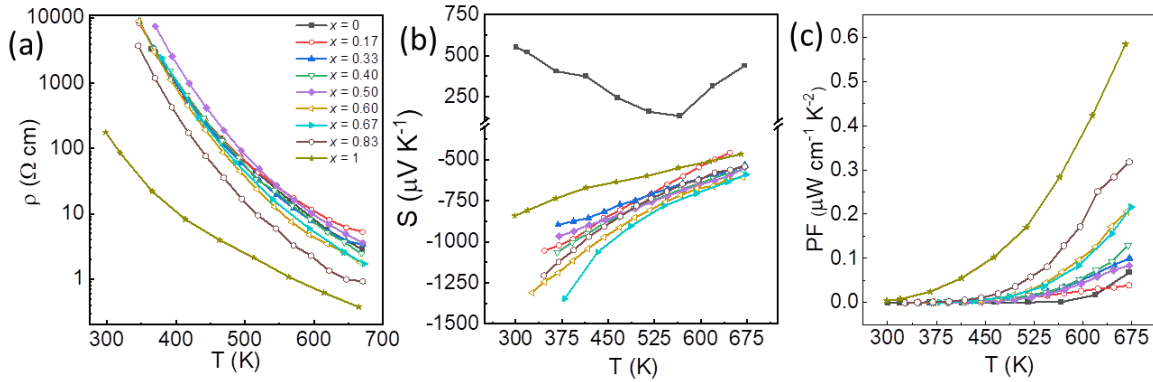


**Figure 3.14.** Temperature dependent electrical properties, (a) electrical conductivity, (b) Seebeck coefficient, and (c) power factor of  $\text{CuPbBiS}_3$  ( $x = 0$ ),  $\text{Cu}_{0.83}\text{Pb}_{0.83}\text{Bi}_{1.17}\text{S}_3$  ( $x = 0.17$ ),  $\text{Cu}_{0.67}\text{Pb}_{0.67}\text{Bi}_{1.33}\text{S}_3$  ( $x = 0.33$ ),  $\text{Cu}_{0.6}\text{Pb}_{0.6}\text{Bi}_{1.4}\text{S}_3$  ( $x = 0.40$ ),  $\text{Cu}_{0.5}\text{Pb}_{0.5}\text{Bi}_{1.5}\text{S}_3$  ( $x = 0.50$ ),  $\text{Cu}_{0.4}\text{Pb}_{0.4}\text{Bi}_{1.6}\text{S}_3$  ( $x = 0.60$ ),  $\text{Cu}_{0.33}\text{Pb}_{0.33}\text{Bi}_{1.67}\text{S}_3$  ( $x = 0.67$ ),  $\text{Cu}_{0.17}\text{Pb}_{0.17}\text{Bi}_{1.83}\text{S}_3$  ( $x = 0.83$ ) and  $\text{Bi}_2\text{S}_3$  ( $x = 1$ )

**Table 3.2.** Carrier concentration and hall mobility of  $\text{CuPbBiS}_3$  ( $x = 0$ ),  $\text{Cu}_{0.83}\text{Pb}_{0.83}\text{Bi}_{1.17}\text{S}_3$  ( $x = 0.17$ ),  $\text{Cu}_{0.67}\text{Pb}_{0.67}\text{Bi}_{1.33}\text{S}_3$  ( $x = 0.33$ ),  $\text{Cu}_{0.6}\text{Pb}_{0.6}\text{Bi}_{1.4}\text{S}_3$  ( $x = 0.40$ ),  $\text{Cu}_{0.5}\text{Pb}_{0.5}\text{Bi}_{1.5}\text{S}_3$  ( $x = 0.50$ ),  $\text{Cu}_{0.4}\text{Pb}_{0.4}\text{Bi}_{1.6}\text{S}_3$  ( $x = 0.60$ ),  $\text{Cu}_{0.17}\text{Pb}_{0.17}\text{Bi}_{1.83}\text{S}_3$  ( $x = 0.83$ ) and  $\text{Bi}_2\text{S}_3$  ( $x = 1$ )

| $x$  | Carrier concentration ( $\text{cm}^{-3}$ ) | Hall mobility ( $\text{cm}^2 \text{V}^{-1} \text{s}^{-1}$ ) |
|------|--|---|
| 0    | $1.9 \times 10^{14}$                       | 2.2   |
| 0.17 | $4.5 \times 10^{13}$                       | 0.7   |
| 0.33 | $3.7 \times 10^{13}$                       | 1.4   |
| 0.40 | $3.7 \times 10^{12}$                       | 7.7   |
| 0.50 | $2.9 \times 10^{12}$                       | 7.7   |
| 0.60 | $5.7 \times 10^{12}$                       | 7.5   |
| 0.83 | $1.1 \times 10^{13}$                       | 15.7  |
| 1    | $1.1 \times 10^{16}$                       | 3.2   |

**Figure 3.14c** illustrates the variation of the power factor ( $PF$ ) with temperature within the  $\text{Cu}_{1-x}\text{Pb}_x\text{Bi}_{1+x}\text{S}_3$  series. The  $PF$  values are notably low for all samples, ranging from 0.05 to 0.6  $\mu\text{W cm}^{-1} \text{K}^{-2}$  at 673 K primarily attributed to the extremely low carrier concentration of these samples. For example, when  $x = 0$ , the maximum  $PF$  reaches 0.05  $\mu\text{W cm}^{-1} \text{K}^{-2}$ , and this value increases with  $x$ . The highest  $PF$  achieved in our study is for  $x = 1$ , reaching 0.6  $\mu\text{W cm}^{-1} \text{K}^{-2}$ , mainly due to the reduction in electrical resistivity. In chapter 2, a detailed comparison of electrical transport of this aikinite series with other Bi rich sulfides is provided. Among all quaternary system,  $x = 0.83$  sample shows highest  $PF$  value of 0.33  $\mu\text{W cm}^{-1} \text{K}^{-2}$  at 673 K.

### 3.3.6. Thermal properties

The temperature dependence of thermal conductivity of the aikinite series are shown in **Figure 3.15a** which displays ultralow thermal conductivity for all samples (except  $\text{Bi}_2\text{S}_3$ ). The  $\kappa_L$  of  $\text{Bi}_2\text{S}_3$  ( $x = 1$ ) decreases with temperature typically like crystalline materials. The room temperature  $\kappa_L$  is  $\sim 0.95 \text{ W m}^{-1} \text{K}^{-1}$  which reduces to  $\sim 0.58 \text{ W m}^{-1} \text{K}^{-1}$  at 673 K. All the other samples from  $x = 0.17$  to 0.83 in the aikinite series exhibit very low  $\kappa_L$  ranging from  $\sim 0.5 - 0.7 \text{ W m}^{-1} \text{K}^{-1}$  at room temperature. The exceptionally low lattice thermal conductivity due to the presence of very low energy vibrations involving Bi, Pb, and Cu, as described in chapter 2 for disordered gladite phase. The low  $\kappa_L$  further decreases with increasing temperature but very slowly (much weaker than  $T^{-1}$  decay) compared to  $\text{Bi}_2\text{S}_3$ . For instance,  $x = 0.17$  and  $x = 0.83$  sample show thermal conductivity of 0.45 and 0.65  $\text{W m}^{-1} \text{K}^{-1}$  at 300 K that decrease to 0.25 and 0.45  $\text{W m}^{-1} \text{K}^{-1}$  at 673 K, respectively (**Figure 3.15a**). The total thermal conductivity is mainly contributed by the lattice contribution as the samples are highly resistive. But a steady decrease in thermal conductivity can be seen with the increase of  $x$ , which is explained by the increasing point defects. As we move from bismuthanite ( $x = 1$ ) to aikinite ( $x = 0$ ), the Bi content reduce and Cu and Pb content increase that elevates the point defects. This point defects help to scatter phonon and decrease the thermal conductivity. A sharp decrease in thermal conductivity can be seen in samples with  $x = 0, 0.17, 0.33, 0.4$  and 0.5 after 623 K which may be due to the sulfur evaporation at high temperature. But in case of higher  $x$  values ( $x > 0.5$ ), the thermal conductivity does not

decrease so sharp which indicates higher thermal stability of those samples at high temperature. The enhancement of thermal stability of samples with larger vacancy can be attributed to increasing Bi content, as described in the TGA analysis.

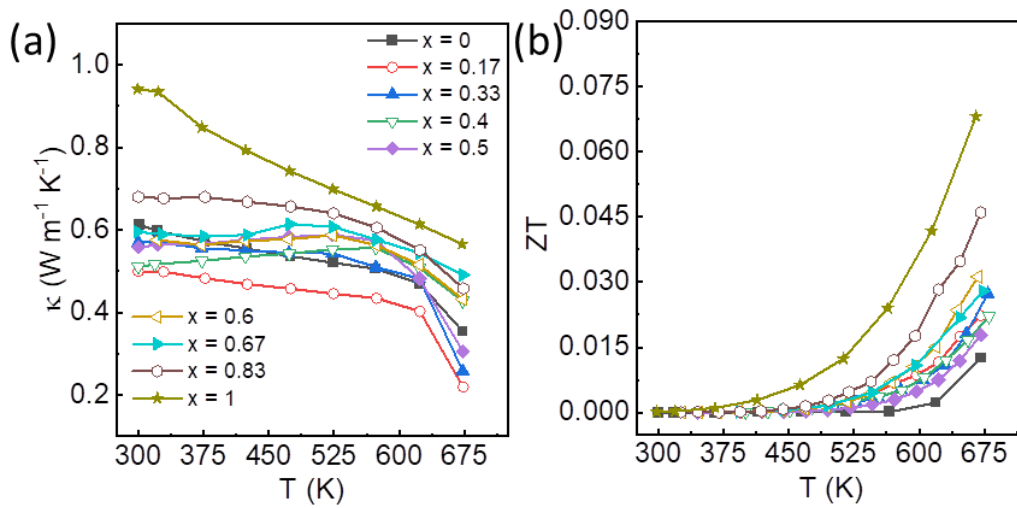


**Figure 3.15.** Temperature dependent (a) total thermal conductivity, (b) thermoelectric figure of merit of  $\text{CuPbBiS}_3$  ( $x = 0$ ),  $\text{Cu}_{0.83}\text{Pb}_{0.83}\text{Bi}_{1.17}\text{S}_3$  ( $x = 0.17$ ),  $\text{Cu}_{0.67}\text{Pb}_{0.67}\text{Bi}_{1.33}\text{S}_3$  ( $x = 0.33$ ),  $\text{Cu}_{0.6}\text{Pb}_{0.6}\text{Bi}_{1.4}\text{S}_3$  ( $x = 0.40$ ),  $\text{Cu}_{0.5}\text{Pb}_{0.5}\text{Bi}_{1.5}\text{S}_3$  ( $x = 0.50$ ),  $\text{Cu}_{0.4}\text{Pb}_{0.4}\text{Bi}_{1.6}\text{S}_3$  ( $x = 0.60$ ),  $\text{Cu}_{0.33}\text{Pb}_{0.33}\text{Bi}_{1.67}\text{S}_3$  ( $x = 0.67$ ),  $\text{Cu}_{0.17}\text{Pb}_{0.17}\text{Bi}_{1.83}\text{S}_3$  ( $x = 0.83$ ) and  $\text{Bi}_2\text{S}_3$  ( $x = 1$ )

The temperature dependence of the figure of merit ( $ZT$ ) of  $\text{Cu}_{1-x}\text{Pb}_x\text{Bi}_{1+x}\text{S}_3$  series is displayed in **Figure 3.15b**. A maximum  $ZT$  value of around 0.07 is obtained at 673 K for  $\text{Bi}_2\text{S}_3$  sample which is the highest among Cu deficient  $\text{Cu}_{1-x}\text{Pb}_x\text{Bi}_{1+x}\text{S}_3$  series. Note that the pristine disordered galdite ( $x = 0.67$ ) shows  $ZT$  value of 0.04 at 673 K. The upward trend observed in  $ZT$  with increasing  $x$  value content can be attributed to the enhancement of power factor ( $PF$ ). Moreover, the rising vacancy content increases the Bi/Pb ratio in samples which leads to a reduction in point defects. This reduction in point defect positively impacts the hall mobility and decreases the electrical resistivity. Ultimately, these improvements contribute to the enhancement of the  $ZT$  value. The enhancement of carrier concentration in  $x = 0.83$  sample has the potential to further increase the figure of merit value. However, considering that the carrier optimization

conducted on disordered gladiate ( $x = 0.67$ ) only enhanced the  $ZT$  value to 0.4 at 700 K for  $\text{CuPbBi}_5\text{S}_{8.97}\text{Cl}_{0.03}$ , it is unlikely that the increase in carrier optimization in the other members of the series will yield significant improvements in the  $ZT$  value.

### 3.4. Conclusion

In summary, this chapter describes the synthesis of a range of compounds within the Cu-deficient aikinite-type sulfide family denoted as  $\text{Cu}_{1-x}\square_x\text{Pb}_{1-x}\text{Bi}_{1+x}\text{S}_3$ , using a combination of mechanical alloying and Spark Plasma Sintering (SPS) techniques. The analysis conducted through X-ray powder diffraction and TEM reveals a disordered distribution of copper and vacancies within the cationic sites, similar to the disordered gladiate phase, as discussed in Chapter 2. Specifically, our research demonstrates that the exceptionally low lattice thermal conductivity observed in these compounds is intrinsic. Sample from this series exhibits notably high electrical resistivity and low carrier concentration showing intrinsic semiconducting behavior. However, the low carrier concentration renders these materials less suitable for thermoelectric applications. Importantly, those results demonstrate that the Bi/Pb mixed occupancy within the  $\text{Bi}_2\text{S}_3$  layers governs the electrical mobility of these series of compounds. The mixed occupancy affect the thermal transport with large lattice thermal conductivity value obtained in the sample with less amount of Pb. The doping strategies on  $x = 0.83$  should be an option to improve the efficiency. However, it is unlikely that the carrier concentration optimization would yield significant improvements in the  $ZT$  value.

### 3.5. References

- (1) Liang, H.; Guo, J.; Zhou, Y. X.; Wang, Z. Y.; Feng, J.; Ge, Z. H. CuPbBi<sub>5</sub>S<sub>9</sub> Thermoelectric Material with an Intrinsic Low Thermal Conductivity: Synthesis and Properties. *J. Mater.* **2021**, *13*. <https://doi.org/10.1016/j.jmat.2021.03.016>.
- (2) Balijapelly, S.; Hauble, A.; Sundaramoorthy, S.; Watts, J. L.; Kauzlarich, S. M.; Chernatynskiy, A.; Choudhury, A. Ultralow Lattice Thermal Conductivity in the Aikinite Structure Family, Cu<sub>x</sub>Pb<sub>x</sub>Bi<sub>2-x</sub>S<sub>3</sub>, and Thermoelectric Properties of Cu<sub>0.14</sub>Pb<sub>0.14</sub>Bi<sub>1.86</sub>S<sub>3</sub>. *ACS Appl. Energy Mater.* **2022**, *5* (11), 14222–14230. <https://doi.org/10.1021/acsaem.2c02790>.
- (3) Carnevali, V.; Mukherjee, S.; Voneshen, D. J.; Maji, K.; Guilmeau, E.; Powell, A. V.; Vaqueiro, P.; Fornari, M. Lone Pair Rotation and Bond Heterogeneity Leading to Ultralow Thermal Conductivity in Aikinite. *J. Am. Chem. Soc.* **2023**, *145* (16), 9313–9325. <https://doi.org/10.1021/jacs.3c02536>.
- (4) Balić-Žunić, T.; Topa, D.; Makovicky, E. The Crystal Structure of Emilite, Cu<sub>10.7</sub>Pb<sub>10.7</sub>Bi<sub>21.3</sub>S<sub>48</sub>, the Second 45 Å Derivative of the Bismuthinite-Aikinite Solid-Solution Series. *Can. Mineral.* **2002**, *40*, 239–245.
- (5) Topa, D.; Makovicky, E.; Balić-Žunić, T. The Structural Role of Excess Cu and Pb in Gladite and Krupkaite Based on New Refinements of Their Structure. *Can. Mineral.* **2002**, *40* (4), 1147–1159. <https://doi.org/10.2113/gscanmin.40.4.1147>.
- (6) Topa, D.; Balić-Žunić, T.; Makovicky, E. The Crystal Structure of Cu<sub>1.6</sub>Pb<sub>1.6</sub>Bi<sub>6.4</sub>S<sub>12</sub>, a New 44.8 Å Derivative of the Bismuthinite-Aikinite Solid-Solution Series. *Can. Mineral.* **2000**, *38*, 611–616.
- (7) Goyal, A.; McKechnie, S.; Pashov, D.; Tumas, W.; Schilfgaarde, M. Van; Stevanović, V. Origin of Pronounced Nonlinear Band Gap Behavior in Lead-Tin Hybrid Perovskite Alloys. *Chem. Mater.* **2018**, *30* (11), 3920–3928. <https://doi.org/10.1021/acs.chemmater.8b01695>.
- (8) Biswas Li-Dong; Kanatzidis, Mercouri G., K. Z. Tellurium-Free Thermoelectric: The Anisotropic N-Type Semiconductor Bi<sub>2</sub>S<sub>3</sub>. *Adv. Energy Mater.* **2012**, *2* (6), 634–638. <https://doi.org/10.1002/aenm.201100775>.

- 
- (9) Labégorre, J. B.; Virfeu, A.; Bourhim, A.; Willeman, H.; Barbier, T.; Appert, F.; Juraszek, J.; Malaman, B.; Huguenot, A.; Gautier, R.; Nassif, V.; Lemoine, P.; Prestipino, C.; Elkaim, E.; Pautrot-d'Alençon, L.; Le Mercier, T.; Maignan, A.; Al Rahal Al Orabi, R.; Guilmeau, E.  $\text{XBi}_4\text{S}_7$  (X = Mn, Fe): New Cost-Efficient Layered *n*-Type Thermoelectric Sulfides with Ultralow Thermal Conductivity. *Adv. Funct. Mater.* **2019**, *29* (48). <https://doi.org/10.1002/adfm.201904112>.
- (10) Xi, M.; Zhu, H.; Wu, H.; Yang, Y.; Yan, Y.; Wang, G.; Wang, G.; Li, J. Y.; Lu, X.; Zhou, X. Thermoelectricity of *n*-Type  $\text{MnBi}_4\text{S}_{7-7x}\text{Se}_{7x}$  Solid Solution. *Chem. Eng. J.* **2020**, *396*, 125219. <https://doi.org/10.1016/j.cej.2020.125219>.
- (11) Tan, G.; Hao, S.; Zhao, J.; Wolverton, C.; Kanatzidis, M. G. High Thermoelectric Performance in Electron-Doped  $\text{AgBi}_3\text{S}_5$  with Ultralow Thermal Conductivity. *J. Am. Chem. Soc.* **2017**, *139* (18), 6467–6473. <https://doi.org/10.1021/jacs.7b02399>.



---

**Rattling of copper in three-fold coordination in  
 $\text{Cu}_3\text{BiS}_3$ : a blockade for hole carrier delocalization but  
a driving force for ultralow thermal conductivity**

---



## 4.1. Introduction

The quaternary sulfides based on Cu-Pb-Bi-S have been investigated in the previous two chapters (chapters 2 and 3). In chapter 2, a novel Cu-deficient aikinite-type sulfide has been synthesized; the structure differs from the previously reported ordered structure by the random distribution of copper and vacancies on the cationic sites. It is noteworthy to mention that the disordered gladite phase is a representative example of a vast group of closely related sulfides denoted as  $(\text{Cu}_{1-x}\square_x)\text{Pb}_{1-x}\text{Bi}_{1+x}\text{S}_3$  ( $x = 0 - 1$ ). Furthermore, the chemical doping technique has been used to optimize the carrier concentration and a moderate figure of merit value was achieved. In Chapter 2, we carried out an optimization study on the vacancy within the copper-deficient aikinite series. The results suggest that increasing vacancy leads to being free of the  $\text{Bi}_2\text{S}_3$  channel, leading to a subsequent reduction in electrical resistivity and an increase in the figure of merit.

In this chapter, the proposed approach involves the synthesis and development of crystalline materials that possess a highly conductive electronic network, while also exhibiting structural characteristics that promote effective phonon scattering.<sup>1-19</sup> In this respect, *p*-type copper-rich sulfides offer an attractive field for investigation. Many of these materials demonstrate promising thermoelectric properties and can be characterized as intrinsic degenerate semiconductors with conduction resembling that of metals. This aligns with the principle of "Cu(I)-Cu(II)" copper mixed valency,<sup>20</sup> which serves as the foundation for hole doping in thermoelectric copper-based sulfides. *P*-type metallic conductivity is a result of charge delocalization attributed to the redox couple  $\text{Cu}^{2+}/\text{Cu}^+$ . The previous phenomenon is demonstrated by two families of materials, tetrahedrites  $\text{Cu}_{12-x}\text{T}_x\text{Sb}_4\text{S}_{13}$  ( $T = \text{Ni}, \text{Zn}$ )<sup>17,21-23</sup> and colusites  $\text{Cu}_{26}\text{T}_2\text{M}_6\text{S}_{32}$  ( $T = \text{Ti}, \text{V}, \text{Cr}, \text{Nb}, \text{Mo}, \text{Ta}, \text{W}; M = \text{Ge}, \text{Sn}, \text{Sb}$ )<sup>24-28</sup>. These materials have garnered attention due to their exceptional thermoelectric (TE) performances, with a thermoelectric figure of merit ( $ZT$ )  $\sim 1$  at 700 K. This is attributed to intrinsic degenerate semiconducting behavior and their intricate crystal structures, which result in significantly low thermal conductivity. However, the origin of the low thermal conductivity is very different in these two families. In colusites, the heat transport is mainly governed by the intrinsic

structural complexity, which arises from the large sphalerite-derivative unit cells in which  $[AS_4]Cu_6$  tetrahedral-octahedral complexes are present and functionalize the “Cu-S” conductive network.<sup>24–26,28–30</sup> Order/disorder phenomena are also known to enhance substantially phonon scattering, while keeping high power factors.<sup>26,31,32</sup> Differently, in tetrahedrites, copper exhibits two different types of coordination, tetrahedral and triangular, and low lattice thermal conductivity was shown to originate from high anisotropic atomic vibrations of copper in triangular coordination.<sup>21,33–35</sup>

The recent synthesis of the copper rich sulfide wittichenite  $Cu_3BiS_3$  with low lattice thermal conductivity,<sup>36,37</sup> which was previously studied as thin films for optoelectronic applications,<sup>38–40</sup> appears as a very interesting route for the investigation of the various parameters governing the electronic and thermal conductivity of these materials. The authors observed *p*-type conductivity and emphasize its potential for thermoelectric applications. Unfortunately, they obtained a very poor figure of merit ( $ZT \sim 0.04$  at 460 K).<sup>36</sup> This sulfide shows a great similarity with tetrahedrite because of the lone pair cation  $Bi^{3+}$  (instead of  $Sb^{3+}$ ) and exhibits also a three fold coordination of copper<sup>41</sup> which may lead to large atomic displacements, as observed in tetrahedrite.<sup>17,21,34,42</sup> The fact that the coordination of copper in this sulfide is exclusively triangular is important and marks a difference from the tetrahedrites, where copper exhibits two kinds of coordination (triangular and tetrahedral). By investigation, we wanted to provide a better understanding of the relationships between structure and properties in the copper rich sulfide wittichenite. Based on these observations, we have, in fact, revisited the synthesis and properties of  $Cu_3BiS_3$ . Bearing in mind that the synthesis at high temperature<sup>36</sup> is difficult to optimize and may lead to deviation from stoichiometry and that the solution-based methods<sup>61</sup> need expensive and environment unfriendly solvent, we have synthesized this material by mechanical alloying combined by spark plasma sintering.

The present investigation on  $Cu_3BiS_3$  clearly establishes that the threefold coordination of copper, or more exactly its strong anisotropic vibration, has a key role on the two antagonist factors, electrical and thermal conductivity, which govern the thermoelectric properties of the Cu-rich sulfides. We observe that all attempts to

introduce hole carriers on the copper lattice by doping the Bi sites with divalent cations or by introducing vacancies on the copper sites are hindered due to the strong rattling of copper. In contrast, by comparing with the tetrahedrite ( $\text{Cu}_{12}\text{Sb}_4\text{S}_{13}$ ) and chalcocite ( $\text{Cu}_2\text{S}$ ), we demonstrate that the anisotropic vibration of copper in the three-fold coordination is the driving force for the appearance of ultra-low thermal conductivity in this sulfide. We also suggest that the  $\text{Bi}^{3+}$  cation, due to its  $6s^2$  electronic lone pair (LP) which forms a weak LP-Cu bond with the nearest  $\text{Cu}^+$  cation, influences its large maximum displacement with respect to the “ $\text{S}_3$ ” plane.

## 4.2. Methods

### 4.2.1. Reagent

High-purity copper powder (Cu, Alfa Aesar, >99.99%), bismuth powder (Bi, Alfa Aesar, >99.5%), and sulfur powder (S, Alfa Aesar, >99.99%) were used as precursors without further purification.

### 4.2.2. Synthesis

Pristine  $\text{Cu}_3\text{BiS}_3$  was synthesized by milling stoichiometric amounts of Cu, Bi, and S powders (3:1:3 ratio, total amount of 6 g) in WC jars of 45 mL (14 WC balls of 10 mm) for 6 h (12 cycles of 30 min with 1 min pause) under an argon atmosphere. The X-ray powder diffraction (XRPD) patterns of mechanochemical alloyed powders after 30 mins, 1 hr, 3 hrs, and 6 hrs are presented in **Figure 4.1a**. The diffraction patterns are equivalent and correspond to the  $\text{Cu}_3\text{BiS}_3$  phase ( $P2_12_12_1$ ,  $a = 7.723 \text{ \AA}$ ,  $b = 10.395 \text{ \AA}$ , and  $c = 6.716 \text{ \AA}$ )<sup>41</sup> indicating that the formation of the phase is fast since it is almost completed after 30 mins.

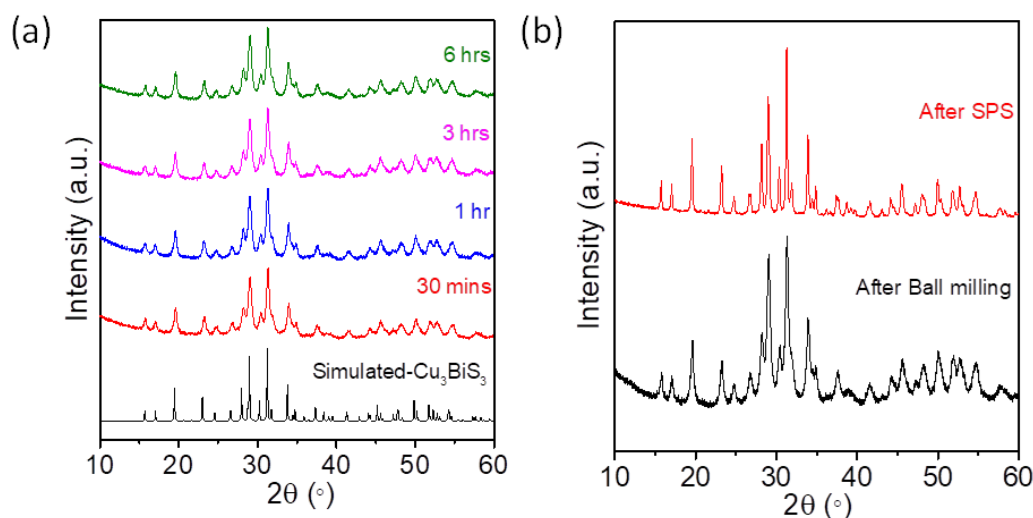


**Figure 4.1.** (a) XRPD patterns of ball-milled powders for different ball-milling times. (b) XRPD patterns after 6 hrs ball milling and after SPS.

The broadness of the diffraction peaks, inherent to the synthesis method,<sup>8,43</sup> is related to low crystallinity and/or small crystallite size of the powder samples similar as the aikinite series samples. Powders were then placed in graphite dies of 10 mm diameter and densified by spark plasma sintering (SPS) at 593 K for 30 mins under a pressure of 64 MPa with heating and cooling rates of 50 and 20 K min<sup>-1</sup>, respectively. This produced 10 mm diameter pellets, c. a. 9 mm thickness, with geometrical densities greater than 95% of the theoretical value. The XRPD pattern after SPS reveals only microstructural evolution of the sample evidenced by the much sharper diffraction peaks after ball-milling, indicating crystallite growth and improvement of crystallinity (**Figure 4.1b**).

## 4.3. Results and Discussion

### 4.3.1. Crystal structure study

The X-ray powder diffraction (XRPD) pattern of pristine  $\text{Cu}_3\text{BiS}_3$  after SPS recorded at RT, is indexed with an orthorhombic unit cell of space group  $P2_12_12_1$  exhibiting refined unit cell parameters  $a = 7.6642(2) \text{ \AA}$ ,  $b = 10.4202(3) \text{ \AA}$ , and  $c = 6.7044(2) \text{ \AA}$ . High quality Rietveld refinement (**Figure 4.2**) is obtained by considering the structural model of wittichenite,  $\text{Cu}_3\text{BiS}_3$ , published by Kocman and Nuffield,<sup>41</sup> where Cu, Bi and S atoms are located on three, one and three different  $4a$  sites of general multiplicity, respectively. Moreover, the absence of non-indexed diffraction peaks suggests the formation of high purity  $\text{Cu}_3\text{BiS}_3$  sample after SPS. The refined cell parameters and atomic coordinates of pristine sample are given in **Table 4.1**.

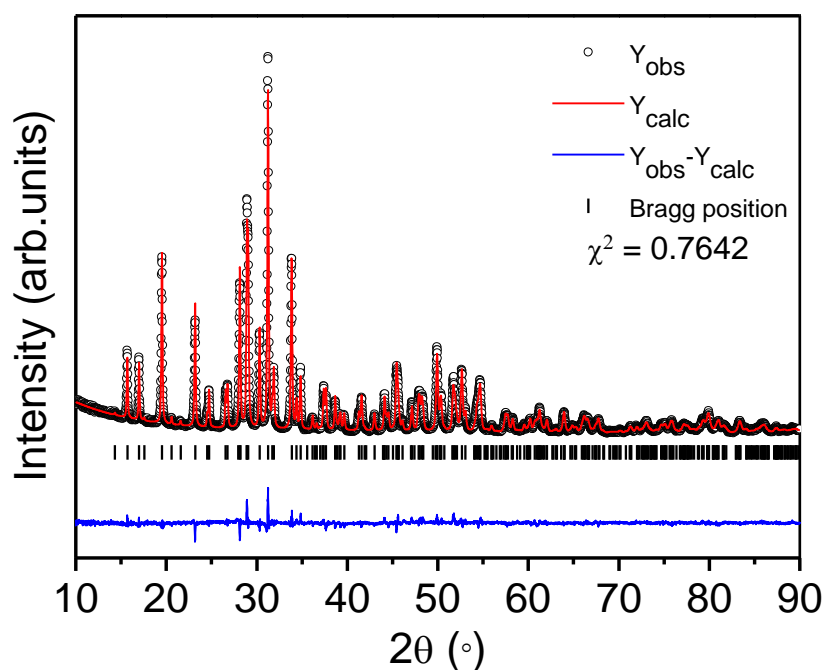


**Figure 4.2.** Rietveld refinement of the PXRD data recorded at RT for  $\text{Cu}_3\text{BiS}_3$  sample ( $\lambda = 1.5406 \text{ \AA}$ ).

**Table 4.1.** Refined Cell Parameters and Atomic Coordinates of Spark Plasma Sintered Pristine  $\text{Cu}_3\text{BiS}_3$  ( $P2_12_12_1$ ).

| atom  | site | x          | y          | z          | $B_{\text{iso}} (\text{\AA}^2)$ | SOF  |
|-------|------|------------|------------|------------|---------------------------------|------|
| Bi(1) | 4a   | 0.1953(1)  | -0.2434(2) | 0.1281(1)  | 0.43(4)                         | 1.00 |
| Cu(1) | 4a   | 0.3477(6)  | 0.4007(4)  | 0.1298(8)  | 1.86(14)                        | 1.00 |
| Cu(2) | 4a   | 0.1897(6)  | 0.1062(5)  | 0.0810(8)  | 3.99(16)                        | 1.00 |
| Cu(3) | 4a   | 0.0568(6)  | 0.4646(4)  | -0.0307(8) | 1.04(14)                        | 1.00 |
| S(1)  | 4a   | -0.4474(8) | 0.2518(13) | 0.1094(12) | 1.01(16)                        | 1.00 |
| S(2)  | 4a   | 0.3215(12) | 0.4379(9)  | 0.4119(15) | 1.01(22)                        | 1.00 |
| S(3)  | 4a   | 0.3145(11) | 0.0732(10) | 0.4118(19) | 1.71(32)                        | 1.00 |

---

$a = 7.6642(2) \text{ \AA}$ ,  $b = 10.4202(3) \text{ \AA}$ ,  $c = 6.7044(2) \text{ \AA}$   
 $R_{\text{Bragg}} = 3.96$ ,  $R_{\text{F}} = 2.15$ ,  $R_{\text{wp}} = 10.2$ ,  $R_{\text{exp}} = 11.95$ ,  $\chi^2 = 0.72$

In  $\text{Cu}_3\text{BiS}_3$ , Bi atom is three-fold coordinated by S (CN = 3, **Figure 4.2c**). Bi-S distances ranging from 2.567 Å to 2.614 Å and S-Bi-S angles from 95.44° to 96.62°, lead to an average Bi-S distance ( $\overline{d_{\text{Bi-S}}}$ ) of 2.584 Å and an average S-Bi-S angle ( $\overline{\alpha_{\text{S-Bi-S}}}$ ) of 96.00°. These values are in fair agreement with those encountered in  $\text{CuBiS}_2$  (**Table 4.2**), a ternary Cu-based sulfide involving  $\text{Bi}^{3+}$  with a similar environment of sulfur,<sup>44</sup> and indicate that the local environment of Bi atoms is intermediate between triangular and tetrahedral coordination. Note that Kocman and Nuffield<sup>41</sup> reported an electron density excess in the proximity of the Bi atoms, which is most probably related to the LP of  $\text{Bi}^{3+}$ . Hence, in wittichenite, the coordination environment of Bi atom should be viewed as a strongly distorted tetrahedron  $\text{BiS}_3\text{LP}$  where one apex is occupied by the  $6s^2$  electronic lone pair of  $\text{Bi}^{3+}$ . This structural feature is encountered in other ternary Cu-based sulfides involving a group VA element with a lone pair of electrons (i.e.  $\text{As}^{3+}$ ,  $\text{Sb}^{3+}$ ,  $\text{Bi}^{3+}$ ), and for which the Cu/M ratio is equal or superior to 1, like sinnerite  $\text{Cu}_6\text{As}_4\text{S}_9$ ,<sup>45</sup> tennantite  $\text{Cu}_{12}\text{As}_4\text{S}_{13}$ ,<sup>46,47</sup> tetrahedrite  $\text{Cu}_{12}\text{Sb}_4\text{S}_{13}$ ,<sup>34,42</sup> skinnerite  $\text{Cu}_3\text{SbS}_3$ ,<sup>48,49</sup> chalcostibite  $\text{CuSbS}_2$ ,<sup>50,51</sup> and emplectite  $\text{CuBiS}_2$ <sup>44</sup> (**Table 4.2**). Moreover, in  $\text{Cu}_3\text{BiS}_3$ , all Cu atoms are in nearly trigonal planar

coordination with S (CN = 3, **Figure 4.2a, b**), characterized by Cu-S distances ranging from 2.211 to 2.330 Å and S-Cu-S angles ranging from 109.97 to 132.85°. This leads to average Cu-S distance ( $\overline{d_{Cu-S}}$ ) of 2.274 Å and an average S-Cu-S angle ( $\overline{\alpha_{S-Cu-S}}$ ) of 119.64°, equivalent to those found for the Cu atoms in triangular coordination of sulfur in  $Cu_4Bi_4S_9$  (**Table 4.2**), another ternary Cu-based sulfide involving  $Bi^{3+}$  cations.<sup>52,53</sup> Such type of Cu triangular planar coordination can also be seen in few ternary Cu-based sulfides involving a group VA element with a LP, and Cu/M ratio  $\geq 1$ , like tennantite ( $Cu_{12}As_4S_{13}$ ),<sup>46,47</sup> tetrahedrite ( $Cu_{12}Sb_4S_{13}$ )<sup>34,42</sup> and skinnerite ( $Cu_3SbS_3$ ),<sup>48,49</sup> (**Table 4.2**). Some of these phases exhibit intrinsically low lattice thermal conductivity due to LPs associated to elements of the group VA and to a large anisotropic thermal displacement of Cu atoms.<sup>49,52,54–56</sup> (See discussion on the thermal properties in the last paragraph).

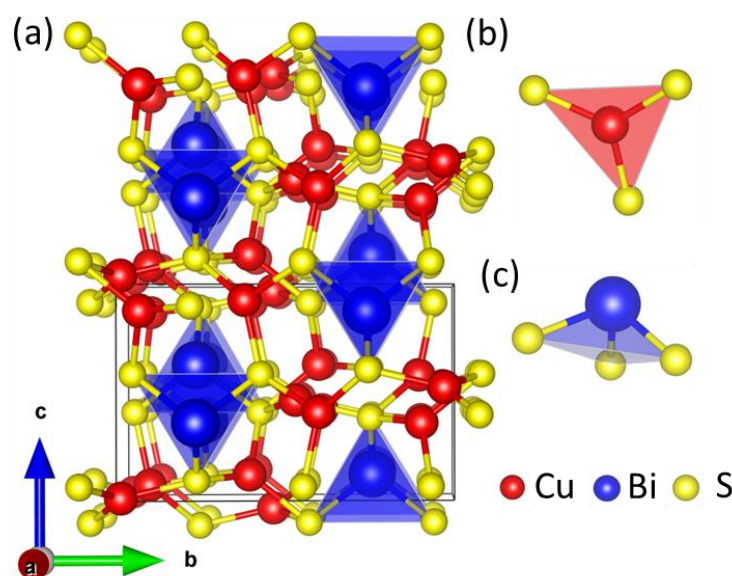


**Figure 4.2.** (a) Orthorhombic crystal structure of  $Cu_3BiS_3$  (space group –  $P2_12_12_1$ ), (b) triangular planar environment of Cu atoms and (c) pyramidal coordination environment of Bi atoms.

**Table 4.2.** Main interatomic distances ( $\text{\AA}$ ) and angles ( $^\circ$ ) encountered in ternary Cu-M-S compounds where M is a group VA chalcogenide with a lone pair of electrons.

| Compound   | Mineral name | T (K) | Space group                                     | CN (Cu) | $\langle d_{\text{Cu-S}} \rangle$ | $\overline{d_{\text{Cu-S}}}$ | $\langle \alpha_{\text{S-Cu-S}} \rangle$ | $\overline{\alpha_{\text{S-Cu-S}}}$ | CN (M)     | $\langle d_{\text{M-S}} \rangle$            | $\overline{d_{\text{M-S}}}$ | $\langle \alpha_{\text{S-M-S}} \rangle$      | $\overline{\alpha_{\text{S-M-S}}}$ | Ref.          |
|--|--------------|-------|---|---------|-----------------------------------|------------------------------|--|-------------------------------------|------------|---|-----------------------------|--|------------------------------------|---------------|
| Cu <sub>6</sub> As <sub>4</sub> S <sub>9</sub>   | sinnerite    | 293   | <i>P1</i>                                       | 4       | 2.110-2.542                       | 2.304                        | 98.57-122.62                             | 109.39                              | 3          | 2.138-2.542                                 | 2.289                       | 98.13-113.15                                 | 105.42                             | <sup>45</sup> |
| Cu <sub>12</sub> As <sub>4</sub> S <sub>13</sub> | tennantite   | 293   | <i>I<math>\bar{4}3m</math></i>                  | 3<br>4  | 2.256-2.297<br>2.284              | 2.270<br>2.284               | 102.69-128.65<br>109.11-110.19           | 120.00<br>109.47                    | 3          | 2.215                                       | 2.215                       | 103.57                                       | 103.57                             | <sup>46</sup> |
| Cu <sub>12</sub> Sb <sub>4</sub> S <sub>13</sub> | tetrahedrite | 293   | <i>I<math>\bar{4}3m</math></i>                  | 3<br>4  | 2.234-2.272<br>2.342              | 2.259,<br>2.342              | 96.31-131.85,<br>106.53-110.96           | 120.00,<br>109.48                   | 3          | 2.446                                       | 2.446                       | 95.132                                       | 95.132                             | <sup>42</sup> |
| Cu <sub>12</sub> Sb <sub>4</sub> S <sub>13</sub> | tetrahedrite | 20    | <i>P<math>\bar{4}c2</math></i>                  | 3<br>4  | 2.179-2.443<br>2.278-2.333        | 2.265,<br>2.313              | 91.15-152.95,<br>96.49-116.49            | 119.92,<br>109.47                   | 3          | 2.410-2.470                                 | 2.447                       | 95.48-100.73                                 | 97.03                              | <sup>34</sup> |
| Cu <sub>3</sub> SbS <sub>3</sub>                 | skinnerite   | 298   | <i>P2<sub>1</sub>/c</i>                         | 3       | 2.239-2.359                       | 2.282                        | 109.48-131.10                            | 119.65                              | 3          | 2.446-2.478                                 | 2.465                       | 96.97-100.77                                 | 98.33                              | <sup>48</sup> |
| Cu <sub>3</sub> SbS <sub>3</sub>                 | skinnerite   | 228   | <i>P2<sub>1</sub>2<sub>1</sub>2<sub>1</sub></i> | 3       | 2.200-2.363                       | 2.296                        | 110.36-133.39                            | 119.66                              | 3          | 2.452-2.498                                 | 2.467                       | 96.28-99.61                                  | 97.79                              | <sup>49</sup> |
| CuSbS <sub>2</sub>                               | chalcocite   | 293   | <i>Pnma</i>                                     | 4       | 2.272-2.316                       | 2.305                        | 105.41-110.90                            | 109.46                              | 3          | 2.449-2.590                                 | 2.543                       | 94.29-95.14                                  | 94.86                              | <sup>51</sup> |
| CuBiS <sub>2</sub>                               | emplectite   | 293   | <i>Pnma</i>                                     | 4       | 2.304-2.343                       | 2.327                        | 107.28-113.52                            | 109.44                              | <b>3</b>   | 2.537-2.653                                 | <b>2.614</b>                | 95.24-96.56                                  | <b>96.12</b>                       | <sup>44</sup> |
| Cu <sub>4</sub> Bi <sub>4</sub> S <sub>9</sub>   | -            | 293   | <i>Pnma</i>                                     | 3<br>4  | 2.228-2.337<br>2.233-2.403        | 2.277,<br>2.357              | 112.04-122.30,<br>100.07-126.44          | 117.28,<br>109.37                   | 5, 6,<br>7 | 2.599-3.067,<br>2.694-3.050,<br>2.631-3.148 | 2.811,<br>2.857,<br>2.949   | 80.21-94.16,<br>80.72-98.40,<br>64.11-140.97 | 87.51,<br>90.01,<br>95.13          | <sup>52</sup> |
| Cu <sub>3</sub> BiS <sub>3</sub>                 | wittichenite | 293   | <i>P2<sub>1</sub>2<sub>1</sub>2<sub>1</sub></i> | 3       | 2.211-2.330                       | 2.274                        | 109.97-132.85                            | 119.64                              | 3          | 2.567-2.614                                 | 2.584                       | 95.44-96.62                                  | 96.00                              | This work     |

In order to broaden our scope into the crystal structure analysis of Cu<sub>3</sub>BiS<sub>3</sub>, precession-assisted electron diffraction tomography (PEDT) measurements have been performed on several specimens, which present good reproducibility. The structural data determined from one PEDT measurement are reported in **Table 4.3** and **Table 4.4**, and the corresponding bond distances and bond angles are gathered in **Table 4.5**.

**Table 4.3.** Anisotropic displacement parameters ( $\text{\AA}^2$ ) of atoms in Cu<sub>3</sub>BiS<sub>3</sub> from PEDT

| Atom  | U11     | U22     | U33     | U12      | U13      | U23      |
|-------|---------|---------|---------|----------|----------|----------|
| Bi(1) | 0.02114 | 0.02127 | 0.02889 | -0.00134 | 0.00336  | -0.00375 |
| Cu(1) | 0.04407 | 0.03862 | 0.02158 | 0.01619  | 0.00390  | -0.00331 |
| Cu(2) | 0.08758 | 0.03627 | 0.03811 | 0.02633  | -0.00085 | 0.00881  |
| Cu(3) | 0.02303 | 0.02282 | 0.05243 | -0.00489 | 0.01052  | -0.00143 |
| S(1)  | 0.01708 | 0.00874 | 0.02282 | 0.00264  | -0.00166 | -0.00271 |
| S(2)  | 0.01892 | 0.01153 | 0.01425 | -0.00431 | 0.00658  | -0.00230 |
| S(3)  | 0.02053 | 0.01935 | 0.00513 | -0.00346 | -0.00396 | -0.00069 |

**Table 4.4.** Room temperature structural data of  $\text{Cu}_3\text{BiS}_3$  from PEDT

| $\text{Cu}_3\text{BiS}_3$ $P2_12_12_1$ , $a = 7.6862 \text{ \AA}$ , $b = 10.3998 \text{ \AA}$ , $c = 6.7317 \text{ \AA}$ , $V = 538.098 \text{ \AA}^3$ |          |          |          |                     |
|--|----------|----------|----------|---------------------|
| Atom   | x        | y        | z        | U( $\text{\AA}^2$ ) |
| Bi(1)  | 0.19762  | -0.24516 | 0.12798  | 0.024               |
| Cu(1)  | 0.34789  | 0.40105  | 0.14037  | 0.035               |
| Cu(2)  | 0.19287  | 0.10504  | 0.07632  | 0.054               |
| Cu(3)  | 0.05761  | 0.46417  | -0.02441 | 0.033               |
| S(1)   | -0.44536 | 0.24979  | 0.10712  | 0.016               |
| S(2)   | -0.31984 | 0.43813  | -0.41179 | 0.015               |
| S(3)   | -0.32082 | 0.06980  | -0.41442 | 0.015               |

These results confirm the structural model published by Kocman and Nuffield<sup>41</sup> and are in excellent agreement with the bond distances and bond angles determined from Rietveld refinement of the XRPD pattern. Moreover these PEDT results evidence unambiguously large anisotropic displacement parameters for all Cu atoms, especially for Cu(2), as illustrated in **Figure 4.3**.

**Table 4.5.** Bond distances and bond angles in  $\text{Cu}_3\text{BiS}_3$  (structural data from PEDT)

|                                 | Distance ( $\text{\AA}$ ) |  | Angle ( $^\circ$ ) |
|---------------------------------|---------------------------|--|--------------------|
| Bi(1)-S(2)                      | 2.5756                    | S(2)-Bi(1)-S(3)                        | 95.93              |
| Bi(1)-S(3)                      | 2.5820                    | S(1)-Bi(1)-S(3)                        | 95.62              |
| Bi(1)-S(1)                      | 2.6093                    | S(1)-Bi(1)-S(2)                        | 97.75              |
| $\overline{d_{\text{Bi-S}}}$    | 2.5890                    | $\overline{\alpha_{\text{S-Bi-S}}}$    | 96.43              |
| Cu(1)-S(1)                      | 2.2472                    | S(3)-Cu(1)-S(3)                        | 112.20             |
| Cu(1)-S(3)                      | 2.2753                    | S(1)-Cu(1)-S(3)                        | 121.67             |
| Cu(1)-S(3)                      | 2.3317                    | S(1)-Cu(1)-S(3)                        | 125.22             |
| $\overline{d_{\text{Cu(1)-S}}}$ | 2.2847                    | $\overline{\alpha_{\text{S-Cu(1)-S}}}$ | 119.70             |
| Cu(2)-S(1)                      | 2.2210                    | S(2)-Cu(2)-S(2)                        | 110.25             |
| Cu(2)-S(2)                      | 2.2786                    | S(1)-Cu(2)-S(2)                        | 116.90             |
| Cu(2)-S(2)                      | 2.3046                    | S(1)-Cu(2)-S(2)                        | 131.07             |
| $\overline{d_{\text{Cu(2)-S}}}$ | 2.2681                    | $\overline{\alpha_{\text{S-Cu(2)-S}}}$ | 119.41             |
| Cu(3)-S(2)                      | 2.2241                    | S(1)-Cu(3)-S(3)                        | 114.93             |

|                          |        |                                 |        |
|--------------------------|--------|---------------------------------|--------|
| Cu(3)-S(1)               | 2.2939 | S(1)-Cu(3)-S(2)                 | 121.18 |
| Cu(3)-S(3)               | 2.3387 | S(2)-Cu(3)-S(3)                 | 123.80 |
| $\overline{d_{Cu(3)-S}}$ | 2.2856 | $\overline{\alpha_{S-Cu(3)-S}}$ | 119.97 |

It is important to analyze the structural behavior of copper and bismuth separately for properly characterizing the relationships between the structure and the electrical/thermal properties of this sulfide. This sulfide exhibits a  $[Cu_3S_3]$  three-dimensional framework built up of corner-sharing triangular  $CuS_3$  groups (**Figure 4.4**). Two copper atoms (labelled Cu(1) and Cu(2)) form infinite corrugated layers (**Figure 4.4a**) of corner-sharing  $CuS_3$  groups parallel to (010). In those layers, each S atom is shared between two  $Cu^+$  cations. The Cu(1)/Cu(2) layers are interleaved with  $Bi^{3+}$  layers whose  $6s^2$  LP is probably alternately up and down oriented. Note that each copper cation belonging to these layers is sandwiched between two bismuth cations of the two adjacent bismuth layers, forming interatomic  $Bi \cdots Cu \cdots Bi$  distances of about 3.8 Å. Bearing in mind that the  $6s^2$   $Bi^{3+}$  lone pair (LP) may behave as an anion, the existence of  $LP^\delta \cdots Cu^+ \cdots LP^\delta$  interactions with distances of about 2.7 Å is most probable. Thus, this geometry explains the anisotropic rattling of the copper cations along the direction perpendicular to the  $S_3$  plane inside a  $LPS_3LP$  cage, like to a strongly distorted trigonal bipyramid. The third copper atom, labeled Cu(3) ensures the connection between two copper layers, sharing two of its apices with a same layer and the third one with the next layer (**Figure 4.4b**).

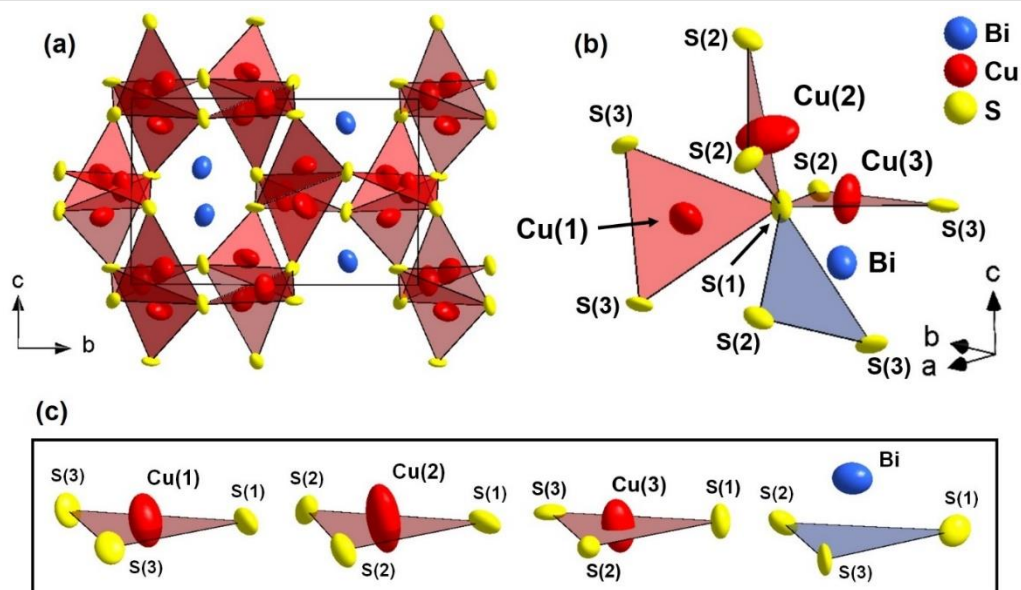


**Figure 4.3.** Crystal structure representations of  $\text{Cu}_3\text{BiS}_3$  highlighting the large anisotropic displacements of Cu atoms in (a) the unit cell, (b) the polyhedron connection around the  $\text{S}(1)$  atom, and (c) the triangular configuration of Cu atoms and tetrahedral  $\text{BiS}_3\text{LP}$  configuration of Bi atom. Displacement ellipsoids are shown at the 90% probability level.

Note that these triangular  $\text{CuS}_3$  groups are isolated one from the others. As already discussed, the bismuth cations are three-fold coordinated to sulfur, forming a tetrahedron  $\text{BiS}_3\text{LP}$  with their  $6s^2$  LP, and they are isolated one from the other atoms in the structure. Finally, it is worth pointing out that the crystal structure consists of infinite  $\text{Cu}_3\text{BiS}_3$  chains parallel to  $[001]$  which are linked by Cu-S bonds to form continuous sheets normal to  $[010]$ , as previously described by Kocman and Nuffield.<sup>41</sup> The short distances, ranging from 2.610 and 2.743 Å, connect  $\text{Cu}(1)$  and  $\text{Cu}(3)$  atoms, making infinite chains along the  $c$  direction.  $\text{Cu}(2)$  atoms are further away from other Cu atoms; the shortest  $\text{Cu}(2)$ -Cu contact is equal to ca. 3 Å.

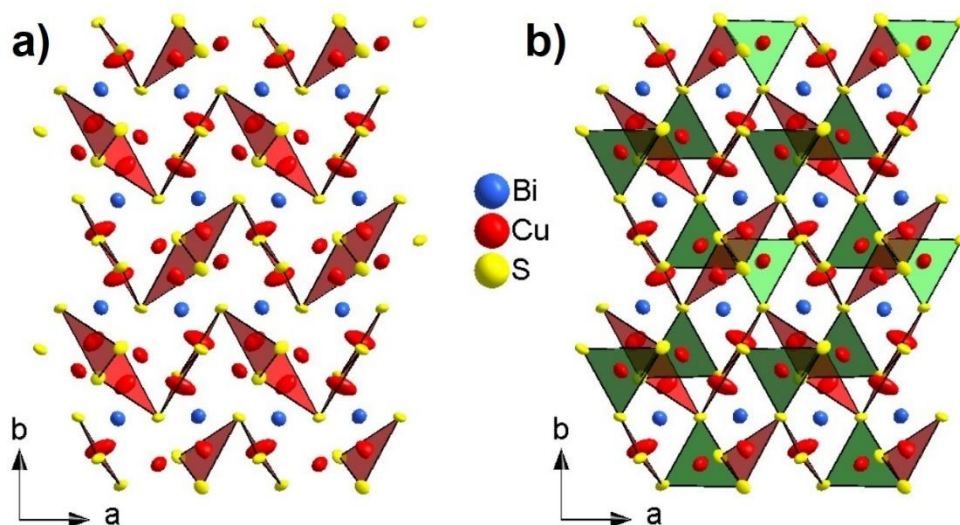


**Figure 4.4.** Three-dimensional “ $\text{Cu}_3\text{S}_3$ ” framework of  $\text{Cu}_3\text{BiS}_3$ : (a) Infinite corrugated layers of corner-sharing three-fold coordinated copper  $\text{Cu}(1)$  and  $\text{Cu}(2)$  parallel to  $(010)$  (red coloured triangles) interleaved with bismuth layers (blue coloured atoms), (b) Introduction of the three-fold  $\text{Cu}(3)$  (green coloured triangles) to form the 3D “ $\text{Cu}_3\text{S}_3$ ” framework.

### 4.3.2. Microstructure study

Scanning electron microscopy (SEM) images of a fractured surface indicate a non-uniform grain size and fine microstructure (as shown in **Figure 4.5a** and **4.5b**). Observations on polished surfaces (**Figure 4.5c** and **4.5d**) confirms a good sample homogeneity and the presence of few secondary phase particles ( $\text{CuS}$  or  $\text{Cu}_{2-\delta}\text{S}$ , as shown in round red circle), which can be observed both in the fractured and polished surface (**Figure 4.5b** and **4.5d**).

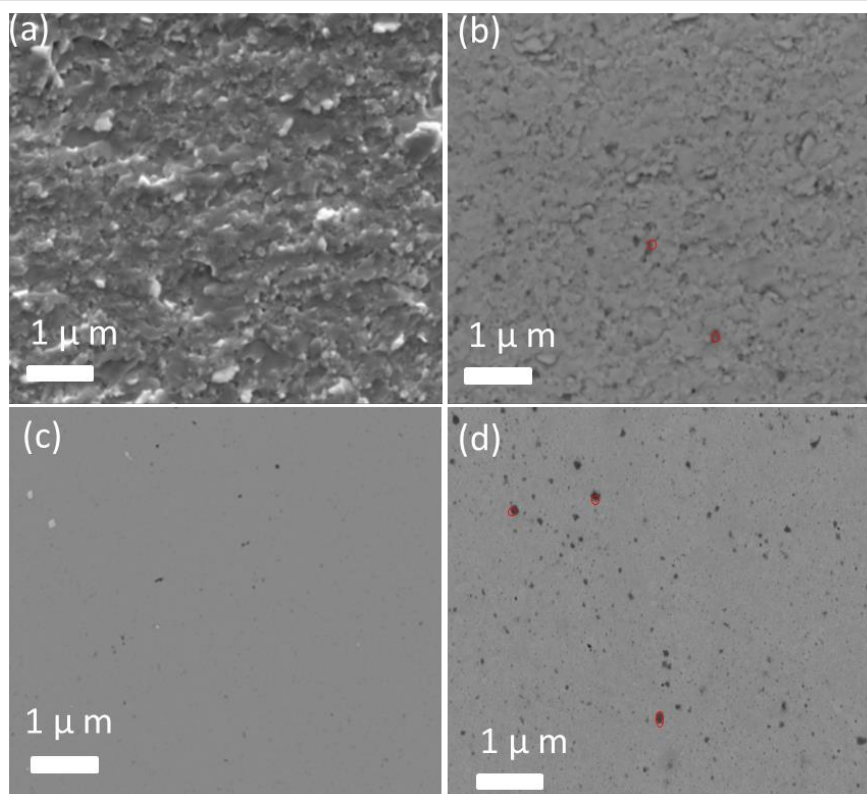


**Figure 4.5.** Back scattered SEM images of pristine  $\text{Cu}_3\text{BiS}_3$ , (a, b) show the small grain from crust sample after SPS. (c, d) show bubble like cavity and very little impurity (probably  $\text{Cu}_2\text{S}$  found in TEM analysis, covered with red circle)

Notably, this secondary phase was not detected by XRPD despite the high quality (i.e. large signal to noise ratio) of the data. Note that bubble-like nano cavities are observed in the SEM images and can be attributed to incomplete sintering and/or sulfur evaporation during SPS process. In general, this phenomenon can be found in sulfide-based materials like in aikinite-type compounds.<sup>8</sup>

The structural, microstructural, and chemical analyses of the pristine  $\text{Cu}_3\text{BiS}_3$  sample were also performed by TEM. As shown in **Figure 4.6a** from low-magnification TEM image, pristine  $\text{Cu}_3\text{BiS}_3$  sample exhibits quite small and isotropic grains with typical sizes ranging between few tens of nanometres to 200 nm. Such small grain size is typically observed in samples prepared by mechanical-alloying followed by SPS treatment.<sup>8,43</sup> High resolution TEM (HRTEM) images obtained along two different

directions through tilting series on the same grain are depicted in **Figure 4.6c and 4.6d**. These two HRTEM images, and related diffraction patterns (insets) can be assigned respectively to the  $[111]$  and  $[\bar{2}5\bar{1}]$  zone axes of the orthorhombic  $\text{Cu}_3\text{BiS}_3$  phase, which further confirm the above structural results. EDX mapping shows large zones with homogenous distribution of Cu, Bi, and S atoms (**Figure 4.6b**).

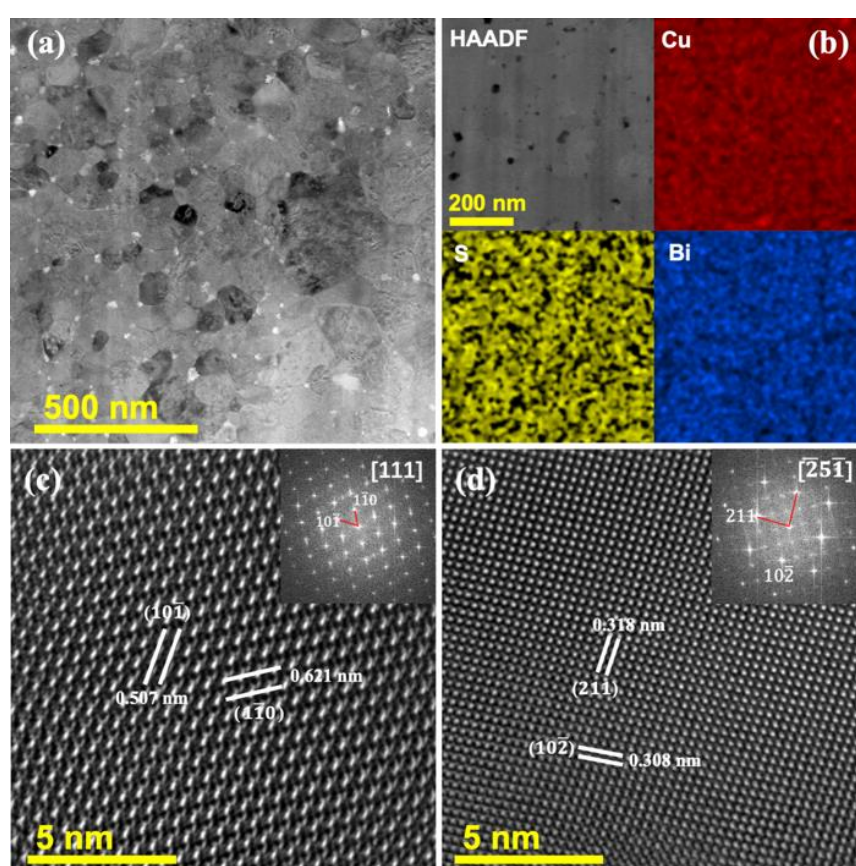


**Figure 4.6.** TEM characterizations of  $\text{Cu}_3\text{BiS}_3$  FIB-lamella. (a) low-magnification TEM image, (b) EDX mapping of  $\text{Cu}_3\text{BiS}_3$ , (c, d) HRTEM images of  $\text{Cu}_3\text{BiS}_3$  crystallites

### 4.3.3. Thermal stability study

Regarding the stability of this compound, a previous article by Makovicky<sup>57</sup> has highlighted that  $\text{Cu}_3\text{BiS}_3$  phase exhibits a phase transition from RT orthorhombic ( $P2_12_12_1$ ) structure to intermediate modulated ( $Pn2_1a$  or  $Pnma$ ) structure at 391.5 K,

above 464 K, the high temperature unmodulated polymorph (*Pnma*) is formed. Lately, high temperature *in situ* XRPD has showed that the phase transition from low temperature  $P2_12_12_1$  polymorph to high temperature polymorph occurs between 373 K to 395 K.<sup>37</sup> We have then measured the evolution of  $C_p$  within the temperature range of 350 K to 573 K (**Figure 4.7a**). These data revealed an abrupt change in  $C_p$  at around 373 K which can be attributed to phase transition from the RT to HT polymorph. Above 450 K, this HT polymorph phase is stabilized which is further confirmed by the differential scanning calorimetry (DSC) study (**Figure 4.7b**). The change of slope observed in the electrical resistivity and Seebeck coefficient around 375 K can then be attributed to this structural transition. The satellite peaks in between 373 K to 450 K represent the intermediate phase(s) reported by Mizota *et al.*<sup>58</sup> To check the thermal stability of our sample, we have performed thermogravimetric analysis (TGA), showing that the compound starts to decompose above 580 K (**Figure 4.7b**). The cycling measurements of TE properties presented later (**Figure 4.11**) indicate the stability up to 563 K.

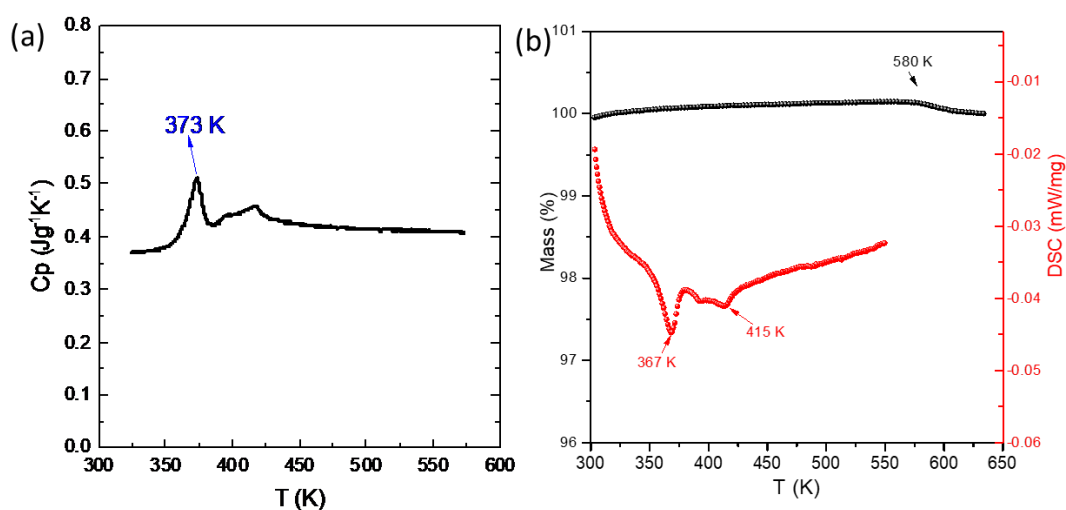


**Figure 4.7.** (a)  $C_p$  versus  $T$  plot for  $\text{Cu}_3\text{BiS}_3$ , (b) Thermogravimetric analysis (TGA) and Differential scanning calorimetry (DSC) of  $\text{Cu}_3\text{BiS}_3$ .

### 4.3.4. Electrical properties

The temperature dependence of the electrical resistivity ( $\rho$ ) is shown in **Figure 4.8a**. The  $\rho(T)$  curve follows a non-degenerate semiconducting behavior with values decreasing from 130  $\Omega$  cm at 300 K to 0.36  $\Omega$  cm at 563 K. In the previous studies on  $\text{Cu}_3\text{BiS}_3$ , Wei *et al.* reported a comparable value of 140  $\Omega$  cm at RT while Adeyemi *et al.* measured an electrical resistivity value of 17.2  $\Omega$  cm at 318 K, i.e. one order of magnitude lower than our value.<sup>36,37</sup> The high electrical resistivity in our sample is consistent with its high Seebeck coefficient of 800  $\mu\text{V K}^{-1}$  at RT (**Figure 4.8b**) and relatively low carrier concentration of  $1.7 \times 10^{16} \text{ cm}^{-3}$ . Those values attest of the high purity and stoichiometry of our compound thanks to the synthesis approach which combines mechanical-alloying followed by SPS, preventing from heavy sulfur loss and stoichiometric deviation.<sup>8</sup> Note that the phase formation of  $\text{Cu}_3\text{BiS}_3$  is extremely fast (less than 30 min) during mechanical-alloying (as described in the experimental section), and the subsequent SPS treatment allows to quickly complete the reaction and crystallization at relatively low sintering temperature.

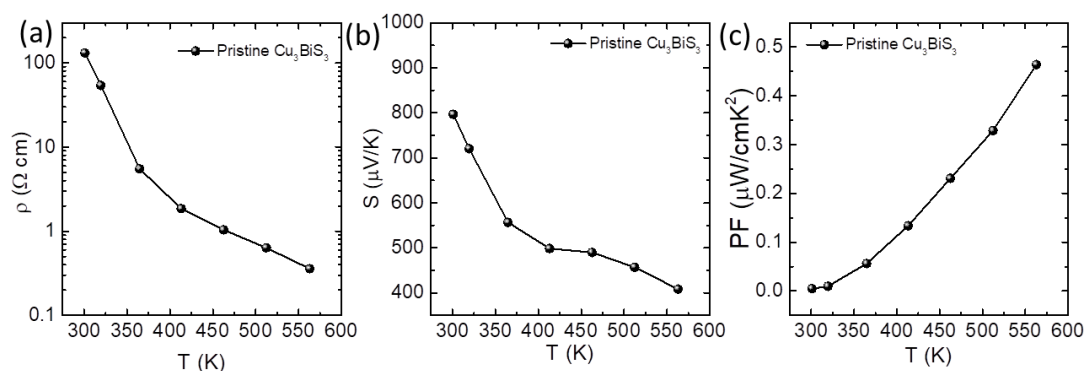


**Figure 4.8.** Temperature dependence from 300 K up to 563 K of (a) electrical resistivity, (b) Seebeck coefficient, (c) power factor, and (d) figure of merit ( $ZT$ ) in pristine  $\text{Cu}_3\text{BiS}_3$ .

All attempts to hole dope  $\text{Cu}_3\text{BiS}_3$  in the present sulfide using different dopants and synthesis techniques were proved fruitless although the structure of  $\text{Cu}_3\text{BiS}_3$ , built up of

a 3D framework of interconnected  $\text{CuS}_3$  triangles should favor an overlapping of the copper and sulfur orbitals and consequently hole delocalization. In order to clarify this point, DOS and COHP for main contacts were computed for  $\text{Cu}_3\text{BiS}_3$ ; corresponding curves are sketched in **Figures 4.9 and Figure 4.10a**. Summing COHP values up to the Fermi level gives access to the contribution of a chemical bond to the distribution of one-particle energies and indicates the total bond strength. Those values are equal to -4.01 eV, -2.99 eV and -1.49 eV for Cu-S, Bi-S and Cu-Cu contacts, respectively, showing that a metal-metal bonding is significant between copper atoms in this structure. The width of the band gap computed at the PBE level is equal to 0.8 eV which is slightly less than the experimental band gap ( $\sim 1.1$  eV) (**Figure 4.10a, b**). The bottom of the conduction band is dominated by Bi atoms and shows significant Bi-S and Cu-S antibonding character. The top of the valence band is mainly centered on copper atoms and exhibit an antibonding Cu-S character. It is noteworthy to mention that these bands located at the top of the valence band are overall Bi-S and Cu-Cu nonbonding. Analysis of the electronic charge distribution and electron localization function (ELF) (**Figure 4.10c**) reveal the presence of directional covalent bonds between  $\text{Bi}^{3+}$  and  $\text{S}^{2-}$ , as well as that of a LP on the  $\text{Bi}^{3+}$  cations.  $\text{Cu}^+$  shows a very weak electrostatic interaction with the environment, which support its high rattling behavior.

Owing to these calculations and assuming a rigid band model, oxidation and/or *p*-doping of the title compound should strengthen the bonding in this structure. The electronic structures of several hypothetical compounds of general formula  $\text{Cu}_3\text{Bi}_{2.75}\text{M}_{0.25}\text{S}_3$  ( $\text{M} = \text{Ca}, \text{Cd}, \text{Pb}, \text{Sn}, \text{Sr}$ ) have been studied; DOS are given in the Supporting Information section. Those results confirm the rigid band model, *i. e.* the band structure is hardly affected by this doping, suggesting that such doping may not enhance the thermopower of this structure. Such a hole blockade was also observed for monoclinic  $\text{Cu}_2\text{S}$  chalcocite whose 3D Cu-S framework is built of corner-sharing  $\text{CuS}_3$  groups exclusively.<sup>59,60</sup> In the same way, the monoclinic or orthorhombic forms of the skinnerite ( $\text{Cu}_3\text{SbS}_3$ ) which involve interconnected  $\text{CuS}_3$  groups were found to exhibit a high resistivity and no possibility of doping was reported for these compounds.<sup>49,55</sup>

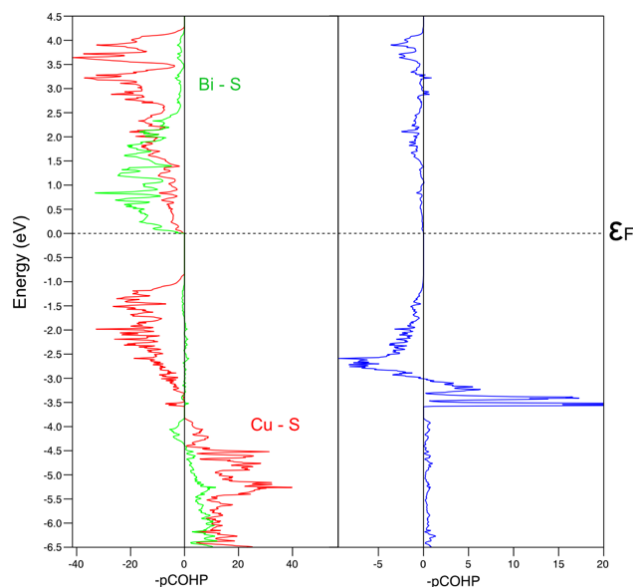


**Figure 4.9.** COHP computed for Cu-S, Cu-Cu and Bi-S contacts in  $\text{Cu}_3\text{BiS}_3$ .

This hole blockade most probably originates from the strong rattling of the copper cations with respect to their three S neighbors, leading to large displacements of  $\text{Cu}^+$ , up to  $0.9 \text{ \AA}$  from the center of the “S3” plane. Consequently, the overlapping of the Cu and S orbitals is significantly weakened, hindering hole carriers exchange between two  $\text{CuS}_3$  groups. This hypothesis is supported by the fact that the replacement of  $\text{CuS}_3$  groups in the chalcocite by  $\text{CuS}_4$  tetrahedra leading to the digenite  $\text{Cu}_{1.96}\text{S}$  structure induces the formation of high carrier concentrations.<sup>61</sup> In a similar way, the metastable cubic form of  $\text{Cu}_3\text{SbS}_3$  consisting of interconnected  $\text{CuS}_4$  tetrahedra can also exhibit high carrier concentration of  $10^{20} \text{ cm}^{-3}$  by doping, in agreement with the fact that the majority of copper is in tetrahedral coordination and does not exhibit any abnormally high anisotropic vibration. In a more general way, we can affirm that all the Cu-rich sulfides which exhibit a pure tetrahedral copper framework (i.e. group A phases with  $\text{Cu}/\text{M} \geq 1$  from copper-based sulfides classification<sup>62</sup> are *p*-type conductors and can exhibit high hole carrier concentration by doping, as previously shown for  $\text{Cu}_5\text{Sn}_2\text{S}_7$ ,<sup>63</sup>  $\text{Cu}_{22}\text{Sn}_{10}\text{S}_{32}$ ,<sup>64</sup>  $\text{Cu}_3\text{SbS}_4$ ,<sup>65</sup>  $\text{Cu}_2\text{SnS}_3$ <sup>66</sup> and  $\text{Cu}_2(\text{Fe,Zn})\text{SnS}_4$ <sup>67,68</sup>. In other words, these results strongly suggest that the three-fold coordination of copper is detrimental to the generation and delocalization of hole carriers in the Cu-rich sulfides, hindering the possibility to induce the mixed valency  $\text{Cu}^+/\text{Cu}^{2+}$ .

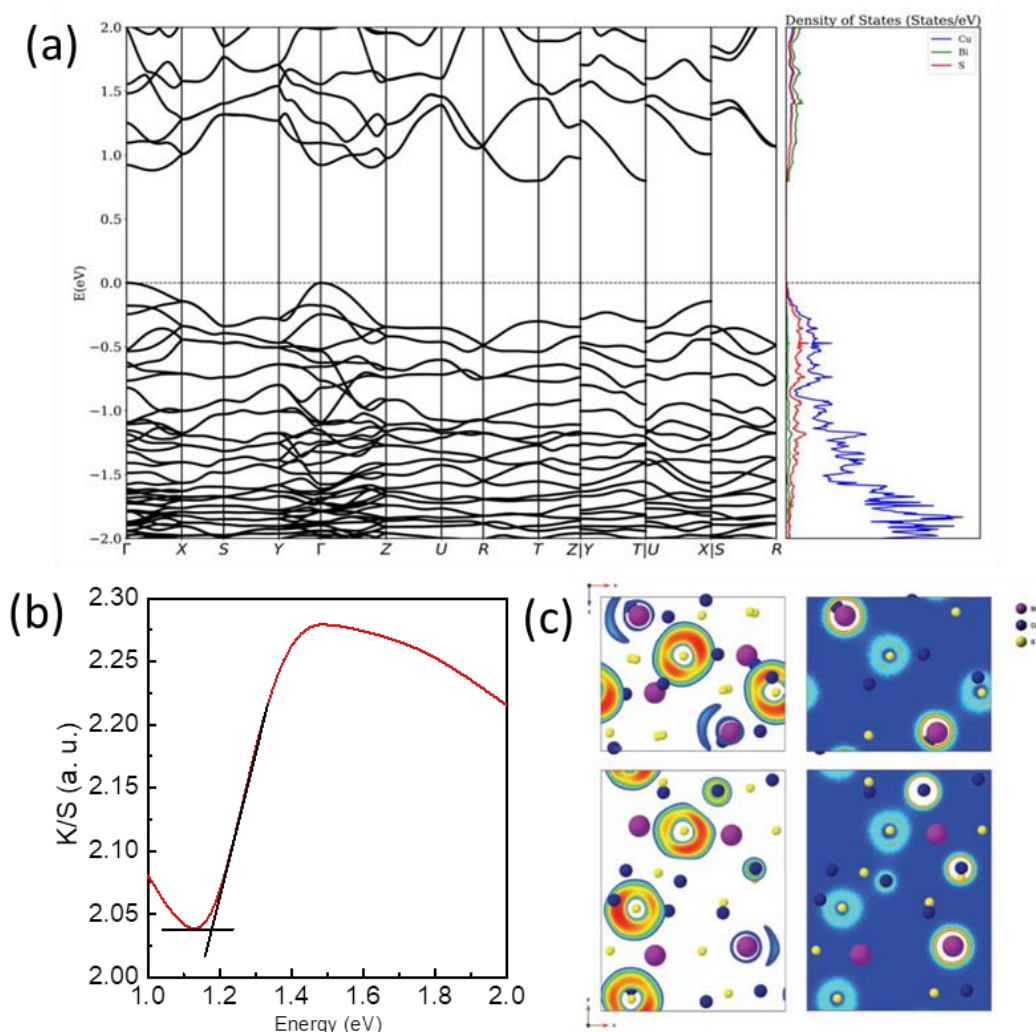


**Figure 4.10.** (a) Electronic bands structure (left panel) and atom-projected electron density of states (right panel) of  $\text{Cu}_3\text{BiS}_3$ . Spin-orbit coupling has been included in the calculation. Hubbard  $U$  corrections are included. The top of the valence band is set to 0 eV. (b) Kubelka-Munk plot of  $\text{Cu}_3\text{BiS}_3$  indicates the band gap around 1.1 eV (c) Contour of the ELF (left panel) and electron charge density (right panel) on the (010) (top) and (001) (bottom) planes. Values for the ELF range between 0 and 1: ELF = 0.5 (blue contour) indicates free electron behavior, and ELF = 1.0 (red contour) indicates perfect localization. Values smaller than 0.5 are less significant and usually point to small local electron densities. The scale bar for the electron charge density plot goes from  $8.79 \times 10^{-4}$  (blue contour) to  $6.61 \times 10^{-1}$  (red contour).

The temperature dependence of the power factor is displayed in **Figure 4.8c**. The maximum value is relatively low, *i.e.* around  $0.45 \mu\text{W cm}^{-1} \text{K}^{-2}$  at 563K, which is due to the high electrical resistivity and low carrier concentration. This value is comparable to the ones reported in some non-degenerate semiconductors like  $\text{Cu}_3\text{SbS}_4$  ( $\sim 1.26 \mu\text{W cm}^{-1} \text{K}^{-2}$  at 623 K),<sup>65</sup>  $\text{Cu}_2\text{SnS}_3$  ( $0.2 \mu\text{W cm}^{-1} \text{K}^{-2}$ , 700 K),<sup>66</sup> but remain much lower than those of degenerate semiconductors  $\text{Cu}_{22}\text{Sn}_{10}\text{S}_{32}$ , ( $9.5 \mu\text{W cm}^{-1} \text{K}^{-2}$  at 700 K),<sup>64</sup>  $\text{Cu}_5\text{Sn}_2\text{S}_7$  ( $\sim 9.4 \mu\text{W cm}^{-1} \text{K}^{-2}$  at 700 K),<sup>63</sup> colusite  $\text{Cu}_{26}\text{V}_2\text{Sn}_6\text{S}_{32}$  ( $7.0 \mu\text{W cm}^{-1} \text{K}^{-2}$  at 675 K)<sup>27</sup> and tetrahedrite  $\text{Cu}_{12}\text{Sb}_4\text{S}_{13}$  ( $\sim 11.9 \mu\text{W cm}^{-1} \text{K}^{-2}$  at 725 K),<sup>69</sup> due to their lower electrical resistivity (higher carrier concentration). Finally, the reversibility of the electrical properties (electrical resistivity and Seebeck coefficient) of pristine  $\text{Cu}_3\text{BiS}_3$  with temperature up to 563 K (five cycles from 345 K to 512 K + five cycles from 345 K to 563 K) indicates the thermal stability of the sample on the temperature range of measurement (**Figure 4.11**).

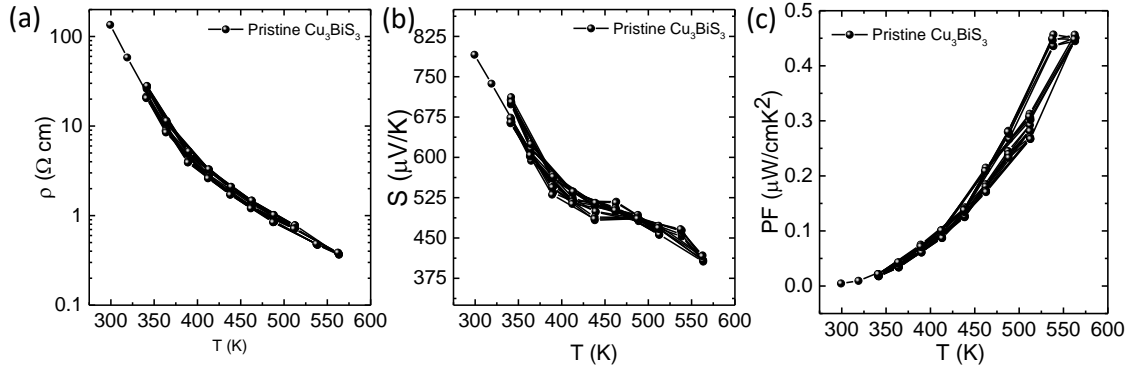


**Figure 4.11.** Cycling measurements of the electrical resistivity (a), and Seebeck coefficient (b), and power factor (c) of pristine  $\text{Cu}_3\text{BiS}_3$ . 5 cycles from 345 K to 512 K + 5 cycles from 345 K to 563 K.

### 4.3.5. Thermal Properties

The pristine phase  $\text{Cu}_3\text{BiS}_3$  has an extremely low lattice total thermal conductivity (the electronic contribution being negligible) of  $0.43 \text{ W m}^{-1} \text{K}^{-1}$  at 300 K, which decreases to  $0.32 \text{ W m}^{-1} \text{K}^{-1}$  at 563 K as the temperature increases (**Figure 4.12a**).

These values are slightly higher than the ones reported by Adeyemi *et al.*<sup>37</sup> (0.29 W m<sup>-1</sup> K<sup>-1</sup> at 313 K) and Wei *et al.*<sup>36</sup> (0.17 W m<sup>-1</sup> K<sup>-1</sup> at 300 K). This slight difference could be the result of additional impurity phases or lower bulk sample densities in the latter.

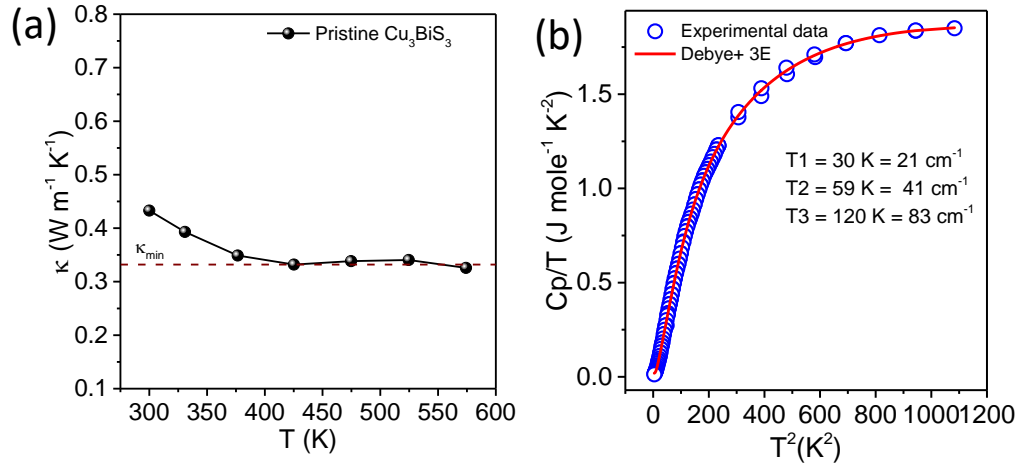


**Figure 4.12.** (a) Total thermal conductivity of Cu<sub>3</sub>BiS<sub>3</sub> in the temperature range of 300 K to 563 K, (b) Debye–Einstein fit of  $C_p/T$  vs  $T^2$  plot of Cu<sub>3</sub>BiS<sub>3</sub>.

To understand the ultralow  $\kappa_L$  values in Cu<sub>3</sub>BiS<sub>3</sub>, we have measured the low temperature heat capacity. We found that the plot  $C_p/T$  vs.  $T^2$  could be well fitted using a combined Debye-Einstein model rather than only Debye model in the temperature range of 2-33 K (**Figure 4.12b**). The Debye model is not sufficient to fit the experimental low temperature heat capacity data due to the presence of weakly dispersive low energy optical phonon modes which corresponds to independent or nearly independent atomic vibrations similar to Einstein oscillators. The Debye-Einstein model can be express by following equation<sup>70</sup>:

$$\frac{C_p}{T} = \gamma + \beta T^2 + \sum_n \left( A_n (\theta_{E_n})^2 \cdot (T^2)^{-3/2} \cdot \frac{e^{\theta_{E_n}/T}}{(e^{\theta_{E_n}/T} - 1)^2} \right)$$

The coefficient of the first term in the equation is the Sommerfeld coefficient  $\gamma$  and represent the electronic contribution, and the coefficient for the second term,  $\beta$ , depicts the lattice contribution. The third term in the equation represents contributions from the

Einstein oscillators corresponding to the localized vibrations where the  $A_n$  is the pre-factor and  $\theta_{E_n}$  is the Einstein temperature of the  $n^{\text{th}}$  Einstein oscillator mode.

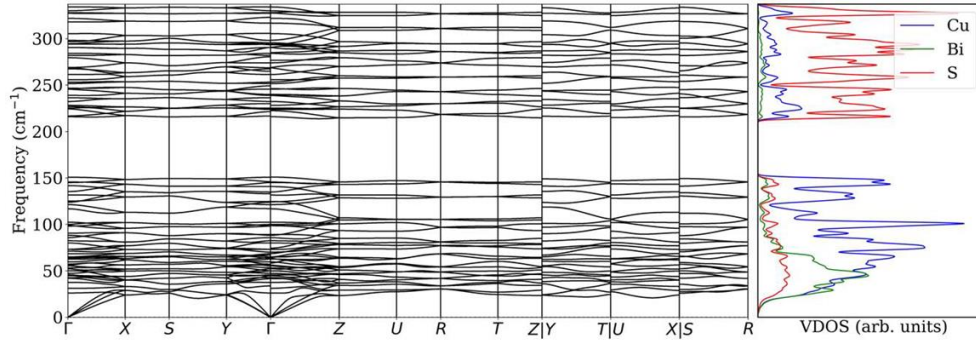


**Figure 4.13.** Phonon dispersions (left) and projected phonon density of states (PDOS) (right) of wittichenite,  $\text{Cu}_3\text{BiS}_3$ .

We have observed a good fit using Debye-Einstein model with three Einstein modes of  $\theta_{E_1} = 30 \text{ K}$  ( $21 \text{ cm}^{-1}$ ),  $\theta_{E_2} = 59 \text{ K}$  ( $41 \text{ cm}^{-1}$ ), and  $\theta_{E_3} = 120 \text{ K}$  ( $83 \text{ cm}^{-1}$ ) (**Figure 4.12b**). These modes involve mainly the vibration of  $\text{Cu}^+$  and  $\text{Bi}^{3+}$ . The ab-initio phonon dispersion and vibrational DOS of  $\text{Cu}_3\text{BiS}_3$  (**Figure 4.13**) mimic the features observed in other copper sulfides, notably a low-frequency manifold centered at about  $30 \text{ cm}^{-1}$ . The presence of low-energy optical modes is expected to lead to low  $\kappa_L$  as in other Cu-based sulfides.<sup>8,64,71</sup> The  $C_p/T^3$  vs.  $T$  fit (**Figure 4.14**) shows the presence of Boson-like peak like other low thermal conductive materials, which signifies excess phonon density of states contributed by the localized and low frequency optical phonon modes.

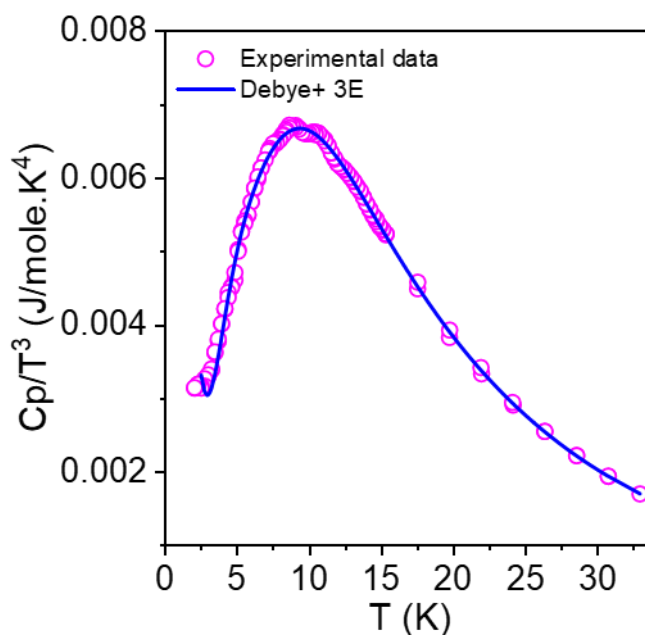


**Figure 4.14.**  $C_p/T^3$  versus  $T$  plot for  $\text{Cu}_3\text{BiS}_3$

The obtained Debye temperature ( $\theta_D$ ) is 232 K which is estimated using the relation  $\beta = C(12\pi^4 N_A k_B / 5) \cdot (\theta_D)^{-3}$  in the Debye-Einstein model where  $C$  can be defined as  $C = 1 - \sum_n A_n / 3NR$ , ( $N$  = number of atoms/formula unit and  $R = 8.314 \text{ J mol}^{-1} \text{ K}^{-1}$ , the universal gas constant), and  $N_A$  and  $k_B$  being the Avogadro's number and Boltzmann constant, respectively. The Debye temperature is comparable to the state-of-the-art low thermal conductivity materials as shown in **Table 4.6**.

For further clarification, longitudinal and transverse sound velocities were measured at room temperature and the average sound velocity was calculated as discussed in **chapter 2**. The low average sound velocity of  $1932 \text{ m s}^{-1}$  at 300 K, which is comparable to those of other ultralow thermal conductive chalcogenides, clearly reinforces the hypothesis of having soft bonding interaction (**Table 4.6**). Moreover, the large Grüneisen parameter  $\gamma$  of 1.93, which is obtained from measured sound velocity, is also quite comparable with other reported materials having ultralow  $\kappa_L$ , clearly backing the strong phonon-phonon interaction in  $\text{Cu}_3\text{BiS}_3$  (see **Table 4.6**). Furthermore, the lattice thermal conductivity reaches the minimum value of  $0.33 \text{ W m}^{-1} \cdot \text{K}^{-1}$  (**Figure**

4.12a), calculated from the measured longitudinal and transverse sound velocity values by using following equation:<sup>72</sup>

$$\kappa_{diff} = 0.76 \frac{K_B}{3} \left[ \frac{n\rho N_A}{M} \right]^{\frac{2}{3}} (2v_t + v_l)$$

where  $N$ ,  $V$ ,  $h$ ,  $k_B$ ,  $v_t$  and  $v_l$  are the number of atoms in unit cell, the volume of the unit cell, the Planck constant, the Boltzmann constant, longitudinal and transverse sound velocity, respectively.

**Table 4.6.** Average sound velocity, grüneisen parameter and debye temperature from measured transverse and longitudinal sound velocity: comparison among several other ultralow thermal conductive chalcogenides.

| Compound                           | Average sound velocity (m sec <sup>-1</sup> ) | Grüneisen parameter | Debye Temp (K) | Ref.      |
|------------------------------------|---|---------------------|----------------|-----------|
| Cu <sub>3</sub> BiS <sub>3</sub>   | 1931.5  | 1.93                | 214.6          | This work |
| CuPbBi <sub>5</sub> S <sub>9</sub> | 1758  | 1.93                | 178.5          | 8         |
| MnBi <sub>4</sub> S <sub>7</sub>   | 1767  | 1.16                | 179.4          | 73        |
| FeBi <sub>4</sub> S <sub>7</sub>   | 1967  | 1.28                | 200.8          | 73        |
| AgSbTe <sub>2</sub>                | 1727  | 2.05                | 125            | 74        |
| BiSbSe <sub>3</sub>                | 1629  | 1.89                | 165            | 75        |
| SnSe                               | 1420  | 3.13                | 142            | 76        |
| Bi <sub>2</sub> Se <sub>3</sub>    | 2083  | 1.65                | 205            | 77        |
| Sb <sub>2</sub> Se <sub>3</sub>    | 1882  | 1.58                | 180            | 75        |

Intriguingly,  $\kappa_L$  shows less temperature dependency than predicted by the  $T^{-1}$  rule for Umklapp scattering, with values that are essentially constant above 375 K. Similarly, the chain-like compounds TlSe, TlInTe<sub>2</sub>, Tl<sub>3</sub>MX<sub>4</sub> ( $M = V, Nb, \text{ and } Ta; X = S \text{ and } Se$ ), AgBiTe<sub>2</sub>, AgSbTe<sub>2</sub>, and Cs<sub>3</sub>Bi<sub>2</sub>I<sub>6</sub>Cl<sub>3</sub> have all shown this divergence from the usual law.<sup>78–82</sup> Theoretically, these deviations have been shown to be a signature of strong intrinsic anharmonicity resulting in pronounced renormalization effects on the phonon

frequencies of optical modes that shape the low-energy part of the phonon spectrum of these materials. These characteristics imply that  $\text{Cu}_3\text{BiS}_3$  exhibits anharmonic behavior as well.

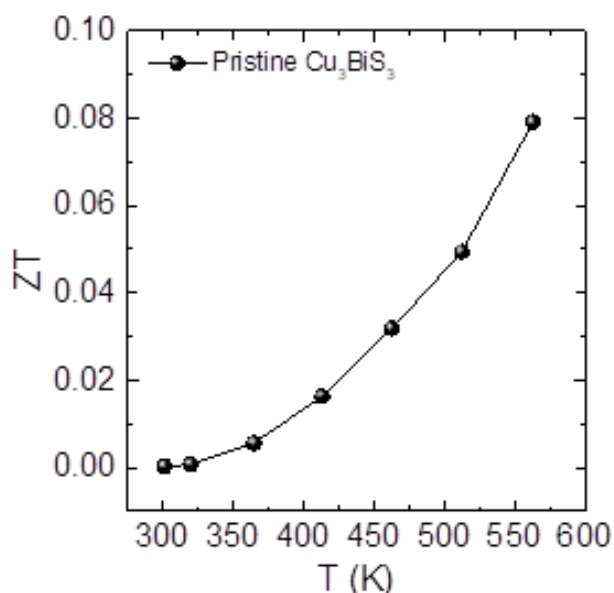


**Figure 4.15.** Temperature dependent figure of merit ( $ZT$ ) of pristine  $\text{Cu}_3\text{BiS}_3$ .

The temperature-dependent figure of merit ( $ZT$ ) is shown in **Figure 4.15**, wherein a maximum value of 0.08 is observed at 563 K. The previous study by Wei *et al.* demonstrates a similar  $ZT$  value (0.04 at 460 K) and on the other hand, Adeyemi *et al.* reports a maximum  $ZT$  value of 0.04 at 513 K.

#### 4.3.6. Discussion

The comparison of crystal structure and properties of  $\text{Cu}_3\text{BiS}_3$  with those of other Cu-rich sulfides strongly suggests that the copper coordination has a key role for the determination of the value of the electrical and thermal conductivity in these materials. One indeed observes that Cu-rich sulfides, with a pure tetrahedral coordination of copper (i.e. group A phases from copper-based sulfides classification<sup>62</sup>:  $\text{Cu}_3\text{SbS}_4$ ,  $\text{Cu}_2\text{SnS}_3$ ,  $\text{Cu}_5\text{Sn}_2\text{S}_7$ ,  $\text{Cu}_{22}\text{Sn}_{10}\text{S}_{32}$  ...) can be easily doped, leading to high electrical conductivity, due to adequate overlapping of the Cu- $3d$  and S- $3p$  orbitals for the

delocalization of hole carriers. This is in contrast with the extremely low electrical conductivity and hole blockade for hole carrier delocalization observed for  $\text{Cu}_3\text{BiS}_3$ , low chalcocite  $\text{Cu}_2\text{S}$  and skinnerite  $\text{Cu}_3\text{SbS}_3$ , which contain three-fold coordinated copper exclusively. In the same way, by comparing the  $\kappa_L$  temperature dependence of  $\text{Cu}_3\text{BiS}_3$  with other Cu-rich thermoelectric sulfides (**Figure 4.16**), it can be quickly figured out that the same structures composed of  $\text{CuS}_4$  tetrahedra exclusively ( $\text{Cu}_3\text{SbS}_4$ ,  $\text{Cu}_2\text{SnS}_3$ ,  $\text{Cu}_5\text{Sn}_2\text{S}_7$ ,  $\text{Cu}_{22}\text{Sn}_{10}\text{S}_{32}$ ) have significantly larger lattice thermal conductivity compared to  $\text{Cu}_3\text{BiS}_3$ . This is illustrated by the famatinite  $\text{Cu}_3\text{SbS}_4$  which exhibits an ordered sphalerite network leading to very weak anisotropic displacement of cations (**Table 4.7 and 4.8, Figure 4.17**). In this compound, all cations are in tetrahedral coordination with average bond angles  $\bar{\alpha}$  values equal to  $109.5^\circ$  (**Table 4.9**) indicating  $sp^3$  hybridization of valence electron orbitals in agreement with the formal charges  $\text{Cu}^+$  and  $\text{Sb}^{5+}$ .

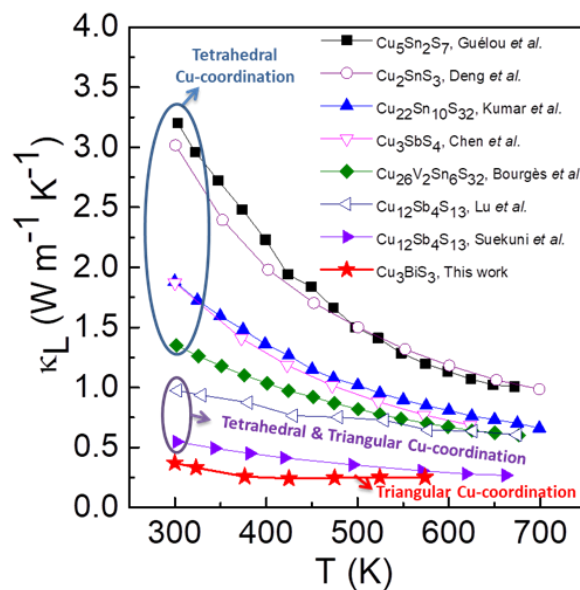


**Figure 4.16.** Comparison of  $\kappa_L(T)$  curves from state-of-the-art Cu-rich thermoelectric sulfides.<sup>17,21,27,64–66,83</sup>

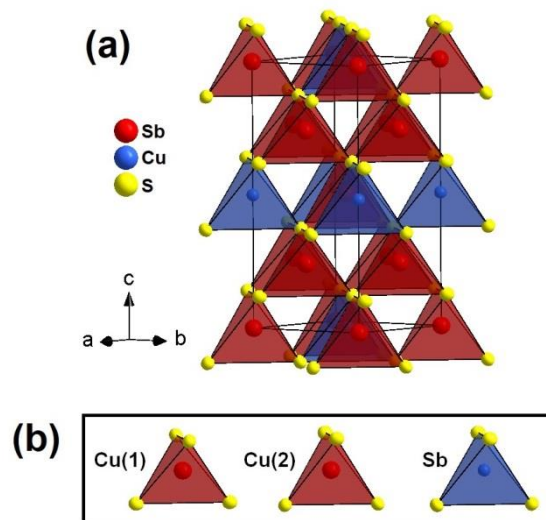


**Figure 4.17.** (a) Crystal structure representation of  $\text{Cu}_3\text{SbS}_4$  highlighting the sphalerite derivative network and (b) the highly isotropic displacements of cations.

Displacement ellipsoids are shown at the 90% probability level.

From the above considerations, it appears that the coexistence of three-fold coordinated copper and tetrahedral copper within the same structure in controlled proportions should be a very attractive challenge for the conciliation of the two antagonist factors, electrical and thermal conductivity, which govern the thermoelectric properties of Cu-rich sulfides. In this respect, the thermoelectric tetrahedrite  $\text{Cu}_{12}\text{Sb}_4\text{S}_{13}$  deserves a particular attention.<sup>17,21–23</sup> This sulfide exhibits an electrical conductivity similar to those of pure tetrahedral Cu-rich sulfides and a thermal lattice conductivity intermediate between those of pure tetrahedral and pure three-fold  $\text{Cu}_3\text{BiS}_3$  sulfides (**Figure 4.16**), leading to attractive thermoelectric characteristics. The analysis of its structure shows that the  $\text{Cu}_{12}\text{S}_{13}$  network consists of two copper sub-lattices, labelled Cu(1) and Cu(2), formed of an equal number of copper cations (**Figure 4.18 (a) and (b)**). The Cu(1) sub-lattice framework is built up of corner-sharing Cu(1)S(1)<sub>4</sub> tetrahedra and can be described as a copper-deficient sphalerite “ $\text{Cu}_6\Box_6\text{S}_{12}$ ” structure with large intersecting tunnels running along the  $\langle 110 \rangle$  and the  $\langle 111 \rangle$  directions (**Figure 4.18 (c) and (d)**). Due to its similarity with the sphalerite derivatives, the geometry of this tetrahedral framework allows a perfect overlapping of the Cu(1)-3d and S(1)-3p orbitals explaining the high electrical conductivity of this material and its

doping ability. One indeed observes for this framework very weak anisotropic displacements of Cu(1) atoms and longer interatomic distances (**Table 4.11** and **4.12**), similar to those observed in Cu<sub>3</sub>SbS<sub>4</sub> (**Table 4.8** and **4.9**).

**Table 4.7.** Room temperature structural data of Cu<sub>3</sub>SbS<sub>4</sub> from SCXRD

| Cu <sub>3</sub> SbS <sub>4</sub> $I\bar{4}2m$ , $a = 5.4085(8)$ Å, $c = 10.7973(17)$ Å, $V = 315.84(11)$ Å <sup>3</sup> |      |             |     |            |                    |
|---|------|-------------|-----|------------|--------------------|
| Atom  | Site | x           | y   | z          | U(Å <sup>2</sup> ) |
| Sb(1)   | 2b   | 0           | 0   | 1/2        | 0.011(1)           |
| Cu(1)   | 4d   | 0           | 1/2 | 1/4        | 0.022(1)           |
| Cu(2)   | 2a   | 0           | 0   | 0          | 0.021(1)           |
| S(1)  | 8i   | 0.24586(12) | x   | 0.12887(9) | 0.013(1)           |

**Table 4.8.** Anisotropic displacement parameters (Å<sup>2</sup>) of atoms in Cu<sub>3</sub>SbS<sub>4</sub> from SCXRD

| Atom  | U11         | U22 | U33       | U12        | U13       | U23 |
|-------|-------------|-----|-----------|------------|-----------|-----|
| Sb(1) | 0.01090(16) | U11 | 0.0106(2) | -          | -         | -   |
| Cu(1) | 0.0220(2)   | U11 | 0.0212(4) | -          | -         | -   |
| Cu(2) | 0.0217(3)   | U11 | 0.0207(5) | -          | -         | -   |
| S(1)  | 0.0136(3)   | U11 | 0.0128(6) | -0.0013(3) | 0.0009(2) | U13 |

**Table 4.9.** Bond distances and bond angles in Cu<sub>3</sub>SbS<sub>4</sub> (structural data from SCXRD)

|               | Distance (Å) |                                 | Angle (°) |
|---------------|--------------|---------------------------------|-----------|
| Sb(1)-S(1) ×4 | 2.3906(10)   | S(1)-Sb(1)-S(1) ×2              | 108.80(5) |
|               |              | S(1)-Sb(1)-S(1) ×4              | 109.81(2) |
|               |              | $\overline{\alpha_{S-Sb(1)-S}}$ | 109.47    |
| Cu(1)-S(1) ×4 | 2.3169(6)    | S(1)-Cu(1)-S(1) ×4              | 108.58(2) |
|               |              | S(1)-Cu(1)-S(1) ×2              | 111.27(4) |
|               |              | $\overline{\alpha_{S-Cu(1)-S}}$ | 109.48    |
| Cu(2)-S(1) ×4 | 2.3394(10)   | S(1)-Cu(2)-S(1) ×2              | 107.00(5) |
|               |              | S(1)-Cu(2)-S(2) ×4              | 110.72(2) |
|               |              | $\overline{\alpha_{S-Cu(2)-S}}$ | 109.48    |

Like for Cu<sub>3</sub>BiS<sub>3</sub>, the Cu(2) cations in Cu<sub>12</sub>Sb<sub>4</sub>S<sub>13</sub> exhibit a three-fold coordination but, differently from the former, the Cu(2)S<sub>3</sub> groups do not give rise to a 2D or 3D

framework by sharing their apices but form isolated  $\text{Cu}_6\text{S}_{13}$  units whose central S(2) atom is shared between six  $\text{Cu}(2)\text{S}(1)_2\text{S}(2)$  groups (**Figure 4.19**). The  $\text{Cu}_6\text{S}_{13}$  units are in the  $\langle 111 \rangle$  tunnels forming columns along this direction and are they are isolated one from the others. Note that the  $\text{Cu}_6\text{S}_{13}$  units, formed exclusively of Cu(2) cations, share the 12 S(1) apices of the their  $\text{Cu}(2)\text{S}(1)_2\text{S}(2)$  groups with the  $\text{Cu}(2)\text{S}(1)_4$  tetrahedra of the “ $\text{Cu}_6\Box\text{S}_{12}$ ” framework. As a consequence, the anisotropic rattling of copper cations perpendicular to the “ $\text{S}_3$ ” plane is limited to the Cu(2) atoms located inside of the  $\langle 111 \rangle$  triangular columns of the copper-deficient sphalerite “ $\text{Cu}_6\Box\text{S}_{12}$ ” framework. Similar to  $\text{Cu}_3\text{BiS}_3$  (**Table 4.3 and 4.5**) a large anisotropic displacement of Cu(2) atoms in the perpendicular direction of the triangular plane with shorter interatomic distances (**Table 4.11 and 4.12**). Nevertheless, on the contrary to  $\text{Cu}_3\text{BiS}_3$ , the copper rattling is not extended over all the 3D frameworks. Hence, the influence of the crystal structure of tetrahedrite  $\text{Cu}_{12}\text{Sb}_4\text{S}_{13}$  upon the thermal conductivity can be viewed as intermediate between that of famatinite  $\text{Cu}_3\text{SbS}_4$  and that of wittichenite  $\text{Cu}_3\text{BiS}_3$ .

**Table 4.10.** Room temperature structural data of  $\text{Cu}_{12}\text{Sb}_4\text{S}_{13}$  from SCXRD

| $\text{Cu}_{12}\text{Sb}_4\text{S}_{13}$ $I\bar{4}3m$ , $a = 10.3064(12)$ Å, $V = 1094.8(4)$ Å <sup>3</sup> |      |            |     |             |                     |
|---|------|------------|-----|-------------|---------------------|
| Atom  | Site | x          | y   | z           | U (Å <sup>2</sup> ) |
| Sb(1)   | 8c   | 0.26853(3) | x   | x           | 0.016(2)            |
| Cu(1)   | 12d  | 1/2        | 1/4 | 0           | 0.022(1)            |
| Cu(2)   | 12e  | 0          | 0   | 0.21798(18) | 0.063(1)            |
| S(1)  | 24g  | 0.11597(9) | x   | 0.36314(12) | 0.016(1)            |
| S(2)  | 2a   | 0          | 0   | 0           | 0.023(1)            |

**Table 4.11.** Anisotropic displacement parameters (Å<sup>2</sup>) of atoms in  $\text{Cu}_{12}\text{Sb}_4\text{S}_{13}$  from SCXRD

| Atom  | U11         | U22       | U33       | U12         | U13 | U23 |
|-------|-------------|-----------|-----------|-------------|-----|-----|
| Sb(1) | 0.01563(11) | U11       | U11       | 0.00096(11) | U12 | U12 |
| Cu(1) | 0.0188(2)   | 0.0268(7) | 0.0188(2) | -           | -   | -   |
| Cu(2) | 0.0838(8)   | U22       | 0.0221(6) | -0.0543(10) | -   | -   |

|      |           |     |           |           |           |     |
|------|-----------|-----|-----------|-----------|-----------|-----|
| S(1) | 0.0165(3) | U11 | 0.0142(5) | 0.0000(4) | 0.0021(3) | U13 |
| S(2) | 0.0230(8) | U11 | U11       | -         | -         | -   |

Moreover, as in  $\text{Cu}_3\text{BiS}_3$ ,  $\text{Cu}_{12}\text{Sb}_4\text{S}_{13}$  contains a  $\text{Sb}^{3+}$  cation with a  $5s^2$  lone pair of electrons, leading to a tetrahedral  $\text{SbS}_3\text{LP}$  coordination. This cation is sandwiched between two  $\text{Cu}_6\text{S}_{13}$  units (**Figure 4.19**), and consequently, may also influence the rattling of copper along the  $\langle 111 \rangle$  directions, as suggested by the orientation of the main axis of Cu atoms ellipsoids directed toward the vacant apex of the pseudo-tetrahedron where the lone pair electrons is expected to be localized (**Figure 4.18**). Nevertheless, contrary to  $\text{Sb}^{3+}$  in tetrahedrite, the  $\text{Bi}^{3+}$   $6s^2$  LP in  $\text{Cu}_3\text{BiS}_3$  cannot be considered itself as significantly responsible for the extremely low thermal conductivity in  $\text{Cu}_3\text{BiS}_3$ . Indeed, according to Skoug et Morelli (PRL, 2011), the average bond angles  $\bar{\alpha}$  value of Bi in  $\text{Cu}_3\text{BiS}_3$  ( $96.00^\circ$  from XRPD and  $96.43^\circ$  from PEDT, CN = 3) should lead to a lattice thermal conductivity value much higher than the one determined experimentally (i.e. between 1.0-1.5 instead of 0.43 W/m K, see **Figure 4** in the publication of Skoug *et al.*<sup>84</sup>

**Table 4.12.** Bond distances and bond angles in  $\text{Cu}_{12}\text{Sb}_4\text{S}_{13}$  (structural data from SCXRD)

|                                 | Distance (Å) |  | Angle (°) |
|---------------------------------|--------------|--|-----------|
| Sb(1)-S(1) × 3                  | 2.4280(13)   | S(1)-Sb(1)-S(1) × 3                    | 95.78(4)  |
| Cu(1)-S(1) × 4                  | 2.3078(8)    | S(1)-Cu(1)-S(1) × 2                    | 106.47(6) |
|                                 |              | S(1)-Cu(1)-S(1) × 4                    | 110.99(3) |
|                                 |              | $\overline{\alpha_{\text{S-Cu(1)-S}}}$ | 109.48    |
| Cu(2)-S(1) × 2                  | 2.2574(16)   | S(1)-Cu(2)-S(1)                        | 96.98(10) |
| Cu(2)-S(2)                      | 2.2466(18)   | S(1)-Cu(2)-S(2) × 2                    | 131.51(5) |
| $\overline{d_{\text{Cu(2)-S}}}$ | 2.2538       | $\overline{\alpha_{\text{S-Cu(2)-S}}}$ | 120.00    |

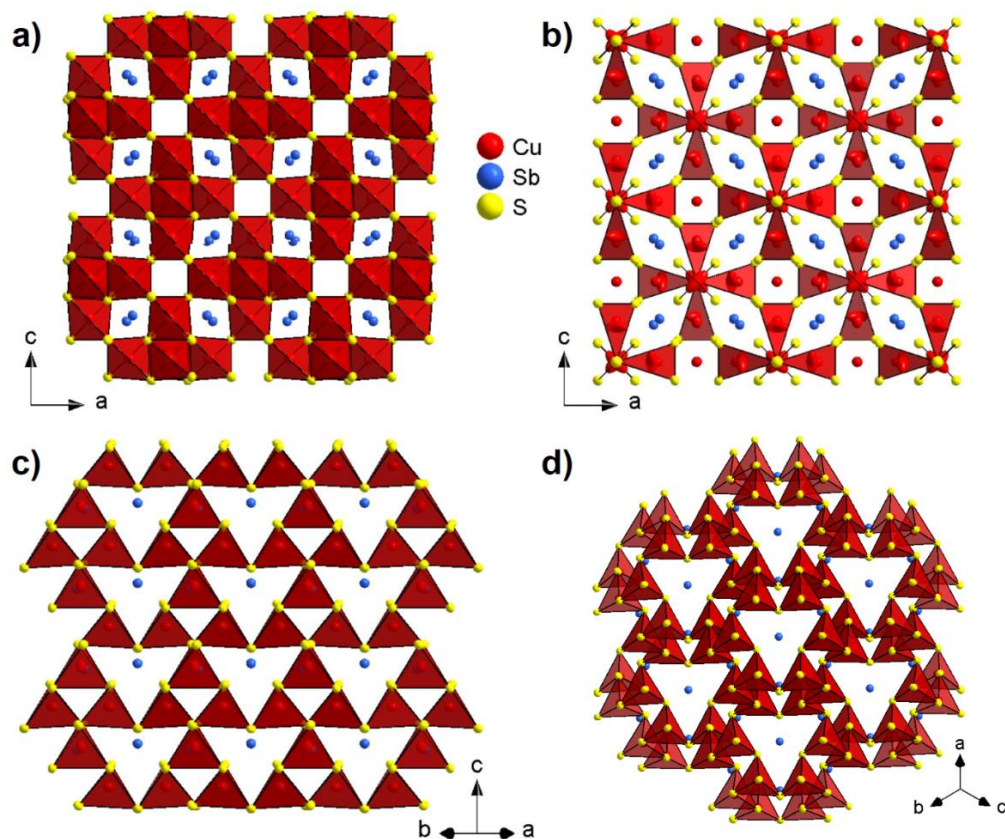


**Figure 4.18.** (a) and (b) crystal structure representation along the  $[010]$  direction of the Cu(1) and Cu(2) sub-lattice frameworks, respectively, highlighting the tetrahedral coordination of Cu(1) atoms and the three-fold coordination of Cu(2) atoms in tetrahedrite  $\text{Cu}_{12}\text{Sb}_4\text{S}_{13}$ . (c) and (d) crystal structure representation of the copper-deficient sphalerite “ $\text{Cu}_6\Box_6\text{S}_{12}$ ” framework (i.e. Cu(1) sub-lattice framework) in tetrahedrite  $\text{Cu}_{12}\text{Sb}_4\text{S}_{13}$  along the  $[110]$  and  $[111]$  direction, respectively, highlighting large triangular tunnels along these directions where are located Sb, Cu(2) and S(2) atoms. For sake of clarity, atoms Cu(2) and S(2) were not represented in (a), (c), and (d). Displacement ellipsoids are shown at the 90% probability level.

Finally, it is worth pointing out that the presence of a LP cation is not necessary to induce a three-fold coordination of copper. This is illustrated by the fact that the low chalcocite  $\text{Cu}_2\text{S}$  structure (space group  $P2_1/c$ )<sup>60</sup> contains  $\text{CuS}_3$  groups exclusively,

showing in a similar way, large anisotropic Cu displacements. Nevertheless, the low stability of this sulfide compared to  $\text{Cu}_3\text{BiS}_3$  or  $\text{Cu}_{12}\text{Sb}_4\text{S}_{13}$  suggests that the presence of a LP cation stabilizes the three-fold coordination of copper.

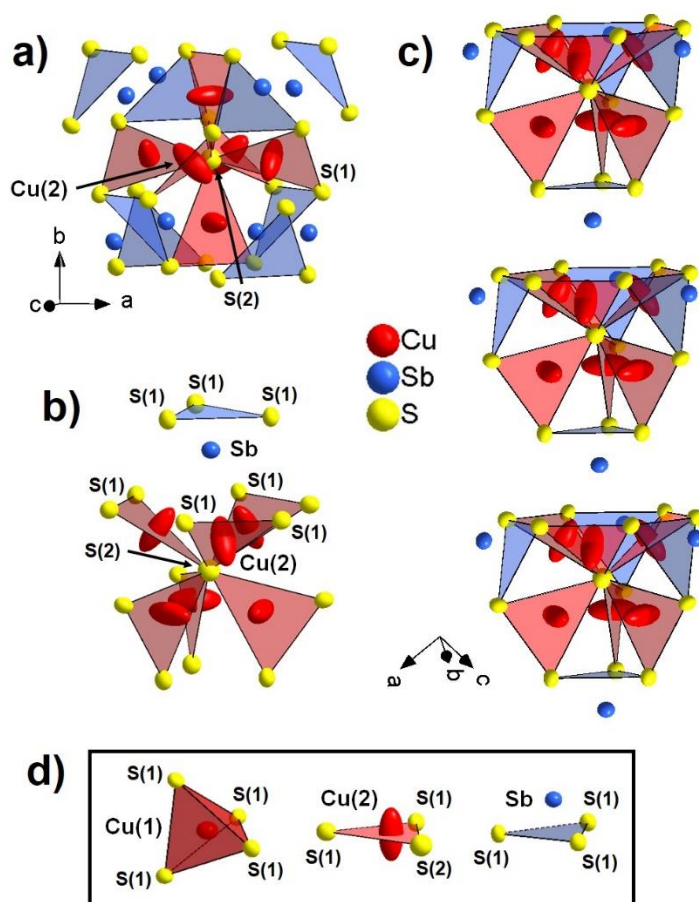


**Figure 4.19.** Representation in tetrahedrite  $\text{Cu}_{12}\text{Sb}_4\text{S}_{13}$  of (a) the  $\text{Cu}_6\text{S}_{13}$  unit formed of six  $\text{Cu}(2)\text{S}(1)_2\text{S}(2)$  groups sharing only the central  $\text{S}(2)$  atom and surrounded by eight  $\text{SbS}_3\text{LP}$  tetrahedra, (b) the  $\text{Cu}_6\text{S}_{13}$  unit highlighting the large anisotropic displacements of  $\text{Cu}(2)$  atoms perpendicularly to the  $\text{S}(1)_2\text{S}(2)$  triangular plane and pointing to the vacant apex of  $\text{Sb}^{3+}$  pseudo-tetrahedron where the lone pair of electrons is expected to be localized, (c) alternatively stacking of  $\text{Cu}_6\text{S}_{13}$  units with  $\text{SbS}_3\text{LP}$  tetrahedra along the  $[111]$  direction highlighting the isolated nature of the  $\text{Cu}_6\text{S}_{13}$  units, and (d) the highly isotropic displacements of  $\text{Cu}(1)$  and  $\text{Sb}$  cations in (pseudo-)tetrahedral coordination and the large anisotropic displacement of  $\text{Cu}(2)$  in three-fold coordination. Displacement ellipsoids are shown at the 90% probability level.

## 4.4. Conclusion

The present study of  $\text{Cu}_3\text{BiS}_3$  and its comparison with the tetrahedrite  $\text{Cu}_{12}\text{Sb}_4\text{S}_{13}$  clearly show that the copper coordination is the key for the generation and optimization of the thermoelectric properties of copper-rich sulfides. The extremely low electrical conductivity of this sulfide as well those of the low chalcocite  $\text{Cu}_2\text{S}$  and skinnerite  $\text{Cu}_3\text{SbS}_3$  and their blockade for hole carrier delocalization exclusively originate from the three-fold coordination of copper. This is in contrast with many other Cu-rich sulfides, whose tetrahedral coordination of copper, forming a 3D corner-sharing framework, allows an adequate overlapping of the Cu-3*d* and S-3*p* orbitals for the delocalization of hole carriers in agreement with the Cu(I)-Cu(II) mixed valence, leading to high electrical conductivity. In contrast, the three-fold coordination of copper favors its anisotropic rattling in the structure and consequently is a trump for the appearance of ultra-low thermal conductivity. Thus, the realization of mixed frameworks involving both, tetrahedral and three-fold coordinated copper, is a very attractive challenge for the discovery of performant thermoelectric copper sulfides. Importantly, the presence of cations with LPs, such as  $\text{Bi}^{3+}$  or  $\text{Sb}^{3+}$  appears as a crucial factor for the stabilisation of the structure. Moreover, the proximity of the electronic LP, acting as an anion, with respect to three-fold coordinated  $\text{Cu}^+$ , is a promising tool for the modulation of the intrinsic Cu-rattling for optimizing the thermal conductivity.

## 4.5. References

- (1) Xie, H.; Su, X.; Zhang, X.; Hao, S.; Bailey, T. P.; Stoumpos, C. C.; Douvalis, A. P.; Hu, X.; Wolverton, C.; Dravid, V. P.; Uher, C.; Tang, X.; Kanatzidis, M. G. Origin of Intrinsically Low Thermal Conductivity in Talmakhite  $\text{Cu}_{17.6}\text{Fe}_{17.6}\text{S}_{32}$  Thermoelectric Material: Correlations between Lattice Dynamics and Thermal Transport. *J. Am. Chem. Soc.* **2019**, *141* (27), 10905–10914. <https://doi.org/10.1021/jacs.9b05072>.
- (2) Snyder, G. J.; Toberer, E. S. Complex Thermoelectric Materials. *Nat. Mater.* **2008**, *7* (2), 105–114. [https://doi.org/10.1142/9789814317665\\_0016](https://doi.org/10.1142/9789814317665_0016).
- (3) You, Y.; Su, X.; Hao, S.; Liu, W.; Yan, Y.; Zhang, T.; Zhang, M.; Wolverton, C.; Kanatzidis, M. G.; Tang, X. Ni and Se Co-Doping Increases the Power Factor and Thermoelectric Performance of CoSbS. *J. Mater. Chem. A* **2018**, *6* (31), 15123–15131. <https://doi.org/10.1039/c8ta05572f>.
- (4) Hwang, J. Y.; Oh, M. W.; Lee, K. H.; Kim, S. W. Strong Correlation between the Crystal Structure and the Thermoelectric Properties of Pavonite Homologue  $\text{Cu}_{x+y}\text{Bi}_{5-y}\text{Ch}_8$  (Ch = S or Se) Compounds. *J. Mater. Chem. C* **2015**, *3* (43), 11271–11285. <https://doi.org/10.1039/c5tc02388b>.
- (5) Ahn, J. Y.; Hwang, J. Y.; Ryu, B. K.; Oh, M. W.; Lee, K. H.; Kim, S. W. Importance of Crystal Chemistry with Interstitial Site Determining Thermoelectric Transport Properties in Pavonite Homologue Cu-Bi-S Compounds. *CrystEngComm* **2016**, *18* (8), 1453–1461. <https://doi.org/10.1039/c5ce02143j>.
- (6) Hwang, J. Y.; Ahn, J. Y.; Lee, K. H.; Kim, S. W. Structural Optimization for Thermoelectric Properties in Cu-Bi-S Pavonite Compounds. *J. Alloys Compd.* **2017**, *704*, 282–288. <https://doi.org/10.1016/j.jallcom.2017.02.018>.
- (7) Labégorre, J. B.; Virfeu, A.; Bourhim, A.; Willeman, H.; Barbier, T.; Appert, F.; Juraszek, J.; Malaman, B.; Huguenot, A.; Gautier, R.; Nassif, V.; Lemoine, P.; Prestipino, C.; Elkaim, E.; Pautrot-d'Alençon, L.; Le Mercier, T.; Maignan, A.; Al Rahal Al Orabi, R.; Guilmeau, E.  $\text{XBi}_4\text{S}_7$  (X = Mn, Fe): New Cost-Efficient Layered n-Type Thermoelectric Sulfides with Ultralow Thermal Conductivity. *Adv. Funct. Mater.* **2019**, *29* (48). <https://doi.org/10.1002/adfm.201904112>.

- (8) Maji, K.; Lemoine, P.; Renaud, A.; Zhang, B.; Zhou, X.; Carnevali, V.; Candolfi, C.; Raveau, B.; Al Rahal Al Orabi, R.; Fornari, M.; Vaqueiro, P.; Pasturel, M.; Prestipino, C.; Guilmeau, E. A Tunable Structural Family with Ultralow Thermal Conductivity: Copper-Deficient  $\text{Cu}_{1-x}\text{Pb}_x\text{Bi}_{1+x}\text{S}_3$ . *J. Am. Chem. Soc.* **2022**, *144* (4), 1846–1860. <https://doi.org/10.1021/jacs.1c11998>.
- (9) Tan, G.; Hao, S.; Zhao, J.; Wolverton, C.; Kanatzidis, M. G. High Thermoelectric Performance in Electron-Doped  $\text{AgBi}_3\text{S}_5$  with Ultralow Thermal Conductivity. *J. Am. Chem. Soc.* **2017**, *139* (18), 6467–6473. <https://doi.org/10.1021/jacs.7b02399>.
- (10) Zhang, A.; Zhang, B.; Lu, W.; Xie, D.; Ou, H.; Han, X.; Dai, J.; Lu, X.; Han, G.; Wang, G.; Zhou, X. Twin Engineering in Solution-Synthesized Nonstoichiometric  $\text{Cu}_5\text{FeS}_4$  Icosahedral Nanoparticles for Enhanced Thermoelectric Performance. *Adv. Funct. Mater.* **2018**, *28* (10), 1705117. <https://doi.org/10.1002/adfm.201705117>.
- (11) Bourgès, C.; Lemoine, P.; Lebedev, O. I.; Daou, R.; Hardy, V.; Malaman, B.; Guilmeau, E. Low Thermal Conductivity in Ternary  $\text{Cu}_4\text{Sn}_7\text{S}_{16}$  Compound. *Acta Mater.* **2015**, *97*, 180–190. <https://doi.org/10.1016/j.actamat.2015.06.046>.
- (12) He, W.; Wang, D.; Wu, H.; Yu, X.; Zhang, Y.; He, D.; Feng, Y.; Hao, Y.-J.; Dong, J.-F.; Chetty, R.; Hao, L.; Chen, D.; Qui, J.; Quiang, Y.; Li, X.; Song, J.-M.; Zhu, Y.; Xu, W.; Niu, C.; Li, X.; Wang, G.; Liu, C.; Ohta, M.; Pennycook, S. J.; He, J.; Li, J.-F.; Zhao, L.-D. High Thermoelectric Performance in Low-Cost  $\text{SnS}_{0.91}\text{Se}_{0.09}$  Crystals. *Science (80-. )*. **2019**, *365* (6460), 1418–1424.
- (13) He, Y.; Day, T.; Zhang, T.; Liu, H.; Shi, X.; Chen, L.; Snyder, G. J. High Thermoelectric Performance in Non-Toxic Earth- Abundant Copper Sulfide. *Adv. Mater.* **2014**, *26* (23), 3974–3978. <https://doi.org/10.1002/adma.201400515>.
- (14) Rathore, E.; Juneja, R.; Culver, S. P.; Minafra, N.; Singh, A. K.; Zeier, W. G.; Biswas, K. Origin of Ultralow Thermal Conductivity in *n*-Type Cubic Bulk  $\text{AgBiS}_2$ : Soft Ag Vibrations and Local Structural Distortion Induced by the  $6s^2$  Lone Pair. *Chem. Mater.* **2019**, *31* (6), 2106–2113. <https://doi.org/10.1021/acs.chemmater.9b00001>.
- (15) Ge, Z. H.; Zhao, L. D.; Wu, D.; Liu, X.; Zhang, B. P.; Li, J. F.; He, J. Low-Cost,

- Abundant Binary Sulfides as Promising Thermoelectric Materials. *Mater. Today* **2016**, *19* (4), 227–239. <https://doi.org/10.1016/j.mattod.2015.10.004>.
- (16) Powell, A. V. Recent Developments in Earth-Abundant Copper-Sulfide Thermoelectric Materials. *J. Appl. Phys.* **2019**, *126* (10). <https://doi.org/10.1063/1.5119345>.
- (17) Lu, X.; Morelli, D. T.; Xia, Y.; Zhou, F.; Ozolins, V.; Chi, H.; Zhou, X.; Uher, C. High Performance Thermoelectricity in Earth-Abundant Compounds Based on Natural Mineral Tetrahedrites. *Adv. Energy Mater.* **2013**, *3* (3), 342–348. <https://doi.org/10.1002/aenm.201200650>.
- (18) Biswas, K.; Zhao, L. D.; Kanatzidis, M. G. Tellurium-Free Thermoelectric: The Anisotropic n-Type Semiconductor  $\text{Bi}_2\text{S}_3$ . *Adv. Energy Mater.* **2012**, *2* (6), 634–638. <https://doi.org/10.1002/aenm.201100775>.
- (19) Guilmeau, E.; Bréard, Y.; Maignan, A. Transport and Thermoelectric Properties in Copper Intercalated  $\text{TiS}_2$  Chalcogenide. *Appl. Phys. Lett.* **2011**, *99* (5), 052107–052109. <https://doi.org/10.1063/1.3621834>.
- (20) Raveau, B. Copper Mixed Valence Concept: “Cu(I)–Cu(II)” in Thermoelectric Copper Sulfides—an Alternative to “Cu(II)–Cu(III)” in Superconducting Cuprates. *J. Supercond. Nov. Magn.* **2020**, *33* (1), 259–263. <https://doi.org/10.1007/s10948-019-05354-8>.
- (21) Suekuni, K.; Tsuruta, K.; Kunii, M.; Nishiate, H.; Nishibori, E.; Maki, S.; Ohta, M.; Yamamoto, A.; Koyano, M. High-Performance Thermoelectric Mineral  $\text{Cu}_{12-x}\text{Ni}_x\text{Sb}_4\text{S}_{13}$  Tetrahedrite. *J. Appl. Phys.* **2013**, *113* (4), 043712–043716. <https://doi.org/10.1063/1.4789389>.
- (22) Suekuni, K.; Tsuruta, K.; Ariga, T.; Koyano, M. Thermoelectric Properties of Mineral Tetrahedrites  $\text{Cu}_{10}\text{Tr}_2\text{Sb}_4\text{S}_{13}$  with Low Thermal Conductivity. *Appl. Phys. Express* **2012**, *5* (5), 051201. <https://doi.org/10.1143/APEX.5.051201>.
- (23) Lu, X.; Morelli, D. T. Natural Mineral Tetrahedrite as a Direct Source of Thermoelectric Materials. *Phys. Chem. Chem. Phys.* **2013**, *15* (16), 5762–5766. <https://doi.org/10.1039/c3cp50920f>.
- (24) Suekuni, K.; Kim, F. S.; Takabatake, T. Tunable Electronic Properties and Low Thermal Conductivity in Synthetic Colusites  $\text{Cu}_{26-x}\text{Zn}_x\text{V}_2\text{M}_6\text{S}_{32}$  ( $x \leq 4$ ,  $\text{M} = \text{Ge}$ ,

- Sn). *J. Appl. Phys.* **2014**, *116* (6), 063706–063710. <https://doi.org/10.1063/1.4892593>.
- (25) Suekuni, K.; Kim, F. S.; Nishiate, H.; Ohta, M.; Tanaka, H. I.; Takabatake, T. High-Performance Thermoelectric Minerals: Colusites  $\text{Cu}_{26}\text{V}_2\text{M}_6\text{S}_{32}$  (M = Ge, Sn). *Appl. Phys. Lett.* **2014**, *105* (13), 132107–132110. <https://doi.org/10.1063/1.4896998>.
- (26) Guélou, G.; Lemoine, P.; Raveau, B.; Guilmeau, E. Recent Developments in High-Performance Thermoelectric Sulphides: An Overview of the Promising Synthetic Colusites. *J. Mater. Chem. C* **2021**, *9* (3), 773–795. <https://doi.org/10.1039/d0tc05086e>.
- (27) Bourgès, C.; Bouyrie, Y.; Supka, A. R.; Al Rahal Al Orabi, R.; Lemoine, P.; Lebedev, O. I.; Ohta, M.; Suekuni, K.; Nassif, V.; Hardy, V.; Daou, R.; Miyazaki, Y.; Fornari, M.; Guilmeau, E. High-Performance Thermoelectric Bulk Colusite by Process Controlled Structural Disordering. *J. Am. Chem. Soc.* **2018**, *140* (6), 2186–2195. <https://doi.org/10.1021/jacs.7b11224>.
- (28) Hagiwara, T.; Suekuni, K.; Lemoine, P.; Supka, A. R.; Chetty, R.; Guilmeau, E.; Raveau, B.; Fornari, M.; Ohta, M.; Al Rahal Al Orabi, R.; Saito, H.; Hashikuni, K.; Ohtaki, M. Key Role of  $d^0$  and  $d^{10}$  Cations for the Design of Semiconducting Colusites: Large Thermoelectric ZT in  $\text{Cu}_{26}\text{Ti}_2\text{Sb}_6\text{S}_{32}$  Compounds. *Chem. Mater.* **2021**, *33* (9), 3449–3456. <https://doi.org/10.1021/acs.chemmater.1c00872>.
- (29) Pavan Kumar, V.; Supka, A. R.; Lemoine, P.; Lebedev, O. I.; Raveau, B.; Suekuni, K.; Nassif, V.; Al Rahal Al Orabi, R.; Fornari, M.; Guilmeau, E. High Power Factors of Thermoelectric Colusites  $\text{Cu}_{26}\text{T}_2\text{Ge}_6\text{S}_{32}$  (T = Cr, Mo, W): Toward Functionalization of the Conductive “Cu–S” Network. *Adv. Energy Mater.* **2019**, *9* (6), 1803249. <https://doi.org/10.1002/aenm.201803249>.
- (30) Pavan Kumar, V.; Guélou, G.; Lemoine, P.; Raveau, B.; Supka, A. R.; Al Rahal Al Orabi, R.; Fornari, M.; Suekuni, K.; Guilmeau, E. Copper-Rich Thermoelectric Sulfides: Size-Mismatch Effect and Chemical Disorder in the  $[\text{TS}_4]\text{Cu}_6$  Complexes of  $\text{Cu}_{26}\text{T}_2\text{Ge}_6\text{S}_{32}$  (T = Cr, Mo, W) Colusites. *Angew. Chemie Int. Ed.* **2019**, *58* (43), 15455–15463. <https://doi.org/10.1002/anie.201908579>.

- (31) Candolfi, C.; Guélou, G.; Bourgès, C.; Supka, A. R.; Al Rahal Al Orabi, R.; Fornari, M.; Malaman, B.; Le Caër, G.; Lemoine, P.; Hardy, V.; Zanotti, J. M.; Chetty, R.; Ohta, M.; Suekuni, K.; Guilmeau, E. Disorder-Driven Glasslike Thermal Conductivity in Colusite  $\text{Cu}_{26}\text{V}_2\text{Sn}_6\text{S}_{32}$  Investigated by Mössbauer Spectroscopy and Inelastic Neutron Scattering Christophe. *Phys. Rev. Mater.* **2020**, *4* (2), 25404–25413. <https://doi.org/10.1103/PhysRevMaterials.4.025404>.
- (32) Bourgès Yohan; Supka, Andrew; Orabi, Rabih Al Rahal Al; Lemoine, Pierric; Lebedev, Oleg I.; Ohta, Michihiro; Suekuni, Koichiro; Nassif, Vivian; Hardy, Vincent; Daou, Ramzy; Miyazaki, Yuzuru; Fornari, Marco; Guilmeau, Emmanuel, C. B. High-Performance Thermoelectric Bulk Colusite by Process Controlled Structural Disorder. *J. Am. Chem. Soc.* **2018**, *140* (6), 2186–2195. <https://doi.org/10.1021/jacs.7b11224>.
- (33) Lai, W.; Wang, Y.; Morelli, D. T.; Lu, X. From Bonding Asymmetry to Anharmonic Rattling in  $\text{Cu}_{12}\text{Sb}_4\text{S}_{13}$  Tetrahedrites: When Lone-Pair Electrons Are Not so Lonely. *Adv. Funct. Mater.* **2015**, *25* (24), 3648–3657. <https://doi.org/10.1002/adfm.201500766>.
- (34) Long, S. O.; Powell, A. V.; Hull, S.; Orlandi, F.; Tang, C. C.; Supka, A. R.; Fornari, M.; Vaqueiro, P. Jahn–Teller Driven Electronic Instability in Thermoelectric Tetrahedrite. *Adv. Funct. Mater.* **2020**, *30* (12), 1909409. <https://doi.org/10.1002/adfm.201909409>.
- (35) Xia, Y.; Ozoliņš, V.; Wolverton, C. Microscopic Mechanisms of Glasslike Lattice Thermal Transport in Cubic  $\text{Cu}_{12}\text{Sb}_4\text{S}_{13}$  Tetrahedrites. *Phys. Rev. Lett.* **2020**, *125* (8), 43–46. <https://doi.org/10.1103/PhysRevLett.125.085901>.
- (36) Wei, K.; Hobbis, D.; Wang, H.; Nolas, G. S. Wittichenite  $\text{Cu}_3\text{BiS}_3$ : Synthesis and Physical Properties. *J. Electron. Mater.* **2018**, *47* (4), 2374–2377. <https://doi.org/10.1007/s11664-017-6053-0>.
- (37) Adeyemi, A. N.; Clemente, M.; Lee, S. J.; Mantravadi, A.; Zaikina, J. V. Deep Eutectic Solvent-Assisted Microwave Synthesis of Thermoelectric  $\text{AgBiS}_2$  and  $\text{Cu}_3\text{BiS}_3$ . *ACS Appl. Energy Mater.* **2022**, *5*, 14858–14868. <https://doi.org/10.1021/acsaem.2c02336>.
- (38) Kumar, M.; Persson, C.  $\text{Cu}_3\text{BiS}_3$  as a Potential Photovoltaic Absorber with High

- Optical Efficiency. *Appl. Phys. Lett.* **2013**, *102* (6), 062109–062112. <https://doi.org/10.1063/1.4792751>.
- (39) Gerein, N. J.; Haber, J. A. One-Step Synthesis and Optical and Electrical Properties of Thin Film  $\text{Cu}_3\text{BiS}_3$  for Use as a Solar Absorber in Photovoltaic Devices. *Chem. Mater.* **2006**, *18* (26), 6297–6630. <https://doi.org/10.1109/WCPEC.2006.279518>.
- (40) Mesa, F.; Gordillo, G.; Dittrich, T.; Ellmer, K.; Baier, R.; Sadewasser, S. Transient Surface Photovoltage of *p*-Type  $\text{Cu}_3\text{BiS}_3$ . *Appl. Phys. Lett.* **2010**, *96* (8), 082113–082115. <https://doi.org/10.1063/1.3334728>.
- (41) Kocman, V.; Nuffield, E. W. The Crystal Structure of  $\text{Cu}_3\text{BiS}_3$ . *Acta Crystallogr. Sect. B* **1973**, *29* (11), 2528–2535. <https://doi.org/10.1016/j.ssc.2010.01.002>.
- (42) Wuensch, B. J. The Crystal Structure of Tetrahedrite,  $\text{Cu}_{12}\text{Sb}_4\text{S}_{13}$ . *Zeitschrift für Krist.* **1964**, *119*, 453–453.
- (43) Chen, X.; Shi, L.; Zhou, J.; Goodenough, J. B. Effects of Ball Milling on Microstructures and Thermoelectric Properties of Higher Manganese Silicides. *J. Alloys Compd.* **2015**, *641*, 30–36. <https://doi.org/10.1016/j.jallcom.2015.04.048>.
- (44) Portheine, J. C.; Nowachi, W. Refinement of the Crystal Structure of Emplectite,  $\text{CuBiS}_2$ . *Zeitschrift für Krist.* **1975**, *141*, 387–402. <https://doi.org/10.1038/197070a0>.
- (45) Bindi, L.; Makovicky, E.; Nestola, F.; De Battisti, L. Sinnerite,  $\text{Cu}_6\text{As}_4\text{S}_9$ , from the Lengnabach Quarry, Binn Valley, Switzerland: Description and Re-Investigation of the Crystal Structure. *Can. Mineral.* **2013**, *51* (6), 851–860. <https://doi.org/10.3749/canmin.51.6.851>.
- (46) Pauling, L.; Neuman, E. W. The Crystal Structure of Binnite,  $(\text{Cu,Fe})_{12}\text{As}_4\text{S}_{13}$ , and the Chemical Composition and Structure of Minerals of the 1 Etrahedrite Group. *Zeitschrift für Krist. Mater.* **1934**, *54* (383), 54–62.
- (47) Yaroslavzev, A. A.; Mironov, A. V.; Kuznetsov, A. N.; Dudka, A. P.; Khrykina, O. N. Tennantite: Multi-Temperature Crystal Structure, Phase Transition and Electronic Structure of Synthetic  $\text{Cu}_{12}\text{As}_4\text{S}_{13}$ . *Acta Crystallogr. Sect. B Struct. Sci. Cryst. Eng. Mater.* **2019**, *75*, 634–642. <https://doi.org/10.1107/S2052520619007595>.

- (48) Pfitzner, A.  $\text{Cu}_3\text{SbS}_3$ : Zur Kristallstruktur Und Polymorphie. *Zeitschrift für Anorg. und Allg. Chemie* **1994**, 620 (11), 1992–1997.
- (49) Pfitzner, A. Disorder of  $\text{Cu}^+$  in  $\text{Cu}_3\text{SbS}_3$ : Structural Investigations of the High- and Low-Temperature Modification. *Zeitschrift für Krist. - New Cryst. Struct.* **1998**, 213 (4), 228–236. <https://doi.org/10.1524/zkri.1998.213.4.228>.
- (50) Hofmann, W. Strukturelle Und Morphologische Zusammenhänge Bei Erzen Vom Formeltyp  $\text{ABC}_2$ . *Zeitschrift für Krist. - Cryst. Mater.* **1933**, 84, 177–203. <https://doi.org/10.1524/zkri.1933.84.1.177>.
- (51) Razmara, M. F.; Henderson, C. M. B.; Patrick, R. A. D.; Bell, A. M. T.; Charnock, J. M. The Crystal Chemistry of the Solid Solution Series between Chalcostibite ( $\text{CuSbS}_2$ ) and Emplectite ( $\text{CuBiS}_2$ ). *Mineral. Mag.* **1997**, 61 (404), 79–88. <https://doi.org/10.1180/minmag.1997.061.404.08>.
- (52) Takéuchi, Y.; Ozawa, T. The Structure of  $\text{Cu}_4\text{Bi}_4\text{S}_9$  and Its Relation to the Structures of Covellite,  $\text{CuS}$  and Bismuthinite,  $\text{Bi}_2\text{S}_3$ . *Zeitschrift für Krist. - New Cryst. Struct.* **1975**, 141, 217–232. <https://doi.org/10.1524/zkri.1975.141.3-4.217>.
- (53) Bente, K.; Kupcik, V. Redetermination and Refinement of the Structure of Tetrabismuth Tetracopper Enneasulphide,  $\text{Cu}_4\text{Bi}_4\text{S}_9$ . *Acta Crystallogr.* **1984**, C40 (Part 12), 1985–1986. <https://doi.org/10.1107/s0108270184010337>.
- (54) Jiang, Y.; Jia, F.; Chen, L.; Wu, L. M.  $\text{Cu}_4\text{Bi}_4\text{Se}_9$ : A Thermoelectric Symphony of Rattling, Anharmonic Lone-Pair, and Structural Complexity. *ACS Appl. Mater. Interfaces* **2019**, 11 (40), 36616–36625. <https://doi.org/10.1021/acsami.9b11115>.
- (55) Du, B.; Zhang, R.; Liu, M.; Chen, K.; Zhang, H.; Reece, M. J. Crystal Structure and Improved Thermoelectric Performance of Iron Stabilized Cubic  $\text{Cu}_3\text{SbS}_3$  Compound. *J. Mater. Chem. C* **2019**, 7 (2), 394–404. <https://doi.org/10.1039/c8tc05301d>.
- (56) Zhu, C.; Ming, H.; Zhang, J.; Li, D.; Chen, T.; Qin, X. Ultralow Lattice Thermal Conductivity and High Thermoelectric Figure of Merit in Dually Substituted  $\text{Cu}_{12}\text{Sb}_4\text{S}_{13}$  Tetrahedrites. *Adv. Electron. Mater.* **2022**, 8 (10), 2200110. <https://doi.org/10.1002/aelm.202200110>.
- (57) Makovicky, E. The Phase Transformations and Thermal Expansion of the Solid

- Electrolyte  $\text{Cu}_3\text{BiS}_3$  between 25 and 300°C. *J. Solid State Chem.* **1983**, *49* (1), 85–92. [https://doi.org/10.1016/0022-4596\(83\)90219-0](https://doi.org/10.1016/0022-4596(83)90219-0).
- (58) Mizota, T.; Inoue, A.; Yamada, T.; Nakatsuka, A.; Nakayama, N. Ionic Conduction and Thermal Nature of Synthetic  $\text{Cu}_3\text{BiS}_3$ . *Mineralogical Journal*. 1998, pp 81–90. <https://doi.org/10.2465/minerj.20.81>.
- (59) Howard T. Evans, J. Djurleite ( $\text{Cu}_{1.94}\text{S}$ ) and Low Chalcocite ( $\text{Cu}_2\text{S}$ ): New Crystal Structure Studies. *Science (80-. )*. **1979**, *203*, 356.
- (60) Evans, H. T. The Crystal Structures of Low Chalcocite and Djurleite. *Zeitschrift fur Krist. - New Cryst. Struct.* **1979**, *150* (1–4), 299–320. <https://doi.org/10.1524/zkri.1979.150.1-4.299>.
- (61) Li, M.; Liu, Y.; Zhang, Y.; Han, X.; Zhang, T.; Zuo, Y.; Xie, C.; Xiao, K.; Arbiol, J.; Llorca, J.; Ibáñez, M.; Liu, J.; Cabot, A. Effect of the Annealing Atmosphere on Crystal Phase and Thermoelectric Properties of Copper Sulfide. *ACS Nano* **2021**, *15* (3), 4967–4978. <https://doi.org/10.1021/acsnano.0c09866>.
- (62) Lemoine, P.; Guélou, G.; Raveau, B.; Guilmeau, E. Crystal Structure Classification of Copper-Based Sulfides as a Tool for the Design of Inorganic Functional Materials. *Angew. Chemie - Int. Ed.* **2022**, *61* (2), e202108686. <https://doi.org/10.1002/anie.202108686>.
- (63) Kumar, V. P.; Lemoine, P.; Carnevali, V.; Lebedev, O. I.; Boullay, P.; Raveau, B.; Al, R.; Al, R.; Fornari, M.; Prestipino, C.; Menut, D.; Candol, C.; Malaman, B.; Guilmeau, E. Ordered Sphalerite Derivative  $\text{Cu}_5\text{Sn}_2\text{S}_7$ : A Degenerate Semiconductor with High Carrier Mobility in the Cu–Sn–S Diagram. *J. Mater. Chem. A* **2021**, *9* (17), 10812–10826. <https://doi.org/10.1039/d1ta01615f>.
- (64) Kumar, V. P.; Lemoine, P.; Carnevali, V.; Guélou, G.; Lebedev, O. I.; Raveau, B.; Al Rahal Al Orabi, R.; Fornari, M.; Candolfi, C.; Prestipino, C.; Menut, D.; Malaman, B.; Juraszek, J.; Suekuni, K.; Guilmeau, E. Local-Disorder-Induced Low Thermal Conductivity in Degenerate Semiconductor  $\text{Cu}_{22}\text{Sn}_{10}\text{S}_{32}$ . *Inorg. Chem.* **2021**, *60* (21), 16273–16285. <https://doi.org/10.1021/acs.inorgchem.1c02105>.
- (65) Chen, K.; Di Paola, C.; Du, B.; Zhang, R.; Laricchia, S.; Bonini, N.; Weber, C.; Abrahams, I.; Yan, H.; Reece, M. Enhanced Thermoelectric Performance of Sn-

- Doped  $\text{Cu}_3\text{SbS}_4$ . *J. Mater. Chem. C* **2018**, *6* (31), 8546–8552. <https://doi.org/10.1039/c8tc02481b>.
- (66) Deng, T.; Qiu, P.; Song, Q.; Chen, H.; Wei, T. R.; Xi, L.; Shi, X.; Chen, L. Thermoelectric Properties of Non-Stoichiometric  $\text{Cu}_{2+x}\text{Sn}_{1-x}\text{S}_3$  Compounds. *J. Appl. Phys.* **2019**, *126* (8), 085111. <https://doi.org/10.1063/1.5115195>.
- (67) Jiang, Q.; Yan, H.; Lin, Y.; Shen, Y.; Yang, J.; Reece, M. J. Colossal Thermoelectric Enhancement in  $\text{Cu}_{2+x}\text{Zn}_{1-x}\text{SnS}_4$  Solid Solution by Local Disordering of Crystal Lattice and Multi-Scale Defect Engineering. *J. Mater. Chem. A* **2020**, *8* (21), 10909–10916. <https://doi.org/10.1039/d0ta01595d>.
- (68) Goto, Y.; Naito, F.; Sato, R.; Yoshiyasu, K.; Itoh, T.; Kamihara, Y.; Matoba, M. Enhanced Thermoelectric Figure of Merit in Stannite–Kuramite Solid Solutions  $\text{Cu}_{2+x}\text{Fe}_{1-x}\text{SnS}_{4-y}$  ( $x = 0-1$ ) with Anisotropy Lowering. *Inorg. Chem.* **2013**, *52*, 9861–9866.
- (69) Zhu, C.; Chen, Q.; Ming, H.; Qin, X.; Yang, Y.; Zhang, J.; Peng, D.; Chen, T.; Li, D.; Kawazoe, Y. Improved Thermoelectric Performance of  $\text{Cu}_{12}\text{Sb}_4\text{S}_{13}$  through Gd-Substitution Induced Enhancement of Electronic Density of States and Phonon Scattering. *ACS Appl. Mater. Interfaces* **2021**, *13*, 25092–25101. <https://doi.org/10.1021/acsami.1c03493>.
- (70) Liu, H.; Yang, J.; Shi, X.; Danilkin, S. A.; Yu, D.; Wang, C.; Zhang, W.; Chen, L. Reduction of Thermal Conductivity by Low Energy Multi-Einstein Optic Modes. *J. Mater.* **2016**, *2*, 187–195. <https://doi.org/10.1016/j.jmat.2016.05.006>.
- (71) Carnevali, V.; Mukherjee, S.; Voneshen, D. J.; Maji, K.; Guilmeau, E.; Powell, A. V.; Vaqueiro, P.; Fornari, M. Lone Pair Rotation and Bond Heterogeneity Leading to Ultralow Thermal Conductivity in Aikinite. *J. Am. Chem. Soc.* **2023**, *145* (16), 9313–9325. <https://doi.org/10.1021/jacs.3c02536>.
- (72) Cahill, D. G.; Watson, S. K.; Pohl, R. O. Lower Limit to the Thermal Conductivity of Disordered Crystals. *Phys. Rev.* **1992**, *46* (10), 6131–6140.
- (73) Labégorre Agathe; Bourhim, Abdelhamid; Willeman, Héloïse; Barbier, Tristan; Appert, Florian; Juraszek, Jean; Malaman, Bernard; Huguenot, Arthur; Gautier, Régis; Nassif, Vivian; Lemoine, Pierric; Prestipino, Carmelo; Elkaim, Erik; Pautrot-d’Alençon, Lauri, J.-B. V.  $\text{XBi}_4\text{S}_7$  ( $X = \text{Mn}, \text{Fe}$ ): New Cost-Efficient

- Layered N-Type Thermoelectric Sulfides with Ultralow Thermal Conductivity. *Adv. Funct. Mater.* **2019**, *29* (48), 1904112-NA. <https://doi.org/10.1002/adfm.201904112>.
- (74) Morelli, D. T.; Jovovic, V.; Heremans, J. P. Intrinsically Minimal Thermal Conductivity in Cubic I-V-VI<sub>2</sub> Semiconductors. *Phys. Rev. Lett.* **2008**, *101* (3), 035901. <https://doi.org/10.1103/PhysRevLett.101.035901>.
- (75) Liu, X.; Wang, D.; Wu, H.; Wang, J.; Zhang, Y.; Wang, G.; Pennycook, S. J.; Zhao, L. D. Intrinsically Low Thermal Conductivity in BiSbSe<sub>3</sub>: A Promising Thermoelectric Material with Multiple Conduction Bands. *Adv. Funct. Mater.* **2019**, *29* (3), 1806558–1806566. <https://doi.org/10.1002/adfm.201806558>.
- (76) Xiao Cheng; Pei, Yanling; Wu, Di; Peng, Kunling; Zhou, Xiaoyuan; Gong, Shengkai; He, Jiaqing; Zhang, Yongsheng; Zeng, Zhi; Zhao, Li-Dong, Y. C. Origin of Low Thermal Conductivity in SnSe. *Phys. Rev. B* **2016**, *94* (12), 125203-NA. <https://doi.org/10.1103/physrevb.94.125203>.
- (77) Gao Meng; Cheng, Yan; Ji, Guang-Fu, X. Z. First-Principles Study of Structural, Elastic, Electronic and Thermodynamic Properties of Topological Insulator Bi<sub>2</sub>Se<sub>3</sub> under Pressure. *Philos. Mag.* **2016**, *96* (2), 208–222. <https://doi.org/10.1080/14786435.2015.1128126>.
- (78) Dutta Shidaling; Prasad, Matukumilli V. D.; Pandey, Juhi; Warankar, Avinash; Mandal, Pankaj; Soni, Ajay; Waghmare, Umesh V.; Biswas, Kanishka, M. M. Ultralow Thermal Conductivity in Chain Like TlSe Due to Inherent Tl<sup>+</sup> Rattling. *J. Am. Chem. Soc.* **2019**, *141* (51), 20293–20299. <https://doi.org/10.1021/jacs.9b10551>.
- (79) Jana, M. K.; Pal, K.; Warankar, A.; Mandal, P.; Waghmare, U. V.; Biswas, K. Intrinsic Rattler-Induced Low Thermal Conductivity in Zintl Type TlInTe<sub>2</sub>. *J. Am. Chem. Soc.* **2017**, *139* (12), 4350–4353. <https://doi.org/10.1021/jacs.7b01434>.
- (80) Mukhopadhyay, S.; Parker, D. S.; Sales, B. C.; Puretzy, A. A.; McGuire, M. A.; Lindsay, L. Two-Channel Model for Ultralow Thermal Conductivity of Crystalline Tl<sub>3</sub>VSe<sub>4</sub>. *Science* (80-. ). **2018**, *360* (6396), 1455–1458. <https://doi.org/10.1126/science.aar8072>.

- 
- (81) Skoug, E. J.; Cain, J. D.; Morelli, D. T. Structural Effects on the Lattice Thermal Conductivity of Ternary Antimony- and Bismuth-Containing Chalcogenide Semiconductors. *Appl. Phys. Lett.* **2010**, *96* (18), 3–6. <https://doi.org/10.1063/1.3425886>.
- (82) Acharyya, P.; Ghosh, T.; Pal, K.; Rana, K. S.; Dutta, M.; Swain, D.; Etter, M.; Soni, A.; Waghmare, U. V.; Biswas, K. Glassy Thermal Conductivity in  $\text{Cs}_3\text{Bi}_2\text{I}_6\text{Cl}_3$  Single Crystal. *Nat. Commun.* **2022**, *13* (1), 5053. <https://doi.org/10.1038/s41467-022-32773-4>.
- (83) Guélou, G.; Pavan Kumar, V.; Carnevali, V.; Lebedev, O. I.; Raveau, B.; Couder, C.; Prestipino, C.; Lemoine, P.; Malaman, B.; Juraszek, J.; Candolfi, C.; Lenoir, B.; Al Rahal Al Orabi, R.; Fornari, M.; Guilmeau, E. Long-Range Cationic Order Collapse Triggered by S/Cl Mixed-Anion Occupancy Yields Enhanced Thermoelectric Properties in  $\text{Cu}_5\text{Sn}_2\text{S}_7$ . *Chem. Mater.* **2021**, *33* (23), 9425–9438. <https://doi.org/10.1021/acs.chemmater.1c03434>.
- (84) Skoug, E. J.; Morelli, D. T. Role of Lone-Pair Electrons in Producing Minimum Thermal Conductivity in Nitrogen-Group Chalcogenide Compounds. *Phys. Rev. Lett.* **2011**, *107* (23), 235901. <https://doi.org/10.1103/PhysRevLett.107.235901>.

---

**Thermoelectric performance enhancement in low  
thermal conductive *n*-type  $\text{PbBi}_2\text{S}_4$  through carrier  
optimization**

---



## 5.1. Introduction

In the previous chapters (chapter 2 and 3), we have investigated quaternary sulfides in the Cu-Pb-Bi-S system. Chapter 2 presented an exploration on the synthesis and characterization of a newly discovered sulfide compound with a Cu-deficient aikinite-type sulfide. Notably, this structure deviates from the previously reported ordered structure due to the random distribution of copper atoms and vacancies on the cationic sites. It is essential to point out that the disordered gladite phase is an example within a large category of closely associated sulfides denoted as  $(\text{Cu}_{1-x}\square_x)\text{Pb}_{1-x}\text{Bi}_{1+x}\text{S}_3$  ( $x = 0 - 1$ ). In addition, the chemical doping approach has been used to enhance the carrier concentration, resulting in the moderately high figure of merit value (0.43 at 700 K for  $\text{CuPbBi}_5\text{S}_{8.91}\text{Cl}_{0.09}$ ). In Chapter 3, we carried out an optimization of the vacancy content within the copper-deficient aikinite series in thermoelectric properties. In this study, a range of compounds were synthesized by changing the  $x$  values and subsequently, the thermoelectric properties of these compounds were explored. The results indicate that an increase in vacancy ( $x$  value) results in an increase of the mobility, leading to a decrease in resistivity and an increase in the figure of merit.

Due to a number of factors, particularly the presence of lone pairs inducing anharmonicity in the crystal structure and the heavy atomic mass of bismuth resulting in reduced acoustic phonon frequency and low lattice thermal conductivity, the thermoelectric community has started giving more attention to bismuth-based sulfides. Bismuthinite ( $\text{Bi}_2\text{S}_3$ ) is one of these sulfides that have garnered a lot of attention in recent years. It has a space group of  $Pbnm$  and a highly anisotropic one-dimensional orthorhombic structure, indicating a high degree of anisotropy.<sup>1</sup> The pristine  $\text{Bi}_2\text{S}_3$  has low thermal conductivity,  $\sim 1.3 \text{ W m}^{-1} \text{ K}^{-1}$  at 300 K.<sup>2</sup> However, thermoelectric applications face a hurdle due to the low power factor, which is mainly controlled by the low electrical conductivity of the material. In order to overcome this issue, numerous strategies have been carried out, including chemical doping (by utilizing elements such as Cl, Br, I, and Se), alloying and nanostructuring.<sup>3-5</sup> These strategies aim to optimize carrier concentration to lower the lattice thermal conductivity and to raise the figure of merit ( $ZT$ ). In addition, several crystal structures derived from  $\text{Bi}_2\text{S}_3$

have been explored to further reduce the lattice thermal conductivity. Ternary systems with low lattice thermal conductivity include  $\text{Cu}_3\text{BiS}_3$ ,  $\text{MnBi}_4\text{S}_7$ ,  $\text{FeBi}_4\text{S}_7$ ,  $\text{Cu}_{1.4}\text{Bi}_{4.8}\text{S}_9$ ,  $\text{AgBi}_3\text{S}_5$ ,  $\text{Cu}_4\text{Bi}_4\text{S}_9$ , while quaternary systems with low thermal conductivity include aikinite and disordered gladite.<sup>6–13</sup> Furthermore, research has been done to investigate the effect of PbS introduction to the  $\text{Bi}_2\text{S}_3$  system. PbS has a simple rock salt type structure. Pseudo-binary compounds can be created through the incorporation of PbS into the  $\text{Bi}_2\text{S}_3$  system which enables the design of complex structures.<sup>14–16</sup> It is essential to have such a complex crystal structure in order to lower thermal conductivity. Therefore, the focus of this chapter will be on ternary sulfides based on Pb-Bi-S having a complex crystal structure. The work of Ohta *et al.* and Cai *et al.* represents significant advancements in the synthesis and characterization of Pb-Bi-based sulfides and their potential as promising thermoelectric materials.<sup>15,16</sup> Ohta *et al.* employed a solid-state melting reaction of the binary precursors PbS and  $\text{Bi}_2\text{S}_3$  to synthesize  $\text{PbBi}_2\text{S}_4$  and  $\text{Pb}_3\text{Bi}_2\text{S}_6$ .<sup>15</sup> The resulting samples exhibit effective phonon scattering, leading to extremely low lattice thermal conductivity. Moreover, degenerate semiconducting behaviour for those compounds was reported, which is unusual as those compounds should exhibit semiconducting behavior. This is most probably due to stoichiometry deviation during the process of solid-state melting. Subsequently, Cai *et al.* developed a solution-based synthesis method for  $\text{PbBi}_2\text{S}_4$  and  $\text{Pb}_3\text{Bi}_2\text{S}_6$  which results in low lattice thermal conductivity but also in degenerate semiconducting behavior.<sup>16</sup>

So, bearing in mind that the synthesis of stoichiometric  $\text{PbBi}_2\text{S}_4$  has never been reported, our motivation was to control the synthesis of this phase to obtain high purity and crystalline compounds. We have synthesized  $\text{PbBi}_2\text{S}_4$  by mechanical alloying combined by spark plasma sintering which permits to have a better control on the final stoichiometry. The sample shows semiconducting behaviour thanks to the synthetic technique. Further, in order to understand the origin of low thermal conductivity, we have performed DFT calculations. The DFT calculation suggests that the effective scattering of acoustic phonons result in very low thermal conductivity of  $\text{PbBi}_2\text{S}_4$ . Furthermore, to improve the thermoelectric performance, carrier concentration optimization has been carried out by introducing Cl on S site.

## 5.2. Methods

### 5.2.1. Reagent

High-purity lead powder (Pb, Alfa Aesar, >99.99%), bismuth powder (Bi, Alfa Aesar, >99.5%), bismuth chloride ( $\text{BiCl}_3$ , Alfa Aesar, >99.99) and sulfur powder (S, Alfa Aesar, >99.99) were used as precursors without further purification.

### 5.2.2. Synthesis

Pristine  $\text{PbBi}_2\text{S}_4$  was synthesized by milling stoichiometric amounts of Pb, Bi, and S powders (total amount of 6 g) in WC jars of 45 ml (14 WC balls of 10 mm) for 6 h (12 cycles of 30 min with 1 min pause) under an argon atmosphere. The main phase after a ball milling for 6 hrs contains orthorhombic  $\text{Bi}_2\text{S}_3$  and tetragonal Bi-Pb alloy (Figure 5.1).

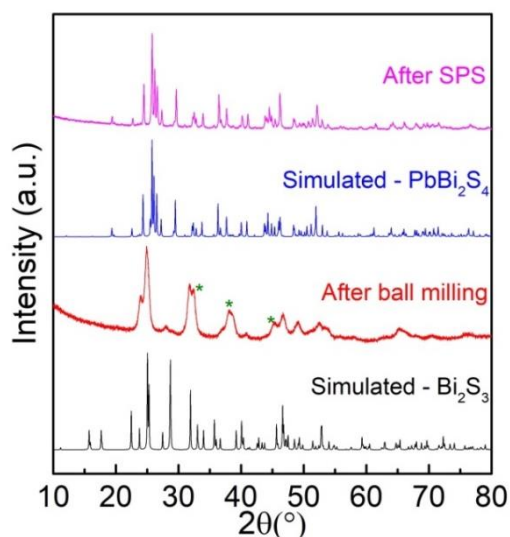


**Figure 5.1.** XRPD patterns after 6 hrs ball milling (red) correspond to  $\text{Bi}_2\text{S}_3$  main phase along with lead bismuth alloy<sup>17</sup> and after SPS (pink) correspond to  $\text{PbBi}_2\text{S}_4$  phase.

The broadness of the diffraction peaks, inherent to the synthesis method, is related to low crystallinity and/or small crystalline size of the powder samples, like in aikinite series samples. Powders were then placed in graphite dies of 10 mm diameter and densified by spark plasma sintering (SPS) at 723 K for 30 min under a pressure of 64 MPa with heating and cooling rates of  $45 \text{ K min}^{-1}$ . The resulting pellets have a diameter of 10 mm and a thickness of 9 mm, exhibiting geometrical densities that

exceeded 97% of the theoretical value. The XRPD patterns after SPS are equivalent and correspond to the  $\text{PbBi}_2\text{S}_4$  phase (space group  $Pnma$ ). The sharp diffraction patterns compared to the ball milled powder also indicate the microstructure evaluation and improvement of crystallinity (**Figure 5.1**).

## 5.3. Results and Discussion

### 5.3.1. Crystal structure

The formula,  $\text{Pb}_m\text{Bi}_2\text{S}_{3+m}$  ( $m = 0, 1, 3$ ) represents a group of Pb-Bi-S-based ternary compounds combining bismuthinite ( $\text{Bi}_2\text{S}_3$ ), galenobismuthite ( $\text{PbBi}_2\text{S}_4$ ) and Xilingolite ( $\text{Pb}_3\text{Bi}_2\text{S}_6$ ) which have shown promising thermoelectric figure of merit (**Table 5.1**).  $\text{Bi}_2\text{S}_3$  exhibits a highly anisotropic one-dimensional orthorhombic structure with a space group of  $Pbnm$ . This crystal structure is characterized by infinite  $\text{Bi}_2\text{S}_3$  chains aligned along the crystallographic  $c$ -axis. The lattice parameters for  $\text{Bi}_2\text{S}_3$  are  $a = 11.170 \text{ \AA}$ ,  $b = 11.319 \text{ \AA}$ ,  $c = 3.992 \text{ \AA}$ , with  $\alpha = \beta = \gamma = 90^\circ$ .  $\text{Bi}_2\text{S}_3$  layers are primarily held together by weak van der Waals forces, giving rise to a quasi-one-dimensional structure. In  $\text{Bi}_2\text{S}_3$ , two  $[\text{BiS}_3]$  trigonal cone units are linked together in serrated chains. These chains expand in the  $[001]$  direction, resulting in the creation of  $[\text{Bi}_4\text{S}_6]$  units shown in **Figure 5.2a**.

**Table 5.1.** Main structural information about  $\text{Pb}_m\text{Bi}_2\text{S}_{3+m}$  ( $m = 0, 1, 3$ ) series.

| $m$ | Composition                        | Mineral name    | Space group | Cell parameter  | Ref. |
|-----|------------------------------------|-----------------|-------------|---|------|
| 0   | $\text{Bi}_2\text{S}_3$            | Bismuthinite    | $Pbnm$      | $a = 11.170 \text{ \AA}$ , $b = 11.319 \text{ \AA}$ , $c = 3.992 \text{ \AA}$ , with $\alpha = \beta = \gamma = 90^\circ$ | 2    |
| 1   | $\text{PbBi}_2\text{S}_4$          | Galenobismutite | $Pnma$      | $a = 11.784 \text{ \AA}$ , $b = 4.069 \text{ \AA}$ , $c = 14.555 \text{ \AA}$ , with $\alpha = \beta = \gamma = 90^\circ$ | 15   |
| 3   | $\text{Pb}_3\text{Bi}_2\text{S}_6$ | Xilingolite     | $Bbmm$      | $a = 13.540 \text{ \AA}$ , $b = 20.637 \text{ \AA}$ , $c = 4.110 \text{ \AA}$ , with $\alpha = \beta = \gamma = 90^\circ$ | 16   |

The crystal structure of  $\text{PbBi}_2\text{S}_4$  consists of two types of strips: NaCl-type and  $\text{Bi}_2\text{S}_3$ -type strips. These strips are connected to each other through sulfur atoms that are either point- or edge-sharing. The NaCl-type strips are composed of alternating Pb and  $\text{BiS}_2$  layers, while the  $\text{Bi}_2\text{S}_3$ -type strips are composed of  $\text{BiS}_6$  octahedra that share edges to form a chain, as shown in **Figure 5.2b**. The two types of strips are arranged in an alternating fashion along the  $c$ -axis, resulting in a layered structure. The crystal structure of  $\text{Pb}_3\text{Bi}_2\text{S}_6$  is different from that of  $\text{PbBi}_2\text{S}_4$ . It consists of stacking NaCl-type (Pb/Bi)S layers, where the Pb and Bi atoms occupy the same crystallographic site (**Figure 5.2c**). The S atoms form a face-centered cubic (fcc) lattice, and the Pb/Bi atoms occupy half of the tetrahedral sites within this lattice. The stacking of these layers along the  $c$ -axis results in a three-dimensional crystal structure.

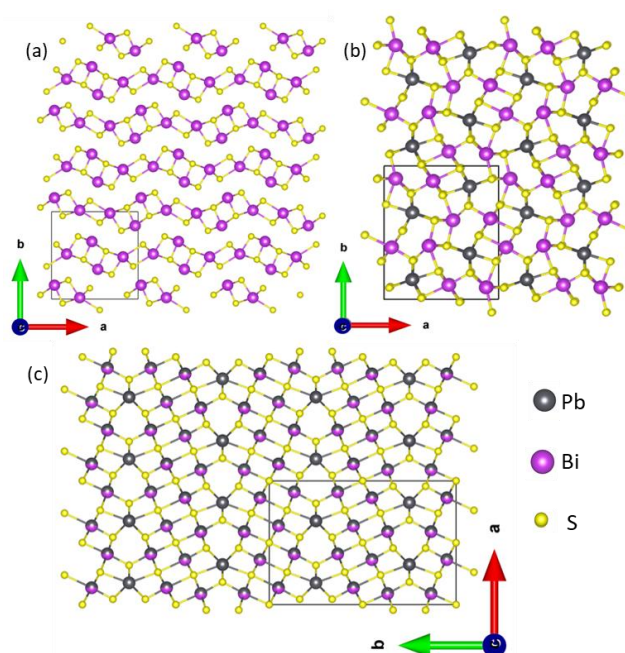


**Figure 5.2.** Crystal structure of (a)  $\text{Bi}_2\text{S}_3$ , (b)  $\text{PbBi}_2\text{S}_4$  (c)  $\text{Pb}_3\text{Bi}_2\text{S}_6$ .

The X-ray powder diffraction (XRPD) pattern of pristine  $\text{PbBi}_2\text{S}_4$  after SPS is indexed with an orthorhombic unit cell of space group  $Pnma$  exhibiting refined unit cell parameters  $a = 11.7842(2) \text{ \AA}$ ,  $b = 4.0693(1) \text{ \AA}$ ,  $c = 14.5555(3) \text{ \AA}$ . The high quality Rietveld refinement (**Figure 5.3**) is obtained by considering previously mentioned structural model. Moreover, the absence of non-indexed diffraction peaks suggests the

formation of high purity  $\text{PbBi}_2\text{S}_4$  sample after SPS. The refined cell parameters and atomic coordinates of pristine sample are given in **Table 5.2**.

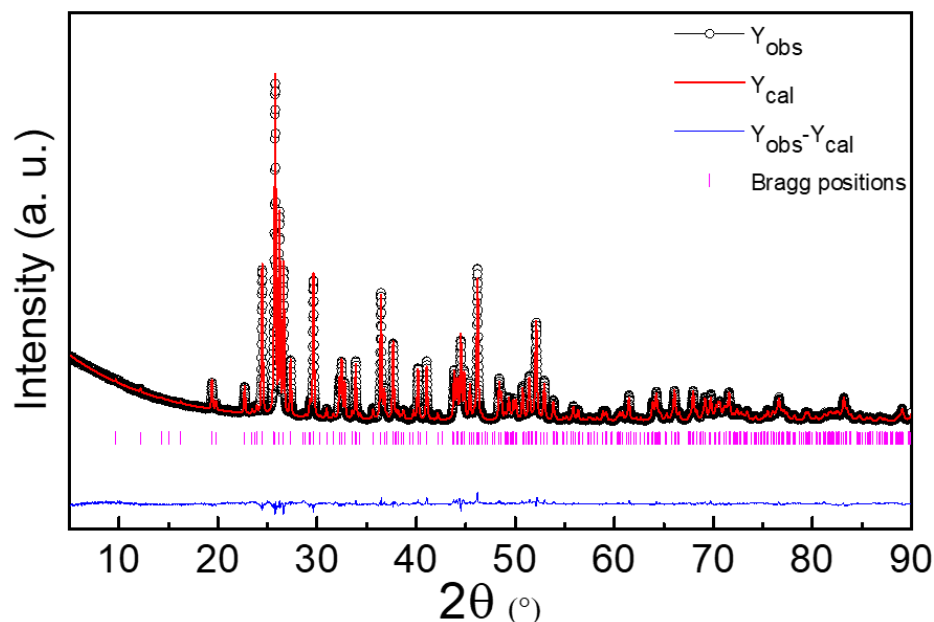


**Figure 5.3.** Rietveld refinement of the monochromated XRPD data recorded at RT for pristine  $\text{PbBi}_2\text{S}_4$  sample ( $\lambda = 1.5406 \text{ \AA}$ ).

**Table 5.2.** Refined cell parameters and atomic coordinates of Spark Plasma Sintered pristine  $\text{PbBi}_2\text{S}_4$  (*Pnma*).

| atom  | site | x         | y   | z         | $B_{\text{iso}} (\text{\AA}^2)$ | SOF |
|-------|------|-----------|-----|-----------|---------------------------------|-----|
| Bi(1) | 4c   | 0.0686(1) | 1/4 | 0.3900(1) | 0.22(3)                         | 1.0 |
| Bi(2) | 4c   | 0.1024(1) | 1/4 | 0.9054(1) | 0.66(3)                         | 1.0 |
| Pb(1) | 4c   | 0.2472(1) | 1/4 | 0.6528(1) | 0.79(3)                         | 1.0 |
| S(1)  | 4c   | 0.3394(5) | 1/4 | 0.0145(5) | 1.14(15)                        | 1.0 |
| S(2)  | 4c   | 0.2665(5) | 1/4 | 0.2984(3) | 0.25(13)                        | 1.0 |
| S(3)  | 4c   | 0.0535(5) | 1/4 | 0.0935(4) | 0.45(13)                        | 1.0 |
| S(4)  | 4c   | 0.0178(4) | 1/4 | 0.7103(3) | 0.34(15)                        | 1.0 |

$a = 11.7842(2) \text{ \AA}$ ,  $b = 4.0693(1) \text{ \AA}$ ,  $c = 14.5555(3) \text{ \AA}$   
 $R_{\text{Bragg}} = 4.41$ ,  $R_{\text{F}} = 2.71$ ,  $R_{\text{wp}} = 8.04$ ,  $R_{\text{exp}} = 3.80$ ,  $\chi^2 = 4.49$

### 5.3.2. Microstructure analysis of pristine $\text{PbBi}_2\text{S}_4$

The scanning electron microscopy (SEM) technique was utilized to investigate insights into the microstructure, grain size distribution, and chemical compositions of  $\text{PbBi}_2\text{S}_4$ . The back scattered image on fractured surface reveals a grain size around 1.2  $\mu\text{m}$ , as shown in **Figure 5.4a**. Additionally, the back scattered image on polished surface confirms the purity of the pristine samples (**Figure 5.4b**). The isoelectronic configuration of  $\text{Pb}^{2+}$  and  $\text{Bi}^{3+}$  in  $\text{PbBi}_2\text{S}_4$  prevents elemental mapping of Pb and Bi. Thus, we performed a comparable Energy-Dispersive X-ray (EDX) spot analysis on several spots of the sample, which supports the sample homogeneity, as shown in **Figures 5.4c and 5.4d**. The presence of bubble like cavities can be observed on both fractured and polished sample which arise due to incomplete sintering and/or the evaporation of sulfur during the SPS process. This phenomenon is commonly seen in sulfide-based materials, which have been discussed in chapter 2 and 3.

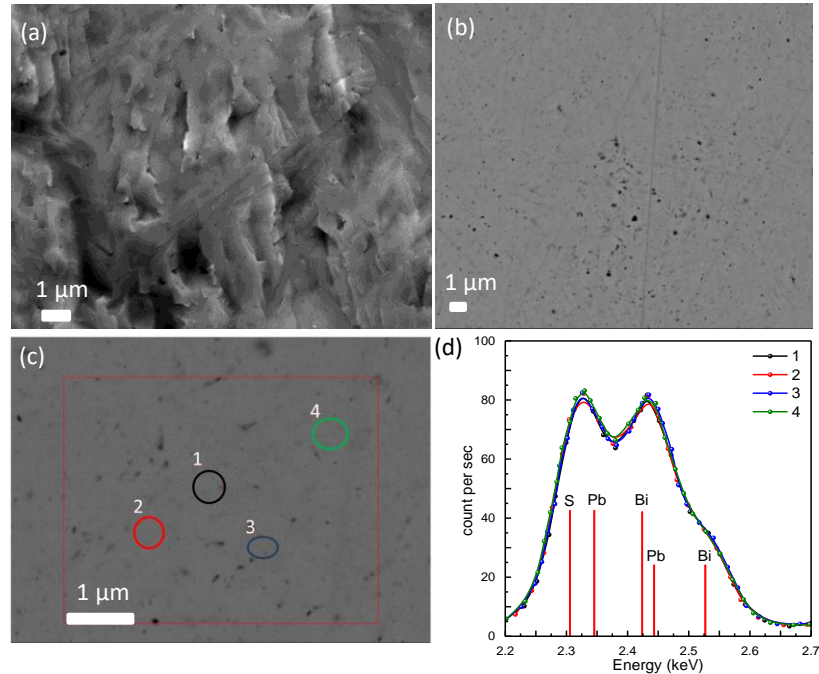


**Figure 5.4.** SEM characterization of pristine  $\text{PbBi}_2\text{S}_4$  (a, b) shows the back scattered images of crushed after SPS and polished sample, respectively; (c, d) the EDS spot analysis demonstrate the generally uniform elemental distribution.

### 5.3.3. Electrical properties of pristine $\text{PbBi}_2\text{S}_4$

The temperature dependence of the electrical resistivity ( $\rho$ ) of pristine  $\text{PbBi}_2\text{S}_4$  is shown in **Figure 5.5a**. The electrical resistivity decreases from  $10 \text{ } \Omega \text{ cm}$  at  $300 \text{ K}$  to  $0.4 \text{ } \Omega \text{ cm}$  at  $673 \text{ K}$ , indicating a semiconducting behavior. It is important to note that the previous reports by Ohta *et al.* and Cai *et al.* showed a degenerate semiconducting behavior, wherein the resistivity increases with temperature.<sup>15,16</sup> This indicates stoichiometry deviations, as confirmed by the large carrier concentration reported by Ohta *et al.* and Cai *et al.* (**Table 5.3**). The high purity of our sample can be attributed to the ball milling synthetic technique combined with SPS, as evidenced by its semiconducting behavior. The sample exhibits a relatively high electrical resistivity due to relatively low carrier concentration of  $4.8 \times 10^{17} \text{ cm}^{-3}$ , which aligns with its high Seebeck coefficient of  $-400 \text{ } \mu\text{V K}^{-1}$  at RT (**Figure 5.5b**, **Table 5.3**). The negative Seebeck coefficient indicates the *n*-type behavior of pristine sample which may due to the sulfur loss occurred during the SPS process. Note that the phase formation of  $\text{PbBi}_2\text{S}_4$  is not so fast compared to the aikinite series as the phase was not formed after 6 hrs of ball milling. SPS treatment allows to quickly complete the reaction and crystallization at relatively low sintering temperature ( $450 \text{ } ^\circ\text{C}$ ). The high electrical resistivity and moderate Seebeck coefficient result in very low power factor of  $0.02 \text{ } \mu\text{W cm}^{-1} \text{ K}^{-2}$  at  $300 \text{ K}$  which increases to  $0.57 \text{ } \mu\text{W cm}^{-1} \text{ K}^{-2}$  at  $673 \text{ K}$ , as shown in **Figure 5.5c**.

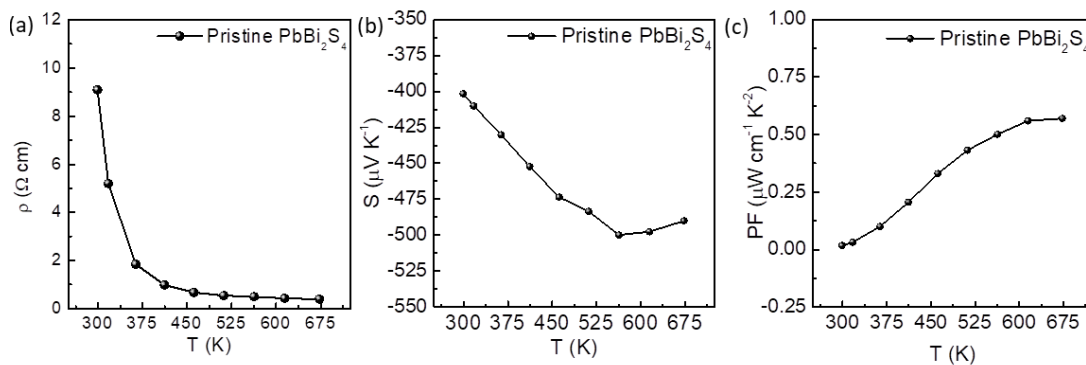


**Figure 5.5.** Temperature dependence from 300 K up to 673 K of (a) electrical resistivity ( $\rho$ ), (b) Seebeck coefficient ( $S$ ), (c) power factor ( $PF$ ) of pristine  $\text{PbBi}_2\text{S}_4$ .

**Table 5.3.** Comparison table of carrier concentration, hall mobility, resistivity and Seebeck coefficient at room temperature and maximum power factor, lattice thermal conductivity ( $RT$ ) and maximum  $ZT$  with previous report.

| author                           | carrier concentration (cm <sup>-3</sup> ) | $\mu$ (cm <sup>2</sup> V <sup>-1</sup> s <sup>-1</sup> ) | $\rho$ ( $\Omega$ cm) | S ( $\mu$ V K <sup>-1</sup> ) | PF ( $\mu$ W cm <sup>-1</sup> K <sup>-2</sup> ) | $\kappa_L$ (W m <sup>-1</sup> K <sup>-1</sup> ) | ZT              |
|----------------------------------|---|--|-----------------------|-------------------------------|---|---|-----------------|
| Ohta <i>et al.</i> <sup>15</sup> | $4.6 \times 10^{19}$                      | 12 ( $\perp$ )   | 0.011                 | -290                          | $\sim 2.7$<br>(610 K)                           | 0.63  | 0.33<br>(710 K) |
|                                  |   | 9.3 ( $\parallel$ )                                      | 0.015                 | -270                          | $\sim 2.5$<br>(610 K)                           | 0.6   | 0.29<br>(710 K) |
| Cai <i>et al.</i> <sup>16</sup>  | $8.8 \times 10^{19}$                      | 16.5   | 0.0043                | -82                           | 3.7<br>(800 K)                                  | 0.4   | 0.46<br>(800 K) |
| This work                        | $4.84 \times 10^{17}$                     | 1.4  | 10                    | -400                          | 0.57<br>(673 K)                                 | $\sim 0.65$                                     | 0.07<br>(673 K) |

**Table 5.4.** Comparison table of carrier concentration, hall mobility, resistivity and Seebeck coefficient at room temperature with other state of art Bi-based sulfides at room temperature.

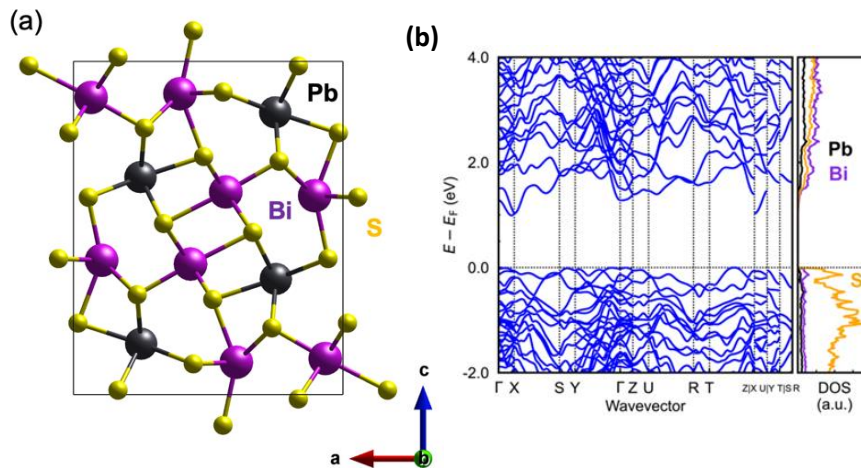
| samples                                       | carrier concentration (cm <sup>-3</sup> ) | $\mu$ (cm <sup>2</sup> V <sup>-1</sup> s <sup>-1</sup> ) | $\rho$ ( $\Omega$ cm) | S ( $\mu$ V K <sup>-1</sup> ) | ref.          |
|---|---|--|-----------------------|-------------------------------|---------------|
| PbBi <sub>2</sub> S <sub>4</sub>              | $4.84 \times 10^{17}$                     | 1.4  | 10                    | -400                          | This work     |
| Bi <sub>2</sub> S <sub>3</sub>                | $3.7 \times 10^{16}$                      | 640  | 0.25                  | -350                          | <sup>2</sup>  |
| AgBi <sub>3</sub> S <sub>5</sub>              | $4.1 \times 10^{18}$                      | 64   | 0.024                 | -155                          | <sup>10</sup> |
| MnBi <sub>4</sub> S <sub>7</sub>              | $6.3 \times 10^{19}$                      | 19   | $5.3 \times 10^{-3}$  | -87                           | <sup>8</sup>  |
| FeBi <sub>4</sub> S <sub>7</sub>              | $5.7 \times 10^{19}$                      | 16   | $7.1 \times 10^{-3}$  | -93                           | <sup>8</sup>  |
| Disordered CuPbBi <sub>5</sub> S <sub>9</sub> | $4.5 \times 10^{12}$                      | 3.7  | $3.5 \times 10^3$     | -1370                         | <sup>13</sup> |

**Table 5.4** shows a comparable study of electrical properties with other state-of-art Bi-based thermoelectric  $n$ -type sulfides. The low carrier concentration of PbBi<sub>2</sub>S<sub>4</sub> compared to AgBi<sub>3</sub>S<sub>5</sub>, MnBi<sub>4</sub>S<sub>7</sub> and FeBi<sub>4</sub>S<sub>7</sub> can be explained by the synthesis technique. The high-temperature melting procedure results in stoichiometry deviation, hence leading to high carrier concentrations for AgBi<sub>3</sub>S<sub>5</sub>, MnBi<sub>4</sub>S<sub>7</sub> and FeBi<sub>4</sub>S<sub>7</sub> which is

further supported by the notably low Seebeck coefficient and low electrical resistivity. Additionally, relatively small grain size that results from ball milling combined with SPS explains the low mobility of  $\text{PbBi}_2\text{S}_4$  and disordered  $\text{CuPbBi}_5\text{S}_9$ .

### 5.3.4. Electronic structure of pristine $\text{PbBi}_2\text{S}_4$

Structure optimizations of pristine  $\text{PbBi}_2\text{S}_4$  are performed using the plane-wave basis projector augmented wave (PAW) method<sup>18</sup> as implemented in Vienna *Ab initio* Simulation Package (VASP) and shown in **Figure 4.16a**.<sup>19,20</sup> The optimized lattice parameters are as follows:  $a = 11.595 \text{ \AA}$ ,  $b = 4.0485 \text{ \AA}$ , and  $c = 14.434 \text{ \AA}$  which are in good agreements with the experimental lattice parameters.

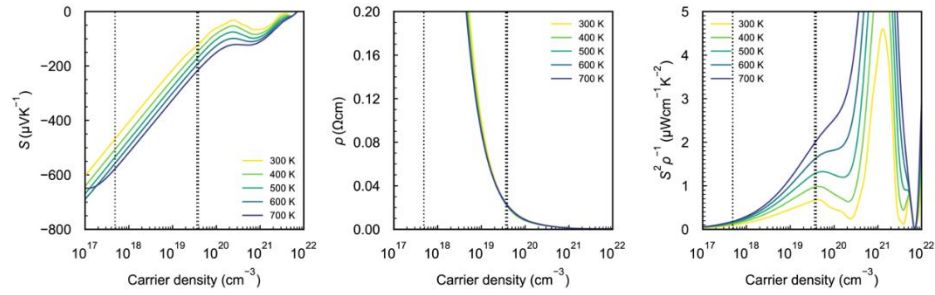
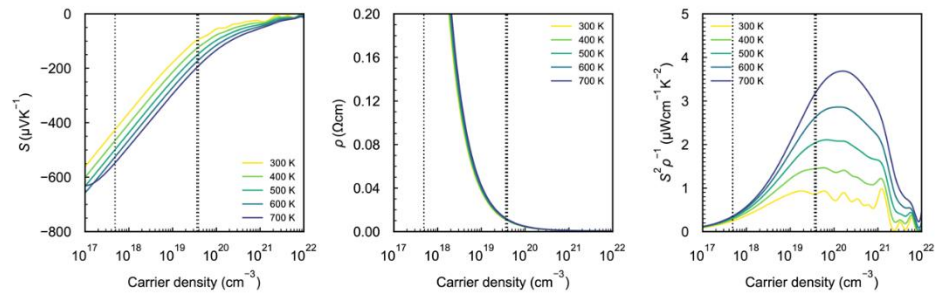
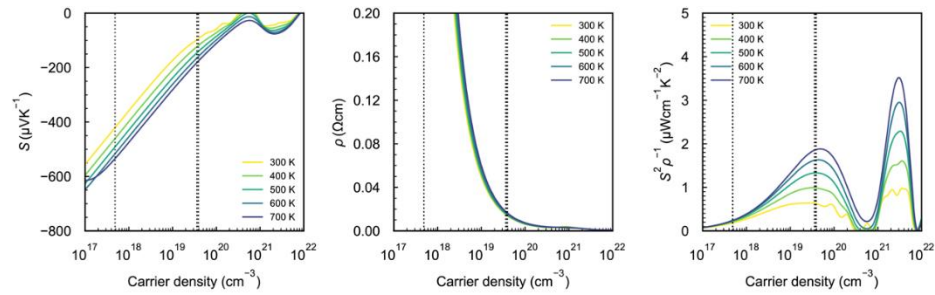


**Figure 5.6.** (a) Optimized structure of  $\text{PbBi}_2\text{S}_4$  were depicted by VESTA,<sup>21</sup> (b) Electronic band structures of  $\text{PbBi}_2\text{S}_4$  along with the element-deconvoluted DOSes

Electronic band structures of  $\text{PbBi}_2\text{S}_4$  along with the element-deconvoluted DOSes are shown in **Figure 5.6b**. This result shows that  $\text{PbBi}_2\text{S}_4$  is non degenerate semiconductor with a calculated bandgap of 1.02 eV, consistent with the previously reported *ab initio* calculations.<sup>14,16</sup> Further orbital decomposition of electronic DOS reveals that the valence band top is hybridized by S 3p, Bi 6s 6p, and Pb 6s 6p orbitals, while the conduction band bottom is hybridized by Bi 6p, S 3p, and Pb 6p, orbitals.

Carrier density and temperature dependences of Seebeck coefficient, resistivity and power factor calculated using the band energies of  $\text{PbBi}_2\text{S}_4$  are shown in **Figures**

**5.7.** Electronic transport properties of  $\text{PbBi}_2\text{S}_4$  were found to be anisotropic, with the optimal carrier densities for the power factor significantly different depending on the axis. Considering that the experimental samples are macroscopically isotropic polycrystals with random crystal orientations, the power factor would be high when the carrier density is  $\sim 1.0 \times 10^{20} \text{ cm}^{-3}$  or  $1.5 \times 10^{21} \text{ cm}^{-3}$  (**Figures 5.7d**).

(a) *a*-axis direction(b) *b*-axis direction(c) *c*-axis direction

(d) average

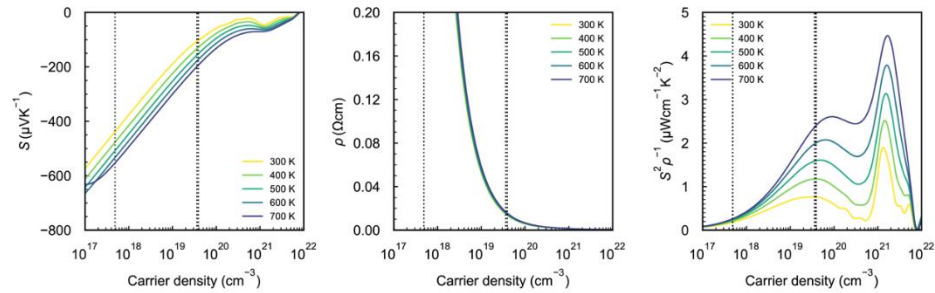


**Figure 5.7.** Seebeck coefficient, resistivity, and power factor calculated using the band energies of the  $\text{PbBi}_2\text{S}_4$  model as a function of carrier density. (a) *a*-axis direction, (b) *b*-axis direction, (c) *c*-axis direction, and (d) their average. The dotted straight lines indicate the measured carrier densities of experimental samples at room temperature shown in **Table 5.6**.

### 5.3.5. Thermal properties of pristine $\text{PbBi}_2\text{S}_4$

The pristine phase  $\text{PbBi}_2\text{S}_4$  has a low lattice total thermal conductivity (the electronic contribution being negligible) of  $0.65 \text{ W m}^{-1} \text{ K}^{-1}$  at 300 K, which decreases to  $0.55 \text{ W m}^{-1} \text{ K}^{-1}$  at 673 K as the temperature increases (**Figure 5.8a**).

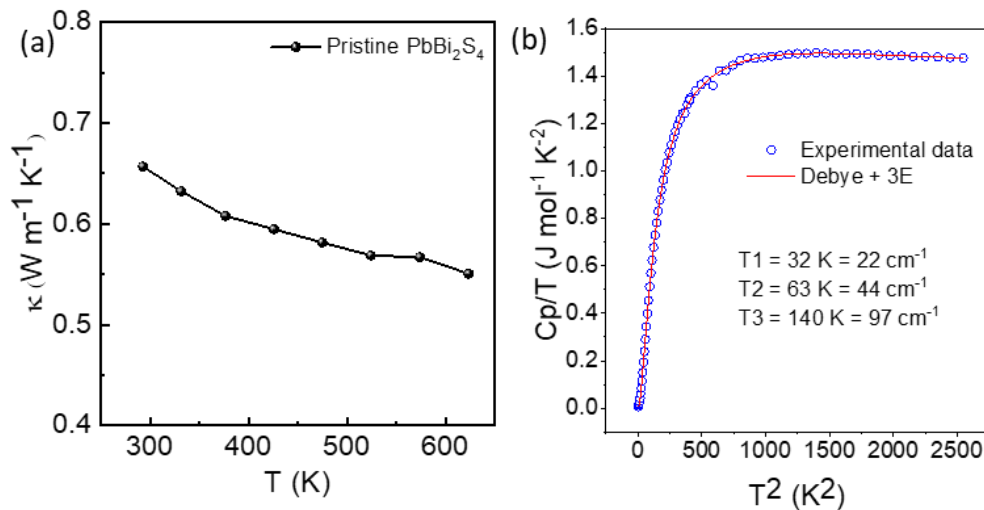


**Figure 5.8.** (a) Total thermal conductivity of  $\text{Cu}_3\text{BiS}_3$  in the temperature range of 300 K to 563 K, (b) Debye–Einstein fit of  $C_p/T$  vs  $T^2$  plot of  $\text{Cu}_3\text{BiS}_3$ .

We measured the low-temperature heat capacity of pristine  $\text{PbBi}_2\text{S}_4$  in order to get a better understanding of the origin of ultralow  $\kappa_L$  values. In the temperature range of 2–30 K, we discovered that a combined Debye–Einstein model, instead of just a Debye model, provided a better fit for the plot  $C_p/T$  vs.  $T^2$  (**Figure 5.8b**). Due to weakly dispersive low energy optical phonon modes, which correspond to independent atomic vibrations comparable to Einstein oscillators, the Debye model is insufficient to match the experimental low-temperature heat capacity data. This is because of the presence of

weakly dispersive low-energy optical phonon modes. The Debye-Einstein model can be expressed by equation (1), which is as follows:

$$\frac{C_p}{T} = \gamma + \beta T^2 + \sum_n \left( A_n (\theta_{E_n})^2 \cdot (T^2)^{-3/2} \cdot \frac{e^{\theta_{E_n}/T}}{(e^{\theta_{E_n}/T} - 1)^2} \right) \quad (1)$$

The equation first term is characterized by the Sommerfeld coefficient  $\gamma$ , which represent the electrical contribution. The second term, represented by the coefficient  $\beta$ , illustrates the lattice contribution. The equation third term accounts for the contributions originating from the Einstein oscillators associated with the localized vibrations. Here,  $A_n$  denotes the pre-factor, while  $\theta_{E_n}$  represents the Einstein temperature of the nth mode of the Einstein oscillator. A satisfactory agreement is obtained observed by employing the Debye-Einstein model, which incorporates three Einstein modes characterized by  $\theta_{E_1} = 32$  K ( $22 \text{ cm}^{-1}$ ),  $\theta_{E_2} = 63$  K ( $44 \text{ cm}^{-1}$ ), and  $\theta_{E_3} = 140$  K ( $97 \text{ cm}^{-1}$ ) (as depicted in **Figure 5.8b** and summarized in **Table 5.5**). The plot of  $C_p/T^3$  vs.  $T$  (**Figure 5.9**) demonstrates the existence of a Boson-like peak around 10 K, which is consistent with the observations in other materials with low thermal conductivity. This peak indicates an excess density of phonon states resulting from the presence of localized and low-frequency optical phonon modes. The Debye temperature ( $\theta_D$ ) was determined to be 221 K using the equation  $\beta = C(12\pi^4 N_A k_B / 5) \cdot (\theta_D)^{-3}$  in the Debye-Einstein model. Here,  $C$  is defined as  $C = 1 - \sum_n A_n / 3NR$ , where  $N$  represents the number of atoms per formula unit and  $R$  is the universal gas constant with a value of  $8.314 \text{ J mol}^{-1} \text{ K}^{-1}$ . Additionally,  $N_A$  and  $k_B$  denote Avogadro's number and the Boltzmann constant, respectively. The Debye temperature exhibits a level of comparability with the low thermal conductivity materials that are currently considered as state-of-the-art materials mentioned in chapter 2.

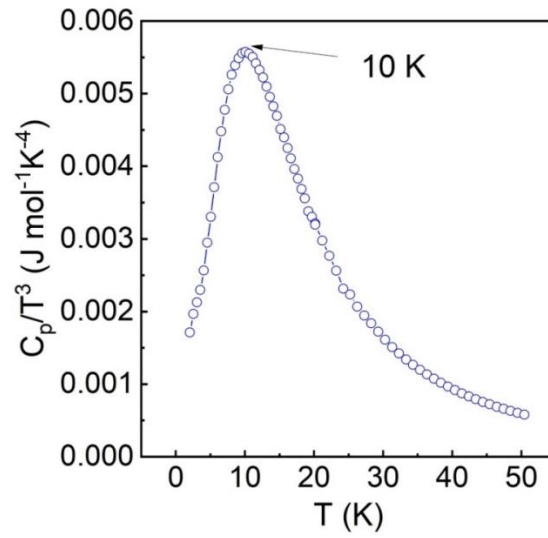


**Figure 5.9.**  $C_p/T^3$  versus  $T$  plot for  $PbBi_2S_4$  indicating Boson-like peak at around 10 K.

**Table 5.5.** Parameters obtained after  $C_p$  fitting using 3 einstein oscillators.

| parameters                                      | values     |
|---|------------|
| $\gamma / \text{Jmol}^{-1}\text{K}^{-2}$        | 0.007      |
| $\beta / 10^{-4} \text{Jmol}^{-1}\text{K}^{-2}$ | 9.19775E-5 |
| $\Theta_{E1}/\text{K}$                          | 32         |
| $\Theta_{E2}/\text{K}$                          | 63         |
| $\Theta_{E3}/\text{K}$                          | 140        |
| $A_1$   | 5.4        |
| $A_2$   | 39.5       |
| $A_3$   | 40.4       |
| $\Theta_D(\text{K})$                            | 221        |
| $R^2$   | 0.9998     |
| $\chi^2$  | 4.80962E-5 |

**Figure 5.10a** shows the phonon band structure of  $PbBi_2S_4$  along with the element-deconvoluted partial DOSes. No imaginary phonon modes were observed, indicating that  $PbBi_2S_4$  is dynamically stable. The partial DOSes show that Pb and Bi atoms

vibrate at lower frequencies and S atoms at higher frequencies without the overlap in frequency. This is due to the large difference in their atomic masses, namely 207.2 for Pb, 208.98 for Bi, and 32.065 for S. Weakly dispersed optical phonon modes were found at the frequency of about 1.2 THz ( $40 \text{ cm}^{-1}$ ), where the partial DOSes of Bi and Pb exhibit the peak values. These phonons have lower group velocities than the phonons at intermediate and high frequency regions (**Figure 5.10b**), and probably contribute to the scattering of acoustic phonon modes.

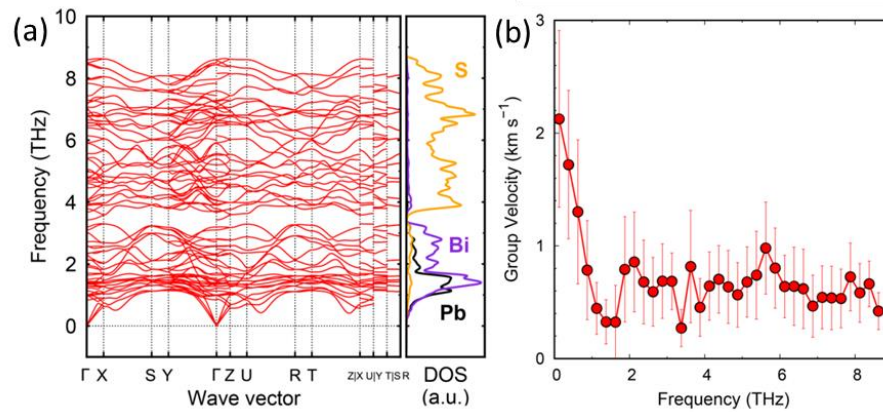


**Figure 5.10.** (a) Phonon band structure of  $\text{PbBi}_2\text{S}_4$  along with the element-deconvoluted DOSes. (b) Averaged group velocities of phonons in  $\text{PbBi}_2\text{S}_4$ , calculated for 0.25 THz frequency windows. Bars indicate the standard deviations of group velocities.

**Figure 5.11** shows calculated lattice thermal conductivity of  $\text{PbBi}_2\text{S}_4$  along each axis. The value is as low as  $0.49 \text{ W m}^{-1} \text{ K}^{-1}$  on average at 300 K, which is consistent with the experiments. The lattice thermal conductivity was found to be anisotropic, with relatively high value along  $b$ -axis, and low value along  $a$ - and  $c$ -axes (**Table 5.5**). The higher thermal conductivity along  $b$ -axis can be attributed to the higher translational symmetry in the crystal structure (shorter unit cell lengths) than  $a$ - and  $c$ -axes. Spectral analysis revealed that phonons at frequencies less than 3 THz, *i.e.*, acoustic phonons, mainly contribute to the lattice thermal conductivity, while optical phonons at frequencies larger than 3 THz ( $100 \text{ cm}^{-1}$ ), which mostly correspond to sulfur vibrations, have negligible contributions (**Figure 5.12**). The effective scattering of acoustic

phonons and the small contribution of optical phonons result in very low thermal conductivity of  $\text{PbBi}_2\text{S}_4$ .

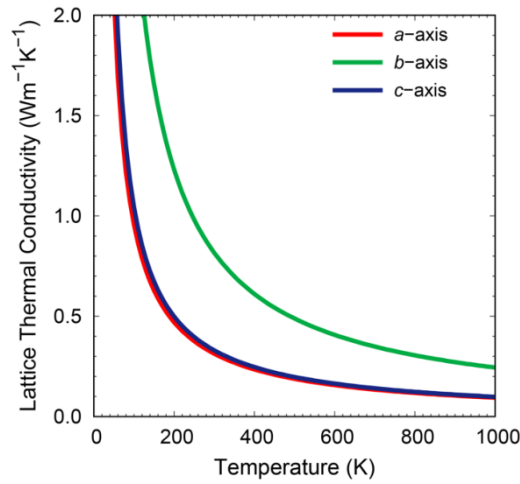


**Figure 5.11.** Temperature dependence of calculated lattice thermal conductivity of  $\text{PbBi}_2\text{S}_4$  in each axial direction.

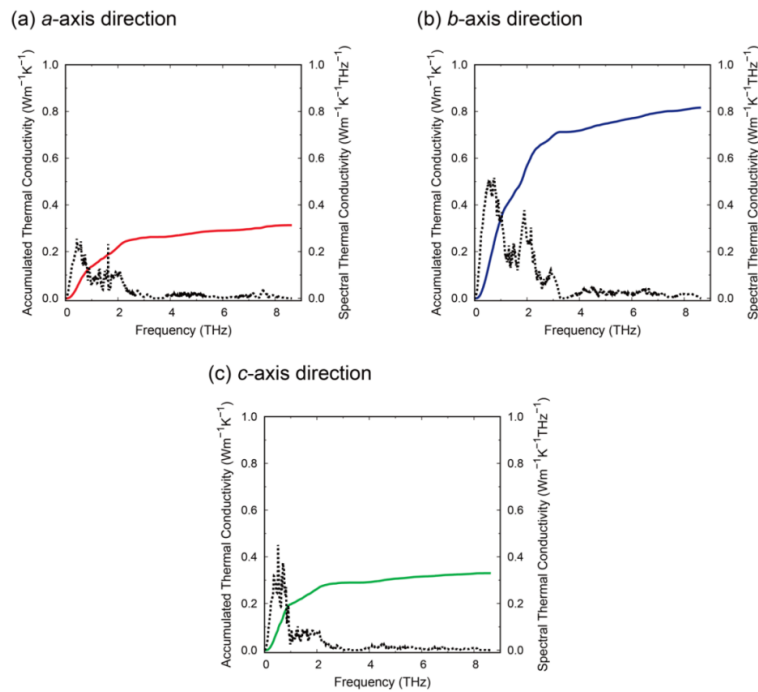


**Figure 5.12.** Accumulated and spectral lattice thermal conductivity of  $\text{PbBi}_2\text{S}_4$  at 300 K in the directions of (a) a-axis, (b) b-axis, and (c) c-axis. Colored solid and black

*dotted lines indicate accumulated and spectral lattice thermal conductivity, respectively.*

To further clarify the reason of the low thermal conductivity in  $\text{PbBi}_2\text{S}_4$ , we calculated the thermal conductivity of  $\text{PbBi}_2\text{S}_4$  with intentionally changing the atomic masses of the cations to that of the lighter S. This calculation yielded the thermal conductivity of  $0.74 \text{ W m}^{-1} \text{ K}^{-1}$  at 300 K on average, only slightly higher than  $0.49 \text{ W m}^{-1} \text{ K}^{-1}$ , as shown in **Table 5.5**. Low thermal conductivity of  $\text{PbBi}_2\text{S}_4$  even with the hypothetical lighter atomic masses indicates that the complex crystal structure, or the asymmetric coordination environments in  $\text{PbBi}_2\text{S}_4$ , is responsible for its very low thermal conductivity.

**Table 5.5.** *Calculated lattice thermal conductivity of  $\text{PbBi}_2\text{S}_4$ , without and with the assumption that the atomic masses of Pb and Bi are the same as that of S.*

| Axis     | Lattice thermal conductivity at 300 K ( $\text{W m}^{-1} \text{ K}^{-1}$ ) |                                      |
|----------|--|--------------------------------------|
|          | $\text{PbBi}_2\text{S}_4$  | $\text{PbBi}_2\text{S}_4$ (mass = S) |
| <i>a</i> | 0.313  | 0.457                                |
| <i>b</i> | 0.816  | 1.213                                |
| <i>c</i> | 0.330  | 0.535                                |
| average  | 0.486  | 0.735                                |

Despite of having a very low power factor, a maximum  $ZT$  value of 0.07 at 673 K temperature was obtained because of the low lattice thermal conductivity, as shown in **Figure 5.12**. The enhancement of the figure of merit is achieved through the process of chemical doping, wherein chlorine (Cl) is substituted for sulfur (S).

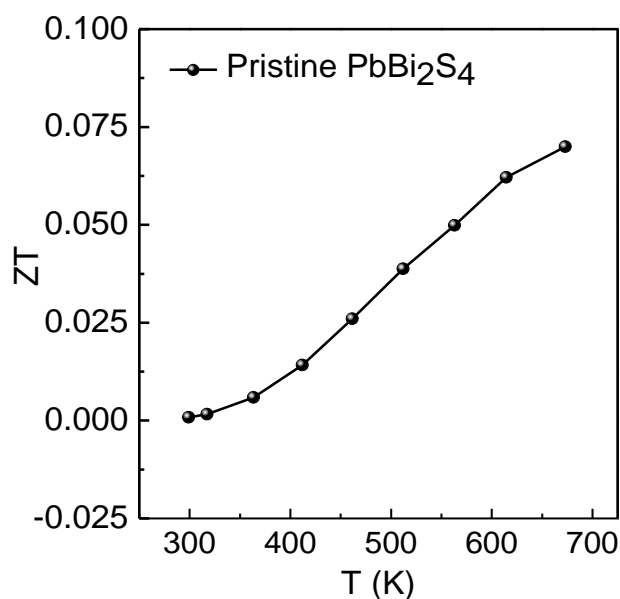


*Figure 5.12.* The figure of merit ( $ZT$ ) of pristine  $PbBi_2S_4$  in the temperature range of 300 K to 673 K.

### 5.3.4. XRPD analysis of doped samples

Despite having low thermal conductivity, pristine  $PbBi_2S_4$  has a high resistivity because of its extremely low carrier concentration, which results in low power factor and, ultimately, a low  $ZT$  value. In order to overcome this limitation and obtain more efficient materials, we substituted S by Cl to increase the carrier concentration. The doped sample  $PbBi_2S_{4-x}Cl_x$  ( $x = 0, 0.04, 0.8$ ) were synthesized using a milling process followed by SPS. Stoichiometric amounts of Pb, Bi,  $BiCl_3$ , and S powders, (total 6 g) were ball milled for 6 hrs. The milling process consisted of 12 cycles, each lasting 30 minutes with a minute pause; all conducted under an argon atmosphere. After that SPS process was carried out at 723 K for 30 mins. This synthesis method is similar to the one used for pristine sample discussed.

In **Figure 5.13**, the XRPD pattern of all chlorine (Cl) doped samples are presented, revealing a distinct correspondence with simulated patterns. Notably, for both doped samples,  $PbBi_2S_{3.96}Cl_{0.04}$  (red) and  $PbBi_2S_{3.92}Cl_{0.08}$  (blue), a minor impurity of  $Bi_2S_3$  is detected.

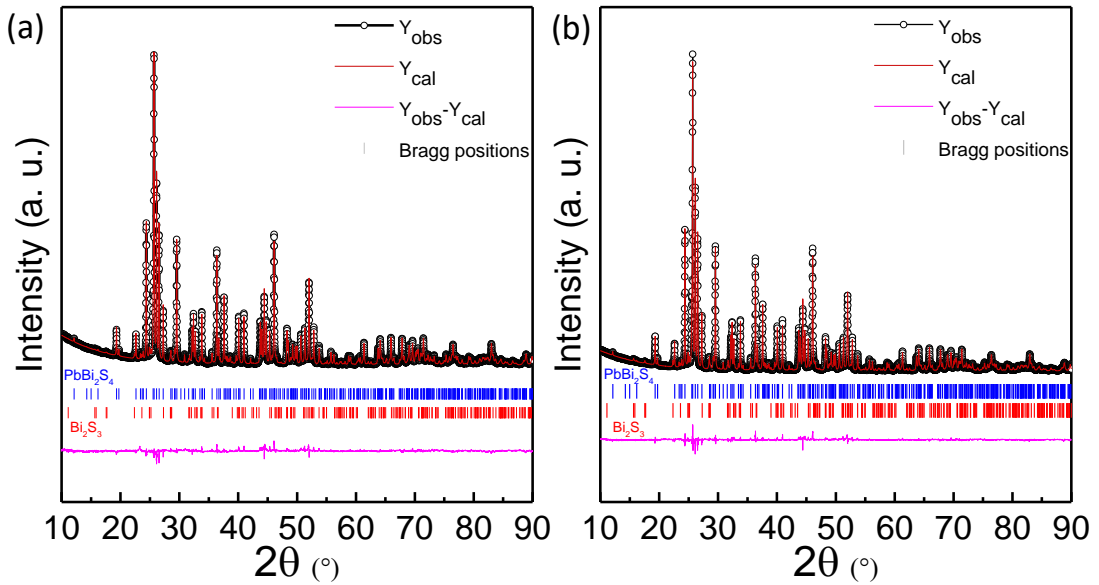


**Figure 5.13.** Rietveld refinement of the XRPD data recorded at room temperature (RT) for (a)  $\text{PbBi}_2\text{S}_{3.96}\text{Cl}_{0.04}$ , and (b)  $\text{PbBi}_2\text{S}_{3.92}\text{Cl}_{0.08}$  sample ( $\lambda = 1.5406 \text{ \AA}$ ).

**Table 5.6.** Refined unit cell parameters and reliability factors of the pristine and  $\text{PbBi}_2\text{S}_{4-x}\text{Cl}_x$  from the Rietveld analysis of the room-temperature XRPD data

|                                  | $\text{PbBi}_2\text{S}_4$ | $\text{PbBi}_2\text{S}_{3.96}\text{Cl}_{0.04}$ | $\text{PbBi}_2\text{S}_{3.92}\text{Cl}_{0.08}$ |
|----------------------------------|---------------------------|--|--|
| Space group                      | <i>Pnma</i>               | <i>Pnma</i>                                    | <i>Pnma</i>                                    |
| $a$ ( $\text{\AA}$ )             | 11.7842(2)                | 11.8015(2)                                     | 11.8105(1)                                     |
| $b$ ( $\text{\AA}$ )             | 4.0693(1)                 | 4.0750(2)                                      | 4.0771(1)                                      |
| $c$ ( $\text{\AA}$ )             | 14.555(3)                 | 14.5808(2)                                     | 14.5910(2)                                     |
| $V$ ( $\text{\AA}^3$ )           | 701.79(4)                 | 701.21(2)                                      | 702.60(2)                                      |
| $R_{\text{Bragg}}, R_{\text{F}}$ | 4.41, 2.71                | 5.39, 3.32                                     | 3.53, 2.28                                     |
| $R_{\text{wp}}, R_{\text{exp}}$  | 8.04, 3.80                | 5.93, 3.10                                     | 5.07, 2.83                                     |
| $\chi^2$                         | 4.49                      | 3.66   | 3.20   |

### 5.3.5. SEM analysis of doped samples.

To evaluate homogeneity, microstructure, and impurity phases, SEM imaging has been done on doped  $\text{PbBi}_2\text{S}_4$  samples. The backscattered images of the polished  $\text{PbBi}_2\text{S}_{3.96}\text{Cl}_{0.04}$  and  $\text{PbBi}_2\text{S}_{3.92}\text{Cl}_{0.08}$  samples revealed the presence of cavities which were attributed to the vaporization of sulfur during the SPS process (**Figure 5.14**). **Figure 5.14** displays the presence of the minor impurity phase of  $\text{Bi}_2\text{S}_3$  as dark contrast (as the Bi/S ratio for  $\text{Bi}_2\text{S}_3$  is less than (Pb+Bi)/S ratio for  $\text{PbBi}_2\text{S}_4$ ) which was further confirmed by XRPD refinement discussed earlier.

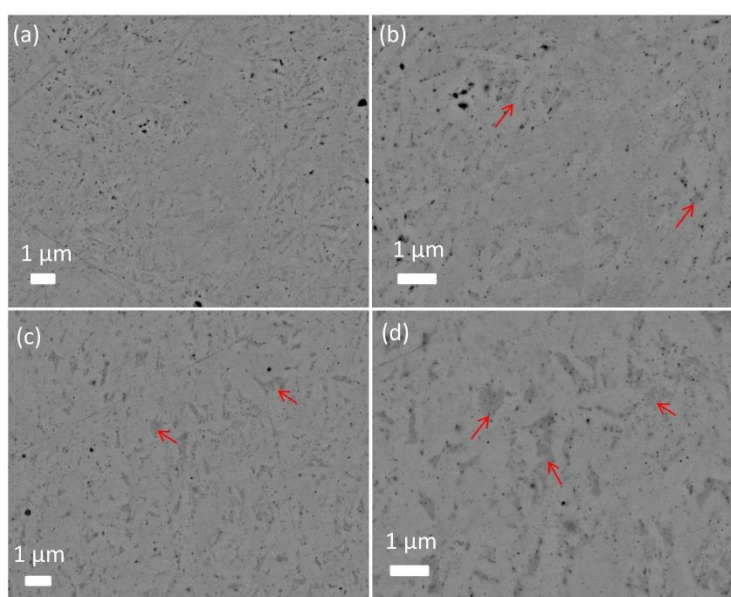


**Figure 5.14.** SEM characterization of  $\text{PbBi}_2\text{S}_{3.96}\text{Cl}_{0.04}$  (a, b) and  $\text{PbBi}_2\text{S}_{3.92}\text{Cl}_{0.08}$  (c, d) show the back scattered images of polished sample. The red arrows indicate the  $\text{Bi}_2\text{S}_3$  impurity phase.

### 5.3.6. Electronic transport properties of doped samples

**Figure 5.15** shows the electrical properties for the series of  $\text{PbBi}_2(\text{S}_{1-x}\text{Cl}_x)_4$  samples over the temperature range of 300 - 673 K (where  $x = 0, 0.04, 0.08$ ). The absolute Seebeck coefficient ( $|S|$ ) and resistivity ( $\rho$ ) values exhibit a steady decrease with the Cl content. As an example,  $\text{PbBi}_2\text{S}_{3.92}\text{Cl}_{0.08}$  shows the values of  $|S|$  and  $\rho$  at 300 K are observed to decrease to  $176 \mu\text{V K}^{-1}$  and  $0.025 \Omega \text{ cm}$ , respectively compare to pristine sample. In all compositions, the absolute values of the Seebeck coefficient ( $|S|$ ) exhibits

a consistent decrease as the temperature increases, whereas the electrical resistivity of both doped sample decrease with temperature till 420 K and subsequently increase with temperature. This behavior indicates that despite the introduction of additional electrons due to S substitution by Cl, the doped materials exhibit in between degenerate and non-degenerate semiconductor characteristics. This observation implies that the electron concentration does not reach a sufficiently high level to induce degeneracy phenomena. The decrease in the absolute value of  $S$  and  $\rho$  as the Cl content increases is consistent with the function of chlorine as an electron-dopant when it replaces sulfur in the crystal lattice.

**Table 5.6.** Carrier concentration and hall mobility of  $PbBi_2(S_{1-x}Cl_x)_4$  ( $x = 0, 0.4, 0.8$ )

| sample                    | carrier concentration<br>( $\text{cm}^{-3}$ ) | mobility<br>( $\text{cm}^2 \text{V}^{-1} \text{Sec}^{-1}$ ) |
|---------------------------|---|---|
| $PbBi_2S_4$               | $4.8 \times 10^{17}$                          | 1.4   |
| $PbBi_2S_{3.96}Cl_{0.04}$ | $3.6 \times 10^{19}$                          | 4.9   |
| $PbBi_2S_{3.92}Cl_{0.08}$ | $3.9 \times 10^{19}$                          | 6.4   |

The carrier concentration at room temperature exhibits an upward trend as the Cl content increases. For  $x = 0.04$ , the carrier concentration reaches approximately  $3.6 \times 10^{19} \text{ cm}^{-3}$ . Similarly, for  $x = 0.08$ , the carrier concentration is approximately  $3.9 \times 10^{19} \text{ cm}^{-3}$ . In contrast, the values of room temperature mobility ( $\mu$ ) are relatively modest, with respective values of 1.4, 4.9, 6.3  $\text{cm}^2 \text{V}^{-1} \text{sec}^{-1}$  for  $x = 0, 0.04$ , and 0.08. These values are notably smaller than those measured in other bismuth-based compounds, which can largely be attributed to the relatively small grain size and/or the disordered structure due to ball milling synthetic technique.

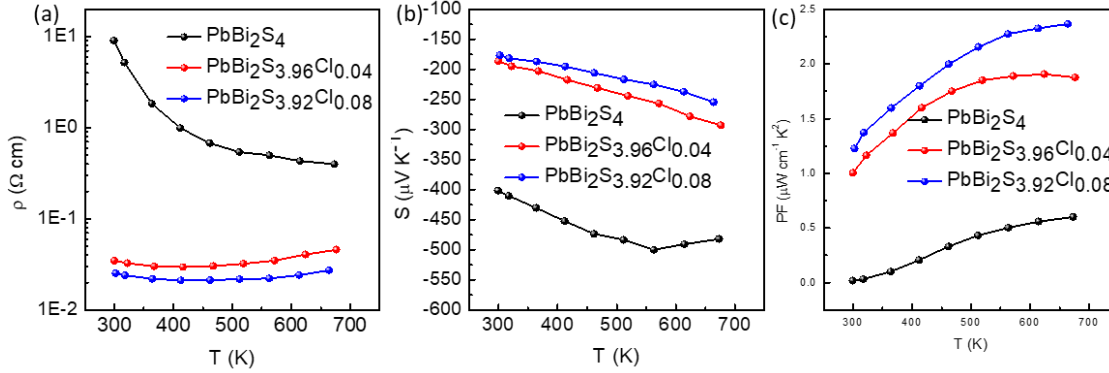


**Figure 5.15.** Temperature dependence of (a) electrical resistivity, (b) Seebeck coefficient and (c) power factor in the  $\text{PbBi}_2(\text{S}_{1-x}\text{Cl}_x)_4$  ( $x = 0.04, 0.08$ ).

The power factor ( $PF$ ) as a function of temperature in the series  $\text{PbBi}_2(\text{S}_{1-x}\text{Cl}_x)_4$  ( $x = 0, 0.04, 0.08$ ) is shown in **Figure 5.15c**. The power factor increases significantly with Cl content to a maximum value of  $2.36 \mu\text{W cm}^{-1} \text{K}^2$  at 700 K for  $\text{PbBi}_2\text{S}_{3.92}\text{Cl}_{0.08}$ .

### 5.3.4. Electronic structure of $\text{PbBi}_2\text{S}_{3.75}\text{Cl}_{0.25}$

The structure optimization of Cl-doped  $\text{PbBi}_2\text{S}_{3.75}\text{Cl}_{0.25}$  is performed and the optimized lattice parameters are as follows:  $a = 11.681 \text{ \AA}$ ,  $b = 4.0999 \text{ \AA}$ , and  $c = 14.456 \text{ \AA}$  for  $\text{PbBi}_2\text{S}_{3.75}\text{Cl}_{0.25}$ . These parameters are in good agreements with the experimental lattice parameters. Note that there are three symmetrically non-equivalent sulfur sites in  $\text{PbBi}_2\text{S}_4$ . We performed structure optimizations of three models where one of these non-equivalent S sites was replaced by Cl, and the model with the lowest energy was used as the representative of Cl-doped  $\text{PbBi}_2\text{S}_{3.75}\text{Cl}_{0.25}$  (**Figure 5.16a**).

The substitution of Cl for S dopes electrons into  $\text{PbBi}_2\text{S}_4$ , as indicated by the shift of Fermi energy into the conduction band (**Figure 5.16b**), with no drastic changes in the electronic band structure and DOS. This is expected from the fact that the Cl doping does not change the structure of  $\text{PbBi}_2\text{S}_4$  significantly (**Figure 5.16, Figure 5.6**). These results support the experimental results that the Cl substitution doped electrons and improved electronic properties.

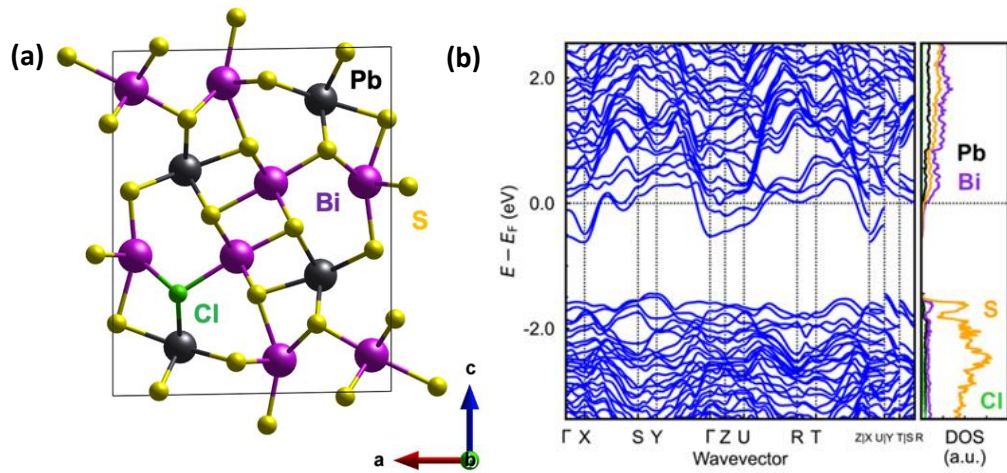


**Figure 5.16.** (a) Optimized structure of  $\text{PbBi}_2\text{S}_4$  were depicted by VESTA,<sup>21</sup> (b) Electronic band structures of (a)  $\text{PbBi}_2\text{S}_{3.75}\text{Cl}_{0.25}$  along with the element-deconvoluted DOSes.

**Figure 5.17** shows the carrier density and temperature dependences of Seebeck coefficient, resistivity, and power factor calculated using the band energies of  $\text{PbBi}_2\text{S}_{3.75}\text{Cl}_{0.25}$ . The measured carrier density of  $\text{PbBi}_2\text{S}_{3.92}\text{Cl}_{0.08}$  at room temperature is about  $3.9 \times 10^{19} \text{ cm}^{-3}$ , which is sufficiently close to the value of  $\sim 1.0 \times 10^{20} \text{ cm}^{-3}$ . Since the carrier electrons increase by thermal excitation as the temperature increases<sup>16</sup> and the carrier density is expected to approach to the value of  $1.0 \times 10^{20} \text{ cm}^{-3}$ , it is confirmed from the calculations that the experimentally optimized carrier density by the Cl doping is highly successful.

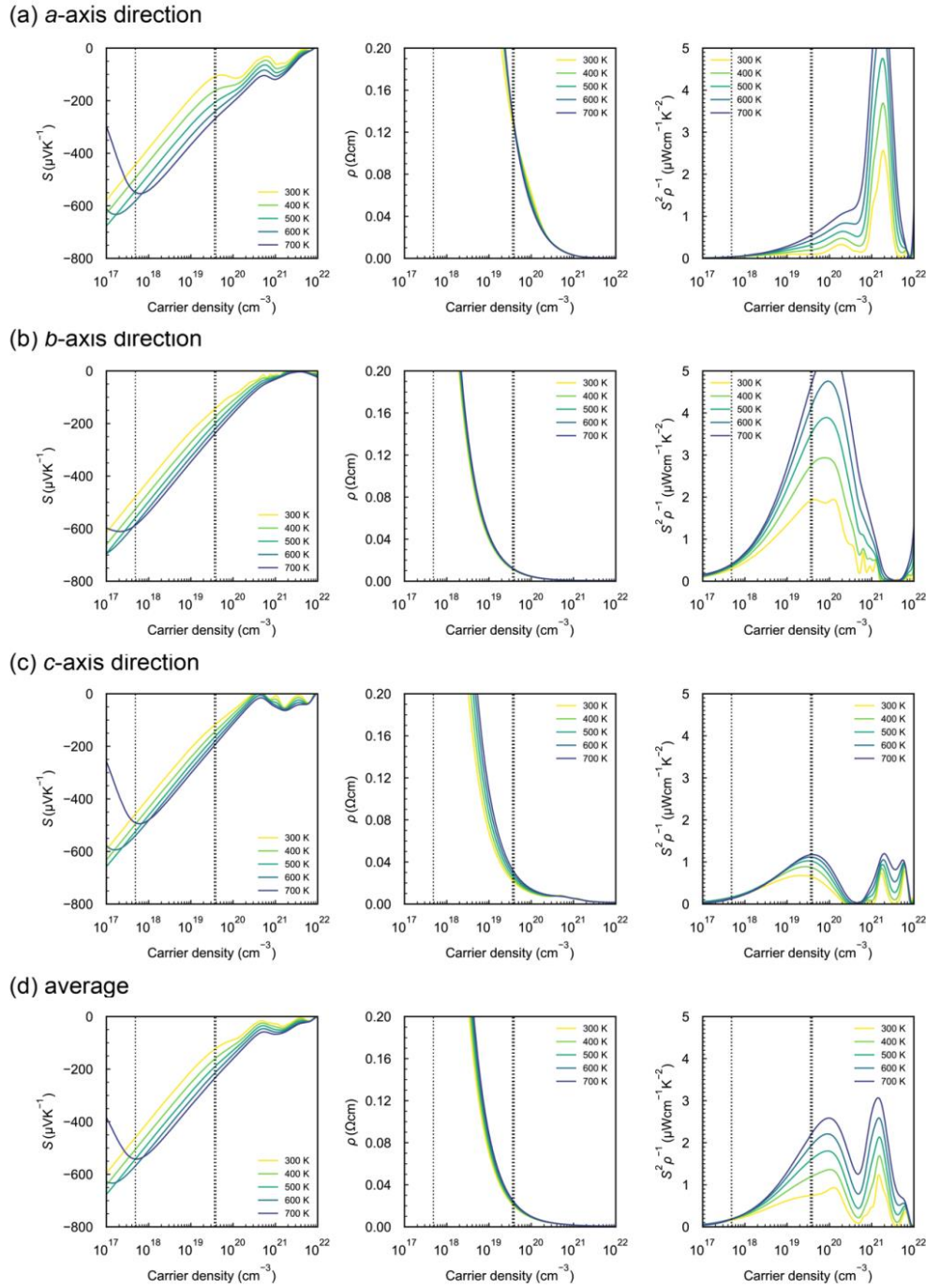


**Figure 5.17.** Seebeck coefficient, resistivity, and power factor calculated using the band energies of the  $\text{PbBi}_2\text{S}_{3.75}\text{Cl}_{0.25}$  model as a function of carrier density. (a) *a*-axis direction, (b) *b*-axis direction, (c) *c*-axis direction, and (d) their average. The dotted straight lines indicate the measured carrier densities of experimental samples at room temperature shown in **Table 4.6**

### 5.3.7. Thermal transport properties and figure of merit of doped samples

The temperature-dependent total thermal conductivity ( $\kappa$ ) of  $\text{PbBi}_2\text{S}_{4-x}\text{Cl}_x$  samples with different chlorine (Cl) concentrations ( $x = 0, 0.04, 0.08$ ) is presented in **Figure 5.18a**. The pristine  $\text{PbBi}_2\text{S}_4$  demonstrates exceptionally low thermal conductivity values of  $0.65 \text{ W m}^{-1} \text{ K}^{-1}$  at a temperature of 300 K, with a slight decrease to  $0.52 \text{ W m}^{-1} \text{ K}^{-1}$  at a temperature of 673 K. The results presented here align with the findings reported by Ohta *et al.* When the concentration of chlorine (Cl) increases, there is a slight fluctuation in thermal conductivity, resulting in a range of values between 0.65 and  $0.7 \text{ W m}^{-1} \text{ K}^{-1}$  at a temperature of 300 K. The electronic contribution ( $\kappa_e$ ) to the overall thermal conductivity ( $\kappa$ ) is considered negligible due to the relatively high electrical resistivity of the samples. As previously mentioned, the lattice component ( $\kappa_L$ ) has a prominent role in determining thermal conductivity.

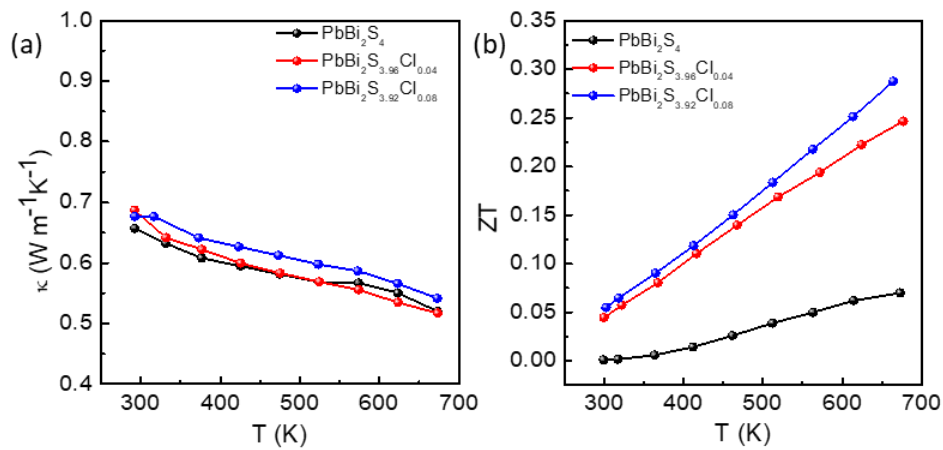


**Figure 5.18.** Temperature dependence of (a) thermal conductivity and (b) figure of merit  $ZT$  for  $\text{PbBi}_2\text{S}_{4-x}\text{Cl}_x$  where  $x = 0, 0.4, 0.08$ .

**Figure 5.18b** displays the temperature-dependent figure of merit ( $ZT$ ) for all Cl doped samples. The  $ZT$  value demonstrates a consistent increase across the temperature range of 300 to 673 K as the Cl content is increased. Note that, this improvement in  $ZT$  is

evident not just at higher temperatures but also at room temperature. The highest obtain  $ZT$  value is 0.3 at 673 K for  $\text{PbBi}_2\text{S}_{3.92}\text{Cl}_{0.08}$  which is 328% increase in comparison to the pristine sample. **Figure 5.19** illustrates a comparison of  $ZT$  values between  $\text{PbBi}_2\text{S}_{3.92}\text{Cl}_{0.08}$  and other state-of-the-art  $n$ -type Bi-based sulfides. The results clearly indicate that the  $ZT$  of the  $\text{PbBi}_2\text{S}_{3.92}\text{Cl}_{0.08}$  sample is modest in comparison to the other bismuth based sulfides. Although the carrier concentrations and  $\kappa$  values associated with maximum  $ZT$  values are comparable to those of other state-of-the-art materials, our compound exhibits lower efficiency due to its high resistivity and low Seebeck coefficient when compared to  $\text{AgBi}_3\text{S}_5$ ,  $\text{Bi}_2\text{S}_3$ , and  $\text{CuPbBi}_5\text{S}_9$ .<sup>10,13</sup> However, our compound demonstrates higher efficiency due to its higher power factor when compared to  $\text{AgBiS}_2$ ,  $\text{MnBi}_4\text{S}_7$ ,  $\text{FeBi}_4\text{S}_7$ , and  $\text{Cu}_{x+y}\text{Bi}_{5-y}\text{S}_8$ .<sup>22-24</sup>

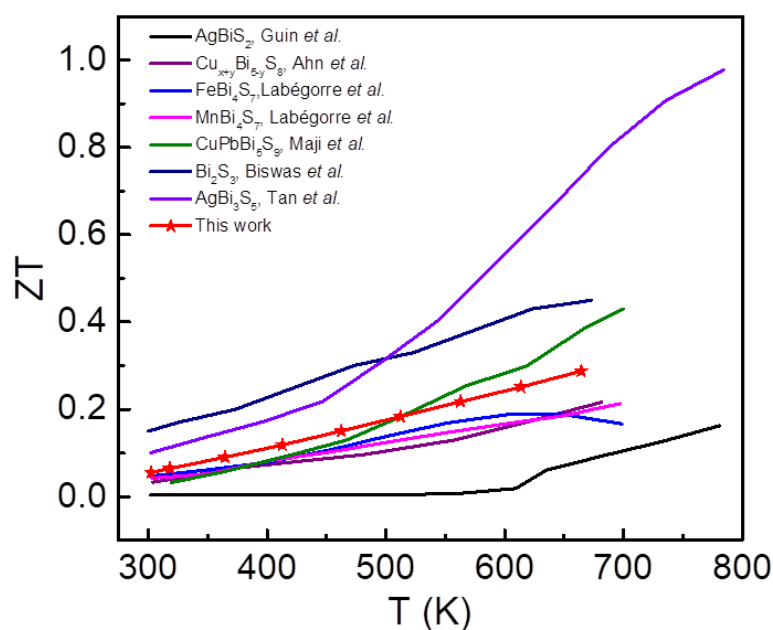


**Figure 5.19.**  $ZT$  comparison table of state of art Bi-rich thermoelectric sulfides along with 2% Cl doped  $\text{PbBi}_2\text{S}_4$  throughout the temperature range.

## 5.4. Conclusion

In conclusion, using a combination of ball milling and SPS, we were able to successfully synthesize a high-purity sample of semiconducting  $\text{PbBi}_2\text{S}_4$  that exhibits a

---

very low lattice thermal conductivity of  $0.65 - 0.55 \text{ W m}^{-1} \text{ K}^{-1}$  in the temperature range of 300 - 673 K. Low-temperature heat capacity analysis revealed the presence of low-frequency optical phonon branches, which are crucial in reducing the heat flow by scattering the heat-carrying acoustic phonon branches. The presence of several low-frequency optical modes and the existence of phonon scattering through anharmonic coupling between acoustic and optical phonon modes are further confirmed by the DFT study. The complex crystal structure and bonding heterogeneity in  $\text{PbBi}_2\text{S}_4$  have a synchronized constructive influence, leading to a significant impact on the propagation of phonons. As a result,  $\text{PbBi}_2\text{S}_4$  exhibits an inherently low lattice thermal conductivity ( $\kappa_L$ ).

## 5.5. References

- (1) Kupčák, V.; Veselá-Nováková, L. Zur Kristallstruktur Des Bismuthinites,  $\text{Bi}_2\text{S}_3$ . *Tschermaks Mineral. und Petrogr. Mitteilungen* **1970**, *14* (1), 55–59. <https://doi.org/10.1007/BF01081780>.
- (2) Biswas, K.; Zhao, L. D.; Kanatzidis, M. G. Tellurium-Free Thermoelectric: The Anisotropic n-Type Semiconductor  $\text{Bi}_2\text{S}_3$ . *Adv. Energy Mater.* **2012**, *2* (6), 634–638. <https://doi.org/10.1002/aenm.201100775>.
- (3) Yang, J.; Liu, G.; Yan, J.; Zhang, X.; Shi, Z.; Qiao, G. Enhanced the Thermoelectric Properties of n-Type  $\text{Bi}_2\text{S}_3$  Polycrystalline by Iodine Doping. *J. Alloys Compd.* **2017**, *728*, 351–356. <https://doi.org/10.1016/j.jallcom.2017.08.148>.
- (4) Fortulan, R.; Aminorroaya Yamini, S.; Nwanebu, C.; Li, S.; Baba, T.; Reece, M. J.; Mori, T. Thermoelectric Performance of N-Type Magnetic Element Doped  $\text{Bi}_2\text{S}_3$ . *ACS Appl. Energy Mater.* **2022**, *5* (3), 3845–3853. <https://doi.org/10.1021/acsaem.2c00295>.
- (5) Liu, W.; Lukas, K. C.; McEnaney, K.; Lee, S.; Zhang, Q.; Opeil, C. P.; Chen, G.; Ren, Z. Studies on the  $\text{Bi}_2\text{Te}_3$ - $\text{Bi}_2\text{Se}_3$ - $\text{Bi}_2\text{S}_3$  System for Mid-Temperature Thermoelectric Energy Conversion. *Energy Environ. Sci.* **2013**, *6* (2), 552–560. <https://doi.org/10.1039/c2ee23549h>.
- (6) Adeyemi, A. N.; Clemente, M.; Lee, S. J.; Mantravadi, A.; Zaikina, J. V. Deep Eutectic Solvent-Assisted Microwave Synthesis of Thermoelectric  $\text{AgBiS}_2$  and  $\text{Cu}_3\text{BiS}_3$ . *ACS Appl. Energy Mater.* **2022**, *5*, 14858–14868. <https://doi.org/10.1021/acsaem.2c02336>.
- (7) Wei, K.; Hobbis, D.; Wang, H.; Nolas, G. S. Wittichenite  $\text{Cu}_3\text{BiS}_3$ : Synthesis and Physical Properties. *J. Electron. Mater.* **2018**, *47* (4), 2374–2377. <https://doi.org/10.1007/s11664-017-6053-0>.
- (8) Labégorre, J. B.; Virfeu, A.; Bourhim, A.; Willeman, H.; Barbier, T.; Appert, F.; Juraszek, J.; Malaman, B.; Huguenot, A.; Gautier, R.; Nassif, V.; Lemoine, P.; Prestipino, C.; Elkaim, E.; Pautrot-d’Alençon, L.; Le Mercier, T.; Maignan, A.; Al Rahal Al Orabi, R.; Guilmeau, E.  $\text{XBi}_4\text{S}_7$  ( $X = \text{Mn}, \text{Fe}$ ): New Cost-Efficient Layered n-Type Thermoelectric Sulfides with Ultralow Thermal Conductivity.

- Adv. Funct. Mater.* **2019**, *29* (48), 1904112–1904124. <https://doi.org/10.1002/adfm.201904112>.
- (9) Bhui, A.; Dutta, M.; Mukherjee, M.; Rana, K. S.; Singh, A. K.; Soni, A.; Biswas, K. Ultralow Thermal Conductivity in Earth-Abundant  $\text{Cu}_{1.6}\text{Bi}_{4.8}\text{S}_8$ : Anharmonic Rattling of Interstitial Cu. *Chem. Mater.* **2021**, *33* (8), 2993–3001. <https://doi.org/10.1021/acs.chemmater.1c00659>.
- (10) Tan, G.; Hao, S.; Zhao, J.; Wolverton, C.; Kanatzidis, M. G. High Thermoelectric Performance in Electron-Doped  $\text{AgBi}_3\text{S}_5$  with Ultralow Thermal Conductivity. *J. Am. Chem. Soc.* **2017**, *139* (18), 6467–6473. <https://doi.org/10.1021/jacs.7b02399>.
- (11) Jiang, Y.; Jia, F.; Chen, L.; Wu, L. M.  $\text{Cu}_4\text{Bi}_4\text{Se}_9$ : A Thermoelectric Symphony of Rattling, Anharmonic Lone-Pair, and Structural Complexity. *ACS Appl. Mater. Interfaces* **2019**, *11* (40), 36616–36625. <https://doi.org/10.1021/acsami.9b11115>.
- (12) Carnevali, V.; Mukherjee, S.; Voneshen, D. J.; Maji, K.; Guilmeau, E.; Powell, A. V.; Vaqueiro, P.; Fornari, M. Lone Pair Rotation and Bond Heterogeneity Leading to Ultralow Thermal Conductivity in Aikinite. *J. Am. Chem. Soc.* **2023**, *145* (16), 9313–9325. <https://doi.org/10.1021/jacs.3c02536>.
- (13) Maji, K.; Lemoine, P.; Renaud, A.; Zhang, B.; Zhou, X.; Carnevali, V.; Candolfi, C.; Raveau, B.; Al Rahal Al Orabi, R.; Fornari, M.; Vaqueiro, P.; Pasturel, M.; Prestipino, C.; Guilmeau, E. A Tunable Structural Family with Ultralow Thermal Conductivity: Copper-Deficient  $\text{Cu}_{1-x}\text{Pb}_{1-x}\text{Bi}_{1+x}\text{S}_3$ . *J. Am. Chem. Soc.* **2022**, *144* (4), 1846–1860. <https://doi.org/10.1021/jacs.1c11998>.
- (14) Savory, C. N.; Ganose, A. M.; Scanlon, D. O. Exploring the  $\text{PbS-Bi}_2\text{S}_3$  Series for Next Generation Energy Conversion Materials. *Chem. Mater.* **2017**, *29* (12), 5156–5167. <https://doi.org/10.1021/acs.chemmater.7b00628>.
- (15) Ohta, M.; Chung, D. Y.; Kunii, M.; Kanatzidis, M. G. Low Lattice Thermal Conductivity in  $\text{Pb}_5\text{Bi}_6\text{Se}_{14}$ ,  $\text{Pb}_3\text{Bi}_2\text{S}_6$ , and  $\text{PbBi}_2\text{S}_4$ : Promising Thermoelectric Materials in the Cannizzarite, Lillianite, and Galenobismuthite Homolog. *J. Mater. Chem. A* **2014**, *2* (47), 20048–20058. <https://doi.org/10.1039/c4ta05135a>.
- (16) Cai, F.; Dong, R.; Sun, W.; Lei, X.; Yu, B.; Chen, J.; Yuan, L.; Wang, C.; Zhang, Q.  $\text{Pb}_m\text{Bi}_2\text{S}_{3+m}$  Homologous Series with Low Thermal Conductivity Prepared by

- the Solution-Based Method as Promising Thermoelectric Materials. *Chem. Mater.* **2021**, *33* (15), 6003–6011. <https://doi.org/10.1021/acs.chemmater.1c01387>.
- (17) Suryanarayana, C.; Anantharaman, T. R. On the Structure of a Metastable Phase in the Lead-Bismuth System. *Solid State Commun.* **1973**, *12*, 87–88.
- (18) Blöchl, P. E. Projector Augmented-Wave Method. *Phys. Rev. B* **1994**, *50* (24), 17953–17979. <https://doi.org/10.1103/PhysRevB.50.17953>.
- (19) Kresse, G.; Furthmüller, J. Efficient Iterative Schemes for Ab Initio Total-Energy Calculations Using a Plane-Wave Basis Set. *Phys. Rev. B* **1996**, *54* (16), 11169–11186. <https://doi.org/10.1103/PhysRevB.54.11169>.
- (20) Kresse, G.; Hafner, J. Ab Initio Molecular-Dynamics Simulation of the Liquid-Metalamorphous- Semiconductor Transition in Germanium. *Phys. Rev. B* **1994**, *49* (20), 14251–14269. <https://doi.org/10.1103/PhysRevB.49.14251>.
- (21) Momma, K.; Izumi, F. VESTA 3 for Three-Dimensional Visualization of Crystal, Volumetric and Morphology Data. *J. Appl. Crystallogr.* **2011**, *44* (6), 1272–1276. <https://doi.org/10.1107/S0021889811038970>.
- (22) Guin, S. N.; Biswas, K. Cation Disorder and Bond Anharmonicity Optimize the Thermoelectric Properties in Kinetically Stabilized Rocksalt AgBiS<sub>2</sub> Nanocrystals. *Chem. Mater.* **2013**, *25* (15), 3225–3231. <https://doi.org/10.1021/cm401630d>.
- (23) Labégorre, J. B.; Virfeu, A.; Bourhim, A.; Willeman, H.; Barbier, T.; Appert, F.; Juraszek, J.; Malaman, B.; Huguenot, A.; Gautier, R.; Nassif, V.; Lemoine, P.; Prestipino, C.; Elkaim, E.; Pautrot-d'Alençon, L.; Le Mercier, T.; Maignan, A.; Al Rahal Al Orabi, R.; Guilmeau, E. XBi<sub>4</sub>S<sub>7</sub> (X = Mn, Fe): New Cost-Efficient Layered n-Type Thermoelectric Sulfides with Ultralow Thermal Conductivity. *Adv. Funct. Mater.* **2019**, *29* (48). <https://doi.org/10.1002/adfm.201904112>.
- (24) Ahn, J. Y.; Hwang, J. Y.; Ryu, B. K.; Oh, M. W.; Lee, K. H.; Kim, S. W. Importance of Crystal Chemistry with Interstitial Site Determining Thermoelectric Transport Properties in Pavonite Homologue Cu-Bi-S Compounds. *CrystEngComm* **2016**, *18* (8), 1453–1461. <https://doi.org/10.1039/c5ce02143j>.

## **Chapter 6**

---

### **General conclusion**

---



My thesis is focused on the synthesis, structural characterization and evaluation of the thermoelectric performances of Bi-based ternary and quaternary sulfide materials.

In the second chapter, a novel Cu-deficient Bi-based quaternary sulfide with an aikinite-type structure, denoted as  $\text{CuPbBi}_5\text{S}_9$ , has been successfully synthesized using a combination of mechanical alloying and Spark Plasma Sintering (SPS) techniques. Although this sulfide shares the same composition as the previously reported gladite by Liang *et al.*, it distinguishes itself by having a disordered arrangement of copper and vacancies within the cationic sites. In contrast to Liang *et al.*, which reported the presence of secondary phases in relatively large quantities, this Cu-deficient aikinite material is highly pure. This purity allows for an in-depth investigation of its transport properties. Remarkably, this synthetic sulfide exhibits an extremely low lattice thermal conductivity. It exhibits an intrinsic semiconducting behaviour with electrical resistivity around  $5.1 \Omega \text{ cm}$  and Seebeck coefficient of  $-1300 \mu\text{V K}^{-1}$  at 400 K, and low carrier concentration of  $4.5 \times 10^{12} \text{ cm}^{-3}$  at RT. This synthetic sulfide serves as an interesting prototype for achieving high thermoelectric performance through doping with Cl or Bi, resulting in thermoelectric figures of merit ranging from 0.30 to 0.43 at 700 K. The thermoelectric performance of this material is mainly attributed to its remarkably low lattice thermal conductivity, primarily due to the involvement of low-energy vibrations associated with Bi, Pb, and Cu. The substantial enhancement in the thermoelectric figure of merit upon Cl or Bi doping is linked to the Bi-S framework capacity to generate *n*-type conductivity. Importantly, this compound, representing the member  $x = 2/3$  in a broader series of closely related sulfides  $\text{Cu}_{1-x}\square_x\text{Pb}_{1-x}\text{Bi}_{1+x}\text{S}_3$  with  $0 \leq x \leq 1$ , serves as a model for a diverse family of *n*-type thermoelectric materials. These materials can be optimized by adjusting their chemical composition, controlling order-disorder phenomena, and fine-tuning carrier concentration through doping.

The third chapter provides an overview of the synthesis process for a range of compounds within the Cu-deficient aikinite-type sulfide family, specifically denoted as  $\text{Cu}_{1-x}\square_x\text{Pb}_{1-x}\text{Bi}_{1+x}\text{S}_3$ . These compounds were synthesized using a combination of mechanical alloying and SPS methods. XRPD and TEM analyses have revealed that these compounds exhibit a disordered arrangement of copper and vacancies within the cationic sites, similar to the disordered gladite phase, as discussed in Chapter 2.

Specifically, our research findings confirm that the remarkably low lattice thermal conductivity observed in these compounds is an inherent characteristic. Samples from this series display notably high electrical resistivity, resembling intrinsic semiconductors, much like the original disordered gladiolite phase. However, due to the low carrier concentration, these materials are less suitable for thermoelectric applications. While some enhancement in the thermoelectric figure of merit is achieved by improve mobility. The increasing  $x$  values in series leads to increase the Bi to Pb ratio which eventually decrease the point defect and increases mobility. For example, compound with  $x = 0.83$  shows best performance among all quaternary sulfides. A maximum  $ZT$  values of around 0.05 is obtained at 673 K for  $x = 0.83$  sample which is the highest among Cu deficient  $\text{Cu}_{1-x}\text{Pb}_x\text{Bi}_{1+x}\text{S}_3$  series due to hall mobility increase. Further enhancement of the thermoelectric figure of merit can be achieved through the optimization of carrier concentration via suitable doping strategies.

In the next chapter, the electrical and thermal properties of Cu-rich Bi-based sulfides,  $\text{Cu}_3\text{BiS}_3$  are discussed and compared to state-of-the-art compounds, in relation with cation coordination and crystal structure. The pivotal role of copper coordination in generating and tuning the thermoelectric properties of copper-rich sulfides is well explained along with its comparison to tetrahedrite  $\text{Cu}_{12}\text{Sb}_4\text{S}_{13}$ . An exceptionally low electrical conductivity is observed in this sulfide. Along with this  $\text{Cu}_3\text{BiS}_3$  is unable to facilitate the delocalization of hole carriers, which can be directly attributed to the three-fold coordination of copper like low chalcocite  $\text{Cu}_2\text{S}$  and skinnerite  $\text{Cu}_3\text{SbS}_3$ . In contrast, tetrahedral copper coordination can form 3D corner-sharing frameworks in many sphalerite-derivative sulfides, allowing for charge delocalization due to the mixed valency Cu(I)-Cu(II), leading to high carrier concentration. In addition, the three-fold coordination of copper favours its anisotropic displacement, thereby contributing significantly to the achievement of extremely low thermal conductivity. Consequently, the research of “composite” frameworks, that incorporate both tetrahedrally and three-fold coordinated copper, becomes an enticing challenge in the quest for high-performance thermoelectric copper sulfides. It is worth emphasizing that the presence of cations with lone pairs (LPs), such as  $\text{Bi}^{3+}$  or  $\text{Sb}^{3+}$ , emerges as a critical factor for stabilizing the structural arrangement. Furthermore, the proximity of electronic LPs to

the three-fold coordinated  $\text{Cu}^+$  offers a promising avenue for modulating intrinsic Cu-rattling to optimize thermal conductivity.

In the final chapter, a successful synthesis of highly-purity semiconducting  $\text{PbBi}_2\text{S}_4$  is achieved through a combination of ball milling and SPS. This material has an impressively low lattice thermal conductivity ranging from 0.65 to 0.55  $\text{W m}^{-1} \text{K}^{-1}$  over the temperature range of 300 to 673 K. A detailed analysis of the low-temperature heat capacity revealed the presence of low-frequency optical phonon branches, which play a pivotal role in reducing heat transfer by scattering the heat-carrying acoustic phonon branches. Our findings were further supported by DFT calculations, confirming the existence of multiple low-frequency optical modes and demonstrating phonon scattering through anharmonic coupling between acoustic and optical phonon modes. The intricate crystal structure and bonding heterogeneity within  $\text{PbBi}_2\text{S}_4$  synergistically contribute to this phenomenon, resulting in a substantial reduction in phonon propagation and, consequently, an inherently low lattice thermal conductivity ( $\kappa_L$ ) for  $\text{PbBi}_2\text{S}_4$ .

In conclusion, using a combination of ball milling and SPS, we were able to successfully synthesize a high-purity sample of semiconducting  $\text{PbBi}_2\text{S}_4$  that exhibits a very low lattice thermal conductivity of 0.65 - 0.55  $\text{W m}^{-1} \text{K}^{-1}$  in the temperature range of 300 - 673 K. Low-temperature heat capacity analysis revealed the presence of low-frequency optical phonon branches, which are crucial in reducing the heat flow by scattering the heat-carrying acoustic phonon branches. The presence of several low-frequency optical modes and the existence of phonon scattering through anharmonic coupling between acoustic and optical phonon modes are further confirmed by the DFT study. The complex crystal structure and bonding heterogeneity in  $\text{PbBi}_2\text{S}_4$  have a synchronized constructive influence, leading to a significant impact on the propagation of phonons. As a result,  $\text{PbBi}_2\text{S}_4$  exhibits an inherently low lattice thermal conductivity ( $\kappa_L$ ). Moreover, a promising thermoelectric figure of merit (0.3) has been achieved by increasing the carrier concentration and lowering the electrical resistivity using Cl dopant in S site.

Furthermore, during my three years of thesis work, I had the opportunity to investigate into issues that extended beyond the realm of simply developing efficient thermoelectric compounds.

The investigation of an alternate synthesis technique to the conventional one was one key challenge I addressed. Conventional synthesis methods involving sealed tubes require prolonged heat treatments at high temperatures, which lead to non-stoichiometric sulfide compounds. Furthermore, other conventional synthesis methods, such as solution-based synthesis are considered environmentally unfriendly due to the utilization of hazardous solvents. Moreover, these conditions hinder the production of large quantities of sample. Consequently, we devoted considerable effort to investigating mechanical-alloying synthesis as an alternative approach. This method has proven to be highly valuable, as it allows for the creation of homogeneous, stoichiometric samples. Subsequently, these powders can be crystallized efficiently through SPS after the ball milling step. This synthesis method represents a substantial advantage in the development of sulfide materials for thermoelectric applications.

Another aspect of my investigation was the crystal chemistry and its impact on thermoelectric properties. Unlike previous studies, our synthetic gladite phase did not exhibit the ordered gladite mineral structure. Instead, it adopted a disordered aikinite structure with copper deficiency and partial replacement of Pb by Bi, as represented by the chemical formula  $\text{Cu}_{1/3}\square_{2/3}\text{Pb}_{1/3}\text{Bi}_{5/3}\text{S}_3$ . Furthermore, we emphasized the significance of the coordination types and networks involving Cu in influencing both electrical and thermal properties in  $\text{Cu}_3\text{BiS}_3$ . Our research revealed that the extremely low thermal conductivity in  $\text{Cu}_3\text{BiS}_3$  primarily arises from the highly anisotropic thermal vibrations of copper due to its threefold coordination. Additionally, the complex crystal structure of  $\text{PbBi}_2\text{S}_4$  also influence the thermoelectric properties by affecting phonon scattering, electronic band structure, charge carrier scattering, charge carrier density, and chemical bonding. All these factors collectively shape the material's thermal and electrical conductivity as well as its thermoelectric efficiency.

Finally, the various works carried out during this period have shown the importance of the development processes on the structure and thermoelectric properties of these materials. These results ultimately open numerous perspectives for the

---

identification and optimization of Bi-based sulfide compounds with promising thermoelectric properties.



## **Chapter 7**

---

### **Appendices**

---



## 7.1. Synthesis and process

### 7.1.1. Mechanochemical alloying/milling

In mechanochemical alloying/milling, reagents are mixed with high-velocity balls and a high level of energy is applied to them in order for them to chemically react. Solids are ground together to produce products with properties that are different from the starter materials. This concept has been used for centuries in various applications, one famous example being the discovery of gunpowder in China well before the 14<sup>th</sup> century. However, it has been applied to synthetic chemistry in the late 60's with the mechanical alloying of oxide-dispersion strengthened superalloys. Mechanochemical alloyed materials have since been improved, and they have become increasingly attractive; not only because they can be made without high-temperature furnaces, but also because they allow control over power microstructures. As a matter of fact, the constant fracturing and welding rewelding process greatly influences the morphology and size of powder particles, and induced defects in the materials' structure. A material's physical properties can be altered by controlling the faults, point defects, or local nonstoichiometric defects. In a dry mechanochemical synthesis, powdered reagents are mixed together and placed in a jar with grinding media (i.e., balls of various sizes and materials). Stainless steel balls are commonly used as grinding media due to their cost-effectiveness and good mechanical properties. However, for certain applications, such as when working with reactive or sensitive materials, harder and more chemically unreactive materials such as yttrium-doped zirconia or tungsten carbide may be preferred to prevent contamination and ensure consistent results. The choice of grinding media can play a crucial role in the success of a mechanochemical synthesis.

Planetary ball mills are widely used in research laboratories for their high efficiency and ability to reduce the particle size of materials to the nanoscale. Unlike the industrial mills where one rotation axis is used, the addition of a sun wheel and an extra rotating disk on which the jar is placed and rotating in opposite direction for increased impact and shear forces, leading to more effective grinding and mixing of the powder mixture in laboratory ball mill allows. A combination of centrifugal, tangential, and impact forces are utilized to transfer energy to a powder material, resulting in a significant

reduction in the average particle size and, potentially, the triggering of a chemical reaction. The forces involved in planetary ball milling are indeed complex and difficult to predict with our current mathematical understanding, as they depend on a variety of factors such as the size and material of the grinding media, the rotation speed of the sun wheel and jar, and the powder mixture itself. However, simplified models can be used to estimate the forces involved and optimize the milling conditions (Shown in **Figure 7.1**). As the jar and sun wheel are rotating in opposite directions, with the sun wheel ( $r_1$ ) generating a centrifugal force ( $F$ ) that interacts with the spinning of the jar ( $r_2$ ). This interaction causes the forces applied on the balls leading to sudden changes in momentum and violent impacts against the wall of the jar, resulting in high-energy collisions. These high-energy impacts can induce changes in the material being processed and facilitate chemical reactions.

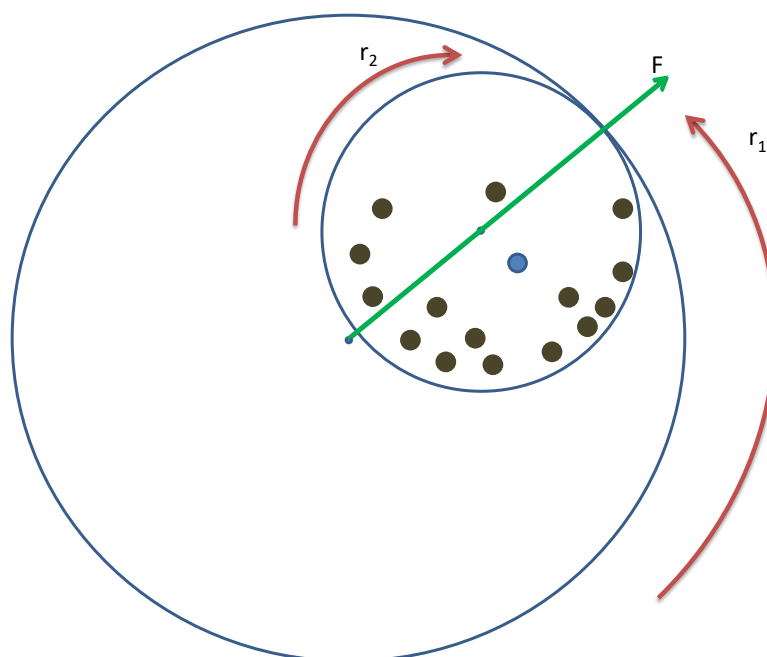


*Figure 7.1. Simplified schematic presentation of a planetary ball mill.*

### 7.1.2. High temperature solid-state reaction

High temperature solid state reaction is a well-established synthetic technique for metal chalcogenides that provide a grate control over stoichiometry of the product, using an oxygen-free environment. This efficient methods was used to synthesise our Bismuth

based sulphides and sulfotellurides, as well as their doped derivatives. The synthesis process involves carefully weighing the starting materials and placing them in evacuated fused silica tubes, which are then heated in a furnace for one or more cycles at elevated temperatures through a solid-state reaction. The solid-state reaction results in the formation of the final product, which is often a compound or alloy. However, the synthesis process requires careful consideration when synthesizing samples containing sulfur to prevent the rapid build-up of pressure that can lead to an explosion. Therefore, a slow heating rate is necessary to avoid the risk of explosion, while a slow cooling rate allows the sulfur to reintegrate into the powder without condensing on the inside wall of the tube. To further reduce the risk of moisture contamination, sulfur flakes are preferred over sulfur powder due to their much lower surface to volume ratio, which limits the adsorption of moisture. Homogeneity is also critical to ensure complete reaction and consistent stoichiometry in the final product, as slow diffusion rates of the solid reagents can lead to partial reactions and variations in stoichiometry. Despite using high temperatures, the synthesis process results in a solid-liquid-gas phase reaction, since sulfur has a low melting point of 388.2 K. This results in good homogeneity, and the reaction time is shorter than the few days or weeks that are typically required for other high-temperature reactions.

### **7.1.3. Spark Plasma Sintering (SPS)**

The Spark Plasma Sintering (SPS) method is an effective sintering technique which combines the utilization of uniaxial pressure and electric current to densify sample. In contrast to traditional techniques like hot pressing (HP), Spark Plasma Sintering (SPS) uses the application of an electric current to the specimen for heating, leading to numerous benefits. A significant advantage is the enhanced regulation of temperature, attributable to the direct resistive heating mechanism. This makes it possible to regulate the temperature precisely and quickly, preventing grain development and achieving ideal densification. SPS enables quicker sintering periods than conventional air convection heating, making it a time-saving procedure. Moreover, SPS exhibits a notable advantage over HP sintering due to its enhanced capacity for regulating sulfur stoichiometry. The employment of Spark Plasma Sintering

(SPS) technique results in a reduced sintering time, thereby minimizing the probability of undesired reactions and facilitating improved regulation of sulfur content. In the process of sample preparation, powders were placed into a die with a diameter of 10 mm and subjected to sintering at a temperature of 723 K under uniaxial pressure of 64 MPa using a graphite die. The heating rate was set at 50 K min<sup>-1</sup>, followed by a cooling rate of 30 K min<sup>-1</sup>, and a vacuum environment was maintained for a holding time of 30 minutes. The previously mentioned conditions were optimized specifically for samples of aikinite series.

*Table 7.1. Supplier and purity of the chemicals.*

| Precursor               | Supplier   | Purity (%) |
|-------------------------|------------|------------|
| <b>Cu</b>               | Alfa Aesar | 99 %       |
| <b>Pb</b>               | Alfa Aesar | 99.99 %    |
| <b>Bi</b>               | Alfa Aesar | 99.99 %    |
| <b>S</b>                | Alfa Aesar | 99.5 %     |
| <b>Te</b>               | Alfa Aesar | 99.99 %    |
| <b>BiCl<sub>3</sub></b> | Alfa Aesar | 99.9 %     |

## 7.2. Structural characterization

### X-ray powder diffraction

The analysis of samples using X-ray powder diffraction is a systematic procedure performed following synthesis steps, typically conducted in a sealed tube or through mechanical synthesis, and subsequent sintering using Spark Plasma Sintering (SPS) equipment. It allows for the determination of the crystal structure of the samples, providing insights into the arrangement of atoms within the material. It helps in verifying the presence of secondary phases within the samples. The detection limit of the X-ray diffraction device is considered during this assessment. It aids in identifying

the nature or composition of any secondary phases present in the samples. The process involves obtaining diffractograms by subjecting previously ground powder samples to X-ray analysis. These samples are prepared by grinding in an agate mortar and then sieving to a particle size of 200  $\mu\text{m}$ . In the CRISMAT laboratory, three different diffractometers were utilized throughout the thesis work. The selection of a particular diffractometer was based on either the sample's characteristics or the desired level of analysis precision. These instruments are described as follows:

X'PERT Pro MPD PANalytical 2-Circle Diffractometer (Philips) with Copper Anticathode: This diffractometer is equipped with a copper anticathode, emitting radiations with wavelengths of  $K_{\alpha 1} = 1.5406 \text{ \AA}$  and  $K_{\alpha 2} = 1.5444 \text{ \AA}$ . A PIXcel detector is employed, and the device incorporates a nickel filter to eliminate  $K_{\beta}$  radiation from copper. The configuration of this diffractometer is in Bragg-Brentano 0-0 geometry.

D8 Advance Variol 2-Circle Diffractometer (Bruker) with Copper Anticathode: This diffractometer features a copper anticathode emitting radiation with a wavelength of  $K_{\alpha 1} = 1.5406 \text{ \AA}$ . It utilizes a LynxEye detector and incorporates a Johansson-type Ge (111) front monochromator to suppress  $K_{\beta}$  and  $K_{\alpha 2}$  radiation from copper. The configuration of this diffractometer is in Bragg-Brentano 0-20 geometry.

### 7.3. Electronic microscopy

Electron microscopy is a valuable characterisation tool that enables the morphology, and the chemical composition of a sample to be investigated. By focusing an electron beam onto a sample's surface, electron microscopes can provide high magnification and resolution. The beam is generated by an electron gun, then directed and focused by magnetic lenses. Two commonly used types of electron microscope are Transmission Electron Microscopes (TEM), which can detect electrons passing through a thin sample, achieving resolutions of a few Angstroms, and Scanning Electron Microscopes (SEM), which require little to no sample preparation and have resolutions of a few nanometres. In this study, SEM with Energy-Dispersive X-ray spectroscopy (EDX) was used to analyze the particle size, morphology, and elemental composition

and TEM was used specifically to determine the crystal structure of the sample by using Electron diffraction (ED) along with previously mentioned physical properties.

### 7.3.1 Scanning Electron Microscopes (SEM)

Scanning electron micrographs and electron energy dispersive spectroscopy (EDS) analyses were collected using a JEOL JSM 7200F scanning electron microscope (SEM) equipped with an EDX X-Flash Bruker detector. In the study, the choice of using secondary electron detection mode and back-scattered electron detection mode for the micrographs was driven by the need to obtain comprehensive information about the surface morphology, composition, and bulk properties of the samples. By utilizing the secondary electron detection mode, it was possible to achieve a high spatial resolution for observing intricate surface details and variations in topography. The method resulted in valuable information regarding the surface characteristics and chemical composition of the sample by detecting the secondary electrons that were emitted from its surface.

Conversely, the utilization of back-scattered electron detection mode was implemented to examine the overall composition of the specimens. The back-scattered electrons are capable of reflecting from the underlying layers of the material, thereby conveying valuable information pertaining to the density and atomic number of the sample. This mode provided valuable data on the overall composition and structure of the samples, particularly in terms of their elemental constituents and density variations. The imaging process was carried out by securely placing the samples onto an aluminium sample holder utilizing carbon tabs. The implementation of carbon tabs obviated the requirement for sample coating, a customary practice for ensuring the electrical insulation of samples. Subsequently, the sample holder containing the affixed samples was introduced into the imaging chamber, which was subjected to a vacuum pressure lower than  $10^{-4}$  Torr, thereby establishing a high-vacuum milieu. To enhance the quality of the image and optimize the signal-to-noise ratio, an accelerating voltage of 20kV was utilized during the imaging process.

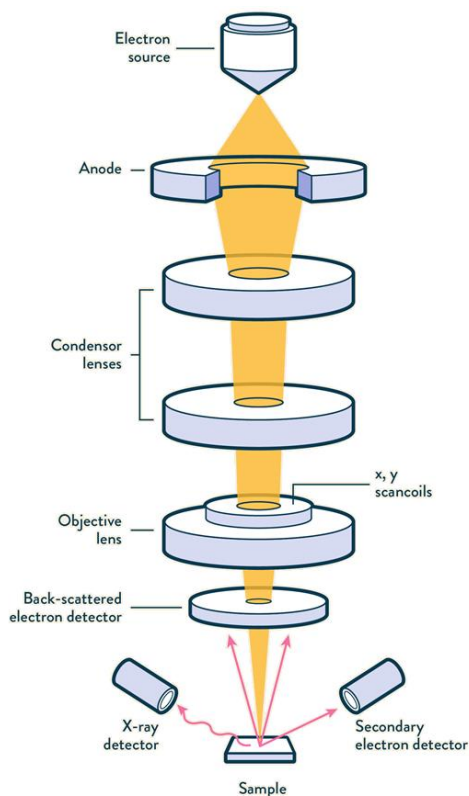


Figure 7.7. Diagram of a SEM instrument

### 7.3.2 EDX analysis

EDX (Energy-Dispersive X-ray Spectroscopy) is a technique used for elemental analysis of a sample. The practical principle involves the identification of distinct X-rays that are emitted as a result of the displacement of inner shell electrons by an electron beam. Every chemical element possesses a distinctive collection of energy transitions, which give rise to its characteristic "atomic signature." The EDX detector is utilized to quantify the emitted X-rays and subsequently match their energies against a pre-existing database to ascertain the composition of the specimen. The technique offers both qualitative and quantitative elemental data, facilitating the examination of the distribution and concentration of elements in the sample. This process is akin to the production of monochromated X-rays in X-ray diffraction (XRD) techniques. In XRD, a monochromator is used to select a specific wavelength of X-rays for diffraction experiments. Similarly, in EDX, the characteristic X-rays emitted by the sample are measured and analyzed to determine the elemental composition.

### 7.3.3. Transmission Electron Microscopy

The samples utilized in this investigation were fabricated through the use of gridding and ion milling methodologies, assisted by a Leica EM Res 102 apparatus. Following the preparation process, the samples were subjected to characterization via transmission electron microscopy (TEM). The analysis of the Transmission Electron Microscopy (TEM) incorporated various methodologies, including High-Resolution TEM (HRTEM), Selected Area Electron Diffraction (SAED), and High Angle Annular Dark Field (HAADF) imaging. The transmission electron microscopy (TEM) analysis was performed utilizing a ThermoScientific Talos F200S microscope, with an acceleration voltage of 200 kV. These techniques allowed for detailed observations of the sample's structure, lattice arrangement, and elemental composition at the nanoscale level.

### 7.4. Thermal Gravimetric Analysis (TGA) and Differential Scanning Calorimetry (DSC)

Thermal Gravimetric Analysis (TGA) is a thermal analysis technique used to determine the changes in the mass of a sample as a function of temperature. It offers details on the composition, thermal stability, and decomposition of a variety of materials. Differential scanning calorimetry (DSC) is a thermal analysis methodology that quantifies the heat flow (power) of a specimen in relation to a reference substance with respect to time or temperature. In heat-flux DSC, a single heater is used to raise the temperature of both the sample and an empty reference. The difference in heat flux between the sample and reference is monitored, allowing small temperature differences resulting from exothermic or endothermic processes in the sample to be recorded. For the experiments in this study, STA 449 F3 Jupiter instrument by Netzsch was utilized. The instrument exhibits a maximum temperature capacity of 2273 K. Throughout the DSC-TGA analysis, a nitrogen purge was consistently applied to the furnace as the temperature underwent a gradual increase from room temperature (RT) to our desire temperature at a heating rate of  $5 \text{ K min}^{-1}$ . The heat flow and temperature changes of the

sample and reference were recorded throughout the experiment, providing valuable information about the thermal behavior, stability, and phase transitions of the materials.

## 7.5. Electronic transport measurement

The power factor of the  $ZT$  expression depends on the product of the Seebeck coefficient and the electrical conductivity. The Seebeck coefficient is the ratio of a resulting electric field gradient to an applied temperature gradient. In a typical measurement, the temperature is varied around a constant average temperature and the slope of the voltage ( $V$ ) vs. temperature difference ( $\Delta T$ ) curve gives the Seebeck coefficient (the slope method) or just  $V/\Delta T$  is measured (single point measurement). Either a specific temperature difference is stabilized before each measurement (steady-state), which takes longer, or measurements are conducted continuously while the temperature difference is varied slowly (quasi-steady-state). Little difference was found between steady-state and quasi-steady-state measurements when good thermal and electrical contact is ensured. The employed temperature difference should be kept small, but too small will lead to decreased accuracy.

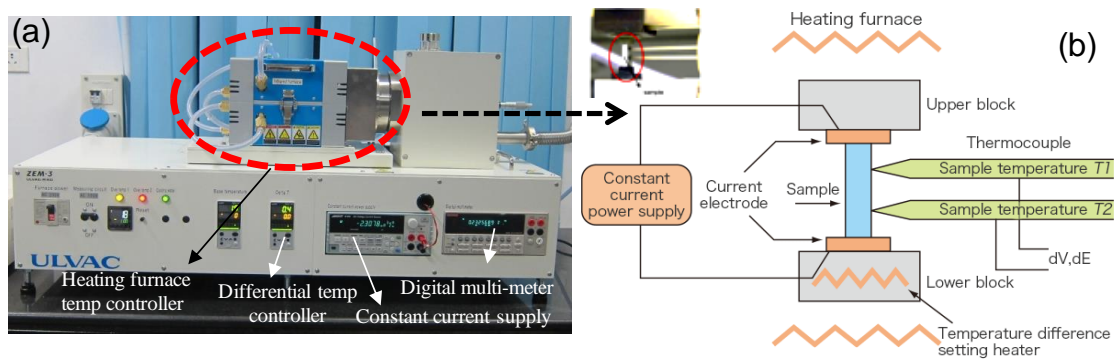


**Figure 6.2.** (a) Photograph of sample-chamber in ULVAC-ZEM3 apparatus. (b) Schematic of ULVAC-ZEM 3 four-probe measurement system.<sup>1</sup>

In the present thesis, temperature dependent Seebeck coefficient measurement has been done using the most popular commercial instruments ULVAC ZEM 3 RIKO using off-axis 4-point geometry under low-pressure helium (He) atmosphere (Figure

7.2. a). In the off-axis, 4-point geometry, the thermocouples, and voltage leads are pressed against the sides of the sample (Figure 7.2. b). The instrument uses slope method to extract the Seebeck coefficient from steady-state measurements. In the slope method, the measured raw data is corrected for constant offset voltages by using the slope of several  $(\Delta T, V)$  points for extracting the Seebeck coefficient. The typical sample for measurement has a rectangular shape with the dimensions of  $\sim 3 \text{ mm} \times 3 \text{ mm} \times 8 \text{ mm}$  and  $\Delta T$  values 10, 20, 30 K have been used in the measurement. The error in the measurement is  $\sim 5\%$ . In a typical measurement, the sample is set in a vertical position between the upper and lower electrode blocks in the heating furnace. For temperature dependent measurement, the sample was first heated to a specified temperature using an infrared (IR) furnace. Thereafter a temperature gradient across the sample was created by heating the lower part of it by a heater. Seebeck coefficient is measured by measuring the upper and lower temperatures  $T_1$  and  $T_2$  with the thermocouples pressed against the side of the sample, followed by measurement of voltage  $(\Delta V)$  between the same wires on one side of the thermocouple.<sup>1</sup>

The electrical conductivity,  $\sigma$  is measured using the four-probe method. Temperature dependent  $\sigma$  has been measured concurrently during Seebeck measurement in ULVAC ZEM 3 RIKO. For the measurement, a constant current  $I$  is applied to both ends of the sample to measure the voltage  $V$  between the thermocouples. By knowing resistance of sample,  $R$  ( $R = V/I$ ), we can calculate  $\sigma$  from resistivity ( $\rho$ ) of the sample using following equations:

$$\rho = R \times \frac{A}{l}$$

$$\sigma = \frac{1}{\rho}$$

Where,  $A$  is sample cross section and  $l$  is the distance between probes.

## 7.6. Hall effect

The Hall effect describes the behavior of the free carriers in a semiconductor when an electric and a magnetic field is applied along the perpendicular direction.<sup>2</sup> Thus, measurement of the Hall voltage is used to determine the type of charge carrier present in the system, the free carrier density and the carrier mobility. When a current-carrying semiconductor is kept in a magnetic field, the charge carriers of the semiconductor experience a force in a direction perpendicular to both the magnetic field and the current. At equilibrium, a voltage appears at the semiconductor edges. The ratio of the induced voltage to the product of the current density ( $I/t$ , where  $I$  is applied current and  $t$  is sample thickness),  $n$  is charge carrier density, and the applied magnetic field ( $B$ ) is defined as Hall coefficient ( $R_H$ ) as shown in the equation:

$$R_H = \frac{Vt}{IB}$$

$$n = \frac{1}{R_H e}$$

Where,  $e$  is the charge of an electron ( $1.602 \times 10^{-19}$  C). In this thesis Hall measurement has been done in an in-house equipment developed by Excel instrument. We have used a four-contact Hall-bar geometry and a varying magnetic field up for the measurements.

## 7.7. Thermal conductivity

The flash diffusivity method most frequently is used for the determination of thermal conductivity ( $\kappa$ ) of material. Non-contact, non-destructive, easy sample preparation, applicability for a wide range of diffusivity values with excellent accuracy and reproducibility makes this method more advantageous than direct method. In the flash diffusivity method, the thermal conductivity is calculated as  $\kappa = DC_p\rho$ , where  $D$  is thermal diffusivity,  $\rho$  is density, and  $C_p$  is the constant pressure heat capacity. In this method, the sample is mounted on a carrier system, which is located in a furnace. After the sample reaches a predetermined temperature, a short heat pulse from a pulsed laser is applied to one side of a thin sample, resulting in homogeneous heating. The relative temperature increase on the rear face of the sample is then measured as a function of time by an IR detector. The temperature will rise to a maximum, after which it will

decay. The time for the temperature to increase to half-maximum,  $t_{1/2}$ , is used to calculate the thermal diffusivity using the following equation:

$$D = 0.1388 \times \frac{l^2}{t_{1/2}}$$

where  $D$  is thermal diffusivity in  $\text{cm}^2 \text{sec}^{-1}$ ,  $l$  is the thickness.<sup>3</sup>

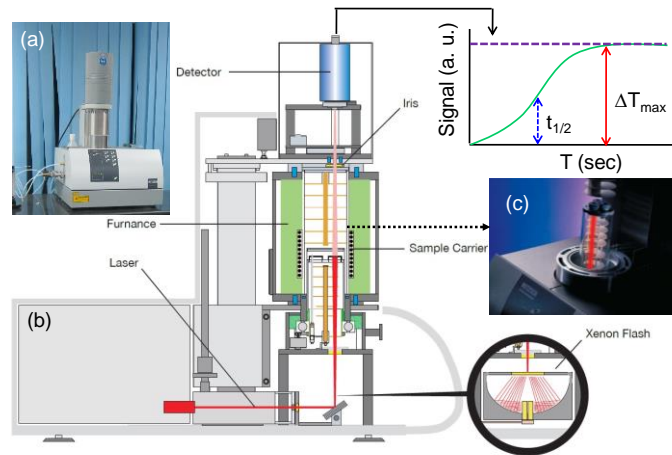


**Figure 7.3.** (a) Photograph of NETZSCH LFA-457 instrument. (b) and (c) Schematic of LFA-457 diffusivity measurement apparatus.

In this thesis, temperature dependent thermal transport measurement (300 - 700 K) has been done using the most popular NETZSCH LFA-457 instrument in  $\text{N}_2$  atmosphere (Figure 7.3.). The samples were coated with a thin layer of graphite ( $\sim 5 \mu\text{m}$ ) in order to enhance the absorption of laser energy and emission of IR radiation to the detector. It also increases the signal to noise ratio. The error for the  $\kappa$  measurement is  $\sim 5\%$ . The samples were placed inside SiC sample holder to mount on carrier system (Figure 7.3.). A Nd-Glass pulsed laser source of wavelength 1054 nm has been used for all the measurement. To measure the increased temperature on the rear face of the sample a liquid  $\text{N}_2$  cooled InSb IR detector has been used. The thermal diffusivity data were analyzed using a Cowan model with pulse correction to account for heat losses on the sample faces.<sup>4</sup>

## 7.8. Heat capacity

The Quantum Design Heat Capacity option measures the heat capacity at constant pressure

$$C_p = \left(\frac{dQ}{dT}\right)_p$$

As with other techniques for measuring heat capacity, the Quantum Design Heat Capacity option controls the heat added to and removed from a sample while monitoring the resulting change in temperature. During a measurement, a known amount of heat is applied at constant power for a fixed time, and then this heating period is followed by a cooling period of the same duration. A platform heater and platform thermometer are attached to the bottom side of the sample platform (Figure 7.4).

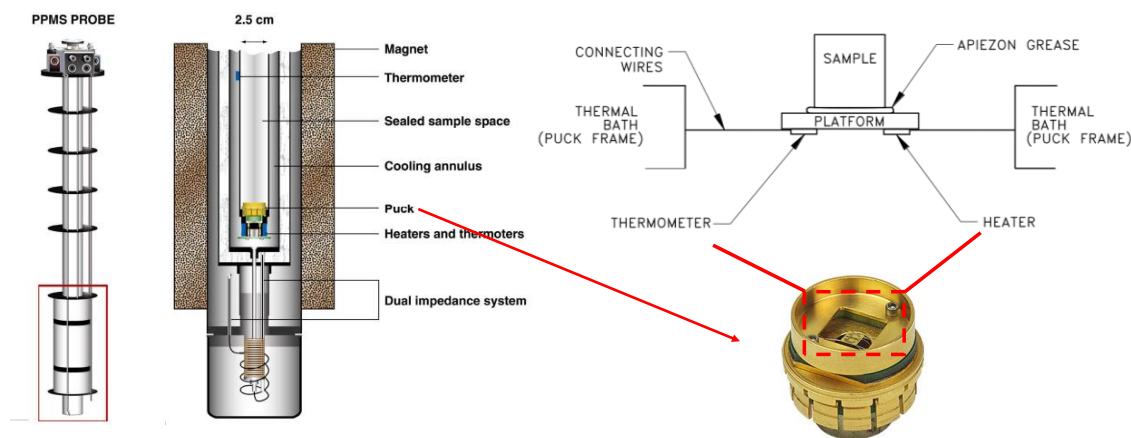


**Figure 7.4.** Left. Detailed view of the sample chamber of PPMS probe. Right. Heat capacity puck along with the schematic diagram of the sample stage.<sup>5</sup>

---

## 7.9. References

- (1) ULVACZEM3RIKO. *Seebeck-Coefficient and Electric-Resistance-Measuring-System Manual*; **2012**.
- (2) Hall, E. H. On a New Action of the Magnet on Electric Currents. *Am. J. Math.* **1879**, 2 (3), 287–292.
- (3) Parker, W. J.; Jenkins, R. J.; Butler, C. P.; Abbott, G. L. Flash Method of Determining Thermal Diffusivity, Heat Capacity, and Thermal Conductivity. *J. Appl. Phys.* **1961**, 32 (9), 1679–1684. <https://doi.org/10.1063/1.1728417>.
- (4) Cowan, R. D. Pulse Method of Measuring Thermal Diffusivity at High Temperatures. *J. Appl. Phys.* **1963**, 34 (4), 926–927. <https://doi.org/10.1063/1.1729564>.
- (5) Design, Q. Physical Property Measurement System, Torque Magnetometer Option User's Manual. *PPMS Man.* **1999**, 1085, 43.

---

## List of publications

---



1. K. Maji, P. Lemoine, A. Renaud, B. Zhang, X. Zhou, V. Carnevali, C. Candolfi, B. Raveau, R. Al Rahal Al Orabi, M. Fornari, P. Vaqueiro, M. Pasturel, C. Prestipino, E. Guilmeau, A Tunable Structural Family with Ultralow Thermal Conductivity: Copper-Deficient  $\text{Cu}_{1-x}\text{Pb}_x\text{Bi}_{1+x}\text{S}_3$ . *J. Am. Chem. Soc.* 2022, **144**, 1846-1860.
2. K. Maji, B. Raveau, P. Lemoine, P. Boullay, P. Acharyya, X. Shen, A. Renaud, V. Pelletier, R. Gautier, V. Carnevali, M. Fornari, B. Zhang, X. Zhou, B. Lenoir, C. Candolfi, E. Guilmeau, Rattling of three-fold coordinated copper in sulfides: a blockade for hole carrier delocalization but a driving force for ultralow thermal conductivity. (under review)
3. V. Carnevali, S. Mukherjee, D. J Voneshen, K. Maji, E. Guilmeau, A. V. Powell, P. Vaqueiro, M. Fornari. Lone Pair Rotation and Bond Heterogeneity Leading to Ultralow Thermal Conductivity in Aikinite. *J. Am. Chem. Soc.* 2023, **145**, 9313–9325.
4. X. Liu, D. Kepaptsoglou, Z. Gao, A. Thomas, K. Maji, E. Guilmeau, F. Azough, Q. M. Ramasse, R. Freer, Controlling the Thermoelectric Properties of Nb-Doped  $\text{TiO}_2$  Ceramics through Engineering Defect Structures. *ACS Appl. Mater. Interfaces.* 2021, **13**, 57326-57340.
5. K. Lohani, H. Nautiyal, N. Ataollahi, K. Maji, E. Guilmeau, P. Scardi, Effects of Grain Size on the Thermoelectric Properties of  $\text{Cu}_2\text{SnS}_3$ : An Experimental and First-Principles Study. *ACS Appl. Energy Mater.* 2021, **4**, 12604-12612.
6. X. Liu, J. Yu, B. Wang, K. Maji, D. T. Alvarez-Ruiz, E. Guilmeau, R. Freer, Enhancing the thermoelectric properties of Nb-doped  $\text{TiO}_2$ -based ceramics through in-situ synthesis of  $\beta$ -Sn inclusions at grain boundaries. *J. Eur. Ceram. Soc.* 2023, **43**, 2523-2533.

